EVOLUTION OF THE QUASAR POPULATION AT HIGH REDSHIFT

by

Linhua Jiang

A Dissertation Submitted to the Faculty of the

DEPARTMENT OF ASTRONOMY

In Partial Fulfillment of the Requirements
For the Degree of

DOCTOR OF PHILOSOPHY

In the Graduate College

THE UNIVERSITY OF ARIZONA

2 0 0 8

THE UNIVERSITY OF ARIZONA
GRADUATE COLLEGE

As members of the Final Examination Committee, we certify that we have read the dissertation prepared by Linhua Jiang
entitled Evolution of the Quasar Population at High Redshift
and recommend that it be accepted as fulfilling the dissertation requirement for the Degree of Doctor of Philosophy.

_____   Date: 10 June 2008
   Xiaohui Fan

_____   Date: 10 June 2008
   Eiichi Egami

_____   Date: 10 June 2008
   Daniel Eisenstein

_____   Date: 10 June 2008
   Richard Green

_____   Date: 10 June 2008
   George Rieke

Final approval and acceptance of this dissertation is contingent upon the candidate's submission of the final copies of the dissertation to the Graduate College.

I hereby certify that I have read this dissertation prepared under my direction and recommend that it be accepted as fulfilling the dissertation requirement.

_____   Date: 10 June 2008
Dissertation Director: Xiaohui Fan

STATEMENT BY AUTHOR

This dissertation has been submitted in partial fulfillment of requirements for an advanced degree at The University of Arizona and is deposited in the University Library to be made available to borrowers under rules of the Library.

Brief quotations from this dissertation are allowable without special permission, provided that accurate acknowledgment of source is made. Requests for permission for extended quotation from or reproduction of this manuscript in whole or in part may be granted by the head of the major department or the Dean of the Graduate College when in his or her judgment the proposed use of the material is in the interests of scholarship. In all other instances, however, permission must be obtained from the author.

SIGNED: _____
Linhua Jiang

ACKNOWLEDGEMENTS

First I would like to thank my advisor Xiaohui Fan for his guidance, encouragement, and his friendship. He always inspires me to develop independent thinking and research skills, and to collaborate with others in different fields. Without his support, I could not have done my doctoral work.

I am grateful for having an excellent committee, and wish to thank Eiichi Egami, Daniel Eisenstein, Richard Green, and George Rieke for their generous time, useful advice, and continual support.

I am also grateful to my collaborators, especially the SDSS quasar group members. I thank them for numerous discussions on my research work and comments on my papers, which have greatly broadened my horizons.

It is a great opportunity to acknowledge all my friends at the Steward Observatory who helped me in the past five years. This hospitality is particularly important for me, an international student from the other side the Earth.

Finally, I would like to thank my family. My wife and I got married two and a half years ago. She is always behind me and supporting me. I dedicate this dissertation to my parents. My mother always told me "I could have gotten a PhD if I had had the chance to go to school." Of course she had no chance to go to school in that time, but I believe what she said.

TABLE OF CONTENTS

TABLE OF CONTENTS – *Continued*

TABLE OF CONTENTS – *Continued*

LIST OF FIGURES

LIST OF FIGURES – *Continued*

LIST OF TABLES

LIST OF TABLES – *Continued*

ABSTRACT

High-redshift ($z \sim 6$) quasars have been served as cosmological probes for studying the early universe. They provide crucial information on the growth of massive black holes (BHs) and formation of galaxies in the first billion years. I focus my dissertation work on exploring various properties of quasars at $z \sim 6$.

Based on our Gemini NIR observations, the metallicity in luminous $z \sim 6$ quasars is supersolar with a typical value of ~ 4 $Z_\odot$, and a comparison with low-redshift observations shows no strong evolution in metallicity up to $z \sim 6$. Central BH masses are found to be $10^9 \sim 10^{10}$ $M_\odot$ and Eddington luminosity ratios are of order unity. Our *Spitzer* observations show that most of $z \sim 6$ quasars have prominent emission from hot dust. Their SEDs are similar to those of low-redshift quasars at rest-frame 0.15–3.5 μm, suggesting that their accretion disks and hot-dust structures have reached maturity. However, two quasars were not detected in our deep 24 μm images, and thus show no hot-dust emission, indicating different dust properties. Our ongoing survey of $z \sim 6$ quasars has resulted in six quasars with $z_{AB} < 21$ in the SDSS deep area. The bright-end power-law slope of the quasar luminosity function (QLF) derived from available SDSS quasars is significantly steeper than the slope of the QLF at $z \sim 4$. Based on this QLF, the quasar population cannot provide enough photons to ionize the IGM at $z \sim 6$ unless the IGM is very homogeneous and the luminosity at which the QLF power law breaks is very low.

My work also includes interesting topics of quasars at lower redshifts. Our deep spectroscopic survey of quasars at $z < 4$ shows that the quasar density at $M_g < -22.5$ peaks at $z \sim 2$, which is later in cosmic time than the peak of $z \sim 2.5$ found from surveys of more luminous quasars ($M_g < -26$). This confirms 'cosmic downsizing' in quasar evolution. Using a sample of more than 30,000 quasars from SDSS, we find that the radio-loud fraction (RLF) in optically-selected quasars

decreases rapidly with increasing redshift and decreasing optical luminosity. This result presents an important constraint on the radio emission mechanism and its cosmic evolution. We obtain 293 quasars with strong N IV] $\lambda 1486$ or N III] $\lambda 1750$ emission lines from SDSS. These nitrogen-rich (N-rich) objects comprise $\sim 1.1\%$ of the SDSS quasars, and have high overall nitrogen abundances. They share many common properties with other quasars. However, the RLF in the N-rich quasars is much higher than that in other quasars with similar redshift and luminosity. This implies that the high nitrogen abundance in N-rich quasars could be an indicator of a special quasar evolution stage, in which the radio activity is also strong.

CHAPTER 1

INTRODUCTION

Quasars (or QSOs, quasi-stellar objects) were first discovered as star-like objects, and were soon identified to be extragalactic sources with extremely high luminosities from radio to X-ray. They are one of the most energetic phenomena known in the universe, powered by large amount of hot gas falling into massive black holes (BHs) at the center of their host galaxies. Because of their high luminosities, quasars can be seen at great distances from the Earth. The most distant quasars known to date are at redshifts ~ 6.4 (Fan et al., 2003; Willott et al., 2007), at this epoch the universe was less than one billion years old. Therefore, these distant quasars can be served as cosmological probes for studying the universe in its first billion years.

1.1 Basic Picture of Quasars

An active galactic nucleus, or AGN, refers to the energetic phenomena in the nuclear regions of galaxies (Peterson, 1997). AGNs are often classified into several broad categories, in which Seyfert galaxies and quasars are the two largest. The fundamental difference between Seyfert galaxies and quasars is their luminosities: quasars are brighter than $M_B = -21.5 + 5 \log h_0$ (Schmidt & Green, 1983). Seyfert galaxies were first systematically studied by Seyfert (1943), who found a sample of galaxies with high central brightness and broad optical emission lines. The sizes of the central bright regions are less than 100 pc, while the masses (inferred from the widths of emission lines) within the central regions can be higher than one billion solar masses. Twenty years later, the first quasars were identified from strong radio sources (Schmidt, 1963). The emission lines in these quasars were redshifted to larger wavelengths with respect to their laboratory wavelengths due to cosmological recession. This indicates that quasars are at great distances and have very high
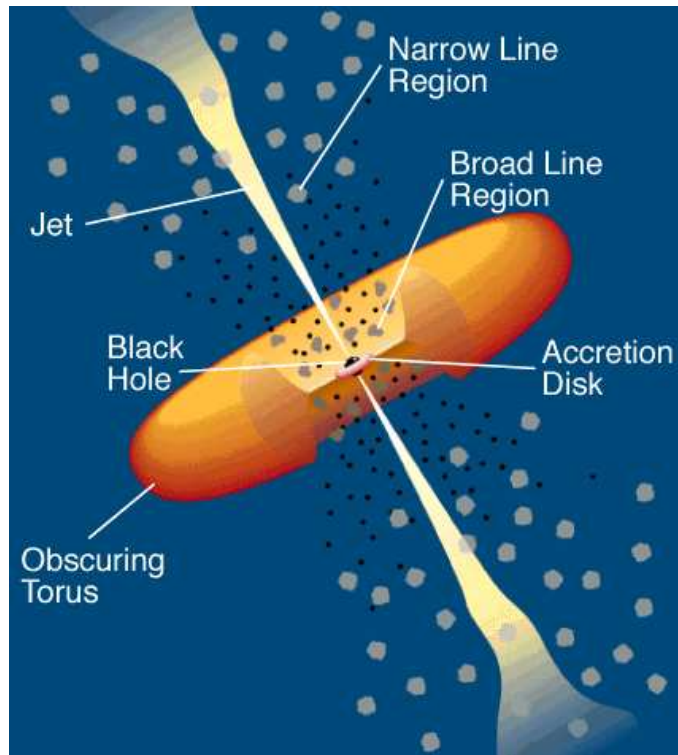
Figure 1.1 A diagram of an AGN, showing the primary components (from http://www.oulu.fi/astronomy/astrophysics/pr/agn_model.gif).

luminosities.

One fundamental question about quasars is how they produce such tremendous energy. It was proposed soon after the discovery of the first quasars that the energy output was related to massive BHs. At the center of each quasar, there lies a BH with a typical mass of a hundred million solar masses. As the surrounding gas falls onto the central BH by gravitational accretion, a huge amount of potential energy is released, and is eventually converted to radiation over a broad spectral range. Unlike normal galaxies, quasars have relatively flat spectral energy distributions (SEDs) from X-ray to infrared (IR), with two bumps, blue (UV) and red (mid-IR; or MIR) bumps, contributed from the disk and dust emission, respectively (e.g. Elvis et al., 1994).

The following basic structure of quasars based on AGN unification models (e.g. Antonucci, 1993) has been broadly accepted (Figure 1.1). Outside of the central

BH, there is a geometrically-thin but optically-thick accretion disk (which therefore emits photons as a black body). The inner edge of the disk is usually a few times the Schwarzschild radius R_S, and the outer edge can be many times R_S. The continuum emission from the disk extends from the UV to near-IR (NIR). Near the central engine, X-ray radiation is produced by inverse-Compton scattering of low-energy photons. Extended X-ray radiation can also be produced by thermal emission from hot gas. Surrounding the accretion disk is the broad-line region (BLR) with a typical size of 10^{16} cm. The BLR gas has a density of $\sim 10^{11}$ cm^{-3}, and produces broad emission lines. It is suggested that the BLR gas is gravitationally bound. The BLR is embedded in a much larger ($\sim 10^{17}$ cm) narrow-line region (NLR). The NLR gas has a relatively low gas density ($10^6 \sim 10^7$ cm^{-3}), and produces narrow emission lines. On an even larger scale, there is an optically thick dusty region called the dust torus. The dust torus absorbs high-energy photons and re-emits them in the IR. Strong radio jets are also commonly seen in quasars. Some jets extend kpc scales. How these jets are exactly maintained is not well understood. Quasars are variable sources in all wavebands. Variability in shorter wavelengths is more violent than that in longer wavelengths.

Quasars have two subclasses, type 1 and type 2 quasars. Type 2 quasars have emission lines narrower than 1000 km s^{-1} with a typical value of 500 km s^{-1}; while line widths in type 1 quasars are usually greater than 1500 km s^{-1}. According to the AGN unification models, type 1 and 2 quasars are the same type of objects, but viewed at different angles. In this work we will not study type 2 quasars.

1.2 Spatial Density Evolution of Quasars

One of the most important properties of quasars is their strong density evolution with cosmic time. The quasar luminosity function (QLF) is thus of particular importance in understanding quasar formation and evolution and exploring physical models of quasars. It has been shown that quasar activity and the formation processes of galaxies and massive BHs are closely correlated (e.g. Kauffmann & Haehnelt,

2000; Wyithe & Loeb, 2003; Hopkins et al., 2005; Croton et al., 2006), so the QLF is essential to study galaxy formation, the accretion history of BHs during the active quasar phase, and its relation to galaxy evolution. Quasars are strong X-ray sources; thus the QLF can provide important constraints on the quasar contribution to the X-ray and ultraviolet background radiation (e.g. Koo & Kron, 1988; Boyle & Terlevich, 1998; Mushotzky et al., 2000; Worsley et al., 2005). The QLF is also useful for understanding the spatial clustering of quasars and its relation to quasar life times (e.g. Martini & Weinberg, 2001).

The differential QLF is defined as the density of quasars per unit comoving volume and unit luminosity interval as a function of luminosity and redshift ($\Phi(L, z)$). If the redshift and luminosity dependence is separable, the QLF can be modeled in terms of pure density evolution, pure luminosity evolution, or a combination of the two forms. Determining QLFs requires large and unbiased samples. Early work based on samples of a few tens of quasars already found that there was a strong decline of quasar activity from $z \sim 2$ to the present universe, and a model with a single power-law shape provided good fits to the observed QLF for $z < 2$ at the bright end (Marshall et al., 1983, 1984; Marshall, 1985). As of the late 1980s, the number of known quasars reached a few hundred, which allowed more accurate QLF determinations. When more fainter quasars were discovered, a break was found in the luminosity function (e.g. Koo & Kron, 1988; Boyle, Shanks, & Peterson, 1988), and the shape of QLF was modeled by a double power-law form with a steep bright end and a much flatter faint end. In this double power-law model, luminosities evolve as pure luminosity evolution, and density evolution is not necessary. For example, Boyle, Shanks, & Peterson (1988) found $\Phi(L, z) \propto L^{-3.7}$ at the bright end and $\Phi(L, z) \propto L^{-1.4}$ at the faint end.

Some studies cast doubt on the claim of double power-law QLFs. First, the existence of the break in the QLF slope is not obvious in a few quasar samples (e.g. Hawkins & Véron, 1995; Goldschmidt & Miller, 1998; Wisotzki, 2000), including the COMBO-17 sample (Wolf et al., 2003). The COMBO-17 survey uses photometric redshifts, and collects quasars in an area of $\leq 1 \deg^2$. Its QLF can be fitted by either a

pure luminosity evolution or a pure density evolution, without a noticeable change in the slope (Wolf et al., 2003). Second, it was found that the pure luminosity evolution model was probably not sufficient to describe the quasar evolution at $z < 2$, and density evolution was needed (e.g. Hewett, Foltz, & Chaffee, 1993; La Franca & Cristiani, 1997; Goldschmidt & Miller, 1998; Wisotzki, 2000).

One of the largest homogeneous samples of low-redshift quasars comes from the 2dF QSO Redshift Survey and 6dF QSO Redshift Survey (hereafter 2QZ; Boyle et al., 2000; Croom et al., 2004). The 2QZ survey includes 25,000 quasars, and covers a redshift range of $0.4 < z < 2.1$ and a magnitude range of $16 < b_J < 20.85$. The QLF derived from the 2QZ can be well fitted by a double power-law form with a steep slope at the bright end and a flatter slope at the faint end, showing a break in the QLF. The evolution is well described by pure luminosity evolution. The Sloan Digital Sky Survey (SDSS; York et al., 2000) is collecting the largest spectroscopic samples of galaxies and quasars to date. The SDSS main quasar survey covers a large redshift range from $z = 0$ to $z > 5$, however, it only selects bright objects: it targets quasars with $i < 19.1$ at $z \leq 3$ and $i < 20.2$ at $z \geq 3$ (Richards et al., 2002). The QLF derived from SDSS Data Release Three (DR3; Schneider et al., 2005) shows some curvature at the faint end, but the survey does not probe faint enough to test the existence of the break (Richards et al., 2006b). The best fit model of the SDSS-DR3 QLF shows, for the first time in a single large redshift range, the flattening of the QLF slope with increasing redshift. Selecting $g < 21.85$ and $z < 2.5$ quasar candidates from SDSS imaging and spectroscopically observing them with the 2dF instrument, the 2dF-SDSS LRG and QSO Survey (2SLAQ) probes deeper than either the SDSS or the 2QZ (Richards et al., 2005). The QLF of the 2SLAQ is consistent with the 2QZ QLF from Boyle et al. (2000), but has a steeper faint-end slope than that from Croom et al. (2004).

The density of luminous quasars reaches a maximum at $2 < z < 3$ (hereafter referred to as the mid-z range), and drops rapidly toward higher redshift (e.g. Pei, 1995). Figure 1.2 shows the evolution of the quasar comoving spatial density at $M_{1450} < -26.8$ in the Λ-model (H$_0 = 70$ km s^{-1} Mpc^{-1}, $\Omega_m = 0.3$, and $\Omega_\Lambda = 0.7$).
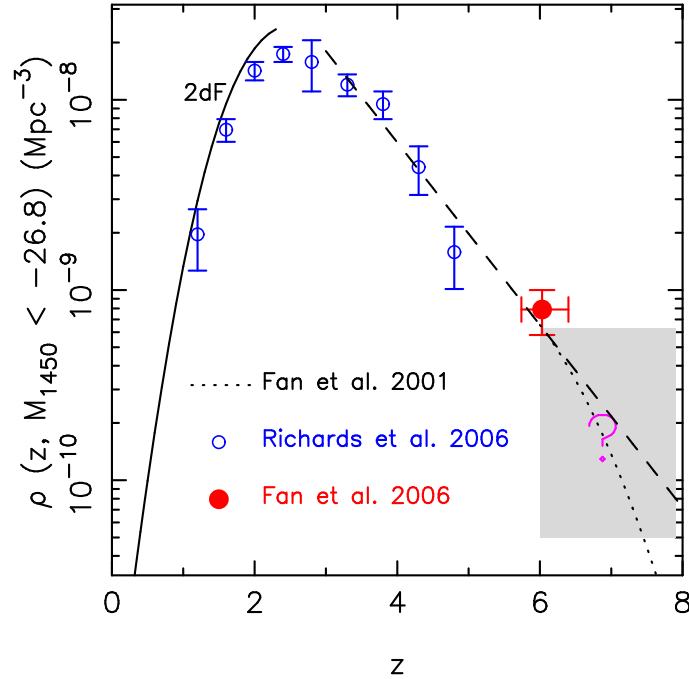
Figure 1.2 Evolution of the quasar comoving spatial density at $M_{1450} < -26.8$ in the Λ-model ($H_0 = 70$ km s^{-1} Mpc^{-1}, $\Omega_m = 0.3$, and $\Omega_\Lambda = 0.7$).

The figure clearly illustrates the general trend of the cumulated density evolution of luminous quasars from $z \sim 6$ to ~ 0: the density increases rapidly from $z \sim 6$ to $z = 2 \sim 3$, and then drops even faster to $z \sim 0$. The exact position of the density peak has not been well determined. The QLF at $z > 3$ was explored only for bright quasars (e.g. Warren, Hewett, & Osmer, 1994; Kennefick, Djorgovski, & De Carvalho, 1995; Schmidt, Schneider, & Gunn, 1995; Fan et al., 2001c; Richards et al., 2006b). At $z \sim 4$, the QLF was fitted by a single power-law form with an exponential decline in density with redshift (Schmidt, Schneider, & Gunn, 1995; Fan et al., 2001c), and its slope is much flatter than the bright-end slope of the QLF at $z < 3$. This has been confirmed by Richards et al. (2006b), who found that the slope at $z \sim 2.0$ is -3.1 ± 0.1 and the slope at $z \sim 4.1$ flattens to -2.1 ± 0.1, indicating that the shape of the QLF evolves with redshift as well.

From the above, we know that the optical QLF over both a large redshift range and a large luminosity range has not been well established. First, the faint-end

slope of the QLF is very uncertain. Most wide-field surveys, including the SDSS, are shallow and can only sample luminous quasars. Although the 2SLAQ survey probed to $g = 21.85$, it only covers the low-redshift range ($z \leq 2.2$). Furthermore, the existence of the break in the QLF slope is uncertain, and different surveys give different slopes at the faint end (e.g. Wolf et al., 2003; Croom et al., 2004; Richards et al., 2005). In addition, it is unclear whether pure density evolution is sufficient to describe quasar evolution at low redshift. Second, the density of luminous quasars peaks between $z = 2$ and $z = 3$, yet the colors of quasars with $2.2 < z < 3$ are similar to those of A and F stars, making selection of these objects difficult (Fan, 1999; Richards et al., 2002, 2006b). Third, the high-redshift ($z \sim 6$) QLF is far from well established due to the limited number of known quasars at this redshift.

In this dissertation we only consider the optical QLF of type 1 quasars. X-ray and infrared surveys provide other ways to determine the QLF of both type 1 and type 2 AGNs (e.g. Ueda et al., 2003; Barger et al., 2005; Hasinger, Miyaji, & Schmidt, 2005; Brown et al., 2006). These studies have shown that a substantial fraction of AGNs are optically obscured at low luminosities. Barger et al. (2005) found a downturn at the faint end of the hard X-ray luminosity function for type 1 AGN, but current optically-selected quasar samples are not sufficiently faint to probe this downturn, if it exists.

1.3 The Sloan Digital Sky Survey and the Discovery of High-Redshift Quasars

High-redshift quasars are among the most luminous objects known and provide direct probes of the distant universe when the first generation of galaxies and quasars formed. In recent years, over twenty $z \sim 6$ quasars with $z_{AB} \leq 20$ have been discovered (e.g. Fan et al., 2000a, 2001a, 2003, 2004, 2006a; Goto, 2006). These luminous quasars are essential for understanding the accretion history of BHs, galaxy formation, and chemical evolution at very early epochs. They harbor supermassive BHs with masses higher than 10^9 $M_\odot$ and emit near the Eddington limit (e.g. Barth et al., 2003; Vestergaard, 2004; Kurk et al., 2007), revealing the rapid growth of central

BHs at high redshift. Their emission lines show solar or supersolar metallicity in the BLRs, indicating that there was vigorous star formation and element enrichment in the first gigayear of cosmic time (e.g. Barth et al., 2003; Maiolino et al., 2003; Kurk et al., 2007). Their absorption spectra show that the intergalactic medium (IGM) at $z \sim 6$ is close to the reionization epoch (e.g. Becker et al., 2001; Djorgovski et al., 2001; Fan et al., 2006b,c).

The majority of the currently known $z \sim 6$ quasars were discovered from ~ 8500 deg^2 of the SDSS imaging data. SDSS is an imaging and spectroscopic survey of the sky (York et al., 2000) using a dedicated wide-field 2.5 m telescope (Gunn et al., 2006) at Apache Point Observatory, New Mexico. Imaging is carried out in drift-scan mode using a 142 mega-pixel camera (Gunn et al., 1998) which gathers data in five broad bands, $ugriz$, spanning the range from 3000 to 10,000 Å (Fukugita et al., 1996), on moonless photometric (Hogg et al., 2001) nights of good seeing. The images are processed using specialized software (Lupton et al., 2001; Stoughton et al., 2002), and are photometrically (Tucker et al., 2006) and astrometrically (Pier et al., 2003) calibrated using observations of a set of primary standard stars (Smith et al., 2002) on a neighboring 20-inch telescope. The photometric calibration is accurate to roughly 2% rms in the g, r, and i bands, and 3% in u and z, as determined by the constancy of stellar population colors (Ivezić et al., 2004; Blanton et al., 2005),while the astrometric calibration precision is better than 0.1 arcsec rms per coordinate (Pier et al., 2003). All magnitudes are roughly on an AB system (Abazajian et al., 2004), and use the asinh scale described by Lupton et al. (1999). From the resulting catalogs of objects, complete catalogs of galaxies (Eisenstein et al., 2001; Strauss et al., 2002) and quasar candidates (Richards et al., 2002) are selected for spectroscopic follow-up (Blanton et al., 2003). Spectroscopy is performed using a pair of double spectrographs with coverage from 3800 to 9200 Å, and a resolution $\lambda/\Delta\lambda$ of roughly 2000. The SDSS main quasar survey targets quasars with $i < 19.1$ at $z \leq 3$ and $i < 20.2$ at $z \geq 3$ (Richards et al., 2002). Its spectroscopic survey is based on its imaging data with an exposure time of 54 seconds, so it is a shallow survey, and can only sample the most luminous quasars.

The SDSS $z \sim 6$ quasars were selected as i-dropout objects using optical colors. The basic selection procedure contains the following separate steps (e.g. Fan et al., 2003). In the first step, i-dropout sources from the SDSS imaging data were selected. Objects with $i_{AB} - z_{AB} > 2.2$ and $\sigma_z < 0.1$ that were not detected in the ugr bands were selected as i-dropout objects. At $z > 5.7$, the Lyα emission line begins to move out of the SDSS i filter, so a simple cut of $i_{AB} - z_{AB} > 2.2$ is used to separate high-redshift quasars (and cool brown dwarfs) from the majority of stellar objects. The $\sigma_z < 0.1$ criterion guarantees a high quasar selection efficiency. Second, false i-dropout objects were removed. All i-dropout objects were visually inspected, and false detections were deleted from the list of candidates. The majority of the contaminants are cosmic rays. An additional step, z-band photometry of i-dropout objects, may be needed to eliminate cosmic rays and improve the photometry of potential candidates (Fan et al., 2001a). In the next step, NIR (usually J-band) photometry of i-dropout objects was carried out, and the $i_{AB} - z_{AB}$ vs. $z_{AB} - J$ color-color diagram was used to separate quasar candidates from brown dwarfs (L and T dwarfs), which have more than ten times higher surface density. Finally, follow-up spectroscopic observations were conducted to identify high-redshift quasars.

Several other high-redshift quasars were discovered based on their IR or radio emission. For example, Cool et al. (2006) discovered one quasar at $z = 5.85$ in the NOAO Deep Wide-Field Survey (NDWFS; Jannuzi & Dey, 1999) Bootes Field using the AGN and Galaxy Evolution Survey (AGES) spectroscopic observations. The quasar was selected from a *Spitzer* MIR quasar sample and has a z_{AB} magnitude of 20.68 and an optical luminosity of $M_B = -26.52$. By matching the FLAMINGOS Extragalactic Survey IR survey (Elston et al., 2006) data to the Faint Images of the Radio Sky at Twenty-cm (FIRST; Becker et al., 1995) data, McGreer et al. (2006) discovered a radio-loud quasar at $z = 6.12$ in 4 deg^2 of the NDWFS region. This quasar is a broad absorption line (BAL) quasar with an optical luminosity of $M_B = -26.9$, comparable to the luminous SDSS quasars at $z \sim 6$.

Currently ongoing surveys of $z \sim 6$ quasars include the UKIRT Infrared Deep Sky Survey (UKIDSS; Warren et al., 2007) and the Canada-France High-redshift

Quasar Survey (CFHQS; Willott et al., 2005). The UKIDSS survey is being carried out in the $YJHK$ bands (different areas may have different band coverages) using the UKIRT Wide Field Camera on the 3.8 m UKIRT telescope. The resulting NIR data together with the SDSS multicolor optical data can be used to select $z \sim 6$ quasar candidates. So far the UKIDSS team has found two quasars (Venemans et al., 2007; Mortlock et al., in prep). These quasars are beyond the z_{AB} magnitude selection limit that the SDSS team used (e.g. Fan et al., 2003). The CFHQS survey is an optical imaging survey of a few hundred square degrees in the $griz$ bands on the Canada-France-Hawaii Telescope. The survey depth is about two magnitudes deeper than SDSS. So far the CFHQS team has found four quasars at $z \sim 6$, including the most distant quasar known at $z = 6.43$ (Willott et al., 2007).

Figure 1.3 shows the number of high-redshift quasars known today. Most of these quasars are bright ($z_{AB} < 20$); very little is known about fainter quasars ($z_{AB} > 20$) at $z \sim 6$. The SDSS main survey only probes the most luminous quasars, and with a density of 1/470 deg^2 (Fan et al., 2006a). The Cool et al. (2006) quasar at $z = 5.85$ was $z_{AB} > 20$, but the sample contains a single object and is selected from an area of less than 10 deg^2. Mahabal et al. (2005) found a very faint quasar with $z_{AB} = 23.0$ at $z = 5.70$ in a 2.5 deg^2 field around the luminous quasar SDSS J114816.64+525150.3 [1] at $z = 6.42$. Willott et al. (2005) imaged a 3.83 deg^2 region down to $z_{AB} = 23.35$ in the first results of the CFHQS survey and did not find any quasars at $z > 5.7$. In these surveys both the quasar samples and the survey areas are very small, thus they do not provide a good statistical study of high-redshift quasars at $z_{AB} > 20$. Recently, Willott et al. (2007) discovered four quasars at $z > 6$ from about 400 deg^2 of the CFHQS. These quasars have z_{AB} magnitudes fainter than 21. Since their follow-up observations are not yet complete, they did not determine the spatial density of these quasars.

Finding faint quasars at $z \sim 6$ is important for studying the evolution of the quasar population and quasars' impact on their environments. Due to the limited

---

[1] The naming convention for SDSS sources is SDSS JHHMMSS.SS±DDMMSS.S, and the positions are expressed in J2000.0 coordinates. We use SDSS JHHMM±DDMM for brevity.
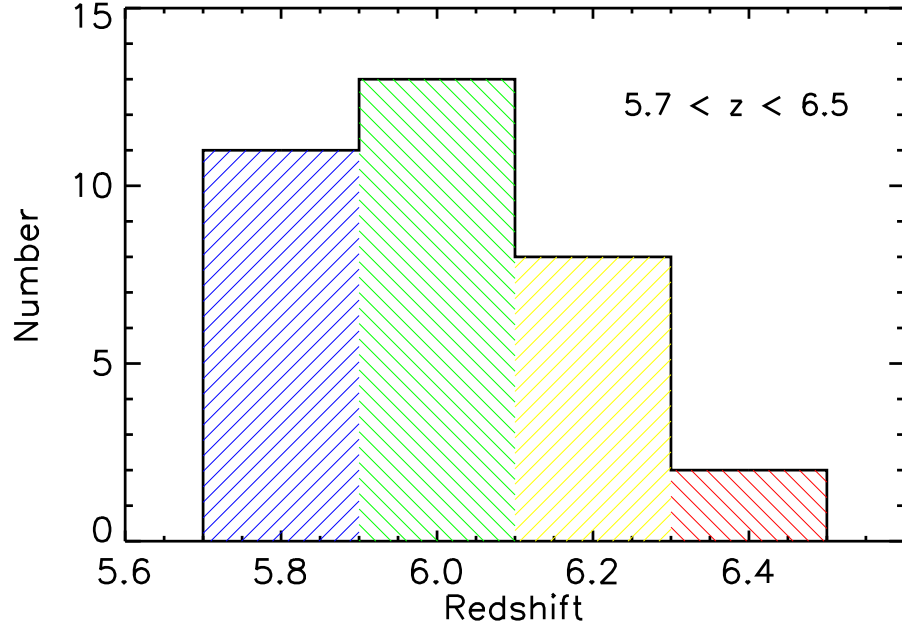
Figure 1.3 Number of high-redshift quasars known today.

number of $z \sim 6$ quasars known, the QLF at this redshift is poorly determined. Fan et al. (2004) obtained the bright-end QLF at $z \sim 6$, but the slope, -3.2 ± 0.7, was very uncertain due to the small luminosity range of the sample. Richards et al. (2004) put a broad constraint on the bright-end slope of > -4.63 (3σ) from the absence of lenses in four quasars at $z \sim 6$. The QLF at $z \sim 6$ is important to understand BH growth at early epochs (e.g. Volonteri & Rees, 2006; Wyithe & Padmanabhan, 2006). While bright quasars at high redshift have central BH masses between 10^9 and 10^{10} $M_\odot$, fainter quasars with $z_{AB} > 20$ are expected to harbor BHs with masses of a few times 10^8 $M_\odot$ or below (e.g. Kurk et al., 2007), which may be associated with galaxies of lower masses. The QLF also enables us to determine the quasar contribution to the UV background at $z \sim 6$. Detection of complete Gunn-Peterson troughs (Gunn & Peterson, 1965) among the highest-redshift quasars indicates a rapid increase of the IGM neutral fraction at $z \sim 6$, and suggests that we have reached the end of the reionization epoch (e.g. Becker et al., 2001; Djorgovski et al., 2001; Fan et al., 2006c). It is unclear what the individual contributions of galaxies and quasars to the reionization are. Although

there is evidence showing that quasars are probably not the main contributor to reionization (e.g. Salvaterra et al., 2007; Srbinovsky & Wyithe, 2007; Shankar & Mathur, 2007), a proper determination of the QLF at $z \sim 6$ is needed to constrain the quasar contribution.

In order to probe faint quasars at high redshift, we are carrying out a deep spectroscopic survey of $z \sim 6$ quasars in the SDSS deep stripe. A primary goal of the SDSS imaging survey is to scan 8500 deg^2 of the north Galactic cap (the SDSS main survey). In addition to the main survey, SDSS also conducts a deep survey by repeatedly imaging a 300 deg^2 area on the Celestial Equator in the south Galactic cap in the Fall (hereafter referred to as the SDSS deep survey; Adelman-McCarthy et al., 2007). This deep stripe (also called Stripe 82) spans $20^{\mathrm{h}} < \mathrm{RA} < 4^{\mathrm{h}}$ and $-1.25° < \mathrm{Dec} < 1.25°$. The multi-epoch images, when coadded, allow the selection of much fainter quasars than the SDSS main survey. The SDSS deep survey will eventually reach a depth of $i_{AB} \sim 24.5$ (5 σ detection for point sources) with more than 60 epochs of data (Adelman-McCarthy et al., 2008). We have already found 8 quasars in this region.

1.4 High-Redshift Quasars: from Radio to X-Ray

Understanding quasars requires observations from X-ray to radio wavelengths, each spectral region revealing different aspects of quasar emission and probing different regions of the active nuclei. One of the main results from the studies of $z \sim 6$ quasars is the apparent lack of strong evolution in their rest-frame UV/optical and X-ray properties. Their emission-line strengths and UV continuum shapes are very similar to those of low-redshift quasars (e.g. Barth et al., 2003; Pentericci et al., 2003; Fan et al., 2004), the emission line ratios indicate solar or supersolar metallicity in emission-line regions as found in low-redshift quasars (e.g. Hamann & Ferland, 1999; Dietrich et al., 2003b; Freudling et al., 2003; Maiolino et al., 2003), and the optical-to-X-ray flux ratios and X-ray continuum shapes show little evolution with redshift (e.g. Strateva et al., 2005; Vignali et al., 2005; Steffen et al., 2006; Shemmer et al.,

Figure 1.4 UV composite spectrum (red) of 20 high-redshift quasars comparing with the composite spectrum (blue) of low-redshift SDSS quasars. At the red side of Lyα, the two spectra look very similar.

2005, 2006). These measurements show that quasar accretion disks and emission-line regions are formed on very short time scales and their properties are not sensitive to the cosmic age.

1.4.1 UV/optical properties

Figure 1.4 shows the UV composite spectrum of 20 high-redshift quasars comparing with the composite spectrum of low-redshift SDSS quasars (Vanden Berk et al., 2001). At the red side of Lyα, the two spectra are very similar, meaning no evolution in UV emission-line strengths and continuum shapes from $z \sim 6$ to ~ 0.

The rest-frame UV spectrum, from the Lyα emission line to the Fe II bump at 2000–3000 Å, contains strong diagnostic emission lines and provides key information on the physical conditions and emission mechanisms of the BLR. The bulk motions of the BLR can be used to determine the mass of the central BH, while chemical abundances in the BLR are important in understanding the history of star formation in the host galaxy. Central BH masses of quasars can be estimated using mass

scaling relations based on broad emission line widths and continuum luminosities. The scaling relations are written as $M_{BH} \propto FWHM^2 L_{opt}^{\beta}$, where L_{opt} is optical luminosity and $\beta \approx 0.5$. Strong emission lines such as Mg II and C IV have been widely used to determine BH masses (e.g. McLure & Dunlop, 2004; Vestergaard & Peterson, 2006; Shen et al., 2008).

Photoionization models have shown that various emission-line ratios provide reliable estimates of metallicity in the BLRs of quasars (e.g. Hamann et al., 2002; Nagao et al., 2006). Strong permitted line ratios, such as N V $\lambda1240$/C IV $\lambda1549$ (hereafter N V/C IV), N V $\lambda1240$/He II $\lambda1640$ (hereafter N V/He II), and Fe II/Mg II $\lambda2800$ (hereafter Fe II/Mg II), are relatively easy to measure even in $z \sim 6$ quasars (e.g. Hamann & Ferland, 1993, 1999). Fe abundance is of particular interest (e.g. Hamann & Ferland, 1993, 1999): most of the Fe in the solar neighborhood is generated by Type Ia supernovae (SNe Ia), whose precursors are believed to be long-lived intermediate-mass stars in close binaries, so appreciable Fe enrichment can only happen on a timescale of one Gyr after the initial starburst (e.g. Greggio & Renzini, 1983). On the contrary, the production of α elements such as Mg and O is dominated by SNe of types II, Ib and Ic, which explode very soon after the initial burst. Therefore, the Fe/α ratio is expected to be a strong function of age in young systems, and thus it puts a useful constraint on the age and chemical enrichment of the gas in the quasar environment.

At low redshift, elemental abundances measured from strong emission and intrinsic absorption lines have revealed that quasar environments have solar or supersolar metallicity. At $z \sim 6$, measurement of these spectral lines is difficult, as the rest-frame UV waveband is redshifted to the NIR range. NIR spectroscopy has been obtained for a few $z \sim 6$ quasars (e.g. Goodrich et al., 2001; Pentericci et al., 2002; Barth et al., 2003; Freudling et al., 2003; Maiolino et al., 2003; Stern et al., 2003; Iwamuro et al., 2004). Soon after the discovery of the first quasar at $z > 5.7$ (Fan et al., 2000a), its J-band spectrum was taken on the Keck telescope (Goodrich et al., 2001). This is a BAL quasar, and the spectrum shows a typical C IV emission line with EW = 19.9 Å and FWHM = 6000 km s^{-1}. Then Pentericci et al.

(2002) obtained NIR spectra of another two $z \sim 6$ quasars with the VLT. They were able to estimate the metallicity from the N v/He ii and N v/C iv line ratios for one of the quasars, and found that the metallicity is consistent with low-redshift measurements. Barth et al. (2003) took the J and K-band spectra of the most distant SDSS quasars known and derived the mass of the central BH from the Mg ii and C iv emission lines based on mass scaling relations. The BH is supermassive $(2 \sim 6 \times 10^9 M_\odot)$. They also measured the Fe ii/Mg ii ratio to be 4.7, typical of low-redshift values. Many of the luminous $z \sim 6$ quasars known have Fe ii/Mg ii measurements, since the Fe ii/Mg ii ratio is relatively easy to measure at $z \sim 6$ (e.g. Freudling et al., 2003; Maiolino et al., 2003; Iwamuro et al., 2004). However, most of the above observations only provide NIR spectra with low signal-to-noise ratios (S/Ns) or partial wavelength coverage. Even basic properties such as the average continuum slope are not well measured.

High-redshift quasar spectra can also be used to study the evolution of strong intergalactic Mg ii absorption at $z < 6$. Quasar absorption lines are an unbiased tracer of intervening gaseous material along the lines of sight to quasars. Strong Mg ii absorption systems are usually directly associated with galaxy halos or disks (e.g. Charlton & Churchill, 1998; Churchill et al., 2000; Steidel et al., 2002). The statistical properties of the Mg ii $\lambda\lambda 2796,2803$ doublet absorbers at low redshift $(z \leq 2.2)$ have been well studied (e.g. Steidel & Sargent 1992; Nestor et al. 2005; Prochter et al. 2006; see a summary of Mg ii absorption surveys by Churchill et al. 2005). At higher redshift, the Mg ii doublet is shifted to the NIR wavelength range. The study of high-redshift Mg ii absorbers is limited by the small number of quasars with good NIR spectra available.

In order to study BH masses and chemical abundances at $z \sim 6$, we observed a sample of six quasars using Gemini-South/GNIRS and Gemini-North/NIRI. The observations on GNIRS were carried out in cross-dispersion mode, giving a simultaneous wavelength coverage of 0.9–2.5 μm with excellent transmission. The high S/Ns and long wavelength coverage of the spectra enable us to measure various UV emission line ratios and determine chemical abundances accurately. Central BH

masses can be estimated from both Mg II and C IV emission lines. The Gemini data are also good enough to probe Mg II absorption systems at $z < 6$.

1.4.2 Radio and millimeter/submillimeter properties

Radio observations of high-redshift quasars were made with the Very Large Array (VLA) at 1.4 GHz (e.g. Petric et al., 2003; Carilli et al., 2004; Frey et al., 2005; Wang et al., 2007, 2008b). Most of the SDSS quasars at $z \sim 6$ have been observed, and roughly one third of them were detected at the $\geq 3\sigma$ level (~ 20 μJy rms). See Wang et al. (2008b) for a summary. Usually a few hours of on-source exposure was required to achieve an rms noise level of ~ 20 μJy. Among the currently known quasars at $z \sim 6$, there is only one radio-loud quasar, which is a radio-selected quasar in the NDWFS field (McGreer et al., 2006), and one intermediate radio-loud quasar (the R parameter is close to 10). The radio-to-far-IR (FIR) luminosity ratios of the most radio-detected quasars are consistent with the radio-FIR correlation found in low-redshift star-forming galaxies; while a few quasars show strong radio excess, indicating a significant AGN contribution to the radio emission (Wang et al., 2008a).

Millimeter/submillimeter (mm/submm) observations of high-redshift quasars were mostly made at 250 GHz with the Max Planck Millimeter Bolometer Array (MAMBO-2) on the IRAM 30m telescope, at 850 and 450 μm with the Submm Common-User Bolometer Array (SCUBA) on the James Clerk Maxwell Telescope (JCMT), and at 350 μm with SHARC-II on the Caltech Submm Observatory (e.g. Petric et al., 2003; Priddey et al., 2003; Bertoldi et al., 2003a; Robson et al., 2004; Wang et al., 2007, 2008a,b). Most of the SDSS quasars at $z \sim 6$ have been observed, and roughly one third of them were detected at the 1 mJy level (see Wang et al. (2008b) for a summary).

The mm/submm (rest-frame FIR) observations of quasars trace the warm/cool dust emission in quasar host galaxies. They have revealed that luminous $z \sim 6$ quasars are extremely FIR luminous ($\sim 10^{13}$ $L_\odot$) and have a large amount of warm/cool dust (10^8–10^9 $M_\odot$). If the FIR emission is mainly powered by star formation in the host galaxies, the star formation rates are estimated to be ~ 1000 $M_\odot$

yr^{-1}. Strong starbursts can be induced by merging gas-rich galaxies (e.g. Hopkins et al., 2006; Li et al., 2007). CO observations have already revealed the presence of $1 \sim 2 \times 10^{10}$ $M_\odot$ of molecular gas in two high-redshift quasars (Walter et al., 2003; Bertoldi et al., 2003b; Walter et al., 2004; Carilli et al., 2007). This amount of gas can sustain the star formation rate of ~ 1000 $M_\odot$ yr^{-1} for more than 10^7 years. However, the individual contributions from AGN activity and star formation to the heating of warm/cool dust are still unclear. On one hand, the shapes of the MIR-to-FIR SEDs at low redshift indicate that AGN activity may dominate the heating of the warm/cool dust (e.g. Polletta et al., 2000; Haas et al., 2003). Observations also show that the FIR-to-B-band luminosity ratios of quasars do not change significantly from $z \sim 2$ to 6. On the other hand, the radio-to-FIR correlation for star-forming galaxies still holds for most IR-luminous quasars out to the highest redshifts (e.g. Carilli et al., 2001, 2004; Wang et al., 2008b), suggesting that the dust could be heated by starbursts in quasar host galaxies rather than quasar central engines.

1.4.3 X-ray properties

X-ray observations of quasars probe the physical conditions of the innermost regions surrounding the central BHs. Observations of high-redshift quasars have been challenging for present-day X-ray missions: exposure times of a few ks are required to obtain a 3σ detection and of a few tens ks for a reliable spectral measurement (e.g. Shemmer et al., 2006). Most of the luminous SDSS quasars at $z \sim 6$ have been observed with *Chandra* or *XMM-Newton* (e.g. Brandt et al., 2001, 2002; Bechtold et al., 2003; Farrah et al., 2004; Schwartz & Virani, 2004; Shemmer et al., 2005, 2006). Statistical studies already revealed that, from $z \sim 0$ to ~ 6, the optical-to-X-ray flux ratios and X-ray continuum shapes show little evolution with redshift (e.g. Strateva et al., 2005; Vignali et al., 2005; St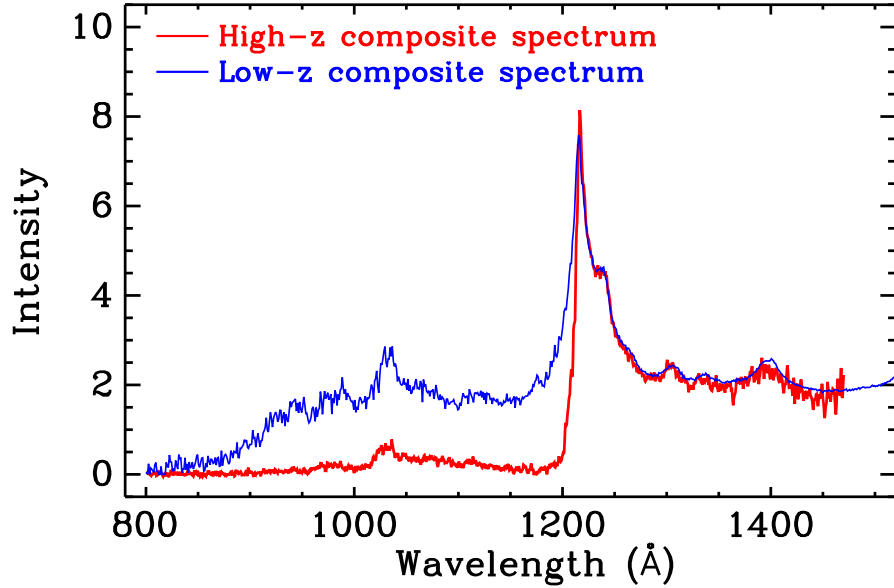effen et al., 2006; Shemmer et al., 2005, 2006). Note that BAL quasars usually have weak X-ray emission due to heavy absorption by large gas column densities.

Two major parameters are used to describe the X-ray emission. One is the

optical-to-X-ray flux ratio α_{ox} (e.g. Tananbaum et al., 1979; Zamorani et al., 1981). A convenient definition of α_{ox} is,

$$\alpha_{\mathrm{ox}} = \frac{\log(f_{2\,\mathrm{kev}}/f_{2500})}{\log(\nu_{2\,\mathrm{kev}}/\nu_{2500})}, \tag{1.1}$$

where $f_{2\,\mathrm{kev}}$ is the flux density at rest-frame 2 kev and f_{2500} is the flux density at rest-frame 2500 Å. The other one is the photon index Γ ($P_E \propto E^{-\Gamma}$ or $f_\nu \propto \nu^{-\Gamma+1}$). X-ray observations of low-redshift quasars/AGNs have confirmed that their X-ray emission is correlated with their UV/optical emission. For example, based on more than 200 optically-selected quasars/AGNs, Strateva et al. (2005) found $\alpha_{\mathrm{ox}} = -0.136\,l_{UV} + 2.616$, where l_{UV} is the UV luminosity in log units. For luminous SDSS quasars at $z \sim 6$, the average α_{ox} value is about -1.7 (Shemmer et al., 2006), which, after being corrected for the UV/optical vs. X-ray correlation, is consistent with α_{ox} found in low-redshift quasars (e.g. Strateva et al., 2005; Vignali et al., 2005; Steffen et al., 2006). While most studies show that α_{ox} does not change with redshift, Kelly et al. (2007) recently pointed out a possible dependence of α_{ox} on cosmic time.

Reliable measurements of Γ require detections of at least a few tens of photons. This is very expensive for high-redshift quasars, and has been done for only two $z \sim 6$ quasars. Schwartz & Virani (2004) obtained the X-ray spectrum of a $z = 5.99$ quasar from a 120 ks *Chandra* observation and found $\Gamma = 1.86$; while Farrah et al. (2004) observed a $z = 6.30$ quasar using *XMM-Newton* with total integration time > 100 ks and found $\Gamma = 2.12$. Both Γ values are consistent with low-redshift measurements. An alternative way to measure the photon index in high-redshift quasars is to jointly fit the spectra of a sample of quasars and derive their mean properties. Based on a sample of 15 quasars at $z > 5$, Shemmer et al. (2006) found a mean Γ of 1.95 (again consistent with low-redshift measurements) and a mean column density of $N_{\mathrm{H}} \leq 6 \times 10^{22}$. Statistical study also showed that there is no strong correlation between Γ and redshift (Kelly et al., 2007).

1.4.4   IR properties

From the studies of $z \sim 6$ quasars, as we mentioned above, there is no strong evolution in the rest-frame UV/optical and X-ray properties. Their radio and mm/submm properties are also similar to their low-redshift counterparts. However, it is not known whether this lack of evolution in high-energy SEDs extends to the IR wavelength range. According to classical AGN unification models (Antonucci, 1993), the accretion disk is surrounded by a dusty torus. Much of the emission from quasars/AGNs is re-processed by the dust and is re-emitted at IR wavelengths, where the quasar/AGN SEDs peak. The hottest dust lies within a few pc and produces NIR radiation, while warm and cool dust can extend to a few kpc and dominates the MIR and FIR emission (e.g. Polletta et al., 2000; Nenkova et al., 2002; Siebenmorgen et al., 2005). The individual contributions from AGN activity and star formation to the heating of warm/cool dust are poorly known (e.g. Wilkes, 2001). However, it is generally believed that emission from hot dust with a temperature of ~ 1000 K is directly powered by central active nuclei (e.g. Rieke & Lebofsky, 1981; Polletta et al., 2000; Haas et al., 2003), and thus is closely related to quasar activity.

The hot dust properties of low-redshift quasars have been explored using IR missions such as ISO (e.g. Polletta et al., 2000; Haas et al., 2003). However, hot dust in high-redshift quasars was not studied until the launch of the *Spitzer Space Telescope* (*Spitzer*; Werner et al., 2004). *Spitzer* allows us, for the first time, to explore the rest-frame NIR range for $z \sim 6$ quasars and to constrain the evolution of hot dust in quasar environments. Hines et al. (2006) have observed thirteen $z > 4.5$ quasars using the Infrared Array Camera (IRAC; Fazio et al., 2004) and Multiband Imaging Photometer for *Spitzer* (MIPS; Rieke et al., 2004). They find that the SEDs of these high-redshift quasars at rest wavelength 0.6–4.3 μm do not significantly differ from those of quasars with similar luminosity at low redshifts. In CHAPTER 3 of this work, we will report on *Spitzer* observations of a large sample of $z \sim 6$ quasars discovered by the SDSS.

1.5   Radio-Loud Fraction of Quasars and Nitrogen-Rich Quasars

1.5.1   Fraction of Radio-Loud Quasars in Optically-Selected Quasars

Although quasars were first discovered by their radio emission (e.g. Matthews &
Sandage, 1963; Schmidt, 1963), it was soon found that the majority of quasars
were radio-quiet (e.g. Sandage, 1965). Quasars are often classified into two broad
categories, radio-loud and radio-quiet, based on their radio properties. There is
mounting evidence that the distribution of radio-to-optical flux ratio for optically-
selected quasars is bimodal (e.g. Kellermann et al., 1989; Miller, Peacock, & Mead,
1990; Visnovsky et al., 1992; Ivezić et al., 2002), although the existence of the
bimodality has been questioned (e.g. Cirasuolo et al., 2003, but see also Ivezić et al.
(2004a) for a response). Radio-loud and radio-quiet quasars are probably powered
by similar physical mechanisms (e.g. Barthel, 1989; Urry & Padovani, 1995), and
their radio properties are also correlated with host galaxy properties, central BH
masses, BH spins, and accretion rates (e.g. Baum et al., 1995; Urry & Padovani,
1995; Best et al., 2005). Radio-loud quasars are likely to reside in more massive
galaxies (e.g. Peacock, Miller, & Longair, 1986; Best et al., 2005), and harbor more
massive central BHs (e.g. Laor, 2000; Lacy et al., 2001; McLure & Dunlop, 2004),
than do radio-quiet quasars.

   Roughly 10%−20% of all quasars are radio-loud (e.g. Kellermann et al., 1989;
Urry & Padovani, 1995; Ivezić et al., 2002). However, the radio-loud fraction (RLF)
of quasars may depend on redshift and optical luminosity. Some studies have found
that the RLF tends to drop with increasing redshift (e.g. Peacock, Miller, & Longair,
1986; Miller, Peacock, & Mead, 1990; Visnovsky et al., 1992; Schneider et al., 1992)
and decreasing luminosity (e.g. Padovani, 1993; Goldschmidt et al., 1999; Cirasuolo
et al., 2003), or evolves non-monotonically with redshift and luminosity (e.g. Hooper
et al., 1995; Bischof & Becker, 1997), while others showed that the RLF does not
differ significantly with redshift (e.g. Goldschmidt et al., 1999; Stern et al., 2000;
Cirasuolo et al., 2003) or luminosity (e.g. Bischof & Becker, 1997; Stern et al., 2000).

   From a sample of 4472 SDSS quasars, Ivezić et al. (2002) found that the RLF

is independent of both redshift and optical luminosity when using marginal distributions of the whole sample; however, they noted that the approximate degeneracy between redshift and luminosity in the SDSS flux-limited sample may cause individual trends in redshift and luminosity to appear to cancel. By stacking the FIRST images, White et al. (2007) were able to probe the radio sky into nanoJansky regime. They found that the median radio loudness of SDSS-selected quasars is a declining function with optical luminosity. After correcting for this effect, they claimed that the median radio loudness is independent of redshift. We will use a sample of more than 30,000 optically-selected quasars from the SDSS, and break the redshift-luminosity dependence to study the evolution of the RLF. We will find that there are indeed strong trends in redshift and luminosity, and that they do in fact roughly cancel in the marginal distributions.

1.5.2   Quasars with Strong Nitrogen Emission Lines

Quasars with prominent nitrogen emission lines at 1486 Å or 1750 Å are rare. A well known example is Q0353-383, a luminous quasar showing strong N IV] $\lambda1486$, N III] $\lambda1750$, and N V $\lambda1240$ emission lines (Osmer & Smith, 1980; Baldwin et al., 2003). Baldwin et al. (2003) claimed that the unusual nitrogen emission in Q0353-383 is likely due to high metallicity in the broad line region of the quasar; the metallicity measured from line strength ratios involving N V, N IV], and N III] is ~15 times the solar abundance.

SDSS provides statistically significant samples to study these nitrogen-rich (N-rich) quasars. From a sample of ~ 5600 objects in the SDSS First Data Release Quasar Catalog (Schneider et al., 2003), Bentz et al. (2004) reported on 20 N-rich quasars in the redshift range $1.6 < z < 4.1$. The fraction of N-rich quasars in their sample is about 0.4%. By comparing with other quasars, they found that the N-rich quasars tend to have stronger Lyα emission lines, and stronger but narrower C IV $\lambda1549$ and C III] $\lambda1909$ emission lines. The two quasars with the strongest N IV] and N III] lines in the Bentz et al. (2004) sample have been studied in detail by Dhanda et al. (2007). Recently Glikman et al. (2007) discovered two quasars with strong

N IV] lines from a sample of 23 faint quasars at $3.7 < z < 5.1$. They suspected that the high detection rate of N-rich quasars is due to the low luminosity and high redshift of the sample.

The number of known N-rich quasars is still small, and most of their properties remain unclear, such as the UV/optical continuum slopes, emission line strengths and widths, and central BH masses, etc. We will present 293 N-rich quasars at $z > 1.7$ selected from the SDSS Fifth Data Release (DR5) Quasar Catalog (Schneider et al., 2007).

1.6   About this Dissertation

In CHAPTER 2 we will present Gemini NIR spectroscopic observations of six luminous quasars at $z = 5.8 \sim 6.3$. Five of them were observed using Gemini-South/GNIRS, which provides a simultaneous wavelength coverage of 0.9–2.5 μm in cross dispersion mode. The other source was observed in K band with Gemini-North/NIRI. We calculate line strengths for all detected emission lines and use their ratios to estimate gas metallicity in the BLRs of the quasars. We measure central BH masses of the quasars based on mass scaling relations, and estimate Eddington luminosity ratios using their BH masses and bolometric luminosities. We search for strong Mg II $\lambda\lambda$2796,2803 absorbers at $z < 6$ in the GNIRS spectra, and study the evolution of the number density (dN/dz) of Mg II absorbers.

In CHAPTER 3 we will study IR properties of quasars. We will present *Spitzer* observations of thirteen $z \sim 6$ quasars using IRAC and MIPS. They are luminous SDSS quasars selected from a series of papers (Fan et al., 2000a, 2001a, 2003, 2004, 2006a). All of them were observed with IRAC. Ten of them were also observed in the MIPS 24μm band, while the 24μm fluxes of the other three were taken from Hines et al. (2006). We measure their IR SEDs and study hot dust properties. We then combine the *Spitzer* observations with X-ray, UV/optical, mm/submm and radio observations to calculate their bolometric luminosities and estimate accretion rates. We also compare their IR properties with those in low-redshift quasars, and

discuss possible evolution of dust properties at high redshift.

In CHAPTER 4 we will present the discovery of five quasars at $z \sim 6$ selected from 260 deg^2 of the SDSS deep stripe. The five quasars with $20 < z_{AB} < 21$ are 1–2 magnitudes fainter than the luminous $z \sim 6$ quasars discovered in the SDSS main survey. One of them was independently discovered by the UKIDSS survey (Venemans et al., 2007). These quasars, combined with another $z \sim 6$ quasar known in this region, make a complete flux-limited quasar sample at $z_{AB} < 21$. We use the $1/V_a$ method to determine the comoving quasar spatial density at $z \sim 6$, and model the bright-end QLF using a power law. Based on the derived QLF, we estimate the quasar contribution to the UV background $z \sim 6$, and discuss whether the quasar/AGN population can provide enough UV photons to ionize IGM at the end of reionization.

In CHAPTER 5 we will present a deep spectroscopic survey of faint quasars in the SDSS deep stripe. Quasar candidates were selected from the deep data with good completeness over $0 < z < 5$, and 2 to 3 magnitudes fainter than the SDSS main survey. Spectroscopic follow-up was carried out on the 6.5m MMT with Hectospec. The preliminary sample of this SDSS faint quasar survey (hereafter SFQS) covers ~ 3.9 deg^2, contains 414 quasars, and reaches $g = 22.5$. The overall selection efficiency is $\sim 66\%$ ($\sim 80\%$ at $g < 21.5$); the efficiency in the most difficult redshift range ($2 < z < 3$) is better than 40%. We use the $1/V_a$ method to derive a binned estimate of the QLF and model the QLF using maximum likelihood analysis. We measure the density peak for this faint quasar sample using a luminosity-dependent density evolution model, and compare the peak with the density peak in luminous quasars. We also compare the SFQS QLF with the results of other quasar surveys, including the 2dF QSO Redshift Survey, the SDSS, and the 2dF-SDSS LRG and QSO Survey.

In CHAPTER 6 we determine the RLF of quasars as a function of redshift and optical luminosity, using a sample of optically-selected quasars from the SDSS DR3. The sample contains more than 30,000 objects and spans a redshift range of $0 < z \leq 5$ and a luminosity range of $-30 \leq M_i < -22$. We break the degeneracy between

redshift and luminosity due to the flux-limited nature of the sample, and find that the RLF of quasars decreases with increasing redshift and decreasing luminosity. We also examine the impact of flux-related selection effects on the RLF determination using a series of tests.

In CHAPTER 7 we report on 293 quasars with strong N IV] λ1486 or N III] λ1750 emission lines (rest-frame equivalent width > 3 Å) at $1.7 < z < 4.0$ selected from the SDSS DR5. These nitrogen-rich (N-rich) objects comprise $\sim 1.1\%$ of the SDSS quasars. We study various properties of N-rich quasars and compare them with those of normal quasars. We show evidence that the nitrogen abundance in the N-rich quasars is closely related to quasar radio properties.

In CHAPTER 8 we will give a short summary and some of our future work.

CHAPTER 2

CHEMICAL ABUNDANCES AND BLACK HOLE MASSES IN $Z \sim 6$
QUASARS

2.1   Introduction

In recent years we have witnessed the discoveries of quasars at $z \sim 6$; at this epoch the universe was less than one Gyr old (e.g. Fan et al., 2003, 2006a; Cool et al., 2006; McGreer et al., 2006). These high-redshift quasars are among the most luminous objects known and provide direct probes of the early universe when the first generations of galaxies and quasars formed. Quasar activity and the formation processes of galaxies and supermassive black holes (BHs) are closely correlated (e.g. Kauffmann & Haehnelt, 2000; Wyithe & Loeb, 2003; Hopkins et al., 2005; Croton et al., 2006), so these $z \sim 6$ objects are essential for studying the accretion history of BHs, galaxy formation, and chemical evolution at very early epochs. High-redshift luminous quasars harbor BHs with masses of 10^9–10^{10} M$_\odot$ and emit near the Eddington limit (e.g. Barth et al., 2003; Vestergaard, 2004; Jiang et al., 2006a; Kurk et al., 2007), revealing the rapid growth of central BHs. Their emission line ratios show solar or supersolar metallicity, as is found in low-redshift quasars (e.g. Barth et al., 2003; Dietrich et al., 2003a; Freudling et al., 2003; Maiolino et al., 2003), indicating that

there was vigorous star formation and element enrichment in the first Gigayear.

Understanding quasars requires observations from X-ray to radio wavelengths; each spectral region is due to different physical mechanisms and probes different regions of the active nucleus. In particular, the rest-frame UV spectrum, from the Lyα emission line to the Fe II bump at 2000–3000 Å, contains strong diagnostic emission lines and provides key information on the physical conditions and emission mechanisms of the broad-line region (BLR). The bulk motions of the BLR can be used to determine the mass of the central BH, while chemical abundances in the BLR are important in understanding the history of star formation in the host galaxy. Photoionization models show that various emission-line ratios provide reliable estimates of metallicity in the BLRs of quasars (e.g. Hamann et al., 2002; Nagao et al., 2006). Strong permitted line ratios, such as N V λ1240/C IV λ1549 (hereafter N V/C IV), N V λ1240/He II λ1640 (hereafter N V/He II), and Fe II/Mg II λ2800 (hereafter Fe II/Mg II), are relatively easy to measure even in $z \sim 6$ quasars (e.g. Hamann & Ferland, 1993, 1999). Fe abundance is of particular interest (e.g. Hamann & Ferland, 1993, 1999): most of the Fe in the solar neighborhood is generated by Type Ia supernovae (SNe Ia), whose precursors are believed to be long-lived intermediate-mass stars in close binaries, so appreciable Fe enrichment can only happen on a timescale of one Gyr after the initial starburst (e.g. Greggio & Renzini, 1983). On the contrary, the production of α elements such as Mg and O is dominated by SNe of types II, Ib and Ic, which explode very soon after the initial burst. Therefore, the Fe/α ratio is expected to be a strong function of age in young systems, and thus it puts a useful constraint on the age and chemical enrichment of the gas in the quasar environment.

At low redshift, elemental abundances measured from strong emission and intrinsic absorption lines have revealed that quasar environments have solar or supersolar metallicity. At $z \sim 6$, measurement of these spectral lines is difficult, as the rest-frame UV waveband is redshifted to the NIR range. NIR spectroscopy has been obtained for a few $z \sim 6$ quasars (e.g. Goodrich et al., 2001; Pentericci et al., 2002; Barth et al., 2003; Freudling et al., 2003; Maiolino et al., 2003; Stern et al., 2003;

Iwamuro et al., 2004). These observations only provide NIR spectra with low signal-to-noise ratios (SNRs) or partial wavelength coverage. Even basic properties such as the average continuum slope are not well measured. Recently, Kurk et al. (2007) obtained NIR spectra with high SNRs for a sample of five $z \sim 6$ quasars with ISAAC on the VLT. They used the ISAAC data to study the Fe II/Mg II ratios, BH masses, and the Strömgren spheres around quasars. In this chapter we present Gemini NIR spectroscopy of six $z \sim 6$ quasars. All these quasars were discovered by the Sloan Digital Sky Survey (SDSS; York et al., 2000) and were selected from Fan et al. 2000, 2001, and 2004 (hereafter quasar discovery papers). They have extensive follow-up observations in X-ray (e.g. Shemmer et al., 2006), *Spitzer* bands (e.g. Jiang et al., 2006a), millimeter/submillimeter and radio wavelengths (e.g. Wang et al., 2007), providing a fundamental dataset to study luminous quasars at $z \sim 6$ in the context of the growth of early BHs and their relation to galaxy formation. The Gemini data have high SNRs and excellent NIR wavelength coverage. They are used to measure the metal abundances in high-redshift environments and estimate central BH masses using empirical mass scaling relations (e.g. McLure & Dunlop, 2004; Vestergaard & Peterson, 2006).

We also use these high-redshift spectra to study the evolution of strong intergalactic Mg II absorption at $z < 6$. Quasar absorption lines are an unbiased tracer of intervening gaseous material along the lines of sight to quasars. Strong Mg II absorption systems are usually directly associated with galaxy halos or disks (e.g. Charlton & Churchill, 1998; Churchill et al., 2000; Steidel et al., 2002). The statistical properties of the Mg II $\lambda\lambda$2796,2803 doublet absorbers at low redshift ($z \leq 2.2$) have been well studied (e.g. Steidel & Sargent 1992; Nestor et al. 2005; Prochter et al. 2006; see a summary of Mg II absorption surveys by Churchill et al. 2005). At higher redshift, the Mg II doublet is shifted to the NIR wavelength range. The study of high-redshift Mg II absorbers is limited by the small number of quasars with good NIR spectra available. Our Gemini/GNIRS spectra with high SNRs have excellent NIR wavelength coverage, so they are efficient to probe the Mg II absorption systems at $z < 6$.

The structure of the chapter is as follows. In § 2.2 we describe our Gemini observations and data reduction of the six quasars. In § 2.3 we conduct a detailed spectral analysis, including the measurement of emission-line strengths. Chemical abundances are calculated and central BH masses are estimated in § 2.4. Mg II absorption systems in the quasar spectra are identified and analyzed in § 2.5. We give a brief summary in § 2.6. In this chapter we use λ (λ_0) to denote observed-frame (rest-frame) wavelength. We use a Λ-dominated flat cosmology with $H_0 = 70$ km s^{-1} Mpc^{-1}, $\Omega_m = 0.3$ and $\Omega_\Lambda = 0.7$ (Spergel et al., 2007).

2.2   Observations and Date Reduction

We obtained NIR spectra for the six luminous $z \sim 6$ quasars using Gemini-South/GNIRS and Gemini-North/NIRI. Five of them were chosen to be easily reached by Gemini-South, and were observed using GNIRS in February and March 2006. The observations on GNIRS were carried out in cross-dispersion mode, giving a simultaneous wavelength coverage of 0.9–2.5 μm with excellent transmission. At $z \sim 6$, strong diagnostic emission lines such as C IV and Mg II are redshifted to this wavelength range, so GNIRS provides us an efficient way to collect NIR information for high-redshift quasars. We used the short camera on GNIRS with a pixel scale of 0.15″/pixel. The slit length in cross-dispersion mode is 6.1″ and we used a slit width of 0.675″ to optimize the combination of resolution and light gain. The resolving power is about 800 and the dispersion varies from $\sim$3 Å per pixel at 0.9 μm to $\sim$6 Å per pixel at 2.5 μm. This is sufficient to separate the Mg II $\lambda\lambda$2796,2803 doublet absorption lines. We used the standard ABBA nodding sequence between exposures. The exposure time at each nod position was five minutes and the distance between the two positions was 3″. Before or after the exposure of each quasar, a nearby A or F spectroscopic standard star was observed for flux calibration and to remove telluric atmosphere absorption. The log of observations is given in Table 2.1, where redshifts, z_{AB} (AB magnitudes) and J (Vega-based magnitudes) are taken from the quasar discovery papers.

Table 2.1. Log of observations

Quasar (SDSS)	Redshift	z_{AB} (mag)	J (mag)	Date	Instrument	t_{exp} (min)
J083643.85+005453.3	5.82	18.74±0.05	17.89±0.05	2006 Feb 19	GNIRS	70
J103027.10+052455.0	6.28	20.05±0.10	18.87±0.10	2006 Mar 20, 26	GNIRS	140
J104433.04−012502.2	5.80	19.23±0.07	18.31±0.10	2006 Mar 28	GNIRS	120
J130608.26+035626.3	5.99	19.47±0.05	18.77±0.10	2006 Mar 26, 27	GNIRS	140
J141111.29+121737.4	5.93	19.65±0.08	18.95±0.05	2006 Mar 28	GNIRS	120
J162331.81+311200.5	6.22	20.09±0.10	19.15±0.10	2004 Aug 16, Sep 14	NIRI (K)	180
				2005 Aug 22, 24		

Note. — Redshifts, z_{AB} (AB magnitudes) and J (Vega-based magnitudes) are from the quasar discovery papers Fan et al. (2000a), Fan et al. (2001a), and Fan et al. (2004).

The GNIRS data were reduced using the Gemini package within IRAF[1]. Briefly, for each quasar the NIR spectroscopic data were sky-subtracted for each pair of images taken at the two nod positions. Then the images were flat-fielded. In cross-dispersion mode, GNIRS uses orders 3–8 to cover 0.9–2.5 μm. A single flat has non-uniform illumination between orders, so three sets of flats with different exposure times were taken each night. The final flat is extracted from the three flats so that each order has good illumination but without saturation. After flat-fielding, distortion correction and wavelength calibration were applied, the frames were combined, and one-dimensional spectra were extracted. Then the spectra were flux calibrated and corrected for telluric atmosphere absorption using the spectra of the spectroscopic standard stars. Finally the spectra in different orders were scaled and connected to a single spectrum. Adjacent orders cover a short common wavelength range, which enables the individual orders to be scaled to form a continuous, smoothly connected spectrum. This arbitrarily scaled spectrum was then calibrated to the J broad-band magnitude listed in Table 2.1 and thereby placed on an absolute flux scale with an uncertainty of 5∼10%. The typical SNR at 1.2 μm reaches ~ 8 per pixel.

Figure 2.1 shows the spectra of the five quasars in the observed frame. The spectra at $\lambda \leq 1.0$ μm are taken from the quasar discovery papers. The spectra have been smoothed by three pixels. The bottom panel shows the sky transparency at an airmass of 1.0 and water vapor of 1.6 mm. There are strong telluric absorption bands around 1.4 and 1.9 μm, so we do not show the spectra in these ranges. In Figure 2.1 we also show a spectrum of a standard star HIP 54027 calibrated using the same procedure as we do for our science objects. For comparison, a spectrum (in red) of a black body with the effective temperature of HIP 54027 is given on top of the spectrum of HIP 54027. The good agreement between the two spectra indicate that spectra in different dispersion orders are properly scaled and connected.

---

[1]IRAF is distributed by the National Optical Astronomy Observatories, which are operated by the Association of Universities for Research in Astronomy, Inc., under cooperative agreement with the National Science Foundation.
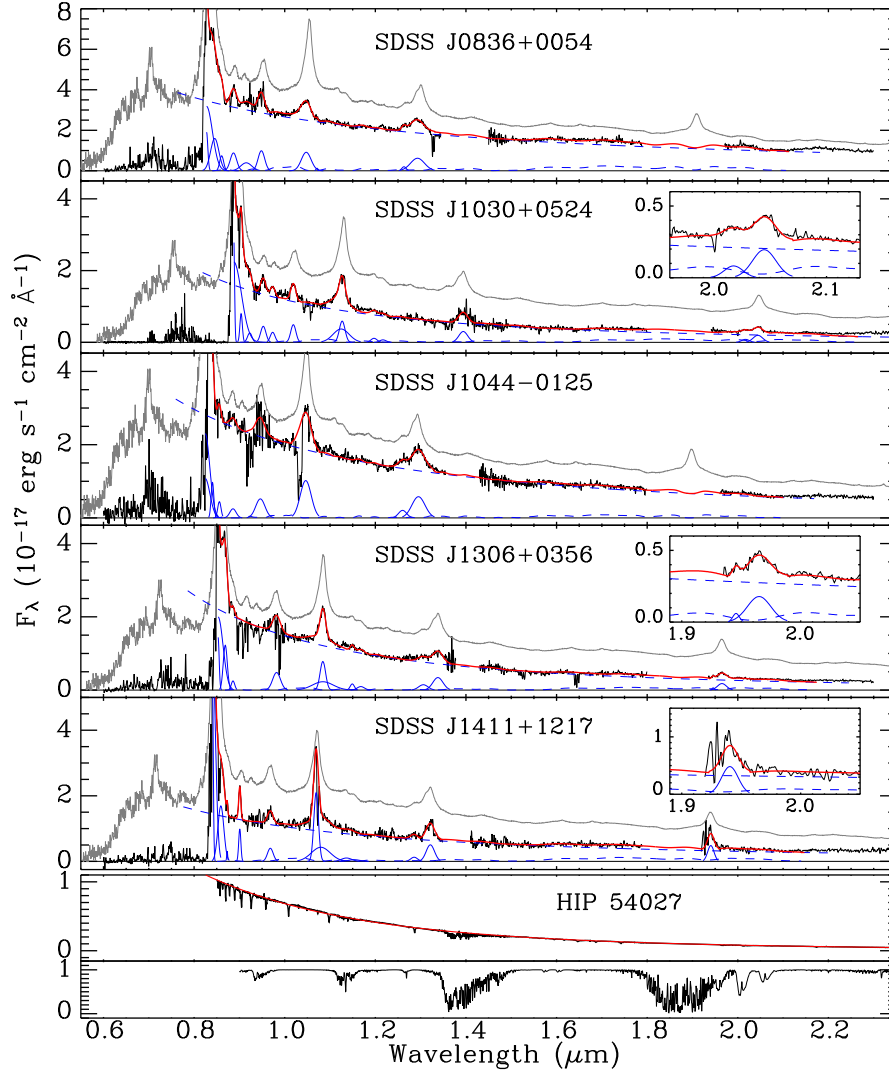
Figure 2.1 Optical and NIR spectra of five $z \sim 6$ quasars in our sample. The spectra at $\lambda > 1.0$ μm were obtained with Gemini-South/GNIRS and the spectra at $\lambda < 1.0$ μm are taken from the quasar discovery papers. The spectra have been smoothed by three pixels. The blue solid lines are the best fits to emission lines and the blue dashed lines are the best fits to the power-law continuum and Fe II emission. The red lines are the sums of all the components. For comparison, we show the low-redshift composite spectrum of Vanden Berk et al. (2001) in gray. A spectrum of a standard star HIP 54027 is also shown in the figure with a black body (with the effective temperature of HIP 54027) spectrum (in red) on top of it. The bottom panel shows the sky transparency at an airmass of 1.0 and water vapor of 1.6 mm.
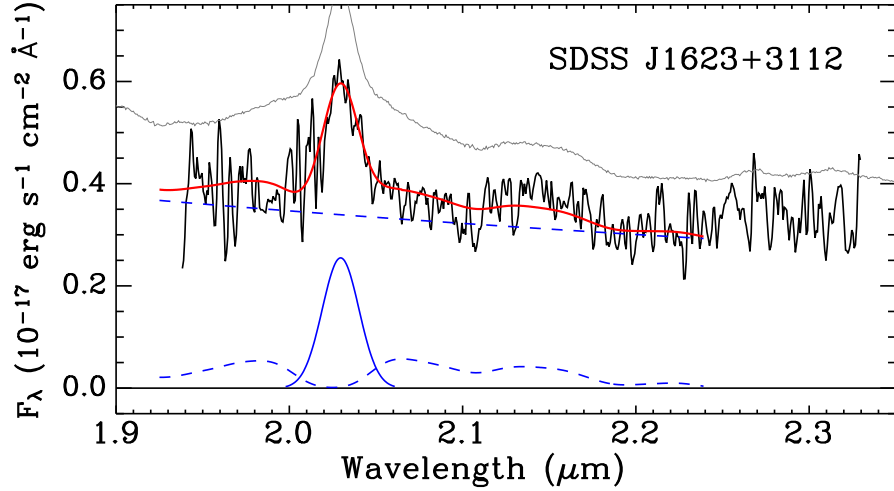
Figure 2.2 Same as Fig. 1 for SDSS J1623+3112, which was observed in K band using Gemini-North/NIRI.

We obtained a K-band spectrum for SDSS J1623+3112 using Gemini-North/NIRI in August and September 2004 and August 2005. The observations were made with a f/6 camera in spectroscopic mode. The long-slit has a length of $110''$ and we chose to use a slit width of $0.75''$, which provides a resolving power of ~ 500. The observing strategy and data reduction are similar to those used for the GNIRS data. The standard ABBA mode was used with a nodding distance of $20''$ and an exposure time of five minutes at each nod position. A nearby A or F spectroscopic standard star was observed before or after the target observation. The NIRI data were also reduced using the Gemini package within IRAF. After sky-subtraction, flat-fielding and wavelength calibration, the frames were combined. Then one-dimensional spectra were extracted from the combined images, and were flux calibrated using the spectra of standard stars. The observing log is given in Table 2.1 and the spectrum is shown in Figure 2.2. Since we do not have K-band photometry for this object, we cannot apply an absolute flux calibration. In Figure 2.2, we have scaled the spectrum to its J magnitude assuming a power-law continuum slope of $\alpha_\nu = -0.5$ ($f_\nu \sim \nu^{\alpha_\nu}$).

2.3   Spectral Fit and Emission-Line Measurements

To analyze broad emission lines such as C IV and Mg II we fit and subtract the UV
Fe II emission that contaminates most of the UV-optical spectral region; thousands
of Fe II lines are emitted at UV-optical energies that blend with other lines in the
spectrum. We use the UV Fe II template presented by Vestergaard & Wilkes (2001)
and adopt the fitting procedure described in detail in § 4.2 by these authors. Briefly,
the fitting is done as an iteration over a power-law fit to the continuum emission
and a model fit to the Fe II emission using a scaled and broadened version of the
Fe II template. The Fe II template is broadened by convolving the template with
Gaussians with a range of sigmas. In the first iteration a power-law is fitted to
regions with very little or no contribution from line emission (e.g. 1275–1295 Å;
1325–1335 Å; 1425–1480 Å; 2180–2220 Å; 3000–3040 Å). Upon subtraction of this
primary continuum fit multiple broadened copies of the Fe II template are scaled
to regions which predominantly contain Fe emission. The broadened, scaled Fe II
template that provides the best overall match to the observed Fe II emission in the
observed spectrum is then selected and subtracted. Some adjustments of the Fe II
fitting regions are sometimes necessary to optimize the fit, as judged by a minimiza-
tion of the residual flux upon subtraction of the Fe II model. After subtraction of
the best matching Fe II model from the original data (i.e., with the continuum not
subtracted) another power-law fit to the continuum emission is performed; the lack
of (most of the) contaminating Fe II enables the fitting to be done over a broader
wavelength range, often resulting in a better and more realistic continuum fit. After
subtraction of this continuum model, the Fe II fitting is repeated. The iteration of
the continuum and Fe II fitting is repeated until these individual fits do not change
and the subtraction of the Fe II model leaves a smooth, featureless spectrum (barring
the strong, broad non-Fe emission lines) with a realistic power-law slope. Conver-
gence is often obtained in the second or third iteration. For SDSS J1623+3112, the
wavelength range of the spectrum is too short to allow a reasonable fit to both the
Fe II emission and a power-law continuum, so we assume a slope of $\alpha_\nu = -0.5$ during

Table 2.2.   Redshifts and continuum slopes

Quasar (SDSS)	Redshift	$\mathrm{Slope_{uv}}(\alpha_\nu)$[a]	$\mathrm{Slope_{opt}}(\alpha_\nu)$[b]
J0836+0054	5.810 ± 0.003[c]	$-0.62^{+0.06}_{-0.06}$	-0.52
J1030+0524	6.309 ± 0.009	$0.46^{+0.18}_{-0.25}$	-0.31
J1044$-$0125	5.778 ± 0.005[d]	$-0.27^{+0.09}_{-0.10}$	-0.30
J1306+0356	6.016 ± 0.005	$0.50^{+0.12}_{-0.14}$	-0.12
J1411+1217	5.927 ± 0.004	$-0.21^{+0.16}_{-0.19}$	-0.51
J1623+3112	6.247 ± 0.005	$\ldots$	-0.32

[a]UV continuum slopes measured from the Gemini spectra.

[b]Optical continuum slopes taken from Jiang et al. (2006a).

[c]Taken from Kurk et al. (2007).

[d]Measured from the C III] $\lambda 1909$ emission line.

the model fitting. This gives a lower limit of the Fe II emission. Balmer continuum could be non-negligible at $\lambda_0 \geq 2000$ Å (e.g. Dietrich et al., 2002, 2003b), however, the wavelength coverage of our spectra is not long enough to provide a realistic fit to it, so we do not consider it in our fits. The power-law continuum fits to each of the quasars in our sample are listed in column 3 of Table 2.2. We note that the accuracy of the derived line width depends on the quality of the spectra. For widths broader than 5000–6000 km/s our ability to accurately determine the intrinsic Fe II line width decreases.

We use Mg II emission lines to determine the redshifts of the quasars. Accurate redshifts are important for various studies such as molecular line searches. The redshifts given in the quasar discovery papers were mostly determined from the Lyα emission lines, where strong Lyα absorption systems usually cause large un-

certainties in redshift measurements. While most of high-ionization, broad emission lines such as C IV can be significantly blueshifted with respect to quasar systematic redshifts, the Mg II emission line has a small blueshift and thus provides a reliable redshift measurement (e.g. McIntosh et al., 1999; Vanden Berk et al., 2001; Richards et al., 2002). The Mg II emission line at $z \sim 6$ is close to a strong telluric absorption band at 1.9 μm, as seen in Figure 2.1. To avoid the effect of the telluric absorption, we measure the line center of each Mg II emission line using a Gaussian profile to fit the top $\sim 50\%$ of the line. The line center is also estimated by calculating the 3$\times$median–2$\times$mean mode of the top $\sim 50\%$ of the line. The two methods give similar results because the top $\sim 50\%$ of the line is almost symmetric. The measured redshifts are given in Column 2 of Table 2.2. They are in good agreement with the values derived in Kurk et al. (2007), but differ by 0.02–0.03 from the values in the discovery papers. We did not detect the Mg II emission line for SDSS J0836+0054 and SDSS J1044−0125, which were observed with high humidity. In Table 2.2, the redshift of SDSS J0836+0054, measured also using the Mg II emission line, is taken from Kurk et al. (2007), and the redshift of SDSS J1044−0125 is measured from the C III] λ1909 emission line using the same method.

We fit individual emission lines after the subtraction of the Fe II emission and power-law continuum. We use one Gaussian profile to fit most isolated lines and use multiple Gaussian profiles to fit blended lines. We allow both the line center and the line width to vary unless stated otherwise. Broad emission lines in quasars usually show asymmetric velocity profiles, so in the cases in which a single Gaussian profile does not provide a reasonable fit, we use double Gaussian profiles. There is no particular physical meaning to the two Gaussian components. For each quasar, the following emission lines (if detected) are fitted. (1) Lyα + N V + Si II λ1262 (hereafter Si II). We use four Gaussian profiles to fit the three lines, with the first two profiles representing the broad and narrow components of Lyα and the last two profiles representing N V and Si II, respectively. During the fit, the line centers are fixed at the values given by Vanden Berk et al. (2001). Since the blue side of the Lyα line is strongly absorbed, we only fit the red side of the Lyα line. (2) O I λ1304,

C II $\lambda1335$, and Si IV $\lambda1397$ (hereafter O I, C II, and Si IV). We use one Gaussian profile to fit each of these lines. (3) C IV. The strong C IV line is fitted using one or two Gaussian components. (4) He II + O III] $\lambda1663$ (hereafter O III]). These two lines are very weak, but He II is important for determining chemical abundances. They were tentatively detected in three quasars and fitted simultaneously using two Gaussians. (5) Al III $\lambda1857$ + C III] $\lambda1909$ (hereafter Al III and C III]). The weak Al III line is often detected on the blue wing of the strong C III] line. We use two Gaussian profiles to fit these two lines simultaneously if Al III is detected, otherwise the C III] line is fitted using a single Gaussian profile. We ignore the weak Si III] $\lambda1892$ line on top of C III]. (6) Mg II. The Mg II emission line can be well fitted by double Gaussians (e.g. Barth et al., 2003), with a weak component located on the blue side of a much stronger component. If the blue side of Mg II is affected by telluric absorptions, we fit the line using a single Gaussian. For the emission lines that are severely affected by broad-absorption lines (BALs), we fix their central wavelengths and fit their red half sides using a single Gaussian profile.

Table 2.3.   Emission line properties

		J0836+0054	J1030+0524	J1044−0125	J1306+0356	J1411+1217	J1623+3112
N V	EW	15.9±0.7	4.9±0.1	3.9±0.2	9.3±0.3	28.9±0.4	...
	FWHM	31.5±1.0	8.7±0.2	10.4±0.3	15.0±0.2	22.3±0.3	...
Si II	EW	3.6±0.3	3.0±0.2	2.3±0.1	1.7±0.1	0.9±0.1	...
	FWHM	15.0±0.6	15.8±0.7	12.7±0.3	12.8±0.4	3.7±0.3	...
O I	EW	7.4±0.1	6.7±0.3	2.6±0.2	...	6.7±0.2	...
	FWHM	24.6±0.5	18.8±0.7	24.3±1.3	...	8.1±0.2	...
C II	EW	5.8±0.5	4.0±0.4	...	...	...	...
	FWHM	41.9±3.1	17.0±1.5	...	...	...	...
Si IV	EW	9.3±4.2	8.5±1.7	8.9±0.7	9.5±0.8	8.1±6.4	...
	FWHM	25.3±5.9	18.4±2.9	35.7±1.8	29.0±2.0	21.5±12.2	...
C IV	EW	15.0±1.6	40.0±3.1	24.7±2.1	29.6±2.4	76.2±5.8	...
	FWHM	37.1±3.0	27.3±2.9	42.2±3.1	24.5±2.3	17.5±1.6	...
He II	EW	...	3.4±2.0	...	2.6±1.8	5.1±2.5	...
	FWHM	...	21.7±8.8	...	15.5±7.5	39.0±26.8	...
O III]	EW	...	2.3±1.3	...	2.7±2.0	2.8±2.5	...

Table 2.3 (cont'd)

		J0836+0054	J1030+0524	J1044−0125	J1306+0356	J1411+1217	J1623+3112
	FWHM	...	22.9±11.0	...	26.9±19.4	42.2±34.0	...
Al II	EW	1.8±0.9	...	5.0±1.6	7.0±3.1	5.1±2.3	...
	FWHM	16.3±6.8	...	31.0±6.7	34.5±14.7	25.6±9.2	...
C III]	EW	18.9±2.3	19.3±2.8	24.0±1.8	19.1±3.9	26.1±3.2	...
	FWHM	53.2±4.9	31.6±3.3	50.3±3.2	37.6±7.4	31.3±2.6	...
Mg II	EW	...	46.1±3.7	...	24.9±2.1	37.5±5.5	27.4±3.9
	FWHM	...	33.8±2.2	...	33.2±2.2	23.7±2.7	34.4±2.4

Note. — Rest-frame FWHM and EW are in units of Å.

Figures 2.1 and 2.2 show the fitting results for the six quasars. The blue solid lines are the best fits to the emission lines and the blue dashed lines are the best model fits to the power-law continuum and Fe II emission. The red lines are the sums of all the components. For comparison, we show the low-redshift composite spectrum of Vanden Berk et al. (2001) in gray. Table 2.3 shows the rest-frame EW and FWHM of emission lines derived from the model fitting results. For the lines which were fitted using double Gaussian profiles, their EW and FWHM are calculated from the combination of the two components. The errors given in the table are the formal uncertainties obtained from our fitting process, so the real errors could be larger in the cases in which the lines are heavily blended, or we fit a profile of the wrong shape. The He II emission is tentatively detected in three quasars at a significance level of $\sim 2\sigma$. We note from Table 2.2 that three quasars have continuum slopes consistent with the slope $\alpha_\nu = -0.44$ of the composite spectrum of low-redshift SDSS quasars (Vanden Berk et al., 2001), while SDSS J1030+0524 and SDSS J1306+0356 show significantly bluer continua with $\alpha_\nu \sim 0.5$. Pentericci et al. (2003) obtained an average slope of $\alpha_\nu = -0.57$ with a scatter of 0.33 from 45 intermediate-redshift SDSS quasars at $3.6 < z < 5.0$. This indicates that the continuum slopes in the two unusual quasars deviate from the average slopes at a $\sim 3\sigma$ significance level. Table 2.2 also shows the rest-frame optical continuum slopes derived from the *Spitzer* IRAC broad-band photometry of the same objects (Jiang et al., 2006a). The optical continua are generally redder than the UV continua measured from the Gemini spectra, as also reported by Vanden Berk et al. (2001).

2.4 Chemical Abundances and Central Black Hole Masses

2.4.1 Chemical abundances

Emission-line ratios can be used to measure gas metallicity in the quasar BLR and track the chemical evolution with redshift. When weak emission lines are difficult to detect in high-redshift quasars, strong broad emission lines such as N V, C IV, and Mg II become a powerful tool to probe metallicity at high redshift (e.g. Hamann &

Ferland, 1992, 1993). Different elements form on different timescales. Elements such as C, O, and Mg are formed in the explosions of massive stars, and their enrichment is rapid; while the second generation element N is produced from previously generated C and O, and its enrichment is relatively slow. Helium is a primordial element and its abundance changes little with cosmic time. Chemical abundances measured from emission lines and intrinsic absorption lines show solar or supersolar metallicity in quasar environments at low redshift (e.g. Hamann et al., 2007), and can be as high as 15 times solar metallicity (Baldwin et al., 2003). Furthermore, studies have shown that there is little chemical evolution up to the highest known redshift (e.g. Barth et al., 2003).

We calculate emission-line fluxes from the model fitting results described in § 2.3. The fluxes are normalized to the C IV fluxes and shown in Table 2.4 and Figure 2.3 (filled circles with errors). Nagao et al. (2006) used a sample of over 5000 quasars from the SDSS Data Release Two to study quasar BLRs. They made quasar composite spectra in the ranges of $2.0 \leq z \leq 4.5$ and $-29.5 \leq M_B \leq -24.5$, and measured emission-line ratios and metallicities in the composite spectra for each redshift and luminosity bin. They found that most of the line ratios (with respect to the C IV line) that they investigated do not show strong evolution with redshift. For the purpose of comparison, we show in Figure 2.3 the line ratios of quasars (filled squares) in the luminosity range of $-27.5 < M_B < -26.5$ from Nagao et al. (2006). Although there are correlations between quasar luminosities and most line ratios (Nagao et al., 2006), most of our quasars have luminosities in a small range of $-27.5 < M_B < -26.5$. Figure 2.3 shows that most of the flux ratios do not exhibit strong evolution up to $z \sim 6$. There is a trend for higher C II/C IV and O I/C IV ratios at higher redshift. Nagao et al. (2006) already noted that the O I/C IV flux ratio is marginally correlated with redshift. This trend could also be caused by the intrinsic dispersion of the flux ratios.

Photoionization models have shown that a series of emission-line ratios can be used to estimate gas metallicity in the BLRs of quasars. Hamann et al. (2002) studied the relative N abundance as a metallicity indicator based on the locally

Table 2.4. Flux ratios

	J0836+0054	J1030+0524	J1044−0125	J1306+0356	J1411+1217	J1623+3112
N v/C iv	1.44±0.17	0.21±0.02	0.23±0.03	0.55±0.05	0.56±0.04	⋯
Si ii/C iv	0.32±0.04	0.12±0.02	0.13±0.02	0.10±0.01	0.02±0.01	⋯
O i/C iv	0.62±0.07	0.26±0.02	0.14±0.02	⋯	0.12±0.02	⋯
C ii/C iv	0.47±0.06	0.14±0.02	⋯	⋯	⋯	⋯
Si iv/C iv	0.72±0.33	0.27±0.06	0.43±0.05	0.41±0.05	0.13±0.10	⋯
He ii/C iv	⋯	0.07±0.04	⋯	0.08±0.05	0.06±0.05	⋯
O iii]/C iv	⋯	0.05±0.03	⋯	0.08±0.06	0.03±0.02	⋯
Al iii/C iv	0.10±0.05	⋯	0.15±0.05	0.15±0.07	0.05±0.02	⋯
C iii]/C iv	0.95±0.15	0.29±0.05	0.68±0.08	0.38±0.08	0.24±0.03	⋯
Fe ii/Mg ii	⋯	5.45±0.58	⋯	5.77±0.72	5.27±0.72	3.21±0.62
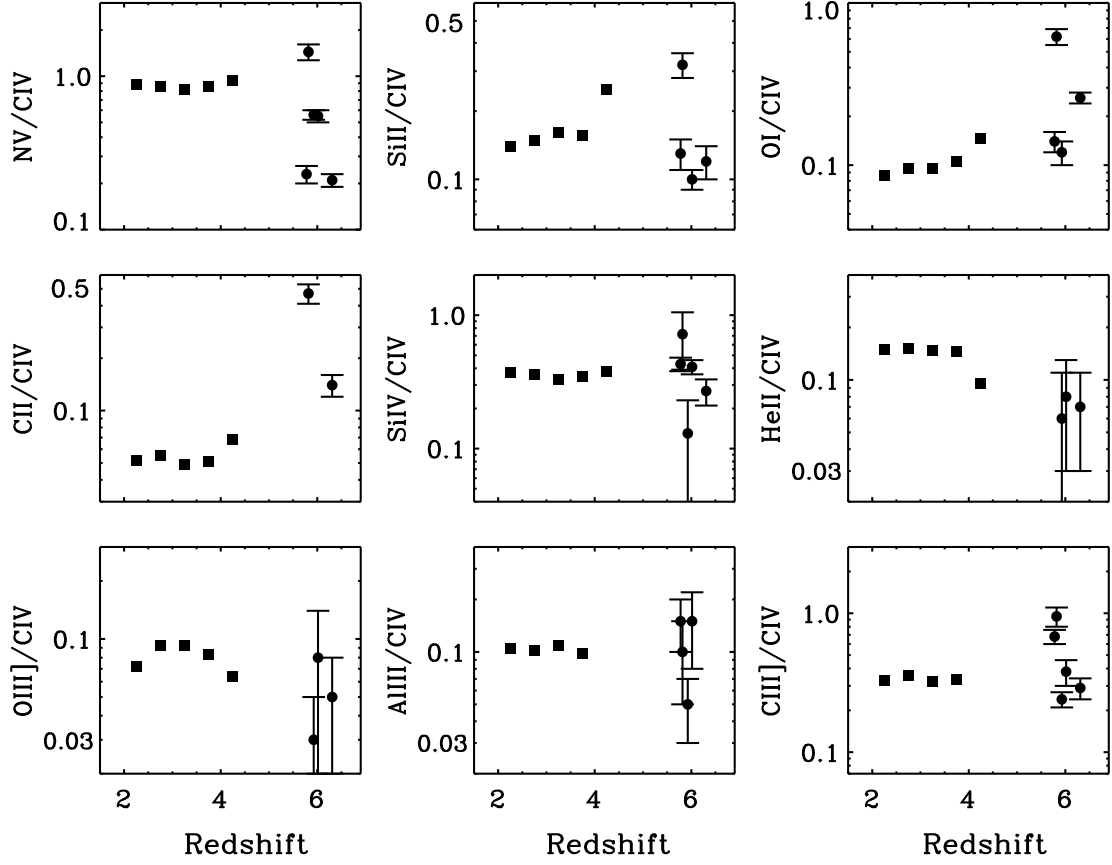
Figure 2.3 Emission line fluxes (filled circles with errors) of the $z \sim 6$ quasars compared to low-redshift measurements. The fluxes have been normalized to the C IV fluxes. The filled squares represent the flux ratios measured in the composite spectra of quasars in the luminosity range $-27.5 < M_B < -26.5$ from Nagao et al. (2006). Most of the flux ratios do not exhibit strong evolution up to $z \sim 6$.

optimally emitting cloud (LOC) model (Baldwin et al., 1995), and calculated theoretical emission-line ratios as a function of metallicity $Z/Z_\odot$. We estimate the metallicity from the N v/C iv and N v/He ii ratios using Figure 2.5 of Hamann et al. (2002). There is a 30% difference between the solar abundances used by Hamann et al. (2002) and the latest solar abundances (Baldwin et al., 2003), so we scale the abundances of Hamann et al. (2002) to match the latest values using the method by Baldwin et al. (2003). The results are shown as the open circles in Figure 2.4. Nagao et al. (2006) also used the LOC model, but included more UV emission lines in their photoionization model. We use Figure 29 of Nagao et al. (2006) to measure the metallicity from various line ratios and show the measurements as the filled circles in Figure 2.4. The two models give similar metallicities from the N v/C iv and N v/He ii ratios. The metallicities in these high-redshift quasars are supersolar, with a typical value of ~ 4 $Z_\odot$. Nagao et al. (2006) computed chemical abundances as a function of redshift for the SDSS composite spectra using their photoionization model. The filled squares in Figure 2.4 show the abundances averaged in the luminosity range of $-28.5 < M_B < -25.5$. The filled triangles represent the chemical abundances of eleven $3.9 < z < 5.0$ quasars from Dietrich et al. (2003a). Figure 2.4 shows that the metallicity is consistent with no strong evolution within the errors up to $z \sim 6$.

The Fe ii/Mg ii ratio is important in understanding chemical evolution at high redshift. We use the Fe ii emission line complex at $\lambda_0 = 2000 \sim 3000$ Å as the Fe ii flux indicator (e.g. Dietrich et al., 2002; Barth et al., 2003). The flux of the Fe ii complex is integrated from 2200 to 3090 Å over the best-fitting Fe ii template. The derived Fe ii/Mg ii ratios (filled circles) with a typical value of 4.9 ± 1.4 are shown in Table 2.4 and Figure 2.5. Using a similar method Kurk et al. (2007) obtained a lower ratio of 2.7 ± 0.8 from their quasar sample. The discrepancy is partly due to the fact that they corrected for Balmer continuum in their spectral fits. For comparison, we also show the Fe ii/Mg ii ratios of $z \sim 6$ quasars from previous measurements (Barth et al., 2003; Maiolino et al., 2003; Freudling et al., 2003; Iwamuro et al., 2004) as open circles in Figure 2.5. Iwamuro et al. (2002) measured the Fe ii/Mg ii
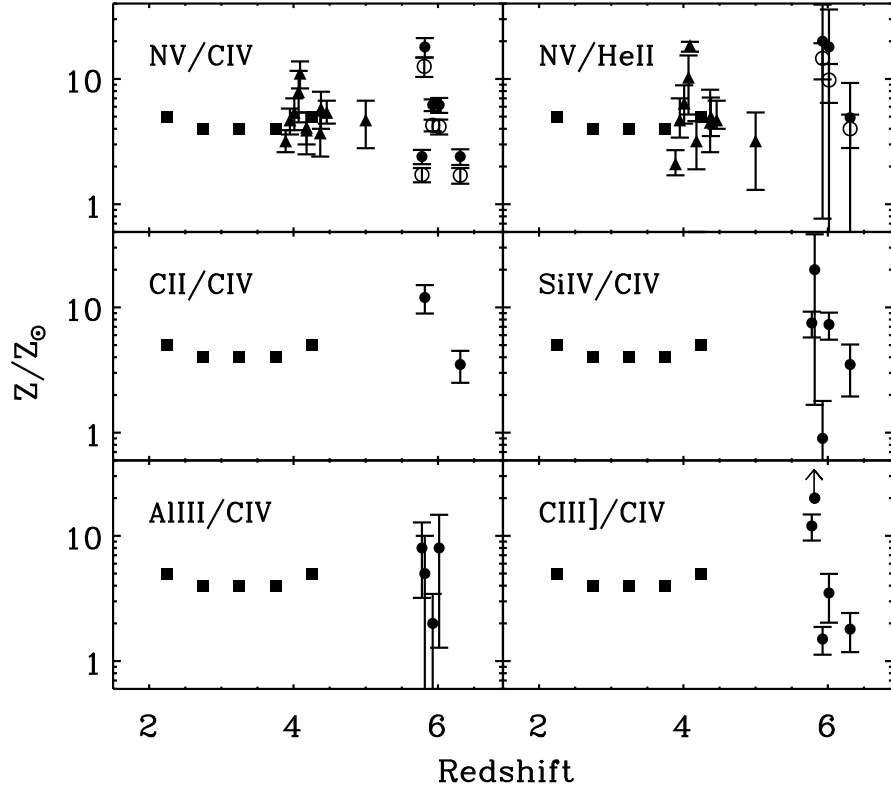
Figure 2.4 Chemical abundances of quasars derived from line ratios as a function of redshift. The open circles represent the metallicities derived from the N V/C IV and N V/He II ratios using Figure 2.5 of Hamann et al. (2002). The filled circles represent the metallicities derived from the line ratios using Figure 29 of Nagao et al. (2006). The filled squares show the averaged metallicities of quasars for the luminosity range $-28.5 < M_B < -25.5$ from Nagao et al. (2006). The filled triangles show the metallicities of eleven $3.9 < z < 5.0$ quasars from Dietrich et al. (2003a). The metallicities estimated from each line ratio show no strong evolution up to $z > 6$ within the errors.
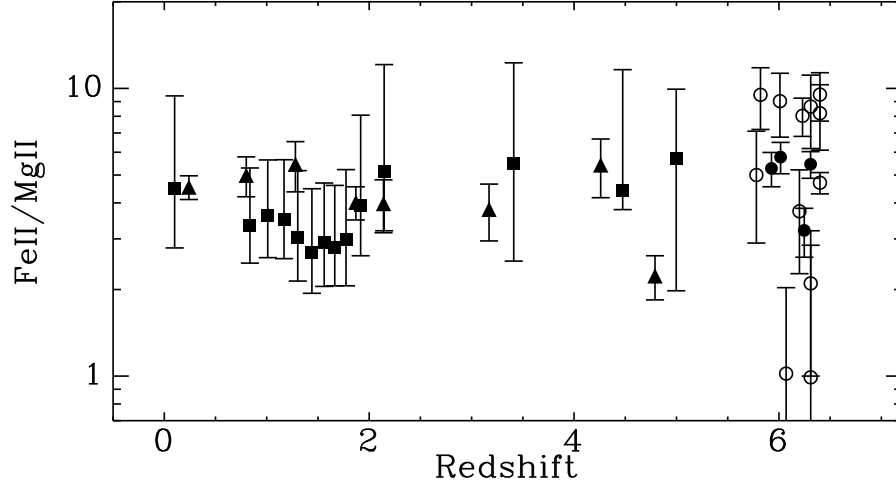
Figure 2.5 The Fe II/Mg II ratio as a function of redshift. The filled circles are our results. The open circles show the Fe II/Mg II ratios of $z \sim 6$ quasars from previous measurements (Barth et al., 2003; Maiolino et al., 2003; Freudling et al., 2003; Iwamuro et al., 2004). The filled squares and triangles represent the low-redshift results from Iwamuro et al. (2002) and Dietrich et al. (2003b). The lack of strong evolution of the Fe II/Mg II abundance continues to $z \sim 6$.

ratios from the spectra of quasars at $0 < z < 5.3$, and computed the median values of the ratios for a range of redshifts. These median ratios are shown as the filled squares in Figure 2.5. To study the evolution of Fe II/Mg II, Dietrich et al. (2003b) made quasar composite spectra from $z = 0$ to 5. The Fe II/Mg II ratios measured from the composite spectra are shown as the filled triangles in Figure 2.5. We note that the Fe II flux in some studies was integrated over the wavelength range of $2150 < \lambda_0 < 3300$ Å (e.g. Freudling et al., 2003; Iwamuro et al., 2004), slightly different from the range that we used. We also note that some of these studies used different Fe II templates to measure Fe II fluxes. These issues usually affect the Fe II/Mg II measurements by less than a factor of two and cause a relatively large scatter in the measurements at $z \sim 6$. Figure 2.5 shows that our results are consistent with those derived from both low-redshift samples and other $z \sim 6$ samples within errors. The details of how the Fe II bump is formed are not well understood (e.g. Baldwin et al., 2004), so we do not derive actual abundances from the Fe II/Mg II ratios.

We have shown that the metallicity in the BLRs of high-redshift quasars is supersolar, and the lack of strong evolution in metallicity continues to $z \sim 6$. The high metallicity at $z \sim 6$ indicates that vigorous star formation and element enrichment have occurred in quasar host galaxies in the first Gyr of cosmic time. Millimeter and submillimeter observations revealed that luminous $z \sim 6$ quasars are extremely far-infrared (FIR) luminous ($\sim 10^{13}$ $L_\odot$) and have a large amount of cool dust (10^8–10^9 $M_\odot$) (Carilli et al., 2001; Bertoldi et al., 2003a; Priddey et al., 2003; Robson et al., 2004). If the FIR emission is mainly powered by star formation in the host galaxies, the star formation rates are estimated to be ~ 1000 $M_\odot$ yr^{-1}. Strong starbursts can be induced by merging gas-rich galaxies (e.g. Hopkins et al., 2006; Li et al., 2007). CO observations have already revealed the presence of $\sim 2 \times 10^{10}$ $M_\odot$ of molecular gas in the highest redshift quasar SDSS J1148+5251 (Walter et al., 2003; Bertoldi et al., 2003b; Walter et al., 2004). This amount of gas can sustain the star formation rate of ~ 3000 $M_\odot$ yr^{-1}, inferred from the FIR luminosity, for 10^7–10^8 years. If the typical duty cycle time of a luminous quasar is 10^7–10^8 years (e.g. Kauffmann & Haehnelt, 2000; Wyithe & Loeb, 2003; Shen et al., 2007), it would have enough time to form a large amount of first generation elements from massive stars.

We have also shown that the Fe II/Mg II ratios of the $z \sim 6$ quasars are consistent with low-redshift measurements. Most of the Fe in the solar neighborhood is produced in intermediate-mass stars, and their enrichment is delayed by ~ 1 Gyr compared to Mg. Mg^+ and Fe^+ have similar ionization potentials and thus the Fe II/Mg II ratio reflects the Fe/Mg abundance (Dietrich et al., 2003b). Therefore, if Fe was generated in the same way as it is in our neighbors, the Fe II/Mg II ratio is expected to be a strong function of cosmic time at high redshift. However, we do not see any evolution in this ratio even at $z \sim 6$. It has been shown that the timescale of Fe enrichment from SNe Ia strongly depends on star formation histories of host galaxies, and can be much shorter in high-redshift quasar environments (e.g. Friaca & Terlevich, 1998; Matteucci & Recchi, 2001). Matteucci & Recchi (2001) found that the timescale for the maximum SN Ia rate (Fe enrichment) can be as short as ~ 0.3 Gyr in an elliptical galaxy with a high star formation rate but a short star

formation history. On the other hand, Venkatesan et al. (2004) pointed out that stars with a present-day initial mass function are sufficient to produce the observed Fe II/Mg II ratios in $z \sim 6$ quasars, and SNe Ia are not necessarily the main contributor. Fe could also be generated in Population III stars, which are suggested to be first generation stars with masses between 100 and 1000 $M_\odot$. These very massive stars produce a large amount of Fe within a few Myr due to their short lifetimes (Heger & Woosley, 2002).

2.4.2 Central black hole masses

The central BH masses of high-redshift quasars are important in understanding the growth of BHs and quasar accretion rates in the early universe. For high-redshift quasars where direct mass measurements are difficult, BH masses can be estimated using mass scaling relations based on broad emission line widths and continuum luminosities. Strong emission lines, including $H\beta$, C IV, and Mg II, have been used to determine BH masses (e.g. Wandel et al., 1999; Dietrich & Hamann, 2004; McLure & Dunlop, 2004; Vestergaard & Peterson, 2006). Based on empirical scaling relations, a few luminous $z \sim 6$ quasars have been found to harbor central BHs with masses of $10^9 \sim 10^{10}$ $M_\odot$ (e.g. Barth et al., 2003; Vestergaard, 2004).

We estimate the central BH masses for the six quasars using the following BH mass scaling relations,

$$M_{BH}(C\,\textsc{iv}) = 4.57 \left(\frac{\text{FWHM}(C\,\textsc{iv})}{\text{km s}^{-1}} \right)^2 \left(\frac{\lambda L_\lambda(1350\text{\AA})}{10^{44} \text{ ergs s}^{-1}} \right)^{0.53} M_\odot \qquad (2.1)$$

and

$$M_{BH}(Mg\,\textsc{ii}) = 3.2 \left(\frac{\text{FWHM}(Mg\,\textsc{ii})}{\text{km s}^{-1}} \right)^2 \left(\frac{\lambda L_\lambda(3000\text{\AA})}{10^{44} \text{ ergs s}^{-1}} \right)^{0.62} M_\odot \qquad (2.2)$$

derived by Vestergaard & Peterson (2006) and McLure & Dunlop (2004), respectively. $L_\lambda(1350\text{\AA})$ and $L_\lambda(3000\text{\AA})$ are luminosities at rest-frame 1350 and 3000 Å. The results are listed in Columns 4 and 5 of Table 2.5. They are in agreement with the masses derived by Kurk et al. (2007). For SDSS J1030+0524 and SDSS J1306+0356, the C IV–based BH masses are greater than the Mg II–based BH

masses by a factor of $\sim$3, but still within the intrinsic scatter (a factor of 3–4) in these scaling relations. The unusual blue continua in the two quasars could cause this discrepancy. The Mg II–based BH masses are also estimated using the latest scaling relation based on FWHM(Mg II) and L_λ(1350Å) by Vestergaard et al. (in preparation). The results are shown in Column 6, and they are consistent with the C IV–based BH masses. Similar to other luminous quasars at $z \sim 6$, our quasars have central BH masses of 10^9–10^{10} M$_\odot$ (e.g. Barth et al., 2003; Vestergaard, 2004; Jiang et al., 2006a).

We calculate the Eddington luminosity ratios of the quasars using their bolometric luminosities and BH masses. We use the Mg II–based BH mass for SDSS J1623+3112 and the C IV–based BH masses for the others. The bolometric luminosities were calculated from multiband observations of the quasars by Jiang et al. (2006a). The results are given in Column 3 of Table 2.5. These luminous $z \sim 6$ quasars have Eddington ratios of order unity, comparable to quasars with similar luminosities at lower redshift (e.g. McLure & Dunlop, 2004; Vestergaard, 2004; Kollmeier et al., 2006).

It is remarkable that billion-solar-mass BHs can form less than one Gyr after the Big Bang. With the reasonable assumption that BH accretion is at the Eddington rate, the BH mass at time t is $M_t = M_0 e^{t/\epsilon\tau}$, where ϵ is the radiative efficiency, $\tau = 4.5 \times 10^8$ years, and M_0 is the initial BH mass or the seed BH mass. Seed BHs can be produced from the collapse of Population III stars or gas clouds, and their masses are roughly 10^2–10^4 M$_\odot$ (e.g. Madau & Rees, 2001; Volonteri & Rees, 2006; Lodato & Natarajan, 2007). Consider the case in which a massive BH at $z = 6$ formed from a seed BH with $M_0 = 10^3$ M$_\odot$ at $z = 20$. The e-folding time $\epsilon\tau$ for the BH growth is roughly 4.5×10^7 years if $\epsilon \sim 0.1$. The BH grows from $z = 20$ to 6 by 15 e-foldings, or a factor of 3.3×10^6, which results in a massive BH with $M_t = 3.3 \times 10^9$ M$_\odot$ at $z = 6$, comparable to the observed BH masses in our sample. If a quasar is shining at half of the Eddington limit, its BH grows from $z = 20$ to 6 by only 7.5 e-foldings, or a factor of ~ 2000, making it very difficult to form billion-solar-mass BHs in this scenario. In addition, if Eddington-limited

Table 2.5.　Central black hole masses (10^9 $M_\odot$)

Quasar (SDSS)	L_{Bol} [a]	L_{Bol}/L_{Edd} [b]	$M_{BH}(C\,IV)$	$M_{BH}(Mg\,II)$	$M'_{BH}(Mg\,II)$ [c]
J0836+0054	47.72	0.44	9.3±1.6	⋯	⋯
J1030+0524	47.37	0.50	3.6±0.9	1.0±0.2	2.1±0.4
J1044−0125	47.63	0.31	10.5±1.6	⋯	⋯
J1306+0356	47.40	0.61	3.2±0.6	1.1±0.1	2.2±0.3
J1411+1217	47.20	0.94	1.3±0.3	0.6±0.1	0.9±0.2
J1623+3112	47.33	1.11	⋯	1.5±0.3	⋯

[a]Bolometric luminosity in log[erg s^{-1}] from Jiang et al. (2006a).

[b]L_{Edd} is derived from $M_{BH}(C\,IV)$ except for SDSS J1623+3112, whose L_{Edd} is derived from $M_{BH}(Mg\,II)$.

[c]M'_{BH} is estimated from the new relation by Vestergaard et al. (in preparation).

accretion is via standard thin disks, BHs are likely to be spun up and the radiative efficiency and Eddington timescale will increase (Volonteri & Rees, 2006; Rees & Volonteri, 2006). In this case it would take much longer to form massive BHs. So super-Eddington accretion or lower radiative efficiency is probably required to form BHs with $M_t = 10^9$–10^{10} M$_\odot$ by $z = 6$.

2.4.3   Notes on individual objects

SDSS J0836+0054 ($z = 5.810$). SDSS J0836+0054 was discovered by Fan et al. (2001a). Its redshift estimated from the Lyα emission line is 5.82, comparable to the redshift 5.810 ± 0.003 determined from the Mg II emission line (Kurk et al., 2007). Due to high humidity, we did not detect the Mg II emission line. Stern et al. (2003) found a very red continuum slope of $\alpha_\nu = -1.55$ in their NIR spectrum of this quasar. However, using the GNIRS spectra with a longer wavelength coverage and a higher spectral quality we obtained a slope of $\alpha_\nu = -0.62$, which is close to $\alpha_\nu = -0.44$, the slope of the SDSS composite spectrum (Vanden Berk et al., 2001). SDSS J0836+0054 is the most luminous quasar known at $z > 5.7$. The central BH mass estimated from the C IV emission line is 9.5×10^9 M$_\odot$. It was also detected by the Faint Images of the Radio Sky at Twenty-cm (FIRST; Becker et al., 1995). The flux at 1.4 GHz measured by FIRST is 1.11±0.15 mJy and measured by Petric et al. (2003) is 1.75±0.04 mJy.

SDSS J1030+0524 ($z = 6.309$). SDSS J1030+0524 is the second highest redshift quasar known to date. The redshift estimated from Lyα is 6.28 (Fan et al., 2001a). We obtained a more accurate and slightly higher redshift 6.309 ± 0.009 from Mg II, consistent with the value 6.311 of Iwamuro et al. (2004). The emission-line ratios and metallicity in this object have been studied by a few groups. In the discovery paper Fan et al. (2001a) estimated lower limits for the N V/C IV and N V/He II ratios: N V/C IV ≥ 0.4 and N V/He II ≥ 3.0. Using VLT NIR observations Pentericci et al. (2002) found N V/C IV $= 0.35$ and N V/He II > 4.3. From our measurements we obtained N V/C IV $= 0.21 \pm 0.02$ and N V/He II $= 2.85 \pm 1.70$, comparable to the previous studies. The Fe II/Mg II ratios of this object measured

in previous papers are quite different. The values reported by Maiolino et al. (2003), Freudling et al. (2003), and Iwamuro et al. (2004) are 8.65 ± 2.47, 2.1 ± 1.1, and $0.99^{+1.86}_{-0.99}$, respectively. We obtained Fe II/Mg II $= 5.46 \pm 0.90$, consistent with the result of Maiolino et al. (2003). Note that the Fe II flux in Freudling et al. (2003) and Iwamuro et al. (2004) was integrated over the wavelength range $2150 < \lambda_0 < 3300$ Å, slightly different from the range $2200 < \lambda_0 < 3090$ Å that Maiolino et al. (2003) and we used. In addition, our NIR spectra have much higher SNRs than those of previous studies.

SDSS J1044−0125 ($z = 5.778$). SDSS J1044−0125 was the first quasar discovered at $z > 5.7$ (Fan et al., 2000a). The redshift estimated from Lyα is 5.80 (Fan et al., 2000a) and that estimated from C IV is 5.74 (Goodrich et al., 2001). However, these measurements could be severely affected by absorption since this is a BAL quasar (Goodrich et al., 2001; Djorgovski et al., 2001). Due to high humidity we did not detect its Mg II emission line. The redshift measured from C III] (Figure 2.1 shows that this line is not affected by absorption) is 5.778 ± 0.005, consistent with the value 5.78 obtained by Freudling et al. (2003). Freudling et al. (2003) also reported a Fe II/Mg II ratio of 5.0 ± 2.1 for this quasar. SDSS J1044−0125 has the highest BH mass of the objects in our sample. Submillimeter observations (Priddey et al., 2003) and *Spitzer* observations (Jiang et al., 2006a) revealed a large amount of cool and hot dust in this object. SDSS J1044−0125 is the only BAL quasar in our sample. The fraction of BAL quasars in the sample is 16.7%, similar to the low-redshift fraction (Trump et al., 2006).

SDSS J1306+0356 ($z = 6.016$). The discovery paper for SDSS J1306+0356 indicated a redshift $z = 5.99$ based on Lyα (Fan et al., 2001a). We obtained a more accurate and slightly higher redshift 6.016 ± 0.005. Pentericci et al. (2002) reported a N V/C IV ratio of 0.67 for this quasar. The ratio we measured is 0.55 ± 0.05. We also obtained a Fe II/Mg II ratio of 5.77 ± 0.72, slightly smaller than the value 9.03 ± 2.26 derived by Maiolino et al. (2003) based on low SNR spectra. We detected four strong Mg II $\lambda\lambda 2796,2803$ absorption systems in the spectra of this quasar, including the two highest redshift Mg II absorbers known (see § 2.5).

SDSS J1411+1217 ($z = 5.927$). SDSS J1411+1217 has the narrowest emission lines in our sample. Its Lyα and N V emission lines are well separated. Therefore the redshift $z = 5.93$ measured from N V and O I in the discovery paper (Fan et al., 2004) is accurate, and is consistent with the redshift 5.927 ± 0.004 measured from Mg II in the Gemini spectrum. SDSS J1411+1217 has the lowest BH mass in the sample. It also has a very weak *Spitzer* 24μm ($\lambda_0 \sim 3.5$ μm) flux, and its SED does not show any hot dust emission (Jiang et al., 2006a). Another quasar SDSS J0005$-$0006 (not in this sample) shows similar IR properties and does not have hot dust emission either. This may reflect dust evolution at high redshift, as such dustless quasars are unknown at lower redshift.

SDSS J1623+3112 ($z = 6.247$). The redshift of SDSS J1623+3112 measured from Lyα in the discovery paper is 6.22. We obtained a higher redshift of 6.247 ± 0.005 from Mg II. This makes it the third highest redshift quasar known to date.

2.5 Mg II Absorption Systems at $z < 6$

We search for Mg II $\lambda\lambda2796,2803$ intervening systems in the spectra of five $z \sim 6$ quasars. SDSS J1623+3112 is excluded in this analysis because it has a short wavelength coverage. The SNRs of the spectra for different quasars are different, as are the dispersions from one order to another. The SNRs at $\lambda \leq 1.2$ μm are usually higher than those at longer wavelengths, especially in the range of $1.4 < \lambda < 1.8$ μm (roughly H band). However, a Mg II $\lambda2796$ absorption line with rest equivalent width $W_0^{\lambda2796}$ greater than 1.0 Å at $z < 3$ or a Mg II $\lambda2796$ absorption line with $W_0^{\lambda2796}$ greater than 1.5 Å at $z > 3$ can be detected at a $\sim 7\sigma$ significance level in the lowest SNR parts of the spectra shown in Figure 2.1. Moreover, previous studies have used similar limits (e.g. Nestor et al., 2005). Our sample is small, and does not provide good statistics by itself, so the comparison with other samples is important. Thus to achieve unbiased statistics, we search for Mg II absorbers with $W_0^{\lambda2796} > 1.0$ Å at $z < 3$ and Mg II absorbers with $W_0^{\lambda2796} > 1.5$ Å at $z > 3$.

We search for pairs of absorption lines with separation matching the Mg II

$\lambda\lambda$2796,2803 doublet. Then we search for absorption lines of other species associated with the identified Mg II absorbers by matching various strong quasar absorption lines known in the literature to the spectra. Five Mg II absorption systems are identified, with one in the spectrum of SDSS J0836+0054 and the other four in the spectra of SDSS J1306+0356. We normalize the absorption lines using the local continua measured by fitting low-order spline curves to the spectra. Figure 2.6 shows the normalized spectra of the five absorption systems, with the identified lines marked. These lines are usually strong and commonly detected in quasar absorption systems, such as C IV $\lambda\lambda$1548,1550 (marked as C IV-D in the figure), Fe II λ1608, Al II λ1670, Al III $\lambda\lambda$1854,1862 (marked as Al III-D), Fe II λ2600, Mg II $\lambda\lambda$2796,2803 (marked as Mg II-D), and Mg I λ2852. The four absorption systems found in the spectra of SDSS J1306+0356 are denoted as (a), (b), (c), and (d).

We measure the redshifts (z_{abs}) and rest-frame equivalent widths (W_0) of the absorption lines by fitting a Gaussian to each line. Unresolved or very weak absorption lines are not fitted. The results are given in Table 2.6. The Mg II doublet ratios are close to one, indicating that these strong Mg II absorbers are saturated. The Mg II absorber identified in the spectra of SDSS J0836+0054 is at $z = 3.742$. A pair of moderate strong Al III $\lambda\lambda$1854,1862 lines in the same absorber are also detected. C IV $\lambda\lambda$1548,1550, which is usually associated with Mg II, is beyond the spectral coverage. We do not detect any strong Fe II absorption in this system. There are four Mg II absorption systems identified in the spectra of SDSS J1306+0356. Systems (a) and (b) are at relatively low redshifts. System (a) at $z = 2.202$ has a strong Mg I λ2852 absorption line. System (b) at $z = 2.532$ has a strong Fe II λ2600 absorption line. C IV $\lambda\lambda$1548,1550 in both systems is beyond the spectral coverage. We discovered two strong Mg II $\lambda\lambda$2796,2803 absorbers at $z = 4.8668$ and 4.8823. They are the most distant Mg II absorbers known to date. The Mg II λ2803 line in system (c) and the Mg II λ2796 line in system (d) almost exactly overlap with each other, so we do not calculate W_0 for the two lines. Note that this is not the so-called line-locking effect, which mainly occurs in BAL quasars or other associated absorption systems with $z_{abs} \sim z_{em}$ (e.g. Foltz et al., 1987; Vilkoviskij & Irwin, 2001;
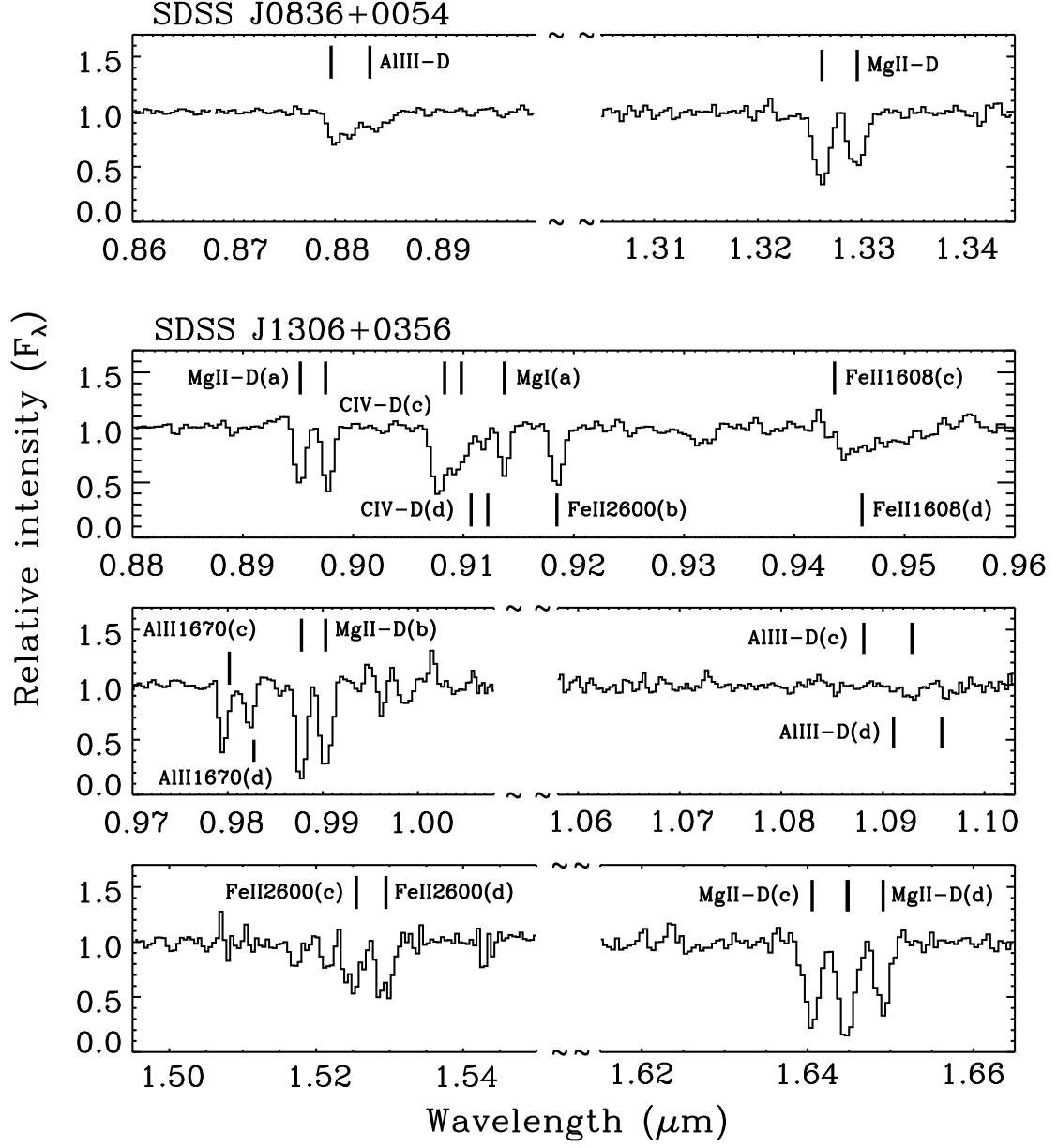
Figure 2.6 Normalized spectra of the five absorption systems in the spectra of SDSS J0836+0054 and SDSS J1306+0356. The positions of the identified lines are marked as vertical lines, and the names of the lines are given nearby. Doublets are expressed as '–D'. The four absorption systems in the spectra SDSS J1306+0356 are denoted as (a), (b), (c), and (d).

Fechner et al., 2004), since the two absorbers are far from SDSS J1306+0356. The proper distance between the two absorbers is about 1.4 Mpc, so they are not likely associated with the same galaxy, but could still belong to the same large-scale structure. Both absorption systems have strong Al II λ1670 and Fe II λ2600 absorption and weak Fe II λ1608 and Al III $\lambda\lambda$1854,1862 absorptions. The C IV $\lambda\lambda$1548,1550 absorption is strong in system (c) but very weak in system (d). It has been found that C IV $\lambda\lambda$1548,1550 is almost always detected in strong Mg II absorption systems at low redshift (e.g. Steidel & Sargent, 1992). The weakness of C IV in system (d) indicates that it is a rare, C IV-deficient system (Churchill et al., 2000). Elston et al. (1996) discovered a strong Mg II absorber at $z = 4.38$ in the spectrum of a $z = 4.68$ quasar. They found that the C IV absorption in this system is also very weak. Thus among the three strong Mg II absorbers at $z > 4$, two have very weak associated C IV, probably indicating that $z > 4$ absorption systems are in a lower ionization state than their low-redshift counterparts (Elston et al., 1996).

We calculate the comoving line-of-sight number densities (dN/dz) of the Mg II absorbers. The sample of the five Mg II absorbers is divided into two subsamples, one with $W_0^{\lambda2796} > 1$ Å at $z < 3$ and the other one with $W_0^{\lambda2796} > 1.5$ Å at $z > 3$. The redshift path covered by a spectrum is,

$$\Delta Z(W_0^{\lambda2796}) = \int_{\Delta z} g(W_0^{\lambda2796}, z)dz, \qquad (2.3)$$

where $g(W_0^{\lambda2796}, z) = 1$ if a Mg II absorber at redshift z and of the given EW would be detected in the spectrum in the redshift range Δz and $g(W_0^{\lambda2796}, z) = 0$ otherwise. The total redshift paths covered by the two subsamples are 3.4 and 10.4, respectively. Then the number density along the redshift path for each subsample is estimated by,

$$dN/dz = \frac{N_a}{\sum \Delta Z(W_0^{\lambda2796})_i}, \qquad (2.4)$$

where N_a is the number of Mg II absorbers and the sum is over all spectra in the subsample. We show our results in Figure 2.7. The filled diamond represents the density for $W_0^{\lambda2796} > 1.0$ Å at $z < 3$ and the filled circle represents the density for $W_0^{\lambda2796} > 1.5$ Å at $z > 3$. The two data points are positioned at the median redshifts

Table 2.6.   Absorption lines

Absorption system	λ_{abs} (Å)	ID	z_{abs}	W_0 (Å)
SDSS J0836+0054	13261.81	Mg II(2796)	3.7426	2.59
	13295.43	Mg II(2803)	3.7424	2.08
SDSS J1306+0356 (a)	8952.03	Mg II(2796)	2.2013	1.86
	8977.30	Mg II(2803)	2.2022	1.99
	9137.13	Mg I(2852)	2.2028	1.29
SDSS J1306+0356 (b)	9877.64	Mg II(2796)	2.5323	3.24
	9903.27	Mg II(2803)	2.5324	3.15
	9185.23	Fe II(2600)	2.5325	1.94
SDSS J1306+0356 (c)	16405.55	Mg II(2796)	4.8668	2.92
	16447.67	Mg II(2803)	. . .	. . .
	9795.84	Al II(1670)	4.8632	1.11
	15252.21	Fe II(2600)	4.8658	1.49
SDSS J1306+0356 (d)	16448.85	Mg II(2796)	. . .	. . .
	16491.08	Mg II(2803)	4.8823	2.11
	9822.93	Al II(1670)	4.8795	0.76
	15293.94	Fe II(2600)	4.8819	1.97
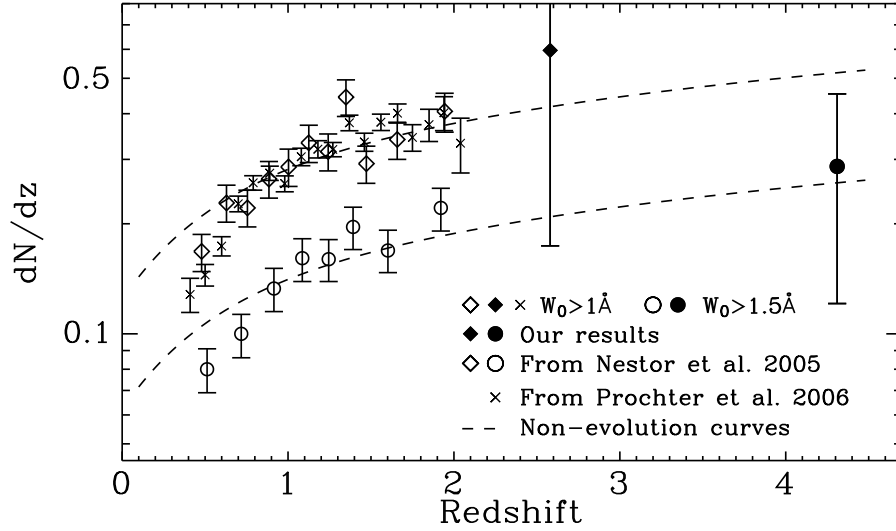
Figure 2.7 Comoving number densities of Mg II absorbers. The filled diamond represents the density for $W_0^{\lambda 2796} > 1$ Å at $z = 2.6$ and the filled circle represents the density for $W_0^{\lambda 2796} > 1.5$ Å at $z = 4.3$. The open diamonds and circles show the number densities for $W_0^{\lambda 2796} > 1.0$ and 1.5 Å from Figure 9 of Nestor et al. (2005). The crosses show the densities of the $W_0^{\lambda 2796} > 1.0$ Å absorbers from Prochter et al. (2006). The dashed lines represent non-evolution curves for the cosmology of $(\Omega_m, \Omega_\Lambda, h) = (0.3, 0.7, 0.7)$. The curves have been scaled to minimize the χ^2 to the data of Nestor et al. (2005). The densities are consistent with no cosmic evolution.

$z = 2.6$ and 4.3, respectively. The statistical uncertainties are Poisson.

The number density of Mg II absorbers at low redshift has been well studied. Steidel & Sargent (1992) collected the spectra of 103 quasars and found that the density of Mg II absorbers with $W_0^{\lambda 2796} > 0.3$ Å does not show cosmic evolution, but the density of strongest Mg II absorbers significantly increases with redshift. Nestor et al. (2005) reached similar results by studying Mg II absorptions in the spectra of thousands of quasars from the SDSS Early Data Release (Stoughton et al., 2002). They divided the sample into subsamples with $W_0^{\lambda 2796} > 0.3$, 0.6, 1.0, 1.5, 2.0, 2.5, and 3.0 Å, respectively, and concluded that dN/dz of the $W_0^{\lambda 2796} > 0.3$, 0.6, 1.0, and 1.5 Å subsamples are consistent with no evolution within errors, while the densities of the other three subsamples show strong evolution with redshift. For comparison, we show in Figure 2.7 the $W_0^{\lambda 2796} > 1.0$ and 1.5 Å samples (open

diamonds and circles) of Nestor et al. (2005). Prochter et al. (2006) studied strong Mg II absorption systems using an even larger quasar sample from the SDSS Data Release Three (Abazajian et al., 2004). They found that there is no evolution in the densities of $W_0^{\lambda 2796} > 1.0$ Å absorbers at $0.8 < z < 2.0$. The crosses in Figure 2.7 show the densities for their $W_0^{\lambda 2796} > 1.0$ Å sample (they did not use a sample of $W_0^{\lambda 2796} > 1.5$ Å). In Figure 2.7 we also show the non-evolution curves (dashed lines) for the cosmology of $(\Omega_m, \Omega_\Lambda, h) = (0.3, 0.7, 0.7)$ with zero curvature,

$$dN/dz = N_0(1 + z)^2[\Omega_m(1 + z)^3 + \Omega_\Lambda]^{-1/2}, \qquad (2.5)$$

where N_0 is a normalization constant. The curves have been scaled to minimize the χ^2 to the data of Nestor et al. (2005). The density of Mg II absorbers with $W_0^{\lambda 2796} > 1.5$ Å that we have measured is consistent with no cosmic evolution up to $z > 4$. However, due to the large uncertainty, we cannot rule out the density evolution of Mg II absorbers.

2.6 Summary

We have obtained high-quality NIR spectra of six luminous $z \sim 6$ SDSS quasars from our Gemini observations. Five of them were observed using Gemini-South/GNIRS in cross dispersion mode, which provides a simultaneous coverage of 0.9–2.5 μm. The sixth was observed in K band with Gemini-North/NIRI. These spectra have higher SNRs and better wavelength coverage than those in previous studies. We use the NIR spectra combined with optical data to study chemical abundances and BH masses in the $z \sim 6$ quasars and strong intergalactic Mg II absorption at $2.2 < z < 6$.

The spectra are fitted using a combination of a power-law continuum, an Fe II emission template, and a series of emission lines. We calculate the fluxes for detected emission lines based on the Gaussian model fitting results. We find that the line flux ratios (normalized to the C IV fluxes) that we have investigated do not show strong evolution with redshift. We calculate gas metallicity from emission-line ratios using the results of photoionization models given by previous studies and find that the metallicity in the BLRs of these high-redshift quasars is supersolar with a typical

value of ~ 4 Z$_\odot$. The comparison with low-redshift observations shows no show strong evolution in metallicity up to $z \sim 6$. The Fe II/Mg II ratio is also measured for each quasar. We find a typical Fe II/Mg II ratio of 4.9 ± 1.4, which is consistent with low-redshift samples. All these measurement indicate the existence of vigorous star formation and element enrichment in host galaxies in the first Gyr after the Big Bang. We have estimated central BH masses from the C IV and Mg II emission lines using empirical mass scaling relations. As found in other luminous $z \sim 6$ quasars, these quasars have BH masses of 10^9–10^{10} M$_\odot$ and Eddington luminosity ratios of order unity.

We have searched for strong Mg II $\lambda\lambda 2796,2803$ intervening systems in the spectra of five quasars. Two Mg II absorbers with rest equivalent width $W_0^{\lambda 2796} > 1$ Å at $2.2 < z < 3$ and three absorbers with $W_0^{\lambda 2796} > 1.5$ Å at $z > 3$ are identified in the spectra of two quasars. The two most distant absorbers are at $z = 4.8668$ and 4.8823, respectively. These are the highest redshift Mg II absorbers known to date. We calculate the comoving line-of-sight number densities for the five identified Mg II absorbers. By comparing with low-redshift studies we find that the densities (dN/dz) of Mg II absorbers with $W_0^{\lambda 2796} > 1.5$ Å are consistent with no cosmic evolution up to $z > 4$. We note that our sample is small. A larger sample is needed to provide a good constraint on the density evolution of Mg II absorbers.

CHAPTER 3

IR PROPERTIES OF $Z \sim 6$ QUASARS: *SPITZER* OBSERVATIONS

3.1   Introduction

High-redshift quasars provide direct probes of the distant early universe where the first generation of galaxies and quasars formed. In the last few years, more than 20 luminous quasars at $z > 5.7$ have been discovered by the Sloan Digital Sky Survey (SDSS; York et al., 2000); the most distant one is at $z = 6.42$ (e.g. Fan et al., 2000a, 2001a, 2003, 2004, 2006a). The discovery of these luminous objects at $z \sim 6$ reveals the existence of supermassive black holes (BHs) with masses higher than $10^9 M_\odot$ (e.g. Barth et al., 2003; Vestergaard, 2004) in the first Gyr of cosmic history. These quasars provide a unique high-redshift sample to answer a series of challenging questions: How did the first billion-solar-mass BHs appear less than 1 Gyr after the Big Bang? How did they grow with time? Did the physical structure of quasars/AGNs evolve with time? Is the emission mechanism in quasars/AGNs the same at $z \sim 6$ as at $z \sim 0$? How were quasars and starburst activity related in the earliest galaxies? What is the role the quasar activity played in early galaxy evolution?

Understanding quasars requires observations from X-ray to radio wavelengths, each spectral region revealing different aspects of quasar emission and probing different regions of the active nuclei. One of the main results from the studies of $z \sim 6$ quasars is the apparent lack of strong evolution in their rest-frame UV/optical and

X-ray properties. Their emission-line strengths and UV continuum shapes are very similar to those of low-redshift quasars (e.g. Barth et al., 2003; Pentericci et al., 2003; Fan et al., 2004), the emission line ratios indicate solar or supersolar metallicity in emission-line regions as found in low-redshift quasars (e.g. Hamann & Ferland, 1999; Dietrich et al., 2003b; Freudling et al., 2003; Maiolino et al., 2003), and the optical-to-X-ray flux ratios and X-ray continuum shapes show little evolution with redshift (e.g. Strateva et al., 2005; Vignali et al., 2005; Steffen et al., 2006; Shemmer et al., 2005, 2006). These measurements show that quasar accretion disks and emission-line regions are formed on very short time scales and their properties are not sensitive to the cosmic age.

However, it is not known whether this lack of evolution in high-energy spectral energy distributions (SEDs) at $z \sim 6$ extends to the rest-frame IR wavelength range. According to classical AGN unification models (Antonucci, 1993), the accretion disk is surrounded by a dusty torus. Much of the emission from quasars/AGNs is re-processed by the dust and is re-emitted at IR wavelengths, where the quasar/AGN SEDs peak. The hottest dust lies within a few pc and produces near-IR (NIR) radiation, while warm and cool dust can extend to a few kpc and dominates the mid-IR (MIR) and far-IR (FIR) emission (e.g. Polletta et al., 2000; Nenkova et al., 2002; Siebenmorgen et al., 2005). The individual contributions from AGN activity and star formation to the heating of warm/cool dust are poorly known (e.g. Wilkes, 2001). On one hand, the shapes of the MIR-to-FIR SEDs indicate that AGN activity may dominate the heating of the warm/cool dust (e.g. Polletta et al., 2000; Haas et al., 2003). On the other hand, the radio-to-FIR correlation for star-forming galaxies (Condon, 1992) still holds for most IR-luminous quasars out to the highest redshifts (e.g. Carilli et al., 2001, 2004), which suggests that the dust could be heated by starbursts in quasar host galaxies rather than quasar central engines. However, it is generally believed that emission from hot dust with temperature of ~ 1000K is directly powered by central active nuclei (e.g. Rieke & Lebofsky, 1981; Polletta et al., 2000; Haas et al., 2003), and thus is closely related to quasar activity.

The *Spitzer Space Telescope* (*Spitzer*; Werner et al., 2004) allows us, for the

first time, to explore the rest-frame NIR range for high-redshift quasars and to constrain the evolution of hot dust in quasar environments. Hines et al. (2006) have observed thirteen $z > 4.5$ quasars using the Infrared Array Camera (IRAC; Fazio et al., 2004) and Multiband Imaging Photometer for *Spitzer* (MIPS; Rieke et al., 2004). They find that the SEDs of these high-redshift quasars at rest wavelength 0.6–4.3 μm do not significantly differ from those of quasars with similar luminosity at low redshifts. In this chapter, we report on *Spitzer* observations of thirteen $z \sim 6$ quasars discovered by the SDSS. All the quasars were observed with IRAC. Ten of them were also observed in the MIPS 24μm band, while the 24μm fluxes of the other three were taken from Hines et al. (2006).

In § 3.2 of this chapter, we present our high-redshift quasar sample and the *Spitzer* photometry of the thirteen quasars. In § 3.3 we show their rest-frame NIR SEDs and study hot dust at $z \sim 6$. We calculate bolometric luminosities and accretion rates for these quasars in § 3.4 and give the summary and discussion in § 3.5. Throughout the chapter we use λ_0 (ν_0) to denote rest-frame wavelength (frequency), and use a Λ-dominated flat cosmology with $H_0 = 70$ km s^{-1} Mpc^{-1}, $\Omega_m = 0.3$ and $\Omega_\Lambda = 0.7$ (e.g. Spergel et al., 2003, 2007).

3.2   Observations

3.2.1   A fundamental sample of luminous $z \sim 6$ quasars from the Sloan Digital Sky Survey

Table 3.1. Optical and NIR properties of the thirteen quasars

Quasar (SDSS)	redshift	M_{1450}	m_{1450}	i	z	J	H	K' (or K)	Ref.
J000239.39+255034.8	5.80	−27.7	19.02	21.47	18.99	...	...	...	4
J000552.34−000655.8	5.85	−26.2	20.23	23.40	20.54	19.87	18.68	...	4
J083643.85+005453.3	5.82	−27.9	18.81	21.04	18.74	17.89	16.95	...	2
J084035.09+562419.9	5.85	−26.9	20.04	22.43	19.76	19.00	18.17	...	5
J103027.10+052455.0	6.28	−27.2	19.66	23.23	20.05	18.87	18.57	17.67	2,6
J104433.04−012502.2	5.74	−27.5	19.21	21.81	19.23	18.31	17.76	17.02(K)	1
J104845.05+463718.3	6.20	−27.6	19.25	22.38	19.86	18.40	17.83	17.12	3,6
J114816.64+525150.2	6.42	−27.8	19.03	23.86	20.12	18.25	17.62	16.98	3,6
J130608.26+035626.3	5.99	−26.9	19.55	22.58	19.47	18.77	...	...	2
J141111.29+121737.4	5.93	−26.8	19.97	22.85	19.65	18.95	...	...	4
J160254.00+422825.0	6.07	−26.8	19.86	22.78	19.89	18.46	...	...	4

Table 3.1 (cont'd)

Quasar (SDSS)	redshift	M_{1450}	m_{1450}	i	z	J	H	K' (or K)	Ref.
J162331.81+311200.5	6.22	−26.7	20.13	24.52	20.09	19.15	. . .	. . .	4
J163033.90+401209.6	6.05	−26.2	20.64	23.38	20.42	19.38	19.18	18.40	3,6

Note. — References (1) Fan et al. (2000a); (2) Fan et al. (2001a); (3) Fan et al. (2003); (4) Fan et al. (2004); (5) Fan et al. (2006a); (6) Iwamuro et al. (2004). Redshifts, M_{1450}, m_{1450}, and the photometry in i, z, and J bands are mostly from the quasar discovery papers (Fan et al., 2000a, 2001a, 2003, 2004, 2006a); K photometry of SDSS J1044−0125 is from Fan et al. (2000a); H and K' photometry of SDSS J1030+0524, J1048+4637, J1148+5251 and J1630+4012 are from Iwamuro et al. (2004); J photometry of SDSS J1044−0125 and H photometry of SDSS J0005−0006, J0836+0054, J0840+5624 and J1044−0125 were carried out in November 2005 using the 6.5m MMT with SWIRC. The SDSS photometry of i and z is on the AB system; J, H, K and K' are on a Vega-based system.

The SDSS is the main source for high-redshift quasar discovery to date, and has discovered more than twenty luminous quasars at $z > 5.7$ from ~ 8000 deg^2. Thirteen of them were observed using *Spitzer* and are included in this chapter. Table 3.1 presents optical and NIR properties of the thirteen quasars. Redshifts, M_{1450}, m_{1450}, and the photometry in i, z, and J bands are mostly from the quasar discovery papers (Fan et al., 2000a, 2001a, 2003, 2004, 2006a); K-band photometry of SDSS J1044−0125 is from Fan et al. (2000a); H- and K'-band photometry of SDSS J1030+0524, J1048+4637, J1148+5251 and J1630+4012 are from Iwamuro et al. (2004); J-band photometry of SDSS J1044−0125 and H-band photometry of SDSS J0005−0006, J0836+0054, J0840+5624 and J1044−0125 were carried out in November 2005 using the 6.5m MMT with SWIRC, which is a J- and H-band camera operating at the f/5 cassegrain focus of the MMT. Note that the SDSS *ugriz* photometric system (Fukugita et al., 1996) is based on the AB magnitude scale of Oke & Gunn (1983), and that the photometry is reported on the asinh scale described in Lupton et al. (1999). The JHK measurements are Vega-based magnitudes.

These $z \sim 6$ quasars also have multiwavelength observations from radio (Petric et al., 2003; Carilli et al., 2004; Frey et al., 2005), mm/submm (Petric et al., 2003; Priddey et al., 2003; Bertoldi et al., 2003a; Robson et al., 2004), to X-ray (Brandt et al., 2001, 2002; Bechtold et al., 2003; Farrah et al., 2004; Schwartz & Virani, 2004; Shemmer et al., 2006). The *Spitzer* observations, combined with X-ray, optical, NIR, mm/submm and radio observations, provide a fundamental sample of quasar SEDs at $z \sim 6$.

3.2.2 *Spitzer* observations of thirteen $z \sim 6$ quasars

IRAC and MIPS 24μm photometry for the $z \sim 6$ quasars was obtained by our *Spitzer* GO-1 program (3198). IRAC observations were carried out in channels 1, 2, 3, and 4 (3.6, 4.5, 5.8 and 8.0 μm) with an exposure time of 1000 s in each channel. Images were processed by the IRAC Basic Calibrated Data (BCD) pipeline, and aperture photometry was performed using customized IDP3 (Schneider & Stobie,

2002) IDL software. We used a 6 pixel (7$''$3) target aperture radius and measured the background in an annulus from 8$-$13 pixels. The contaminant sources within the background area were masked by hand. Finally aperture corrections were derived from the *Spitzer* Tiny Tim simulations (Krist, 2002). The pixel-to-pixel fluctuations in the background annuli were used to estimate the measurement uncertainties. In addition, there is an uncertainty of 3$-$5% in absolute calibration (Reach et al., 2005).

MIPS 24μm photometry for ten quasars was obtained in our *Spitzer* GO program, and the other three were observed in a MIPS GTO program (Hines et al., 2006). The integration time was 1400 s for quasars with high background, and 1260 s for others. The background is estimated using the *Spitzer* background estimator, and high background over the *Spitzer* 24μm passband is about 65.6 MJy/sr. Images were processed by the MIPS BCD pipeline and aperture photometry was performed in the same way as the procedure for IRAC. The target aperture radius was chosen to be 6 pixels (15$''$0) and the background annulus from 8–13 pixels. The background fluctuations were also used to estimate the measurement uncertainties. The uncertainty in absolute calibration is about 10%.

Table 3.2. *Spitzer* photometry of the thirteen quasars

Quasar (SDSS)	3.6μm(mJy)	4.5μm(mJy)	5.8μm(mJy)	8.0μm(mJy)	24μm(mJy)	70μm(mJy)[a]
J0002+2550	0.128±0.002	0.131±0.002	0.131±0.009	0.159±0.019	0.876±0.055	5.21
J0005−0006	0.034±0.002	0.047±0.003	0.046±0.009	0.019±0.017[b]	0.004±0.022[b]	⋯
J0836+0054	0.258±0.003	0.366±0.004	0.258±0.015	0.308±0.032	1.010±0.080[c]	6.29
J0840+5624	0.051±0.001	0.069±0.002	0.076±0.008	0.079±0.013	0.568±0.051	⋯
J1030+0524	0.074±0.002	0.088±0.003	0.078±0.009	0.081±0.023	0.509±0.041	⋯
J1044−0125	0.100±0.002	0.133±0.004	0.103±0.011	0.222±0.026	1.575±0.038	10.4
J1048+4637	0.098±0.002	0.101±0.002	0.087±0.009	0.154±0.016	0.860±0.090[c]	⋯
J1148+5251	0.124±0.002	0.140±0.003	0.133±0.010	0.241±0.016	1.520±0.130[c]	9.73
J1306+0356	0.068±0.002	0.073±0.002	0.048±0.005	0.075±0.011	0.444±0.041	⋯
J1411+1217	0.081±0.002	0.146±0.003	0.087±0.006	0.115±0.013	0.179±0.046	⋯
J1602+4228	0.134±0.001	0.124±0.002	0.143±0.008	0.181±0.012	0.964±0.034	⋯

Table 3.2 (cont'd)

Quasar (SDSS)	3.6μm(mJy)	4.5μm(mJy)	5.8μm(mJy)	8.0μm(mJy)	24μm(mJy)	70μm(mJy)[a]
J1623+3112	0.076±0.001	0.103±0.002	0.058±0.008	0.104±0.012	0.442±0.029	⋯
J1630+4012	0.031±0.001	0.043±0.002	0.030±0.004	0.042±0.006	0.229±0.035	⋯

Note. — Errors given in this table are measurement uncertainties only. The absolute calibration uncertainty for IRAC is 3–5%, and for MIPS is about 10%.

[a]2σ upper limits.

[b]Using smaller apertures than others for photometry; see § 3.2.2.

[c]From Hines et al. (2006).

Images at 70 μm were obtained for four of the objects in the sample (2 from the GTO program and 2 from our GO program). These data were reduced with the MIPS Data Analysis Tool (Gordon et al., 2005). Photometry was performed using a 35″ aperture with 39–65″ background annulus. None of the objects was detected at 70 μm. In order to increase the sensitivity of our measurements, we combined the observations into a median stacked image containing these four objects. While the measured noise decreased approximately by a factor of 2, no detection was achieved in the stacked image.

The observed fluxes and measurement uncertainties of the thirteen quasars are given in Table 3.2. The upper limits are constructed from the measured flux density in the target aperture plus two times the measurement uncertainty. All quasars except SDSS J0005−0006 were detected with high S/N in all IRAC bands and the MIPS 24μm band. SDSS J0005−0006 was marginally detected in the IRAC 8.0μm band, and not detected in the MIPS 24μm band. Because of its faintness, we use small apertures on this source (3 and 4 pixels respectively at 8.0 and 24 μm) to suppress noise; the measurements use appropriate aperture corrections. Figure 3.1 shows the IRAC and MIPS 24μm images for SDSS J0005−0006 (images in the second line) comparing with those of SDSS J0002+2550 (images in the first line), whose SED in the *Spitzer* bands is consistent with low-redshift SED templates (see § 3.3 and Figure 3.2).

3.3 Spectral Energy Distributions and Hot Dust at High Redshift

3.3.1 Spectral energy distributions

Figure 3.2 shows the SEDs of the thirteen quasars from the *Spitzer* observations. Dotted lines are the average quasar SED from Elvis et al. (1994) and dashed lines are the SED template of luminous SDSS quasars from Richards et al. (2006a). The SED templates have been normalized at rest-frame 1450 Å. All these quasars have $[3.6]_{AB}-[4.5]_{AB} > -0.1$ ($[3.6]_{AB}$ and $[4.5]_{AB}$ are AB magnitudes at 3.6 and 4.5 μm, respectively), which is a MIR selection criterion for AGN used by Cool et al. (2006).
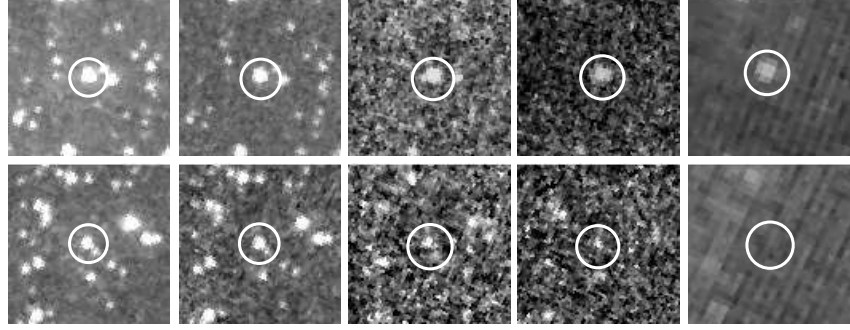
Figure 3.1 IRAC and MIPS 24μm images of SDSS J0005−0006 (images in the second line) compared with those of SDSS J0002+2550 (images in the first line), whose SED in the *Spitzer* bands is consistent with low-redshift SED templates (see § 3.3 and Figure 3.2). The images from left to right correspond to IRAC channels 1, 2, 3 and 4, and the MIPS 24μm band. The size of the images is $1' \times 1'$. SDSS J0005−0006 was marginally detected in the IRAC 8.0μm band, and is not detected in the MIPS 24μm band.

The IRAC 4.5μm fluxes in some objects are significantly increased by strong Hα emission lines. For most quasars, the continuum shapes at the wavelengths that the IRAC and MIPS 24μm bands cover (0.5 μm$< \lambda_0 <$3.5 μm) are well predicted by the low-redshift SEDs. In a type I quasar, the radiation at $\lambda_0 < 1$ μm is from the accretion disk; at longer wavelengths of a few microns, emission from hot dust dominates over the disk emission. Figure 3.2 shows that even at $z \sim 6$, accretion disks and hot-dust structures for most quasars may already have reached maturity.

However, two quasars in this sample, SDSS J0005$-$0006 ($z = 5.85$) and SDSS J1411+1217 ($z = 5.93$), stand out as having unusual SEDs in this wavelength range: their fluxes at 24 μm ($\lambda_0 \sim$3.5 μm) and/or 8 μm ($\lambda_0 \sim$1 μm) significantly deviate from the low-redshift SEDs. For SDSS J1411+1217, the observed flux at 24 μm is a factor of ~ 3 lower than that of the standard low-redshift templates. SDSS J0005-0006 is more extreme: it is marginally detected at 8 μm and is completely undetected at 24 μm, at least an order of magnitude fainter than that predicted by the standard templates.

3.3.2   Hot dust in $z \sim 6$ quasars

We use a simple model to fit SEDs to our broad-band data at rest-frame 0.15$-$3.5 μm, consisting of a power-law disk component and a hot dust blackbody (Glikman et al., 2006). Glikman et al. (2006) find that a 1260K blackbody provides a good description of hot dust from their NIR quasar composite spectrum. Because only the 24μm fluxes are available to constrain hot dust for these $z \sim 6$ quasars, we fix the hot-dust temperature as 1260 K in our model fitting. Figure 3.3 shows the results of this fit. The dotted lines show the two components, and the dashed line is the sum of the two. The power-law slope α ($f_\nu \sim \nu^\alpha$) is also given in the figure. Most quasars have prominent hot-dust components seen as excess emission in the 24μm band, above the power-law disk components, while SDSS J0005$-$0006 and SDSS J1411+1217 do not show any hot-dust emission. The SED of SDSS J1411+1217 is consistent with a pure power-law over the full spectral range, and the fluxes of SDSS J0005$-$0006 at $\lambda_0 \sim$1 and 3.5 μm lie significantly below the power-law. At
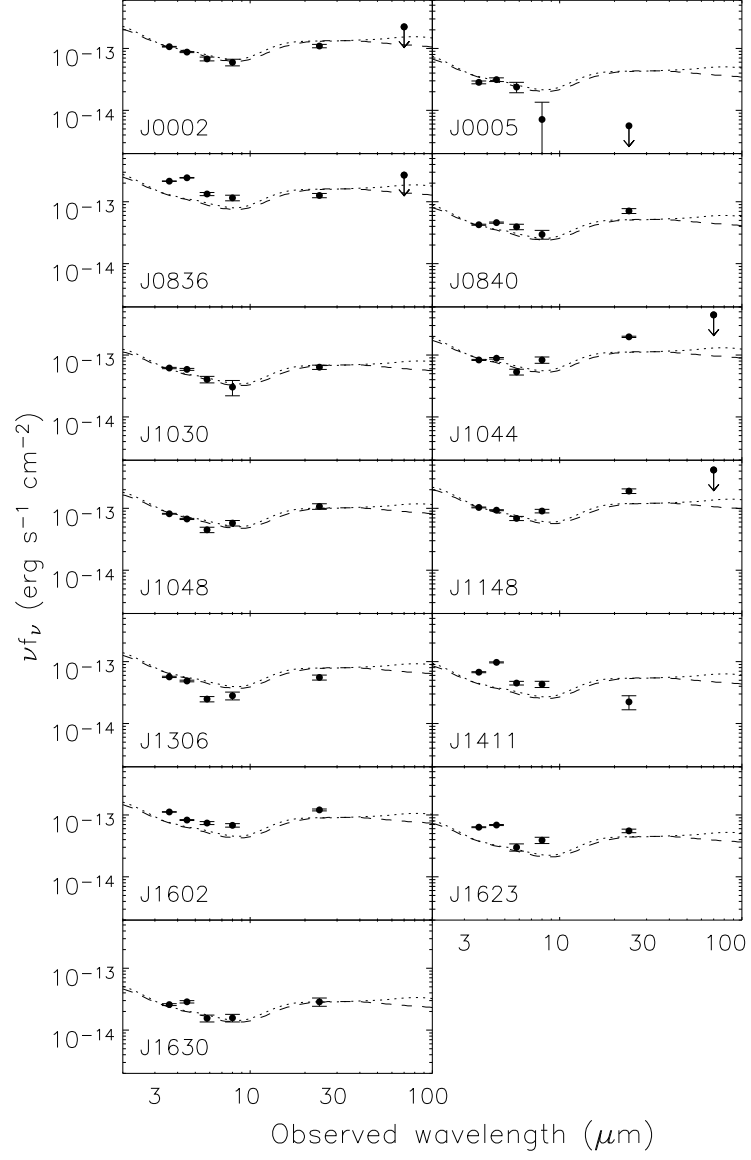
Figure 3.2 SEDs of the thirteen quasars from the *Spitzer* observations. The dotted and dashed lines are the average SEDs of type I low-redshift quasars from Elvis et al. (1994) and Richards et al. (2006a), respectively, and have been normalized at rest-frame 1450 Å. Filled circles with downward arrows are 2σ upper limits. The measurement uncertainties are also given in the figure.

$z \sim 6$, quasar host galaxies are very young. It is possible that the properties of dust, including its temperature, composition and geometry, are different in such young objects from those at lower redshift (see § 3.5 for a detailed discussion).

Radio and mm/submm (e.g. Bertoldi et al., 2003a; Priddey et al., 2003; Robson et al., 2004; Carilli et al., 2004) observations have revealed that these luminous $z \sim 6$ quasars have large amounts of warm/cool dust with masses higher than $10^8 M_\odot$. The warm/cool dust has temperatures from a few tens to a few hundred kelvins, while hot dust has temperatures of ~ 1000 K. In Figure 3.3 we fit the hot dust emission using a single-temperature blackbody, so we cannot calculate the hot-dust mass. However, we may estimate a lower limit to this mass by assuming that the hot dust radiates as a gray body. The dust mass M_d is determined by the following relation (Hughes et al., 1997),

$$M_d = \frac{F_1 D_L^2}{k_0 B(\nu_0, T_d)(1 + z)}, \tag{3.1}$$

where F_1 is the observed flux density, D_L is the luminosity distance, k_0 is the rest-frame dust absorption coefficient, and $B(\nu_0, T_d)$ is the Planck function at rest frequency ν_0 and temperature T_d. We calculate the mass absorption coefficient k_0 according to Loeb & Haiman (1997) based on the extinction law of Mathis (1990). The lower limits of hot-dust masses are given in Figure 3.3.

In the analysis above we have neglected the contribution from the host galaxies of quasars. According to the correlation between central BH mass and host luminosity (Peng et al., 2006), the R-band luminosity is about $M_R = -24$ for a galaxy hosting a BH with a mass of a few 10^9 $M_\odot$. Quasars with similarly massive BHs in our sample (see § 3.4) are more luminous than $M_i = -27$. Using the elliptical galaxy template of Fioc & Rocca-Volmerange (1997), we find that the contribution from the host galaxies is expected to be less than 10% at rest-frame 1.6 μm, the peak of the template. We also use galaxy templates (Sbc, Scd, and Im) of Coleman et al. (1980), and find that the contribution from the host galaxies is less than 10% at rest-frame 5000–6000Å, the peak of the optical band in the templates.

Figure 3.4 shows the correlation between rest-frame 4400Å luminosity and 3.5μm luminosity for low-z type I quasars, compared with our measurements at high red-
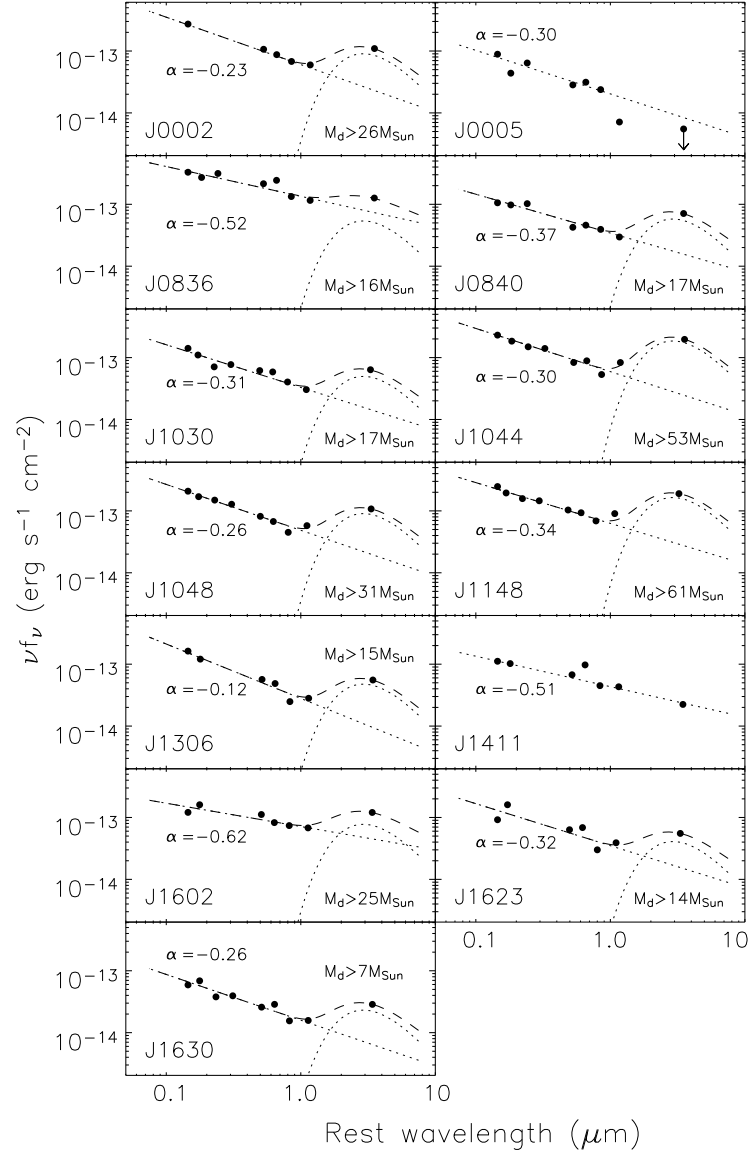
Figure 3.3 A simple model fitting to the high-redshift quasar SEDs at rest-frame 0.15 − 3.5 μm. The dotted lines in each panel show a power-law disk component and a blackbody component of hot dust, and the dashed line is the sum of the two. The power-law slope α and the lower limit of hot-dust mass M_d for each object are also given in the figure.

shift (red points). We include PG quasars (green points; Schmidt & Green, 1983) that were observed at 3.7μm (Neugebauer et al., 1987), 4.8μm, 6.7μm or 7.3μm (Haas et al., 2000, 2003). We also include SDSS quasars (blue points) in the *Spitzer* Extragalactic First Look Survey and three *Spitzer* Wide-Area Infrared Extragalactic Survey areas (Richards et al., 2006a). Cyan points present $z \sim 5$ quasars from Hines et al. (2006). Dashed lines show the best linear fit and its 3σ range. The correlation given in Figure 3.4 suggests that the dust emission at 3.5 μm in quasars is heated directly by central engines (e.g. Rieke & Lebofsky, 1981; Polletta et al., 2000; Haas et al., 2003). The NIR-to-optical flux ratios for most $z \sim 6$ quasars follow those at low redshift. However, SDSS J0005−0006 and SDSS J1411+1217 lie significantly below the linear fit. SDSS J1411+1217 is as IR-weak (IR-weak in this chapter means small IR-to-optical ratios rather than weak absolute IR fluxes) as the most extreme examples at low redshift, while SDSS J0005−0006 is the most IR-weak object at any redshift in the figure. It is worth noting the quasars in Figure 3.4 are all typical type I quasars, and we do not consider other types of AGNs. For example, in Seyfert galaxies host galaxies may dominate the radiation at optical and IR wavelengths; while in blazars the optical emission could be boosted due to beaming effects, resulting in small IR-to-optical ratios.

3.3.3   Notes on individual objects

SDSS J000552.34−000655.8 ($z = 5.85$). SDSS J0005−0006 is selected from the SDSS Southern Survey, a deep survey repeatedly imaging the Fall Celestial Equatorial Stripe in the Southern Galactic Cap. It is the faintest quasar ($z_{AB} = 20.54$) in our sample. It also has the narrowest Lyα emission line of $z \sim 6$ quasars (Fan et al., 2004). This object is marginally detected in the IRAC 8.0μm band and is not detected in the MIPS 24μm band. Due to large measurement uncertainties, its SED is poorly constrained at both wavelengths. Further deep *Spitzer* observations, such as the IRAC 8.0μm, the Infrared Spectrograph (IRS) Peak-Up Imaging 16μm and the MIPS 24μm photometry, are needed to place a strong constraint on its IR SED.
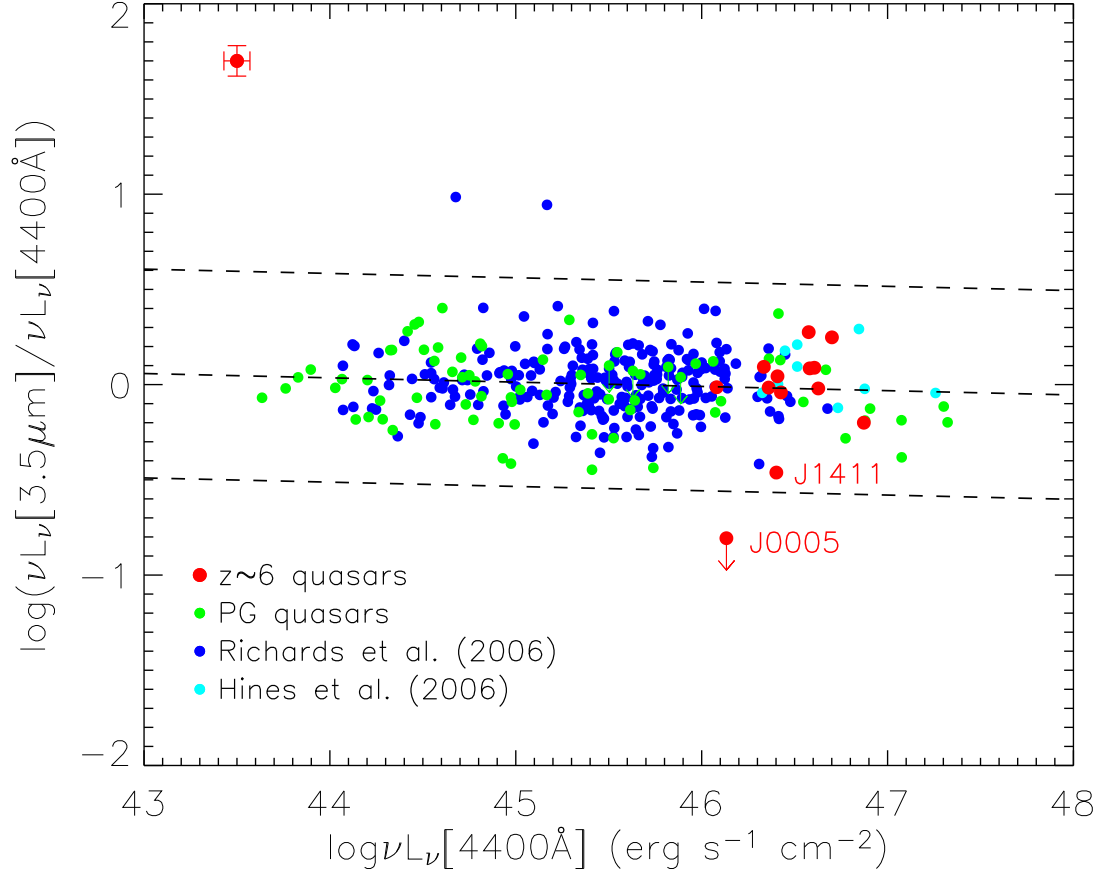
Figure 3.4 Correlation between rest-frame 4400Å luminosity and 3.5μm luminosity for type I quasars. Red points are our $z \sim 6$ quasars. Green points are PG quasars (Schmidt & Green, 1983) that were observed at 3.7μm (Neugebauer et al., 1987), 4.8μm, 6.7μm or 7.3μm (Haas et al., 2000, 2003). Cyan points are $z \sim 5$ quasars from Hines et al. (2006). Filled circles with downward arrows are 2σ upper limits. Dashed lines show the best linear fit and its 3σ range. Typical errors for $z \sim 6$ quasars are given in the upper left corner. SDSS J1411+1217 is as IR-weak as the most extreme examples at low redshift, while SDSS J0005−0006 is the most IR-weak quasar at any redshift in the figure.

SDSS J083643.85+005453.3 ($z = 5.82$). SDSS J0836+0054 is the only known quasar at $z > 5.7$ detected by the Faint Images of the Radio Sky at Twenty-cm (FIRST; Becker et al., 1995). Its radio flux is variable. The flux at 1.4 GHz changed from 1.11±0.15 mJy as measured by FIRST to 1.75±0.04 mJy of Petric et al. (2003), a change of a factor of $\sim 60\%$, and the flux at 5 GHz changed from 0.58±0.06 mJy of Petric et al. (2003) to 0.34±0.06 mJy of Frey et al. (2005) by a factor of $\sim 70\%$. SDSS J0836+0054 has a strong and broad Lyα emission line (Fan et al., 2001a) and a relatively weak MIPS 24μm flux.

SDSS J104433.04−012502.2 ($z = 5.74$). SDSS J1044−0125 is the first quasar discovered at $z > 5.7$ (Fan et al., 2000a). It has weak X-ray emission (Brandt et al., 2001) and was confirmed to be a broad absorption line (BAL) quasar (Goodrich et al., 2001; Djorgovski et al., 2001). Submm observations at 850 μm reveal the existence of $\sim 4 \times 10^8$ M$_\odot$ of cool dust in this object (Priddey et al., 2003). It is also bright at 24μm, and thus has a large amount of hot dust.

SDSS J104845.05+463718.3 ($z = 6.20$). SDSS J1048+4637 is the most distant known BAL quasar (Maiolino et al., 2004b). It has been marginally detected at 1.4 GHz (Carilli et al., 2004), and not detected at 450 and 850 μm (Robson et al., 2004). Bertoldi et al. (2003a) detected it at 250 GHz and estimated a cool dust mass of $\sim 4 \times 10^8$ M$_\odot$ in this object. It was observed with IRS Peak-Up Imaging at 16μm (Charmandaris et al., 2004), and the updated 16μm flux is 0.49 mJy.

SDSS J114816.64+525150.2 ($z = 6.42$). SDSS J1148+5251 is the most distant quasar known. It has strong MIPS 24μm output, indicating the existence of prominent hot dust. It was also detected at 450 and 850 μm (Robson et al., 2004), 250 GHz (Bertoldi et al., 2003a) and 1.4 GHz (Carilli et al., 2004). These observations show that it has copious cool dust with a mass of $5 - 7 \times 10^8$ M$_\odot$. CO observations (Bertoldi et al., 2003b; Walter et al., 2003, 2004) reveal the presence of $\sim 2 \times 10^{10}$ M$_\odot$ of molecular gas in this object. It was also observed with IRS Peak-Up Imaging at 16μm (Charmandaris et al., 2004), and its updated 16μm flux is 0.84 mJy. Mahabal et al. (2005) discovered a very faint quasar RD J114816.2+525339 with $z_{AB} = 23.0$ at $z = 5.7$ near SDSS J1148+5251. We detected this faint source

with IRAC at 3.6 and 4.5 μm with flux densities of 0.013±0.002 and 0.013±0.003 mJy, respectively, which are consistent with standard low-z SED templates.

SDSS J141111.29+121737.4 ($z = 5.93$). SDSS J1411+1217 has a very weak MIPS 24μm flux, and its SED at 1 μm$< \lambda_0 < 3.5$ μm can be fitted with a pure power-law. It also has a narrow Lyα emission line (Fan et al., 2004).

3.4   Bolometric Luminosities and Accretion Rates

Figure 3.5 presents the SEDs (filled circles) of the thirteen $z \sim 6$ quasars from X-ray to radio. The data other than our *Spitzer* observations are taken from the literature mentioned in § 3.2.1. Filled circles with downward arrows are 2σ upper limits. Dotted lines are the average quasar SED from Elvis et al. (1994) and dashed lines are the SED template of luminous SDSS quasars from Richards et al. (2006a). The templates have been normalized at IRAC 3.6 μm. Due to the anticorrelation between X-ray emission and optical luminosity in AGNs (e.g. Strateva et al., 2005; Steffen et al., 2006), the SED template of Richards et al. (2006a) at X-ray band is well below that of Elvis et al. (1994) and the X-ray fluxes of the most luminous $z \sim 6$ quasars are often smaller than the Richards et al. (2006a) template. After correcting for this effect, the X-ray emission from these $z \sim 6$ quasars is consistent with the low-z SED templates (Shemmer et al., 2006). To calculate bolometric luminosities, we first determine the full SED for each quasar. The SED between any two adjacent data points is interpolated using the Richards et al. (2006a) mean SED, and the SED beyond the leftmost or rightmost points is directly scaled to this point using the mean SED. Table 3.3 gives the bolometric luminosities as well as optical and IR luminosities. Column 5 is the bolometric correction from rest-frame B band for all the quasars. The mean correction and standard deviation are 9.1 ± 2.2, consistent with 11.8 ± 4.3 from Elvis et al. (1994) and 10.4 ± 2.5 from Richards et al. (2006a).

We estimate central BH masses for the quasars that have been spectroscopically observed at rest-frame UV/optical wavelength (e.g. Goodrich et al., 2001; Barth et al., 2003) using the BH mass scaling relations (McLure & Dunlop, 2004; Vestergaard
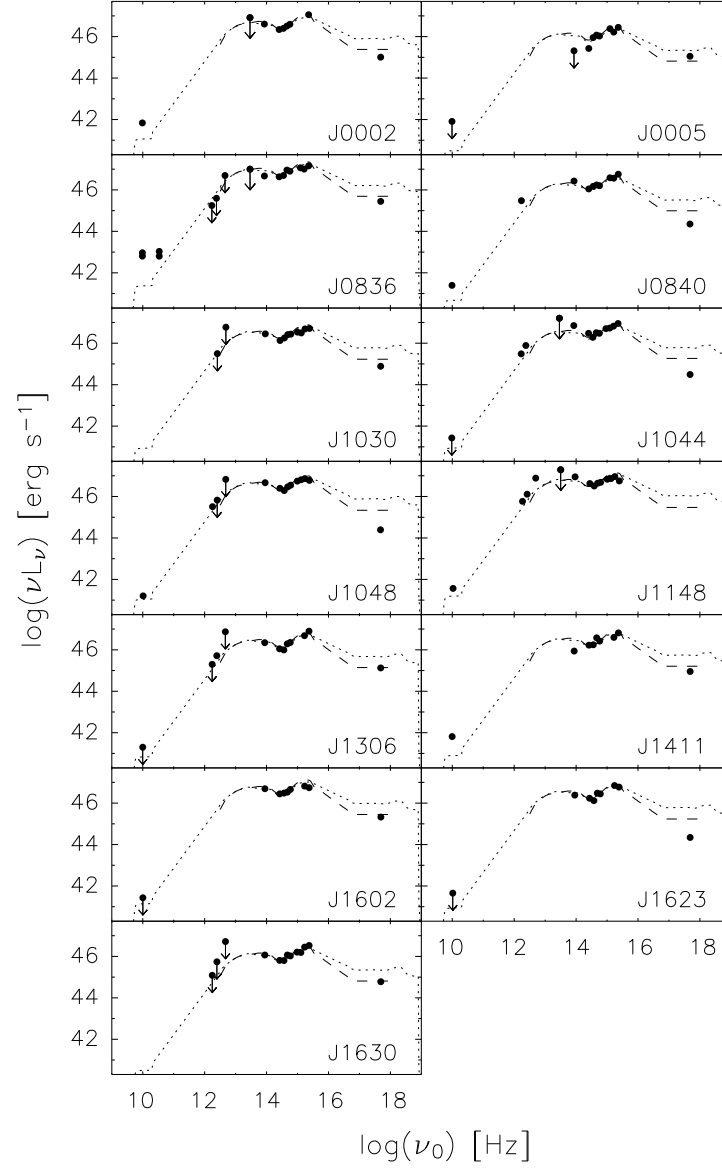
Figure 3.5 SEDs of the thirteen quasars from X-ray to radio. The data other than our *Spitzer* observations are taken from the literature mentioned in § 3.2.1. Filled circles with downward arrows are 2σ upper limits. The dotted and dashed lines are the average SEDs of low-redshift quasars from Elvis et al. (1994) and Richards et al. (2006a), respectively, and have been normalized at IRAC 3.6 μm ($\lambda_0 \sim 5000$Å).

Table 3.3.   Optical, IR and bolometric luminosities for the thirteen quasars

Quasar (SDSS)	L_{Bol}[a]	L_{Opt}[b]	L_{IR}[c]	$L_{Bol}/\nu L_\nu(4400\text{Å})$	$M_{BH}(10^9 M_\odot)$	L_{Bol}/L_{Edd}
J0002+2550	47.57	47.19	47.18	8.5	$\cdots$	$\cdots$
J0005$-$0006	46.94	46.67	45.96	6.0	$\cdots$	$\cdots$
J0836+0054	47.72	47.36	47.28	7.0	6.8	0.54
J0840+5624	47.34	46.81	47.11	9.9	$\cdots$	$\cdots$
J1030+0524	47.37	46.91	47.04	8.7	$\cdots$	$\cdots$
J1044$-$0125	47.63	47.06	47.43	11.3	6.4	0.53
J1048+4637	47.55	47.08	47.29	9.1	$\cdots$	$\cdots$
J1148+5251	47.85	47.19	47.68	14.3	5.6	1.01
J1306+0356	47.40	46.94	47.04	10.3	$\cdots$	$\cdots$
J1411+1217	47.20	46.91	46.61	6.3	$\cdots$	$\cdots$
J1602+4228	47.59	47.13	47.27	9.6	$\cdots$	$\cdots$
J1623+3112	47.33	46.98	46.97	7.6	3.4	0.50
J1630+4012	47.06	46.57	46.75	9.8	$\cdots$	$\cdots$

[a]Bolometric luminosity (3cm to 10keV) in log(ergs/s).

[b]Optical luminosity (0.1μm to 1.0μm) in log(ergs/s).

[c]IR luminosity (1.0μm to 100.0μm) in log(ergs/s).

& Peterson, 2006). The BH mass of SDSS J0836+0054 is taken from Pentericci et al. (2006, in prep.) based on the relation of McLure & Dunlop (2004). Iwamuro et al. (2004) measured the MgII emission lines for four of the quasars. Due to low S/N, their measured MgII width for SDSS J1148+5251 is lower than that determined by Barth et al. (2003) by a factor of ~ 2, which results in a factor of 4 lower estimated BH mass. We thus did not use the measurements of Iwamuro et al. (2004). The derived BH masses and Eddington luminosity ratios are given in Table 3.3. These luminous $z \sim 6$ quasars have supermassive BHs with masses of a few 10^9 $M_\odot$ and Eddington ratios of order unity, comparable to quasars with similar luminosities at lower redshift (e.g. McLure & Dunlop, 2004; Vestergaard, 2004; Kollmeier et al., 2006).

3.5   Summary and Discussion

We have carried out IRAC and MIPS 24μm photometry for thirteen $z \sim 6$ quasars. All the quasars except SDSS J0005$-$0006 were detected with high S/N in the IRAC and MIPS 24μm bands, while SDSS J0005$-$0006 was marginally detected in the IRAC 8.0μm band, and not detected in the MIPS 24μm band. The sample of the quasars is used to study the properties of IR SEDs and hot dust in high-redshift quasars. We find that the SEDs of most quasars follow low-redshift SEDs at the probed wavelengths. However, two quasars, SDSS J0005$-$0006 and SDSS J1411+1217, have unusual SEDs that lie significantly below the prediction of low-redshift SED templates at 24 μm and/or 8 μm, showing a strong IR deficit. A simple model shows that most of the quasars have substantial hot dust, while the two IR-weak quasars do not show any hot-dust emission. We combine the *Spitzer* observations with X-ray, UV/optical, mm/submm and radio observations to determine bolometric luminosities for the high-redshift quasars. We find that these quasars have Eddington ratios of order unity.

   It has been revealed that $z \sim 6$ quasars show a lack of evolution in their rest-frame UV/optical and X-ray SEDs. Our *Spitzer* observations show that, for most

$z \sim 6$ quasars, NIR-to-MIR SEDs also do not differ significantly from those at low redshift. This suggests that accretion disks, emission-line regions and dust structures in most high-redshift quasars have reached maturity very early on. However, we found two quasars with a strong IR deficit. As shown in Figure 3.4, NIR-weak Type I quasars like SDSS J1411+1217 are very rare; and Type I quasars with extremely weak NIR fluxes like SDSS J0005$-$0006 are not found in a large sample at low redshift, but exist in a small sample of thirteen quasars at $z \sim 6$, suggesting that some quasars at high redshift may have different dust properties.

In the local universe, most dust in the ISM is produced by low and intermediate-mass AGB stars, which develop 0.5$-$1 Gyr after the initial starburst. At $z \sim 6$, the age of the universe is less than 1 Gyr, so quasar host galaxies are very young, with their first star formation likely to have occurred less than half a Gyr earlier. The two NIR-weak quasars SDSS J0005$-$0006 and SDSS 1411+1217 could be too young to have formed dust tori around them, or perhaps, dust properties in such young systems differ from those of lower-redshift quasars. Thus the unusual IR SEDs of the two quasars may be a reflection of different dust properties in very young host galaxies at high redshift. Maiolino et al. (2004a) found that the dust extinction curve in quasar SDSS J1048+4836 ($z = 6.20$) is different from that observed at $z < 4$ (which is SMC-like, Hopkins et al. (2004)), implying a grain size distribution more similar to that expected from dust produced by supernovae. While other dust production mechanisms (e.g. Elvis et al., 2002) are also possible, it is currently unknown what their emission spectra are. SDSS J0005$-$0006 is especially interesting. If it has no hot dust, the observed SED at 1 μm$< \lambda_0 < 3.5$ μm comes from the disk only. This provides a strict constraint on disk models.

Hot dust in SDSS J0005$-$0006 and SDSS J1411+1217 could also be hidden by dust tori. According to AGN unification models, the accretion disk is surrounded by a dust torus. The hottest dust, with temperature more than 1000K, lies within a few pc, while cool dust with temperature of a few tens of kelvins can extend to a few kpc. As the angle between the torus axis and the line of sight increases, more hot dust could be hidden by the cool dust torus. Thus the hot-dust radiation

in the NIR would be suppressed, and the $\lambda_0 \sim 1\mu$m dip could be shifted toward longer wavelengths (Haas et al., 2003). Intriguingly, the emission line widths in the two NIR-weak quasars are the narrowest in our sample of $z \sim 6$ quasars. This suggests that the weak NIR SEDs in two sources could be caused by an obscuration with hot dust hidden by cooler dust tori. On the other hand, both objects show normal UV continuum and UV-to-X-ray flux ratio, and are thus not type II obscured objects in the normal sense, but could be intermediate objects in which the hot dust contribution is somewhat reduced. Further deep *Spitzer* observations are needed to constrain the SED shapes at $1\mu m < \lambda_0 < 4\mu m$, and NIR spectra are also needed to detect possible narrow line components.

CHAPTER 4

SPATIAL DENSITY EVOLUTION OF $Z \sim 6$ QUASARS

4.1 Introduction

High-redshift quasars are among the most luminous objects known and provide direct probes of the distant universe when the first generation of galaxies and quasars formed. In recent years, over twenty $z \sim 6$ quasars with $z_{AB} \leq 20$ have been discovered (e.g. Fan et al., 2000a, 2001a, 2003, 2004, 2006a; Goto, 2006). These luminous quasars are essential for understanding the accretion history of black holes (BHs), galaxy formation, and chemical evolution at very early epochs. They harbor supermassive BHs with masses higher than 10^9 $M_\odot$ and emit near the Eddington limit (e.g. Barth et al., 2003; Vestergaard, 2004; Jiang et al., 2006a; Kurk et al., 2007), revealing the rapid growth of central BHs at high redshift. Their emission lines show solar or supersolar metallicity in the broad line regions, indicating that there was vigorous star formation and element enrichment in the first gigayear of cosmic time (e.g. Barth et al., 2003; Maiolino et al., 2003; Jiang et al., 2007a; Kurk et al., 2007). Their absorption spectra show that the intergalactic medium (IGM) at $z \sim 6$ is close to the reionization epoch (e.g. Becker et al., 2001; Djorgovski et

al., 2001; Fan et al., 2006b,c).

The majority of the currently known $z \sim 6$ quasars were discovered from ~ 8000 deg^2 of imaging data of the Sloan Digital Sky Survey (SDSS; York et al., 2000). They were selected as i-dropout objects using optical colors. Several other high-redshift quasars were discovered based on their infrared or radio emission. For example, Cool et al. (2006) discovered one quasar at $z = 5.85$ in the NOAO Deep Wide-Field Survey (NDWFS; Jannuzi & Dey, 1999) Bootes Field using the AGN and Galaxy Evolution Survey (AGES) spectroscopic observations. The quasar was selected from a *Spitzer* mid-infrared quasar sample and has a z_{AB} magnitude of 20.68 and an optical luminosity of $M_B = -26.52$. By matching the FLAMINGOS Extragalactic Survey IR survey (Elston et al., 2006) data to the Faint Images of the Radio Sky at Twenty-cm (FIRST; Becker et al., 1995) data, McGreer et al. (2006) discovered a radio-loud quasar at $z = 6.12$ in 4 deg^2 of the NDWFS region. This quasar is a broad absorption line (BAL) quasar with an optical luminosity of $M_B = -26.9$, comparable to the luminous SDSS quasars at $z \sim 6$.

Despite the high-redshift quasar surveys mentioned above, very little is known about faint quasars ($z_{AB} > 20$) at $z \sim 6$. The SDSS main survey only probes the most luminous quasars, and with a density of $1/470$ deg^2 (Fan et al., 2006a). The Cool et al. (2006) quasar at $z = 5.85$ was $z_{AB} > 20$, but the sample contains a single object and is selected from an area of less than 10 deg^2. Mahabal et al. (2005) found a very faint quasar with $z_{AB} = 23.0$ at $z = 5.70$ in a 2.5 deg^2 field around the luminous quasar SDSS J114816.64+525150.3 at $z = 6.42$. Willott et al. (2005) imaged a 3.83 deg^2 region down to $z_{AB} = 23.35$ in the first results of the Canada-France High-redshift Quasar Survey (CFHQS) and did not find any quasars at $z > 5.7$. In these surveys both the quasar samples and the survey areas are very small, thus they do not provide a good statistical study of high-redshift quasars at $z_{AB} > 20$. Recently, Willott et al. (2007) discovered four quasars at $z > 6$ from about 400 deg^2 of the CFHQS, including the most distant known quasar at $z = 6.43$. Three of these quasars have z_{AB} magnitudes fainter than 21. Since their follow-up observations are not yet complete, they did not determine the spatial density of

these quasars.

Finding faint quasars at $z \sim 6$ is important for studying the evolution of the quasar population and quasars' impact on their environments. Fan et al. (2004) obtained the bright-end quasar luminosity function (QLF) at $z \sim 6$, but the slope, -3.2 ± 0.7, was very uncertain due to the small luminosity range of the sample. Richards et al. (2004) put a broad constraint on the bright-end slope of > -4.63 (3σ) from the absence of lenses in four quasars at $z \sim 6$. With the discovery of faint high-redshift quasars, the QLF can be well determined. The QLF at $z \sim 6$ is important to understand BH growth at early epochs (e.g. Volonteri & Rees, 2006; Wyithe & Padmanabhan, 2006). While bright quasars at high redshift have central BH masses between 10^9 and 10^{10} $M_\odot$, fainter quasars with $z_{AB} > 20$ are expected to harbor BHs with masses of a few times 10^8 $M_\odot$ or below (e.g. Kurk et al., 2007), which may be associated with galaxies of lower masses. The QLF also enables us to determine the quasar contribution to the UV background at $z \sim 6$. Detection of complete Gunn-Peterson troughs (Gunn & Peterson, 1965) among the highest-redshift quasars indicates a rapid increase of the IGM neutral fraction at $z \sim 6$, and suggests that we have reached the end of the reionization epoch (e.g. Becker et al., 2001; Djorgovski et al., 2001; Fan et al., 2006c). It is unclear what individual contributions of galaxies and quasars to the reionization are. Although there is evidence showing that quasars are probably not the main contributor to reionization (e.g. Salvaterra et al., 2007; Srbinovsky & Wyithe, 2007; Shankar & Mathur, 2007), a proper determination of the QLF at $z \sim 6$ is needed to constrain the the quasar contribution.

In this chapter we present the discovery of five $z \sim 6$ quasars with $20 < z_{AB} < 21$ selected from 260 deg^2 of the SDSS southern survey, a deep imaging survey obtained by repeatedly scanning a 300 deg^2 area in the Fall Celestial Equatorial Stripe (Adelman-McCarthy et al., 2007). One of the five quasars, SDSS J020332.39+001229.3 (hereafter SDSS J0203+0012), was independently discovered by matching the UKIRT Infrared Deep Sky Survey (UKIDSS; Warren et al., 2007) data to the SDSS data (Venemans et al., 2007). These five quasars, together with

another quasar, SDSS J000552.34–000655.8 (hereafter SDSS J0005–0006) previously discovered in this region (Fan et al., 2004), form a well-defined low-luminosity quasar sample at high redshift. We use this sample and the luminous SDSS quasar sample to measure the QLF and constrain the quasar contribution to the reionization of the universe at $z \sim 6$.

The structure of the chapter is as follows. In § 4.2 we introduce the quasar selection criteria and photometric and spectroscopic observations of quasar candidates. In § 4.3 we describe the properties of the five new quasars. We derive the QLF at $z \sim 6$ in § 4.4, and discuss the contribution of quasars to the ionizing background in § 4.5. We give a brief summary in § 4.6. Throughout the chapter we use a Λ-dominated flat cosmology with $H_0 = 70$ km s^{-1} Mpc^{-1}, $\Omega_m = 0.3$, and $\Omega_\Lambda = 0.7$ (Spergel et al., 2007).

4.2   Candidate Selection and Observations

4.2.1   SDSS deep imaging data

The SDSS is an imaging and spectroscopic survey of the sky (York et al., 2000) using a dedicated wide-field 2.5 m telescope (Gunn et al., 2006) at Apache Point Observatory. Imaging is carried out in drift-scan mode using a 142 mega-pixel camera (Gunn et al., 1998) which gathers data in five broad bands, $ugriz$, spanning the range from 3000 to 10,000 Å (Fukugita et al., 1996), on moonless photometric (Hogg et al., 2001) nights of good seeing. The effective exposure time is 54 seconds. The images are processed using specialized software (Lupton et al., 2001), and are photometrically (Tucker et al., 2006; Ivezić et al., 2004) and astrometrically (Pier et al., 2003) calibrated using observations of a set of primary standard stars (Smith et al., 2002) on a neighboring 20-inch telescope. All magnitudes are roughly on an AB system (Oke & Gunn, 1983), and use the asinh scale described by Lupton et al. (1999).

A primary goal of the SDSS imaging survey is to scan 8500 deg^2 of the north Galactic cap (hereafter referred to as the SDSS main survey). In addition to the

main survey, SDSS also conducts a deep survey by repeatedly imaging a 300 deg^2 area on the Celestial Equator in the south Galactic cap in the Fall (hereafter referred to as the SDSS deep survey; Adelman-McCarthy et al., 2007). This deep stripe (also called Stripe 82) spans $20^h < $ RA $ < 4^h$ and $-1.25° < $ Dec $ < 1.25°$. The multi-epoch images, when coadded, allow the selection of much fainter quasars than the SDSS main survey. Jiang et al. (2006b) have used the deep data to find low-redshift faint quasars selected from the SDSS coadded catalog, i.e., each run goes through the photometric pipeline PHOTO separately, and the resulting catalogs are coadded. The SDSS deep survey will eventually reach a depth of $i_{AB} = 24.0 \sim 24.5$ (5 σ detection for point sources) with more than 50 epochs of data (Adelman-McCarthy et al., 2008). The area and the depth will then be comparable to the CFHQS, which has covered ~ 400 deg^2 to a limit of $i_{AB} \sim 24.5$ (Willott et al., 2007).

At the time the coadded images used in this chapter were made, 2005, a given area of sky on Stripe 82 had been scanned 5–18 times under standard SDSS imaging conditions, and all available data were included in this version of the coadds. The construction of the coadds is summarized as follows. First, each input image was calibrated to a standard SDSS zeropoint using the median of the SDSS photometric solutions for the runs covering the area. For each image we made an inverse variance image to serve as a weight map, and within the map we assigned near-zero values to pixels with the INTERP bit set in the fpMask files of PHOTO, which indicates that a bad pixel, bad column, or cosmic ray has been interpolated over. After the images were sky subtracted using the PHOTO sky estimate, each image was mapped onto a uniform rectangular output astrometric grid using a modified version of the registration software SWARP (Bertin et al., 2002). The main modification was to incorporate the known SDSS camera distortions into the astrometry. The weight maps were subjected to the same mapping. The mapping used the LANCZOS3 kernel for the images and weights, while the INTERP bit images were mapped using NEAREST before being used to set near-zero values in the weight map images. The mapped images were then coadded using a flux scaled inverse-variance weighted average. The resulting images had known photometric and astrometric calibrations.

For precision photometry, the PSFs as a function of position on the images were required. We used an algorithm (implemented in PHOTO) that coadded the PSFs as a function of position known from each input image using the same weights as the images were averaged. Once the photometry, astrometry, and PSF were known, we proceeded to run a version of FRAMES (the main portion of PHOTO) slightly modified to take effective gains and sky noises into account when calculating error estimates. The uncalibrated output of PHOTO was adjusted and placed on the SDSS AB system using a slightly modifed version of the SDSS target selection software TARGET. The details of the construction of the coadds will be left for a forthcoming paper.

The resulting data were tested in three ways. First, object by object comparisons were made against single-run SDSS data. Second, object by object comparisons were made with the SDSS coadded catalogs produced by suitably averaging all the catalog information from the individual runs covering Stripe 82 (courtesy of R. Scranton and D. Johnston). Third, statistical internal measurements, such as stellar color-color diagrams, were made. These tests show that the images were properly coadded and the depth of the coadds is close to what was expected from standard error propagation. Figure 4.1 compares the photometric errors of PSF magnitudes for point sources in the SDSS main survey data and the SDSS coadded data. The error estimates were produced by the SDSS photometric pipeline PHOTO. From Figure 4.1 the photometric errors in the coadded data are significantly smaller than those in the single-run data.

In this chapter we used the data in the range $310° <$ RA $< 60°$, as there were significantly fewer than 10 runs covering the range $300° <$ RA $< 310°$. The data also contains some "holes" in which the coadded images were not available. The effective area for this work is 260 deg^2. The median seeing as measured in the riz bands was $1.2'' \pm 0.05''$, where the error is the standard deviation of the seeing measured by PHOTO across the coadded images on Stripe 82.
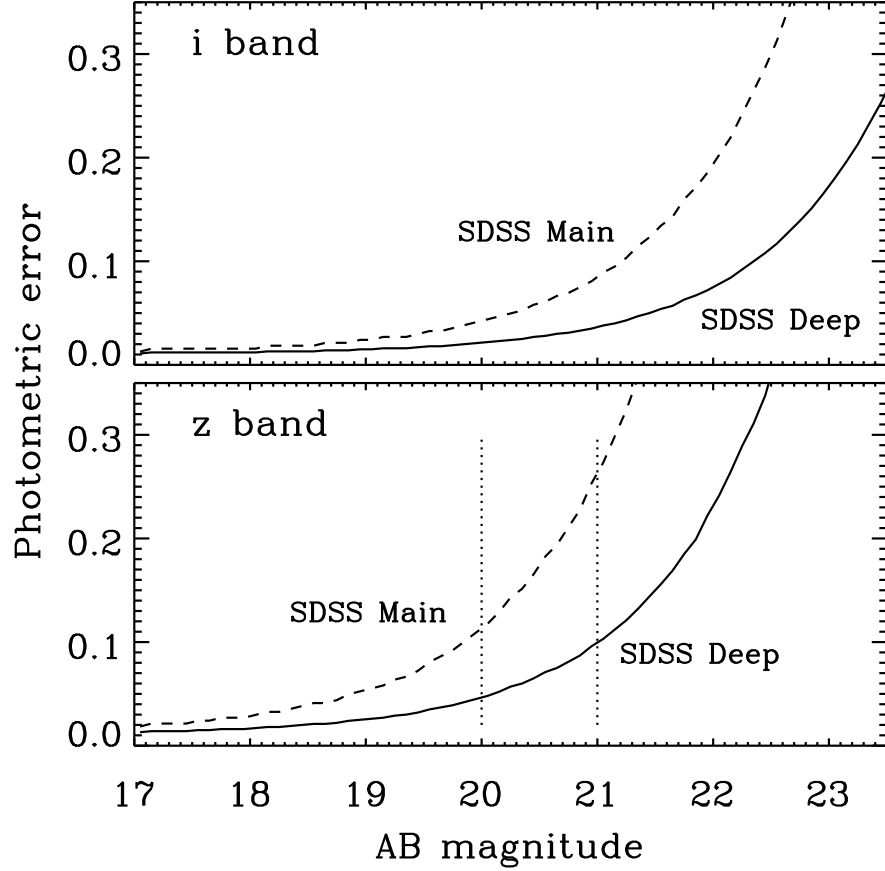
Figure 4.1 Photometric errors of PSF magnitudes for point sources as a function of i_{AB} and z_{AB} magnitudes. The error estimates were produced by the SDSS photometric pipeline PHOTO. The errors in the SDSS coadded data are significantly smaller than those in the SDSS main survey data. They are close to those expected from $\sigma_{\rm single}/N_{\rm epoch}^{1/2}$, where $\sigma_{\rm single}$ is the error in SDSS single-run data and $N_{\rm epoch}$ is the number of the runs used in the coadds. The flux limits of the $z \sim 6$ quasar surveys used in the SDSS main survey (e.g. Fan et al., 2001a) and in our work are indicated as the two vertical dotted lines, at which $\sigma(z_{AB}) \sim 0.1$.

4.2.2 Quasar selection procedure

Because of the rarity of high-redshift quasars and the overwhelming number of contaminants, our selection procedure for $z > 5.7$ faint quasars from the multi-epoch SDSS imaging data contains the following separate steps (see also Fan et al., 2001a, 2003).

1. Select i-dropout sources from the SDSS deep stripe. Objects with $i_{AB} - z_{AB} > 2.2$ and $z_{AB} < 21$ that were not detected in the ugr bands were selected as i-dropout objects. We rejected sources with one or more of the following SDSS processing flags: BRIGHT, EDGE, BLENDED, SATUR, MAYBE_CR, and MAYBE_EGHOST (see Stoughton et al., 2002). At $z > 5.7$, the Lyα emission line begins to move out of the SDSS i filter, so a simple cut of $i_{AB} - z_{AB} > 2.2$ is used to separate high-redshift quasars (and cool brown dwarfs) from the majority of stellar objects (e.g. Fan et al., 2001a). At $z_{AB} = 21$, the photometric errors of the coadded data reach $\sigma(z_{AB}) \sim 0.1$ as shown in Figure 4.1, so the $z_{AB} < 21$ criterion guarantees a high quasar selection efficiency due to small photometric errors.

2. Remove false i-dropout objects. All i-dropout objects were visually inspected, and false detections were deleted from the list of candidates. The majority of the contaminants are cosmic rays. Although the SDSS photometric pipeline effectively rejects cosmic rays, the leakage of a tiny fraction of cosmic rays will contribute a large contamination to our sample. Cosmic rays were recognized by comparing the individual multi-epoch images making up the coadds. Brown dwarfs with high proper motions can be removed in a similar way, since the multi-epoch images were taken over a period of five years. In the selection of luminous $z \sim 6$ quasars in the SDSS main survey, Fan et al. (2001a) used an additional step, z-band photometry of i-dropout objects, to eliminate cosmic rays and improve the photometry of potential candidates. In this work we did not use this step, as the photometry of the coadds is robust. About 60 i-dropout objects remained in this step.

3. Near-infrared (NIR) photometry of i-dropout objects. We then carried out NIR (J or H band) photometry of i-dropout objects selected from the previous step. The details of the NIR observations are described in § 4.2.3. Using the $i_{AB} - z_{AB}$ vs. $z_{AB} - J$ (or H) color-color diagrams (Figure 4.2), high-redshift quasar candidates were separated from brown dwarfs (L and T dwarfs), which have more than ten times higher surface density. The open circles in Figure 4.2 represent known L/T dwarfs from Golimowski et al. (2004), Knapp et al. (2004), and Chiu et al. (2006). The crosses represent simulated quasars at $5.8 < z < 6.6$. Although there is no clear separation between the dwarf locus and the quasar locus due to photometric errors, we selected quasars with the following criteria,

$$i_{AB} - z_{AB} > 2.2 \text{ \&\& } z_{AB} - J < 0.5(i_{AB} - z_{AB}) + 0.5, \quad (4.1)$$

$$\text{or} \quad i_{AB} - z_{AB} > 2.2 \text{ \&\& } z_{AB} - H < 0.5(i_{AB} - z_{AB}) + 1.0. \quad (4.2)$$

A total of 14 objects satisfied the criteria.

4. Follow-up spectroscopy of quasar candidates. The final step is to carry out optical spectroscopic observations of quasar candidates to identify high-redshift quasars. The details of the spectroscopic observations are described in § 4.2.3.

4.2.3 NIR photometry and optical spectroscopic observations

In the first two steps we described above, we selected about 60 i-dropout objects with $i_{AB} - z_{AB} > 2.2$ and $z_{AB} < 21$ from 260 deg^2 of the SDSS coadded imaging data. After the selection of i-dropouts, we carried out J or H-band[1] photometry of these i-dropouts using the SAO Widefield InfraRed Camera (SWIRC) on the MMT in November 2005 and October 2006 to separate quasar candidates and cool dwarfs. We used a 5×5 dither pattern to obtain good sky subtraction and to remove

---

[1]The J-band photometry is more efficient for selecting $z \sim 6$ quasars. Due to an instrument problem, however, the filter wheel was stuck and only the H filter was available on the night of October 2006.
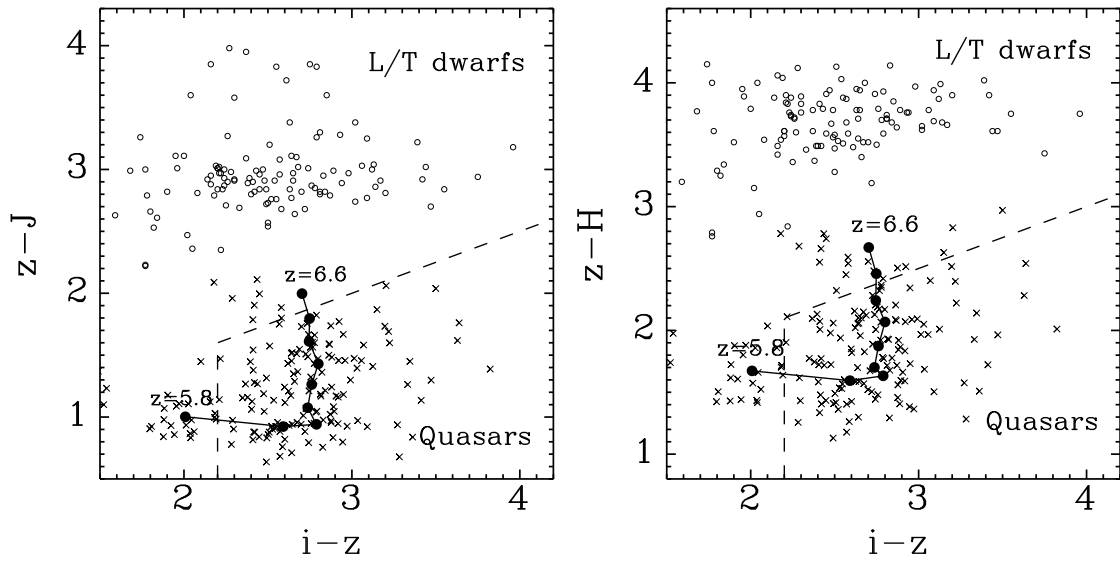
Figure 4.2 The $i_{AB} - z_{AB}$ vs. $z_{AB} - J$ (and H) color-color diagrams. The open circles represent known L/T dwarfs from Golimowski et al. (2004), Knapp et al. (2004), and Chiu et al. (2006). The crosses represent simulated quasars at $5.8 < z < 6.6$. The median track of quasar colors as a function of redshift is shown as the filled circles. We use the dashed lines to separate high-redshift quasar candidates from L/T dwarfs. Note that in practice there is no unambiguous separation between the dwarf locus and the quasar locus due to photometric errors.

cosmic rays. The exposure time at each dither position was 30 seconds. The total exposure time for each target was calculated to achieve an uncertainty of σ_J (or σ_H) ~ 0.08. The typical exposure time on individual targets is 10 minutes. The SWIRC data were reduced using standard IRAF routines. Five bright objects from the Two Micron All Sky Survey (2MASS; Skrutskie et al., 2006) in the field of each target were used to apply the aperture correction and absolute flux calibration.

After the NIR photometry of the i-dropouts, we selected quasar candidates that satisfied the criteria of Equation 1 or 2 . Optical spectroscopy of the candidates was carried out using the Echelle Spectrograph and Imager (ESI; Sheinis et al., 2002) on the Keck-II in January 2006 and the Low Dispersion Survey Spectrograph (LDSS-3) on Magellan-II in October 2006. The observations with ESI were performed in echellette mode, which provides excellent sensitivity from 4000 to 10,000 Å. The observations with LDSS-3 were performed in longslit mode. LDSS-3 was designed to be very red sensitive. We used the VPH red grism with a ruling density of 660 lines/mm. The VPH red grism offers excellent throughput in the wavelength range from 6000 to 10,000 Å. The exposure time for each target was 20 minutes, which is sufficient to identify $z \sim 6$ quasars in our sample. If a target was identified as a quasar, several further exposures were taken to improve the spectral quality. The quasar data were reduced using standard routines. After bias subtraction, flat-fielding, and wavelength calibration were applied to the frames, one-dimensional spectra were extracted, and were flux calibrated using the spectra of spectroscopic standard stars.

4.3   Discovery of Five New Quasars at $z \sim 6$

From the spectroscopic observations on Keck/ESI and Magellan/LDSS-3 we discovered five $z \sim 6$ quasars in the SDSS deep stripe. The other candidates are late type stars. The z-band finding charts of the quasars are shown in Figure 4.3. Note that SDSS J0203+0012 was independently discovered by Venemans et al. (2007). Another $z \sim 6$ quasar in this area, SDSS J0005–0006 discovered by Fan et al. (2004),

was recovered by our selection criteria. These six quasars comprise a complete flux-limited sample at $z_{AB} < 21$. The optical and NIR properties of the quasars are given in Table 4.1. The i_{AB} and z_{AB} magnitudes of the newly discovered quasars are taken from the SDSS deep imaging data, and their J and H magnitudes are obtained from our MMT/SWIRC observations. All the quasars have z_{AB} magnitudes between 20 and 21. The surface density of $z \sim 6$ quasars with $z_{AB} < 20$ is about $1/470$ deg^2 (Fan et al., 2006a), so it is reasonable to find no quasars with $z_{AB} < 20$ in a 260 deg^2 area.
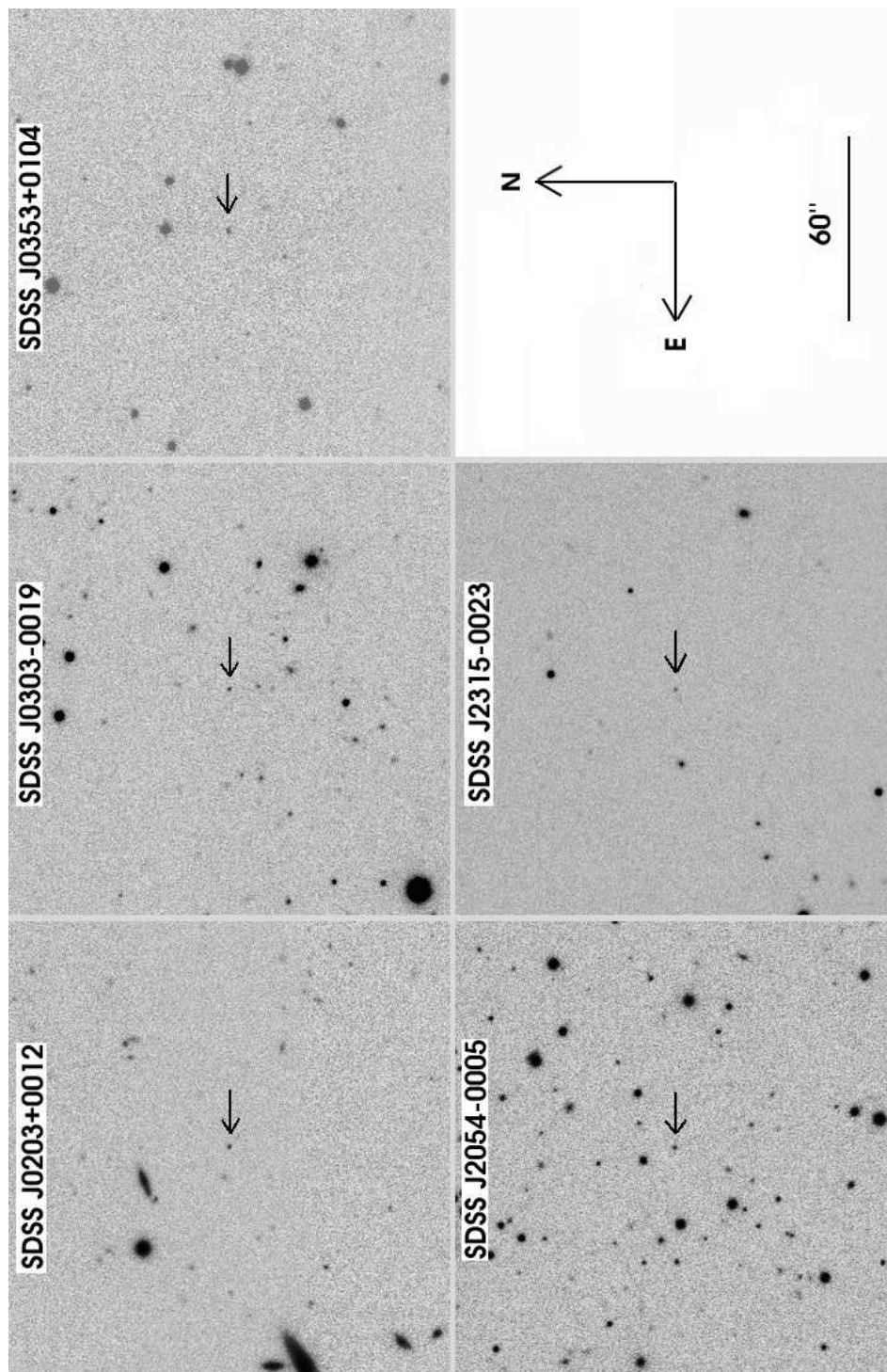
Figure 4.3 The z-band finding charts of the five new $z \sim 6$ quasars discovered in the SDSS deep stripe.

The optical spectra of the six quasars are shown in Figure 4.4. The spectrum of SDSS J0005–0006 was taken from Fan et al. (2004). The spectra of SDSS J035349.72+010404.4 (hereafter SDSS J0353+0104) and SDSS J231546.57–002358.1 (hereafter SDSS J2315–0023) were taken on Keck/ESI with a total exposure time of 60 minutes on each source. The spectra of the other three quasars were obtained with Magellan/LDSS-3, and the total exposure time on each source was 100 minutes. Each spectrum shown in Figure 4.4 has been scaled to the corresponding z_{AB} magnitude given in Table 4.1, and thereby placed on an absolute flux scale.

We estimate the redshifts for the new quasars from either the Lyα, N V $\lambda 1240$ (hereafter N V), or the O I $\lambda 1304$ (hereafter O I) emission line. For each quasar, we measure the line center of one strong emission line using a Gaussian profile to fit the top $\sim 50\%$ of the line. This provides a rough estimate of the redshift. Using this redshift we subtract the power-law continuum and decompose the blended Lyα and N V emission lines into individual components. The details are described in the next paragraph. Then we determine the redshifts from individual emission lines. The redshift of SDSS J030331.40–001912.9 (hereafter SDSS J0303–0019) is measured from the N V emission line, which is well separated from Lyα due to the narrow line width. The measured redshift 6.070 ± 0.001 is consistent with the redshift 6.069 ± 0.002 determined from the weak O I emission line. SDSS J0353+0104 is a BAL quasar as seen from strong absorption features around Lyα, so its redshift is measured from the O I emission line. The redshifts of the other three quasars are estimated from the Lyα emission lines. They are usually biased because the blue side of Lyα is affected by the Lyα forest absorption (Schneider et al., 1991). The mean shift with respect to the systemic redshift at $z > 3$ is about 600 km s^{-1} (Shen et al., 2007), corresponding to $\delta z \sim 0.015$ at $z \sim 6$. We correct for this bias for the redshifts measured from Lyα. The results are listed in Column 2 of Table 4.1. The errors in the table are the uncertainties obtained from our fitting process. For the redshifts measured from Lyα, their real errors could be much larger due to the scatter in the relation between Lyα redshifts and systemic redshifts (Shen et al., 2007). In our sample four quasars have redshifts greater than 6. The most distant

Table 4.1.   Optical and NIR photometry

Quasar (SDSS)	Redshift[a]	i_{AB} (mag)	z_{AB} (mag)	J (mag)	H (mag)
J000552.34−000655.8[b]	5.850±0.003	23.40 ± 0.34	20.54 ± 0.10	19.87 ± 0.10	⋯
J020332.39+001229.3[c]	5.854±0.002	23.72 ± 0.22	20.87 ± 0.10	19.05 ± 0.08	⋯
J030331.40−001912.9	6.070±0.001	23.92 ± 0.23	20.85 ± 0.07	⋯	19.46 ± 0.10
J035349.72+010404.4	6.049±0.004	24.03 ± 0.30	20.54 ± 0.08	⋯	18.55 ± 0.06
J205406.49−000514.8	6.062±0.004	23.30 ± 0.22	20.72 ± 0.09	19.18 ± 0.06	⋯
J231546.57−002358.1	6.117±0.006	24.90 ± 0.28	20.88 ± 0.08	19.94 ± 0.08	⋯

[a]The errors of the redshifts are the uncertainties obtained from our fitting process.

[b]This quasar was discovered by Fan et al. (2004). The magnitudes were taken from Fan et al. (2004), and the redshift was determined from the Mg II emission line by Kurk et al. (2007).

[c]This quasar was independently discovered by Venemans et al. (2007).

Note. — The i_{AB} and z_{AB} magnitudes are AB magnitudes and the J and H magnitudes are Vega-based magnitudes.

quasar, SDSS J2315–0023, is at $z = 6.12$.

We measure the rest-frame equivalent width (EW) and full width at half maximum (FWHM) of Lyα and N v for each quasar except the BAL quasar SDSS J0353+0104. To allow the analysis of the emission lines we first fit and subtract the continuum. The wavelength coverage of each spectrum is too short to fit the continuum slope, so we assume it is a power law with a slope $\alpha_\nu = -0.5$ ($f_\nu \sim \nu^{\alpha_\nu}$), and normalize it to the spectrum at rest frame 1275–1295 Å, a continuum window with little contribution from line emission. Lyα and N v are usually blended with each other, so we use three Gaussian profiles to simultaneously fit the two lines, with the first two profiles representing broad and narrow components of Lyα and the third representing N v. Since the blue side of the Lyα emission line is strongly absorbed by Lyα forest absorption systems, we only fit the red side of the line and assume that the line is symmetric. We ignore the weak Si ii λ1262 emission line on the red side of N v. The measured EW and FWHM in units of Å are shown in Table 4.2. We also give the FWHM of Lyα in units of km s^{-1}. We emphasize that the EW and FWHM of Lyα in the table have taken into account the absorbed emission by the Lyα forest, while most previous studies did not take this absorption into account.

The distributions of the Lyα EW and FWHM are broad. The average Lyα EW and FWHM measured from the low-redshift SDSS composite spectrum of Vanden Berk et al. (2001) are about 90 Å and 20 Å ($\sim$ 5000 km s^{-1}), respectively. The EW of Lyα+N v from a sample of quasars at $3.6 < z < 5.0$ is 69±18 Å (Fan et al., 2001b), although this is affected by the Lyα forest absorption. We analyzed a sample of 20 luminous SDSS quasars at $z \sim 6$, and find that the mean Lyα EW and FWHM are 56 Å and 25 Å (also corrected for the Lyα forest absorption) with large scatters of 40 Å and 11 Å, respectively. In Table 4.2, three of our quasars (SDSS J0005–0006, SDSS J0303–0019, and SDSS J2315–0023) have Lyα FWHM less than half of the typical value. The Lyα FWHM in both SDSS J0005–0006 and SDSS J0303–0019 is only $\sim$ 1600 km s^{-1}. However, their EW are close to or stronger than the typical Lyα EW. On the contrary, the other two quasars, SDSS J0203+0012 and
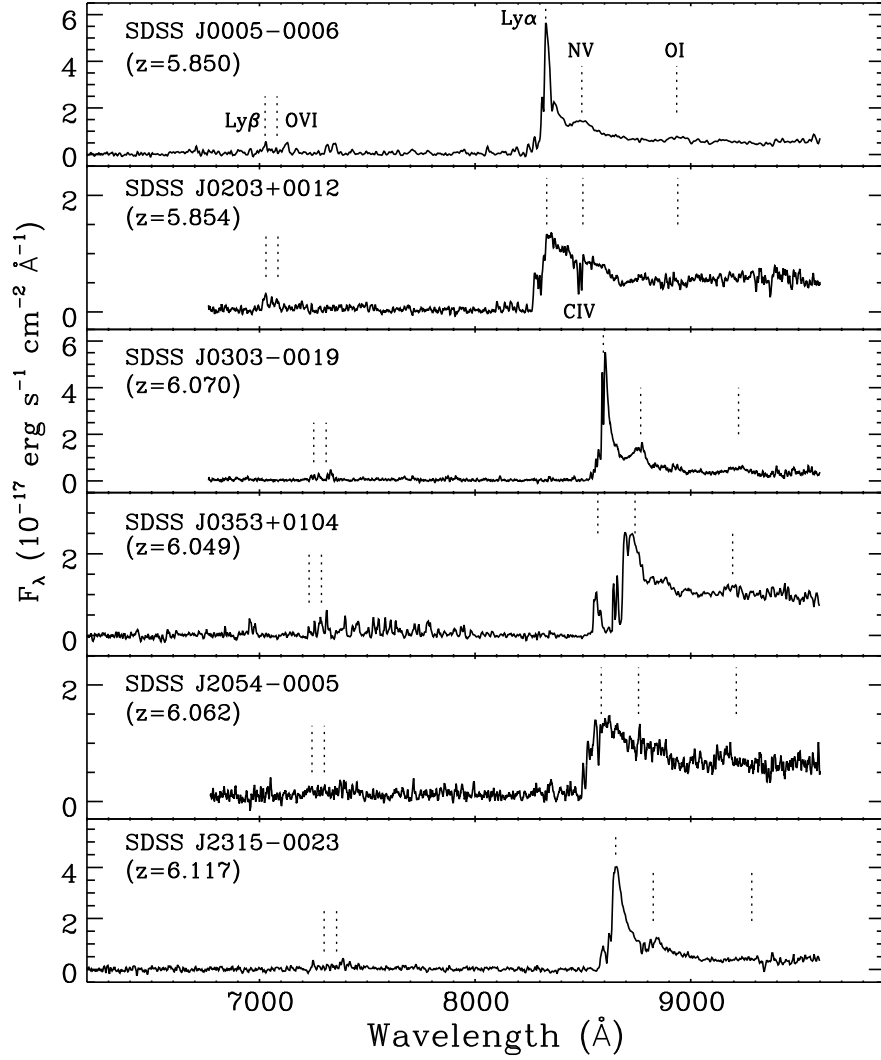
Figure 4.4 Optical spectra of the six high-redshift quasars discovered in the SDSS deep stripe. The spectra of SDSS J0005−0006, SDSS J0353+0104, and SDSS J2315−0023 were taken on Keck/ESI with a total exposure time of 60 minutes on each source. The spectra of the other three quasars were taken on Magellan/LDSS-3 with a total exposure time of 100 minutes on each source. The ESI spectra have been binned by 10 pixels and the LDSS-3 spectra been smoothed by 5 pixels. Four quasars in this sample are at $z > 6$. Three quasars have narrow Lyα emission lines. SDSS J0353+0104 is a BAL quasar.

Table 4.2. Properties of the Lyα and N v emission lines

Quasar (SDSS)	Redshift	EW (Lyα)	FWHM (Lyα)	EW (N v)	FWHM (N v)
J0005−0006	5.850	81.5±2.5	6.8±0.4 (1680 km s^{-1})	25.0±1.0	18.9±0.6
J0203+0012	5.854	35.9±1.5	31.0±2.4 (7650 km s^{-1})	8.1±0.5	20.6±0.9
J0303−0019	6.070	139.4±2.4	6.4±0.5 (1580 km s^{-1})	24.4±0.6	9.9±0.2
J0353+0104[a]	6.049	⋯	⋯	⋯	⋯
J2054−0005	6.062	17.0±1.1	19.4±3.8 (4890 km s^{-1})	12.8±0.7	30.8±1.4
J2315−0023	6.117	126.8±3.2	9.8±0.5 (2420 km s^{-1})	37.4±1.4	17.7±0.7

[a]This is a BAL quasar, so we did not measure its emission line properties.

Note. — Rest-frame FWHM and EW are in units of Å. The EW and FWHM of the Lyα emission lines have been corrected for Lyα forest absorption.

Table 4.3. Continuum properties of the quasars

Quasar (SDSS)	Redshift	m_{1450} (mag)	M_{1450} (mag)
J0005−0006	5.850	20.83±0.10	−25.82±0.10
J0203+0012	5.854	20.94±0.10	−25.72±0.10
J0303−0019	6.070	21.28±0.07	−25.43±0.07
J0353+0104	6.049	20.22±0.08	−26.49±0.08
J2054−0005	6.062	20.60±0.09	−26.11±0.09
J2315−0023	6.117	21.34±0.08	−25.38±0.08

SDSS J205406.49–000514.8 (hereafter SDSS J2054–0005), have typical Lyα FWHM, but very weak Lyα EW.

The best-fitting power-law continuum is also used to calculate m_{1450} and M_{1450}, the apparent and absolute AB magnitudes of the continuum at rest-frame 1450 Å. The results are given in Table 4.3. The sample spans a luminosity range of $-26.5 \leq M_{1450} \leq -25.4$. Because the Ly$\alpha$ emission usually consists of a large fraction of the total emission in the z-band spectra of these quasars, the large scatter in the Lyα EW results in a large scatter in the distributions of m_{1450} and M_{1450}, even though the z_{AB} magnitudes lie in the small range $20.5 < z_{AB} < 20.9$.

4.3.1   Notes on individual objects

SDSS J0005–0006 $\left(z = 5.850\right)$**.** SDSS J0005–0006 was discovered by Fan et al. (2004). This quasar has a very narrow Lyα emission line. The rest-frame FWHM of Lyα is only 1680 km s^{-1} (after being corrected for the Lyα forest absorption). The strong N v emission line is well separated from Lyα. The central BH mass is $3 \times 10^8\ M_\odot$ (Kurk et al., 2007), an order of magnitude lower than the BH masses in other luminous quasars at $z \sim 6$ (e.g. Barth et al., 2003; Vestergaard, 2004; Jiang

et al., 2007a; Kurk et al., 2007). SDSS J0005–0006 was marginally detected in the *Spitzer* IRAC 8.0μm band and was not detected in the *Spitzer* MIPS 24μm band, indicating that there is no hot dust emission in this quasar (Jiang et al., 2006a).

SDSS J0203+0012 ($z = 5.854$). SDSS J0203+0012 was independently discovered by matching the UKIDSS data to the SDSS data (Venemans et al., 2007). Its Lyα emission line is broad but weak. The Lyβ and O VI λ1033 (hereafter O VI) emission lines are clearly seen at $\sim$ 7000 Å. A C IV $\lambda\lambda$1548,1550 absorption doublet is detected at $\lambda\lambda$ = 8480.1, 8494.3 Å; this was also noticed by Venemans et al. (2007).

SDSS J0303–0019 ($z = 6.070$). SDSS J0303–0019 also has a very narrow Lyα emission line. The rest-frame FWHM of Lyα is 1580 km s^{-1}, similar to the Lyα width of SDSS J0005–0006. The strong N V emission line is well separated from Lyα. The Lyβ and O VI emission lines are clearly detected at $\sim$ 7300 Å. The continuum emission in this quasar is very weak. The absolute magnitude M_{1450} is -25.43, roughly two magnitudes fainter than the luminous SDSS quasars at $z \sim 6$.

SDSS J0353+0104 ($z = 6.049$). SDSS J0353+0104 is a BAL quasar, as seen from strong absorption features around the Lyα emission line. Its redshift was measured from O I. The fraction of BAL quasars in this small sample is one out of six, similar to the low-redshift fraction (Trump et al., 2006), although C IV observations may yield further BAL examples. The Lyβ and O VI emission lines are seen at $\sim$ 7300 Å.

SDSS J2054–0005 ($z = 6.062$). SDSS J2054–0005 has a very weak Lyα emission line. The rest-frame EW of Lyα is only 17.0 Å, significantly smaller than the typical EW. But the FWHM of Lyα, $\sim$ 30 Å, is similar to the mean value of Lyα FWHM.

SDSS J2315–0023 ($z = 6.117$). SDSS J2315–0023 is the most distant quasar in this sample. The properties of the Lyα and N V emission lines are similar to those of SDSS J0005–0006 and SDSS J0303–0019. It has a narrow but strong Lyα emission line. The rest-frame EW and FWHM of Lyα are 127 Å and 2420 km s^{-1}, respectively. It also has a very strong N V emission line.

4.4 QLF at $z \sim 6$

The six quasars presented in this chapter provide a flux-limited quasar sample at $z > 5.8$. The survey area is 260 deg^2 and the magnitude limit is $z_{AB} = 21$. In this section we calculate the spatial density of the $z > 5.8$ quasars in the SDSS deep stripe, and combine this faint quasar sample with the SDSS bright quasar sample to derive the QLF at $z \sim 6$.

We use the selection function to correct the sample incompleteness due to the selection criteria we applied. The selection function is defined as the probability that a quasar with a given magnitude, redshift, and intrinsic spectral energy distribution (SED) meets our selection criteria. By assuming a distribution for the intrinsic SEDs, we calculate the average selection probability as a function of magnitude and redshift. To do this, we first calculate the synthetic distribution of quasar colors for a given (M_{1450}, z), following the procedures in Fan (1999) and Fan et al. (2001a). Then we calculate the SDSS magnitudes from the model spectra and incorporate photometric errors into each band. For an object with given (M_{1450}, z), we generate a database of model quasars with the same (M_{1450}, z). The detection probability for this quasar is then the fraction of model quasars that meet the selection criteria. The details of the model and simulation are described in Fan (1999) and Fan et al. (2001a).

Figure 4.5 shows the selection function as a function of M_{1450} and z for the two selection criteria (Equations 1 and 2) based on J and H bands. The contours in the figure are selection probabilities from 0.9 to 0.1 with an interval of 0.1. The sharp decrease of the probability at $z \sim 5.8$ is due to the color cut of $i_{AB} - z_{AB} > 2.2$. The two selection functions are slightly different. Due to smaller photometric errors in the i and z bands, our survey probes ~ 1.5 magnitude deeper than the SDSS main survey (see Fan et al., 2001a). The solid circles are the locations of the six $z \sim 6$ quasars. All the quasars have selection probabilities greater than 0.5.

We derive the spatial density of the $z > 5.8$ quasars using the traditional $1/V_a$ method (Avni & Bahcall, 1980). The available volume for a quasar with absolute
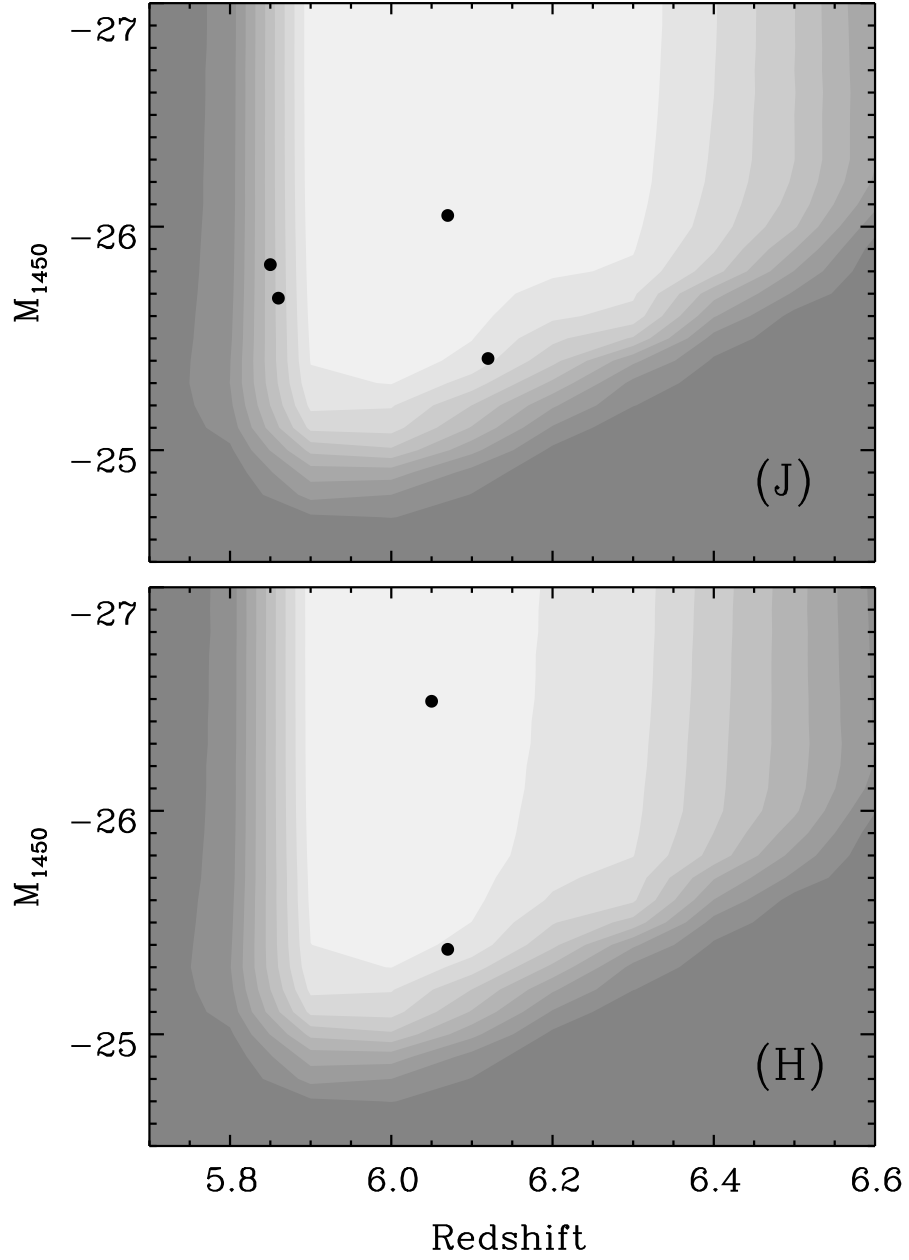
Figure 4.5 Quasar selection function as a function of M_{1450} and z for the two selection criterion equations (1a and 1b) based on J and H bands. The contours in the figure are selection probabilities from 0.9 to 0.1 with an interval of 0.1. The solid circles are the locations of the six $z \sim 6$ quasars in our sample.

magnitude M_{1450} and redshift z in a magnitude bin ΔM and a redshift bin Δz is

$$V_a = \int_{\Delta M} \int_{\Delta z} p(M_{1450}, z) \frac{dV}{dz} dz\, dM, \qquad (4.3)$$

where $p(M_{1450}, z)$ is the selection function used to correct the sample incompleteness. We use one M_{1450}–z bin for our small sample. The redshift integral is over the range $5.7 < z < 6.6$ and the magnitude integral is over the range that the sample covers. The spatial density and its statistical uncertainty can be written as

$$\rho = \sum_i \frac{1}{V_a^i}, \quad \sigma(\rho) = \left[\sum_i \left(\frac{1}{V_a^i} \right)^2 \right]^{1/2}, \qquad (4.4)$$

where the sum is over all quasars in the sample. This is similar to the revised $1/V_a$ method of Page & Carrera (2000), since $p(M_{1450}, z)$ has already corrected the incompleteness at the flux limit. We find that the spatial density at $\langle z \rangle = 6.0$ and $\langle M_{1450} \rangle = -25.8$ is $\rho = (5.0 \pm 2.1) \times 10^{-9}$ Mpc^{-3} mag^{-1}.

In the SDSS main survey, more than 20 quasars at $z > 5.8$ have been discovered. Seventeen of them were selected using similar criteria, and consist of a flux-limited quasar sample with $z_{AB} < 20$. This bright quasar sample includes 14 published quasars (e.g. Fan et al., 2006a) and three new quasars (Fan et al. in preparation). We combine this sample with our sample to derive the QLF at $z \sim 6$. The quasars in the combined sample are divided into four luminosity bins as shown in Figure 4.6. The QLF at the bright end at $z \sim 6$ is well fit to a single power law $\Phi(L_{1450}) \propto L_{1450}^\beta$, or,

$$\Phi(M_{1450}) = \Phi^* 10^{-0.4(\beta+1)(M_{1450}+26)}, \qquad (4.5)$$

where we only consider luminosity dependence and neglect redshift evolution over our narrow redshift range. The best fits are $\Phi^* = (5.2 \pm 1.9) \times 10^{-9}$ Mpc^{-3} mag^{-1} and $\beta = -3.1 \pm 0.4$. The slope $\beta = -3.1 \pm 0.4$ is consistent with the slope -3.2 ± 0.7 derived from the luminous sample alone by Fan et al. (2004) and with the slope > -4.63 (3σ) constrained by the lack of lenses in four high-redshift quasars (Richards et al., 2004).
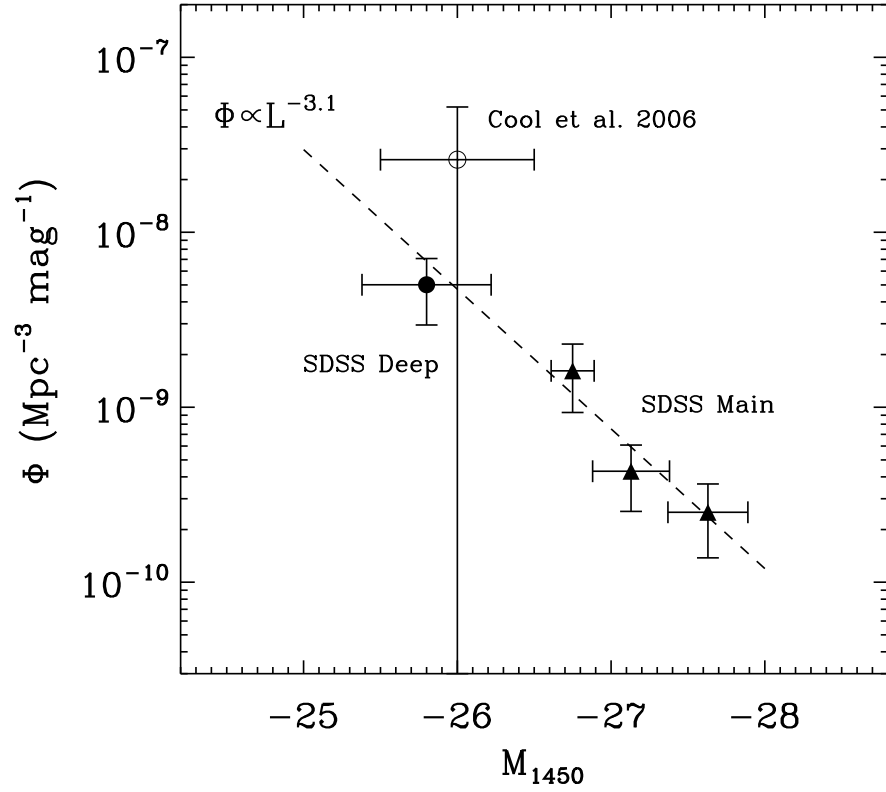
Figure 4.6 QLF at $z \sim 6$. The filled circle represents the density of the six quasars in the SDSS deep stripe and the filled triangles represent the densities from a study of 17 quasars from the SDSS main survey. The open circle is the constraint from the quasar discovered by Cool et al. (2006). The dashed line shows the best power-law fit to the SDSS quasars. The slope of the QLF is -3.1 ± 0.4.

4.5   Discussion

We have derived the QLF at $z \sim 6$ and found a steep slope ($\beta = -3.1$) at the bright end. From the SDSS Data Release Three, Richards et al. (2006b) showed strong evidence that the bright-end slope of the QLF significantly flattens from $z \sim 2$ to 4. They found that the slope at $z \sim 2.0$ is -3.1 ± 0.1 and the slope at $z \sim 4.1$ flattens to -2.1 ± 0.1. At $z \sim 6$ the slope steepens again to -3.1 ± 0.4. The steepening of the QLF is at $\sim 2.5\sigma$ significance. The flattening of the slope at $z \sim 4$ has been questioned by Fontanot et al. (2007), who argued that the spectral index Richards et al. (2006b) used to correct for sample incompleteness was too blue. Hopkins et al. (2007) have analyzed the bolometric QLF from multiple surveys and stress that the flattening is seen at high significance. The lack of flattening claimed by Fontanot et al. (2007) would be real only if the distribution of quasar SEDs was redshift-dependent, contrary to what is found in most observations. Hence, the slope change from $z \sim 4$ to $z \sim 6$ is highly likely to be physical. The steepening of the slope at $z \sim 6$ has important consequences in understanding early BH growth in quasars. Quasar evolution at $z \sim 6$ is limited by the number of e-folding times available for BH accretion, therefore the shape of the QLF at $z \sim 6$ puts strong constraints on models of BH growth (e.g. Wyithe & Loeb, 2003; Hopkins et al., 2005; Volonteri & Rees, 2006; Wyithe & Padmanabhan, 2006; Li et al., 2007), and helps determine whether standard models of radiatively efficient Eddington accretion from stellar seeds are still allowed, or alternative models of BH birth (e.g. from intermediate-mass BHs) and BH accretion (super-Eddington or radiatively inefficient) are required (e.g. Volonteri & Rees, 2006).

The steepening of the QLF slope also has a strong impact on the quasar contribution to the ionizing background at $z \sim 6$. The reionization of the universe occurs at $z = 11 \pm 4$ (Spergel et al., 2007) and ends at $z \sim 6$ (Fan et al., 2006b). Studies have shown that quasars/AGN alone are not likely to ionize the IGM at $z \sim 6$ (e.g. Dijkstra et al., 2004; Meiksin, 2005; Willott et al., 2005; Douglas et al., 2007; Salvaterra et al., 2007; Srbinovsky & Wyithe, 2007; Shankar & Mathur, 2007), and galaxies

probably can provide enough photons for the reionization (e.g. Yan & Windhorst, 2004; Bouwens et al., 2006; Kashikawa et al., 2006; McQuinn et al., 2007). However, the individual contributions of galaxies and quasars to the reionization are not well determined. The galaxy contribution is uncertain due to our lack of knowledge of factors such as the star-formation rate, the faint-end slope of the galaxy luminosity function, and the escape fraction of ionizing photons from galaxies (e.g. Bunker et al., 2004; Bouwens et al., 2006; Gnedin, 2008); while the quasar contribution is poorly determined because the total number of known quasars at $z \sim 6$ was only ~ 20 so that even the QLF at the bright end was not well established before this study.

A few small-area deep observations with one or no quasar detections have put strong constraints on the ionizing photon density from $z \sim 6$ quasars. For example, Willott et al. (2005) did not find any quasars at $z > 5.7$ down to $z_{AB} = 23.35$ in a 3.83 deg^2 area of CFHQS, and thus concluded that the quasar population make a negligible contribution to reionization. Shankar & Mathur (2007) have considered the implications of all existing $z \sim 6$ quasar observations, including deep X-ray surveys, for the faint end of the high-redshift QLF. Based predominantly on the X-ray surveys, they argue that there is a flattening of the QLF at $M_{1450} \geq -24.67$. Although our sample is not deep enough to reach the break luminosity of the QLF, the combination of our sample and the SDSS luminous sample with more than 20 quasars allows us to improve these constraints.

We estimate the rate at which quasars emit ionizing photons at $z \sim 6$ from the QLF derived in § 4.4. Following Fan et al. (2001a), we calculate the photon emissivity of quasars per unit comoving volume at $z \sim 6$ as

$$\dot{\mathcal{N}}_q = \epsilon^q_{1450}\, n^p_{1450}, \tag{4.6}$$

where ϵ^q_{1450} is the quasar emissivity at 1450 Å in units of erg s^{-1} Hz^{-1} Mpc^{-3} and n^p_{1450} is the number of ionizing photons for a source with a luminosity of 1 erg s^{-1} Hz^{-1} at 1450 Å. We estimate ϵ^q_{1450} from

$$\epsilon^q_{1450} = \int \Phi(M_{1450}) L_{1450} \, dM_{1450}, \tag{4.7}$$

where $\Phi(M_{1450})$ is the QLF at $z \sim 6$ and the integral is over the range $-30 <$ $M_{1450} < -16$. At low redshift, the shape of the QLF can be well modeled as a double power law with a steep bright end and a flat faint end (e.g. Boyle et al., 2000; Richards et al., 2005; Jiang et al., 2006b). At $z \sim 6$, we assume a double power-law form for the QLF as well,

$$\Phi(M_{1450}) = \frac{\Phi^*}{10^{0.4(\alpha+1)(M_{1450}-M_{1450}^*)} + 10^{0.4(\beta+1)(M_{1450}-M_{1450}^*)}}, \tag{4.8}$$

where β is the bright-end slope of the QLF, α is the faint-end slope, and M_{1450}^* corresponds to the characteristic luminosity L_{1450}^*. At $z \leq 2$, α is roughly -1.6 and M_{1450}^* is a function of redshift. Little is known about α and M_{1450}^* at $z > 4$. At $z \sim 6$, the lower limit of M_{1450}^* is about -25 as seen from Figure 4.6. Therefore we calculate ϵ_{1450}^q for a range of α between -1.2 and -2.2 and for a range of M_{1450}^* between -21 and -25. The bright-end slope β is fixed to -3.1 at the first step. We assume Φ^* to be the value derived from Equation 4.5. This is a good approximation in the α and M_{1450}^* ranges that we investigate here.

We calculate n_{1450}^p by assuming the quasar SED following

$$L_\nu \propto \begin{cases} \nu^{-0.5}, & \text{if } \lambda > 1050 \text{ Å}; \\ \nu^{-1.8}, & \text{if } \lambda < 1050 \text{ Å}, \end{cases} \tag{4.9}$$

and integrating the SED over an energy range of 1–4 Rydberg. The SED slope at $\lambda > 1050$ Å is taken from Vanden Berk et al. (2001) and at $\lambda < 1050$ Å from Zheng et al. (1997).

The total photon emissivity per unit comoving volume required to ionize the universe is estimated to be

$$\dot{\mathcal{N}}_{ion}(z) = 10^{51.2} \,\text{Mpc}^{-3} \,\text{s}^{-1} \left(\frac{C}{30}\right) \times \left(\frac{1+z}{6}\right)^3 \left(\frac{\Omega_b h^2}{0.02}\right)^2 \tag{4.10}$$

(Madau et al., 1999), where the baryon density $\Omega_b h^2 = 0.02$ (Spergel et al., 2007) and C is the clumping factor of the IGM. We examine the effects of three values 1, 10, and 30 for C.

Figure 4.7 shows that the quasar/AGN population cannot provide enough photons to ionize the IGM unless the IGM is very homogeneous and the break luminosity
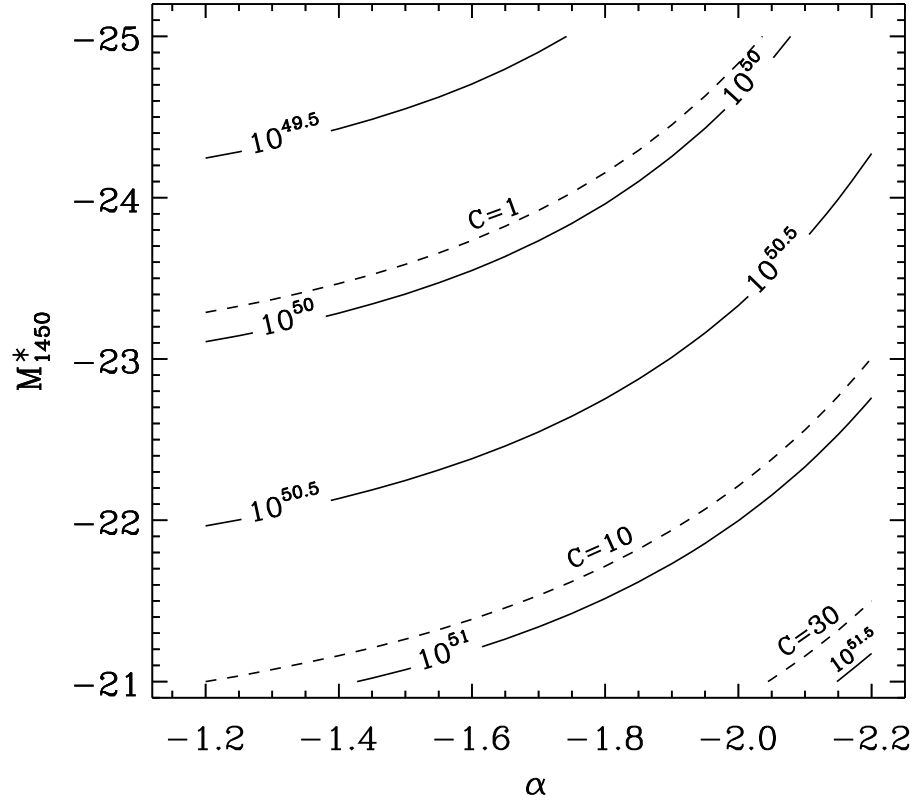
Figure 4.7 Photon emissivity (per unit comoving volume) from quasars as a function of the faint-end QLF slope α and the characteristic luminosity M^*_{1450}. The solid lines represent the total photon emissivity from quasars. The dashed lines show the photon emissivity required to ionize the IGM at $z \sim 6$ for the clumping factors $C = 1$, $C = 10$, and $C = 30$, respectively. According to the results by Willott et al. (2005) and Shankar & Mathur (2007), the range $M^*_{1450} \geq -23$ has been ruled out.

is very low. At low redshift, M^*_{1450} varies with redshift and the typical value is between –23 and –21. At $z \sim 6$, the lower limit of M^*_{1450} is about -25. According to the results by Willott et al. (2005) and Shankar & Mathur (2007), the range $M^*_{1450} \geq -23$ has been ruled out. To measure M^*_{1450} at $z \sim 6$, much deeper surveys are needed. The clumping factor C is also poorly constrained. Previous studies used a range of values from 1 to $\sim$100. If the typical value of C is 10–30 (e.g. Gnedin & Ostriker, 1997; Madau et al., 1999), the quasar population with $\beta = -3.1$ is not likely to provide enough ionizing photons. However, if the reionization occurs outside-in and denser gas is ionized at a later time when most of the volume of the universe has been reionized, clumpiness does not significantly increase the number of photons required for reionization (Miralda-Escudé et al., 2000). In this case, the equivalent C is close to 1, and quasars can relatively easily provide the required number of photons if the break luminosity is low.

4.6 Summary

We have discovered five quasars at $z > 5.8$ in 260 deg^2 of the SDSS deep stripe, including one previously discovered by Venemans et al. (2007). The most distant one is at $z = 6.12$. These quasars were selected as i-dropout objects from the coadds of 10 SDSS imaging runs, going ~ 1.5 magnitudes fainter than the SDSS main survey. The five quasars, with $20 < z_{AB} < 21$, are 1–2 magnitudes fainter than the luminous $z \sim 6$ quasars found in the SDSS main survey. The Lyα emission lines in two quasars SDSS J0303–0019 and SDSS J2315–0023 are narrow (FWHM $\sim$ 1600 and 2400 km s^{-1}) but strong (EW $\sim$ 139 and 127 Å), while the Lyα emission lines in another two quasars SDSS J0303–0019 and SDSS J2315–0023 are broad (FWHM $\sim$ 7700 and 4900 km s^{-1}) but weak (EW $\sim$ 36 and 17 Å). The fifth one, SDSS J0353+0104, is a BAL quasar.

The new quasars, together with a previously discovered quasar, SDSS J0005–0006, comprise a flux-limited quasar sample with $z_{AB} < 21$ at $z \sim 6$ over 260 deg^2. The sample covers the luminosity range $-26.5 \leq M_{1450} \leq -25.4$. The spatial

density of the quasars at $\langle z \rangle = 6.0$ and $\langle M_{1450} \rangle = -25.8$ is $(5.0 \pm 2.1) \times 10^{-9}$ Mpc^{-3} mag^{-1}. We use a single power-law form to model the bright-end QLF at $z \sim 6$ and find a slope of -3.1 ± 0.4, which is significantly steeper than the slope of the QLF at $z \sim 4$. Using the derived QLF, we find that the quasar/AGN population can provide enough photons to ionize the IGM at $z \sim 6$ only if the IGM is very homogeneous and the characteristic luminosity of the QLF is very low. To put better constraints on the quasar contribution, much deeper surveys are needed.

The quasars in this chapter were selected from the SDSS coadded images with 5–18 runs. Currently the SDSS deep stripe has been scanned between 40 and 50 times, reaching $2 \sim 3$ magnitudes deeper than the main survey when co-added. We are performing a deeper survey of $z \sim 6$ quasars down to $z_{AB} \sim 22$ in this region. We expect to obtain a flux-limited sample with $z_{AB} < 22$ in the next few years.

CHAPTER 5

SPATIAL DENSITY EVOLUTION OF QUASARS AT $Z < 4$

Observations reported here were obtained at the MMT Observatory, a joint facility of the Smithsonian Institution and the University of Arizona.

5.1   Introduction

One of the most important properties of quasars is their strong evolution with cosmic time. The quasar luminosity function (QLF) is thus of particular importance in understanding quasar formation and evolution and exploring physical models of quasars. It has been shown that quasar activity and the formation processes of galaxies and supermassive black holes (SMBHs) are closely correlated (e.g. Kauffmann & Haehnelt, 2000; Wyithe & Loeb, 2003; Hopkins et al., 2005; Croton et al., 2006), so the QLF is essential to study galaxy formation, the accretion history of SMBHs during the active quasar phase, and its relation to galaxy evolution. Quasars are strong X-ray sources, thus the QLF can provide important constraints on the quasar contribution to the X-ray and ultraviolet background radiation (e.g. Koo & Kron, 1988; Boyle & Terlevich, 1998; Mushotzky et al., 2000; Worsley et al., 2005). The QLF is also useful for understanding the spatial clustering of quasars and its relation to quasar life times (e.g. Martini & Weinberg, 2001).

The differential QLF is defined as the density of quasars per unit comoving volume and unit luminosity interval as a function of luminosity and redshift. If the redshift and luminosity dependence are separable, the QLF can be modeled in terms of pure density evolution (PDE), pure luminosity evolution (PLE), or a combination of the two forms. Earlier work found that there was a strong decline of quasar activity from $z \sim 2$ to the present universe, and a model with a single power-law shape provided good fits to the observed QLF for $z < 2$ at the bright

end (Marshall et al., 1983, 1984; Marshall, 1985). When more faint quasars were discovered, a break was found in the luminosity function (e.g. Koo & Kron, 1988; Boyle, Shanks, & Peterson, 1988), and the shape of QLF was modeled by a double power-law form with a steep bright end and a much flatter faint end. In this double power-law model, luminosities evolve as PLE, and density evolution is not necessary (e.g. Boyle, Shanks, & Peterson, 1988). Some studies cast doubt on this claim, however. First, the existence of the break in the QLF slope is not obvious (e.g. Hawkins & Véron, 1995; Goldschmidt & Miller, 1998; Wisotzki, 2000; Wolf et al., 2003). Second, it was found that the PLE model was not sufficient to describe the quasar evolution at $z < 2$ (e.g. Hewett, Foltz, & Chaffee, 1993; La Franca & Cristiani, 1997; Goldschmidt & Miller, 1998; Wisotzki, 2000).

The density of luminous quasars reaches a maximum at $2 < z < 3$ (hereafter referred to as the mid-z range), and drops rapidly toward higher redshift (e.g. Pei, 1995). The high-z ($z > 3$) QLF has been explored only for bright quasars (e.g. Warren, Hewett, & Osmer, 1994; Kennefick, Djorgovski, & De Carvalho, 1995; Schmidt, Schneider, & Gunn, 1995; Fan et al., 2001c). At $z \sim 4$, the QLF was fitted by a single power-law form with an exponential decline in density with redshift (Schmidt, Schneider, & Gunn, 1995; Fan et al., 2001c), and its slope is much flatter than the bright-end slope of the QLF at $z < 3$. This indicates that, at high redshift, the shape of the QLF evolves with redshift as well (Fan et al., 2001c). However, a large sample of high-z quasars is needed to prove this claim.

One of the largest homogeneous samples of low-z quasars comes from the 2dF QSO Redshift Survey and 6dF QSO Redshift Survey (hereafter 2QZ; Boyle et al., 2000; Croom et al., 2004). The 2QZ survey includes 25,000 quasars, and covers a redshift range of $0.4 < z < 2.1$ and a magnitude range of $16 < b_J < 20.85$. The QLF derived from the 2QZ can be well fitted by a double power-law form with a steep slope at the bright end and a flatter slope at the faint end, showing a break in the QLF. The evolution is well described by the PLE. The Sloan Digital Sky Survey (SDSS; York et al., 2000) is collecting the largest spectroscopic samples of galaxies and quasars to date. The SDSS main survey covers a large redshift range

from $z = 0$ to $z > 5$, however, it only selects bright objects: it targets quasars with $i < 19.1$ at $z \leq 3$ and $i < 20.2$ at $z \geq 3$ (Richards et al., 2002). The QLF derived from SDSS Data Release Three (DR3; Schneider et al., 2005) shows some curvature at the faint end, but the survey does not probe faint enough to test the existence of the break (Richards et al., 2006b). The best fit model of the SDSS-DR3 QLF shows, for the first time in a single large redshift range, the flattening of the QLF slope with increasing redshift. Selecting $g < 21.85$ and $z < 2.5$ quasar candidates from SDSS imaging and spectroscopically observing them with the 2dF instrument, the 2dF-SDSS LRG and QSO Survey (2SLAQ) probes deeper than either the SDSS or the 2QZ (Richards et al., 2005). The QLF of the 2SLAQ is consistent with the 2QZ QLF from Boyle et al. (2000), but has a steeper faint-end slope than that from Croom et al. (2004).

Despite the investigations described above, the optical QLF over both a large redshift range and a large luminosity range is far from well established. First, the faint-end slope of the QLF is still uncertain. Most wide-field surveys, including the SDSS, are shallow and can only sample the luminous quasars. Although the 2SLAQ survey probed to $g = 21.85$, it only covers the low-z range ($z \leq 2.2$). Furthermore, the existence of the break in the QLF slope is uncertain, and different surveys give different slopes at the faint end (e.g. Wolf et al., 2003; Croom et al., 2004; Richards et al., 2005). Second, it is unclear whether PLE is sufficient to describe quasar evolution at low redshift. Third, the high-z ($z > 3$) QLF has not been well established, especially at the faint end. In addition, the density of luminous quasars peaks between $z = 2$ and $z = 3$, yet the colors of quasars with $2.2 < z < 3$ are similar to those of A and F stars, making selection of these objects difficult (Fan, 1999; Richards et al., 2002, 2006b). X-ray and infrared surveys provide other ways to determine the QLF of both type I and type II AGNs (e.g. Ueda et al., 2003; Barger et al., 2005; Hasinger, Miyaji, & Schmidt, 2005; Brown et al., 2006). These studies have shown that a substantial fraction of AGNs are optically obscured at low luminosities. Barger et al. (2005) found a downturn at the faint end of the hard X-ray luminosity function for type I AGN, but current optically-selected quasar

samples are not sufficiently faint to probe this downturn, if it exists.

To probe these issues, we need a large, homogeneous, faint quasar sample. This sample should be deep enough to study quasar behavior at the faint end, and large enough to provide good statistics. The sample should also span a large redshift range, straddling the peak of quasar activity. All these require a wide-field spectroscopic survey of faint quasars selected from deep multi-color imaging data. Such data are provided by the SDSS Southern Survey, a deep survey based on repeated imaging of the Fall Celestial Equatorial Stripe in the Southern Galactic Cap (SGC). The SGC imaging data, when co-added, reach more than two magnitudes deeper than does the SDSS main survey, allowing efficient selection of much fainter quasar candidates. The goal of the SDSS faint quasar survey (SFQS) is to obtain more than 1000 faint quasars from 10 deg^2 of the SDSS deep stripe. This chapter presents the first results of the SFQS, in an area of ~ 3.9 deg^2. The spectroscopic observations were performed on MMT/Hectospec (Fabricant et al., 2005). The preliminary faint quasar sample reaches $g = 22.5$, and fills in the crucial gap between large-area, shallow surveys such as the SDSS and 2QZ, and deep, pencil beam surveys such as the *Chandra* Deep Field (CDF) survey (e.g. Barger et al., 2005) and COMBO-17 survey (e.g. Wolf et al., 2003).

In § 5.2 of this chapter, we introduce the SDSS deep imaging survey and the color selections of faint quasars from the deep data. In § 5.3, we describe follow-up spectroscopic observations on MMT/Hectospec, and present the preliminary sample of the SFQS. We derive the QLF for the SFQS sample in § 5.4, and compare our results to other surveys in § 5.5. Throughout the chapter we use a Λ-dominated flat cosmology with $H_0 = 70$ km s^{-1} Mpc^{-1}, $\Omega_m = 0.3$, and $\Omega_\Lambda = 0.7$ (e.g. Spergel et al., 2003).

5.2 Quasar Selection in the SDSS Southern Survey

5.2.1 The SDSS southern survey

The Sloan Digital Sky Survey (SDSS) is an imaging and spectroscopic survey of the sky (York et al., 2000) using a dedicated wide-field 2.5 m telescope (Gunn et al., 2006) at Apache Point Observatory, New Mexico. Imaging is carried out in drift-scan mode using a 142 mega-pixel camera (Gunn et al., 1998) which gathers data in five broad bands, $ugriz$, spanning the range from 3000 to 10,000 Å (Fukugita et al., 1996), on moonless photometric (Hogg et al., 2001) nights of good seeing. The images are processed using specialized software (Lupton et al., 2001; Stoughton et al., 2002), and are photometrically (Tucker et al., 2006) and astrometrically (Pier et al., 2003) calibrated using observations of a set of primary standard stars (Smith et al., 2002) on a neighboring 20-inch telescope. The photometric calibration is accurate to roughly 2% rms in the g, r, and i bands, and 3% in u and z, as determined by the constancy of stellar population colors (Ivezić et al., 2004; Blanton et al., 2005), while the astrometric calibration precision is better than 0.1 arcsec rms per coordinate (Pier et al., 2003). All magnitudes are roughly on an AB system (Abazajian et al., 2004), and use the asinh scale described by Lupton et al. (1999). From the resulting catalogs of objects, complete catalogs of galaxies (Eisenstein et al., 2001; Strauss et al., 2002) and quasar candidates (Richards et al., 2002) are selected for spectroscopic follow-up (Blanton et al., 2003). Spectroscopy is performed using a pair of double spectrographs with coverage from 3800 to 9200 Å , and a resolution $\lambda/\Delta\lambda$ of roughly 2000. The SDSS main quasar survey targets quasars with $i < 19.1$ at $z \leq 3$ and $i < 20.2$ at $z \geq 3$ (Richards et al., 2002). Its spectroscopic survey is based on its imaging data with an exposure time of 54 seconds, so it is a shallow survey, and can only sample the most luminous end of the QLF.

In addition to the main imaging survey, the SDSS also conducts a deep imaging survey, the SDSS Southern Survey, by repeatedly imaging the Fall Celestial Equatorial Stripe in the Southern Galactic Cap. When completed, the 300 deg^2 area will be imaged up to 30 times. The multi-epoch images, when co-added, allow the

selection of much fainter quasar candidates than the SDSS main survey.

5.2.1.1 Co-added catalog

Quasar candidates are selected from the co-added catalog of the SDSS deep stripe, i.e., each run goes through the photometric pipeline separately, and the resulting catalogs are co-added. A better way to use multi-epoch images for quasar selection is to use co-added images, instead of multi-epoch catalogs. At the time when the spectroscopic observations were carried out, co-added images were not available, so in this chapter quasar candidates were selected from the co-added catalog.

To construct the co-added catalog, we matched the multi-epoch data against themselves using a $0\rlap{.}{''}5$ tolerance. Given N_{epoch} epochs for a given object, a proper co-addition requires that we transform from $asinh$ magnitudes (Lupton et al., 1999) into flux. For a given SDSS band j, the conversion of magnitude m_j into flux f_j in Jy is given by

$$f_j = 2F_0 L_j \sinh\left[-m_j/P - \ln L_j\right], \tag{5.1}$$

where $F_0 = 3630.78$ Jy, $P = 1.08574$ and $L = [1.4, 0.9, 1.2, 1.8, 7.4] \times 10^{-10}$ for the u, g, r, i, and z bands, respectively (Stoughton et al., 2002). We then take the mean of the flux $\bar{f}_j$ from the N_{epoch} epochs and use the inverse of Equation 5.1 to recover the co-added magnitude $\bar{m}_j$. For the error on the co-added magnitude, we calculate the standard deviation of the fluxes from the epoch data Δf_j and convert it to a magnitude error Δm_j using

$$\Delta m_j = \frac{P\Delta f_j}{2F_0} \left[\sinh^2\left(-\bar{m}_j/P - \ln L_j\right) + L_j^2\right]^{-\frac{1}{2}}. \tag{5.2}$$

Figure 5.1 gives $u - g$, $g - r$ color-color diagrams for point sources ($20.5 < g < 21.0$) in the SDSS main survey (single-epoch data) and the deep survey (multi-epoch data) with $N_{epoch} \sim 13$. Each panel in Figure 5.1 includes 10,000 objects. Compared to the main survey, the stellar locus in the deep survey is much more concentrated due to the smaller photometric errors, and UVX quasar candidates (confined by solid lines; see § 5.2.2) are well separated from the stellar locus. This enables us to
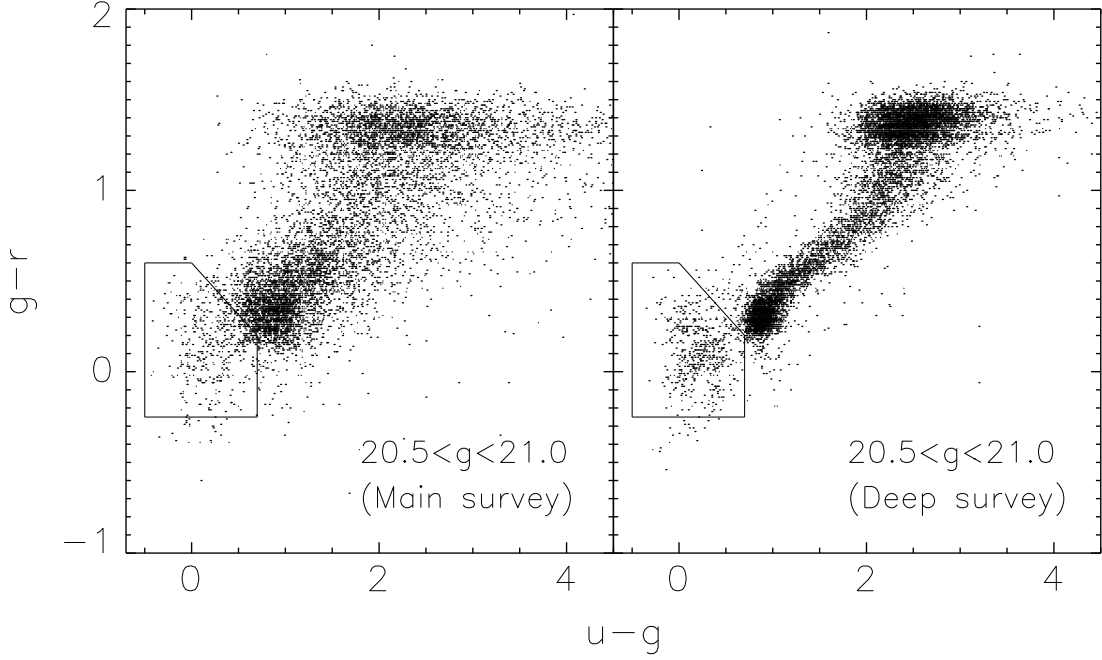
Figure 5.1 The $u-g$ vs. $g-r$ color-color diagrams for point sources ($20.5 < g < 21.0$) in the SDSS main survey and deep survey with $N_{epoch} \sim 13$. Each panel includes 10,000 objects. Compared to the main survey, the stellar locus in the deep survey is more concentrated, and UVX quasar candidates (confined by solid lines) are well separated from the stellar locus.

improve the quasar candidate selection and select much fainter quasars in color-color diagrams.

Figure 5.2 compares the magnitude limit and area of the SFQS with the LBQS (Foltz et al., 1987), 2QZ (Boyle et al., 2000; Croom et al., 2004), SDSS (Richards et al., 2002), 2SLAQ (Richards et al., 2005), COMBO-17 (Wolf et al., 2003) and the CDF (Barger et al., 2005) surveys of quasars and AGNs. The SFQS goes $\geq$ 2 magnitude deeper than 2QZ and SDSS, reaching the traditional quasar/AGN boundary at $z \sim 2.5$, the peak of luminous quasar density evolution. It fills in the crucial gap between large-area, shallow surveys such as the SDSS, and deep, pencil beam surveys such as the CDF survey.
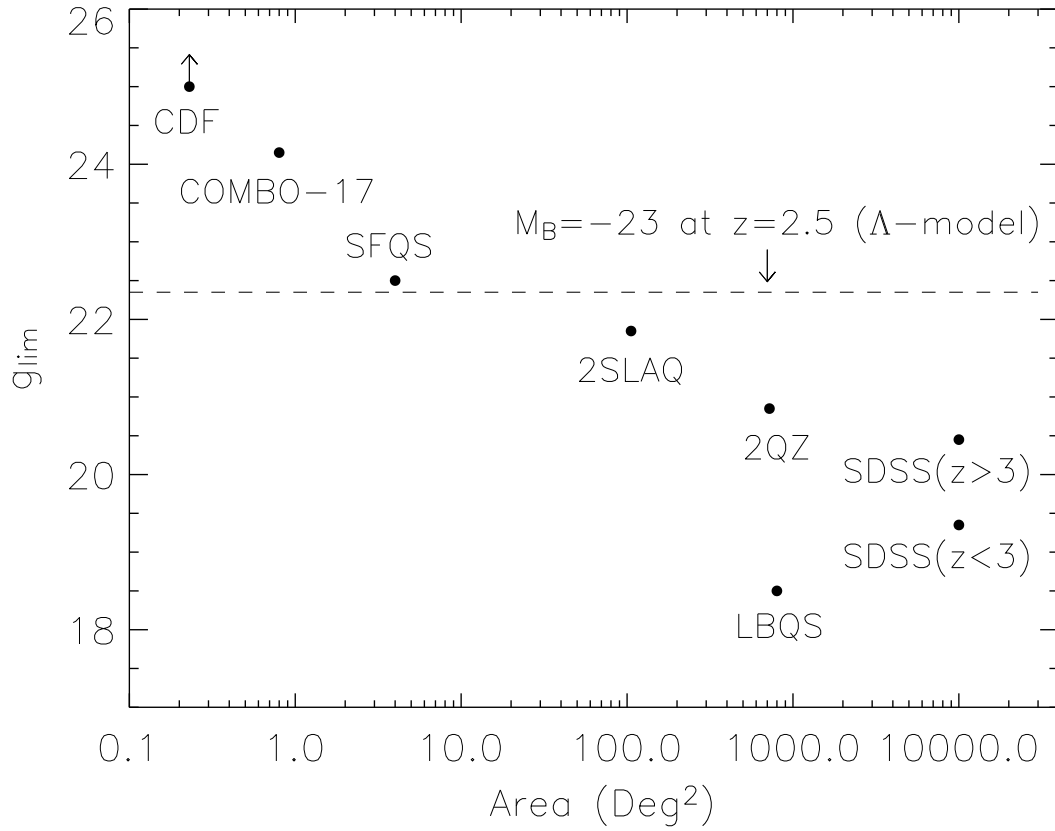
Figure 5.2 The comparison between the SFQS and the LBQS (Foltz et al., 1987), 2QZ (Boyle et al., 2000; Croom et al., 2004), SDSS (Richards et al., 2002), 2SLAQ (Richards et al., 2005), COMBO-17 (Wolf et al., 2003) and CDF (Barger et al., 2005, the area given here is the total area of CDF-N and CDF-S) surveys of quasars and AGNs.

5.2.2 Quasar candidate selection

Quasar candidates are selected as outliers from the stellar locus in color-color diagrams (e.g. Newberg & Yanny, 1997). The SDSS selects quasar candidates based on their morphology and non-stellar colors in $ugriz$ broad bands. The loci of simulated quasars and Galactic stars in the SDSS $ugriz$ space are given in Fan (1999), and the quasar color-selection in the SDSS is addressed in detail in Richards et al. (2002). In the SDSS main quasar survey, stellar outliers are defined as those more than 4σ from the stellar locus in the $u-g$, $g-r$, $r-i$ and $g-r$, $r-i$, $i-z$ 3-D color spaces (Richards et al., 2002). We modify the SDSS selection criteria and select quasar candidates in 2-D color-color diagrams in the SFQS survey. First, we generate a database of simulated quasars in different redshift ranges (Fan, 1999; Richards et al., 2006b). We make sure that our selection criteria can recover a substantial fraction of the simulated quasars in each redshift ranges, including the mid-z range. The photometric errors increase as quasar candidates go fainter, so we use slightly different selection criteria in different magnitude ranges, and find a compromise between completeness and efficiency. There is a small number of bright candidates that were already observed spectroscopically in the SDSS main survey, and we do not observe them in the SFQS. The final consideration is the fiber density of MMT/Hectospec (see § 5.3.1). The candidate density (excluding those that already have spectra from the SDSS) in the sky is set to be $\sim$15% larger than the fiber density used for the quasar survey, so that every fiber will be used in the case that candidates are closer than the separation (20$''$) of adjacent fibers.

The spectroscopic observations were carried out on the 6.5m MMT with Hectospec in June 2004 (hereafter Run I) and November 2004 (hereafter Run II). Run I was a pilot run, and used to test the integration time, target selection criteria, and the data reduction software. We then adjusted the integration time, and improved the quasar selection in Run II based on the observations in Run I, so the selection criteria in the two runs were different. In the following subsections we mainly discuss the color selection in Run II, and briefly in Run I. The Run II candidates were

selected from the co-added catalog with average epoch number $N_{epoch} \sim 13$. We restricted ourselves to objects with $g > 16.0$ selected from regions with $N_{epoch} > 7$. We only selected point candidates in the two runs.

5.2.2.1 UVX and mid-z candidates

The ultraviolet excess (UVX) and mid-z quasar candidates were selected using $u - g$, $g - r$ diagrams. In Run II, the g magnitude limit was 22.5. For different magnitude ranges, we used slightly different color cuts. As candidates go fainter, σ increases, and the loci of stars in color-color diagrams become less concentrated. So our selection regions at fainter ranges are a little further from the stellar loci to reduce the contamination from stars. The selection is summarized in Figure 5.3. The regions confined by solid lines in Figure 5.3 are our selection regions. The left-hand box in each panel defines UVX candidates, and the right-hand box defines mid-z candidates. In the top panels of Figure 5.3 where objects are bright, quasar candidates are well separated from Galactic stars. But in the lower panels where objects are much fainter, quasars and stars blend together heavily. In this case, we find a compromise between completeness and efficiency so that the selection can recover a large fraction of simulated quasars, and the candidate density exceeds the Hectospec fiber density used for our quasar survey by $\sim 15\%$.

In each panel of Figure 5.3, the right-hand selection box is used to recover a fraction of mid-z quasars ($2 < z < 3$). The colors of mid-z quasars are similar to those of stars (mainly late A and early F stars), so in $u - g$, $g - r$ diagrams, the locus of mid-z quasars partially overlaps the stellar locus (Fan, 1999; Richards et al., 2002). The SDSS main survey selects mid-z candidates using the selection similar to that shown in Figure 5.3, however, it only targets bright objects, and its mid-z selection box is overwhelmed by contaminant stars. To limit the reduction in efficiency, the main survey targets only 10% of the objects in this selection box (Richards et al., 2002). In the SFQS, we target all mid-z candidates with acceptable efficiency, because contaminant A and F stars in the mid-z selection box become less abundant at fainter magnitudes. Figure 5.3 shows that the number of A and
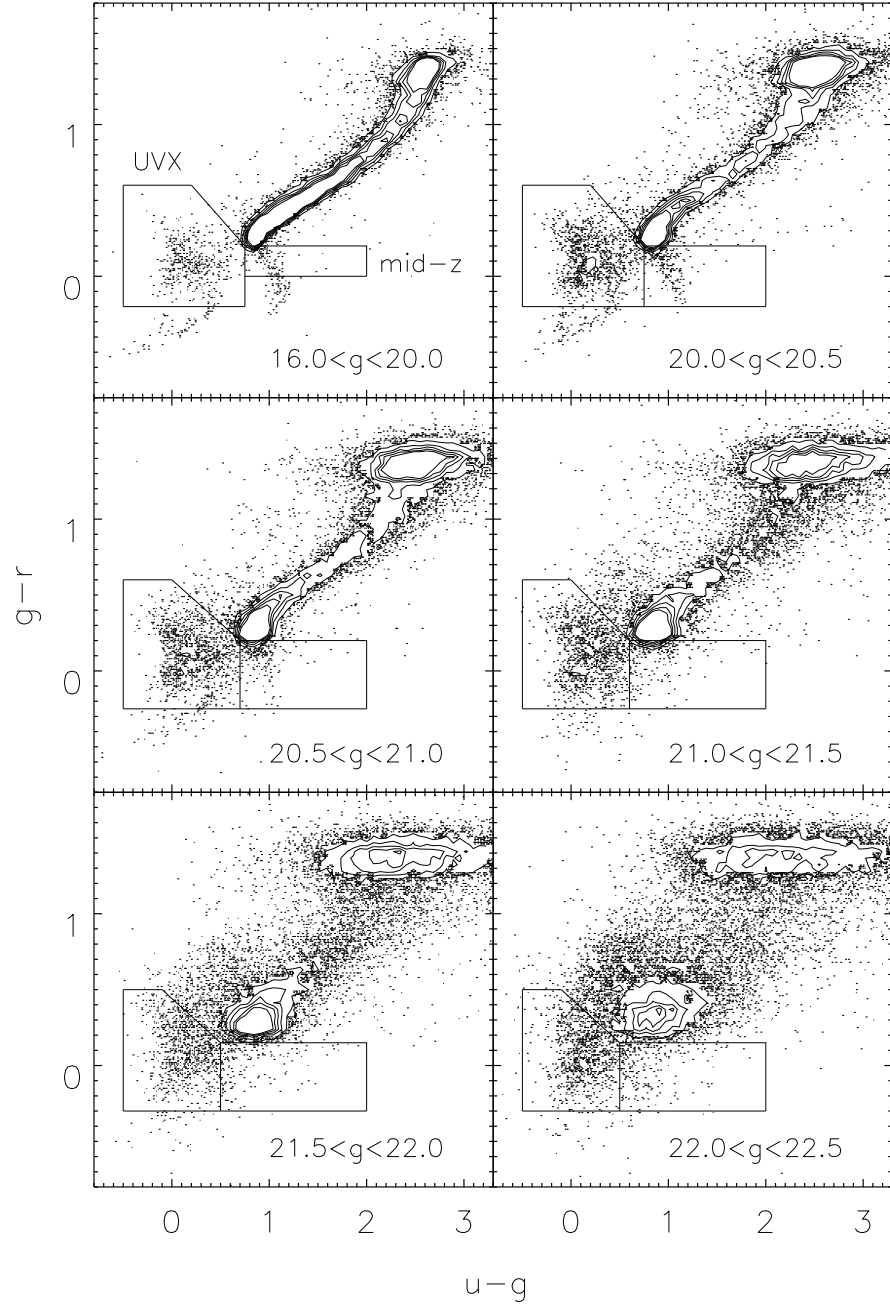
Figure 5.3 The selection of UVX and mid-z candidates from $g = 16.0$ to 22.5 in $u - g$, $g - r$ diagrams. The inner parts of the diagrams are shown in contours, which linearly increase inwards in the density of stars. For the purpose of comparison, each panel includes 20,000 objects. The regions confined by solid lines are our selection of UVX and mid-z candidates.

F stars drops rapidly at $g \sim 20.5$, due to the fact that we have reached the most distant early F dwarfs in the Galactic halo at this magnitude.

In addition to the candidates selected by Figure 5.3, we obtain another candidate sample down to $g = 22.0$ independently from the co-added catalog using the kernel density estimator (KDE; Silverman, 1986) technique described by Richards et al. (2004) who applied this method to the SDSS-DR1 imaging area. The KDE method (Gray et al., 2004) is a sophisticated extension of the traditional color selection technique for identifying quasars (e.g. Richards et al., 2004). For our case, we have applied the algorithm to data that is considerably fainter than was used by Richards et al. (2004) ($g = 22.0$ as compared to $g = 21.0$). While the SDSS imaging is complete to this depth, the errors are larger than is ideal for the application of this method.

Our final candidate sample is the combination of the two independent samples. In fact, the two samples contain roughly the same candidates at $g < 22.0$. In Run II, there are only 15 quasars included by the KDE sample but not included by the selection in Figure 5.3.

The candidate selection in Run I was slightly different: (1) In Run I, the average epoch number of the co-added catalog was 7.4, so the photometric errors were larger than those in Run II; (2) The selection in Run I was based on r magnitude, and the selection of UVX and mid-z candidates was down to $r = 22.5$ (but the selection efficiency is only 10% at $22.0 < r < 22.5$, see § 5.3), and the bright limit was $r > 15.5$; (3) In Run I we did not use the mid-z selection box in the first panel of Figure 5.3 ($r < 20.0$), which means that we missed bright mid-z quasars in Run I; (4) We did not use the KDE method to obtain an independent candidate sample. Therefore the selection efficiencies and incompleteness are different for the two runs, and we will correct their incompleteness separately.

5.2.2.2   High-z candidates

The color selection of high-z quasar candidates in the SDSS color space is well studied in a series of papers by Fan et al. (1999, 2000b, 2001a). Similar to Richards

et al. (2002), we define three regions for high-z quasars in ugr, gri, riz color space. They are used to recover quasars at $z > 3.0$, 3.6, and 4.5 respectively. When $z > 3.7$, the Lyα line enters the r band, so the selection of high-z candidates is based on the i magnitude and down to $i = 22.5$. Again, we use slightly different selection criteria for different i magnitude ranges, due to increasing photometric errors with decreasing brightness.

5.3   Observation and Data Reduction

5.3.1   Spectroscopic observation and data reduction

The spectroscopic survey of faint quasars was carried out with the 6.5m MMT with Hectospec (Fabricant et al., 2005). Hectospec is a multiobject optical spectrograph with 300 fibers, and a 1° field of view. With a 300 line mm^{-1} grating, Hectospec covers a wavelength range of 3700 to 9200 Å at a moderate resolution of ~ 6 Å. This is sufficient to measure the redshifts of quasars at any redshift lower than 6, and provide robust line-width measurement.

Simultaneously with the faint quasar survey, we also conducted a spectroscopic survey of luminous early-type galaxies in the same SDSS fields. The early-type galaxy survey is described in detail in Cool et al. (2006). We divided Hectospec fibers equally between quasar and galaxy targets. For each configuration, 30 sky fibers and 5 F subdwarf standard stars were used for calibration, and approximately 130 fibers were used to target quasar candidates. In 2004, five Hectospec fields in Runs I and II were observed. The central position and exposure time for each field are given in Table 5.1.

The Hectospec data were reduced using HSRED, an IDL package developed for the reduction of data from the Hectospec (Fabricant et al., 2005) and Hectochelle (Szentgyorgyi et al., 1998) spectrographs on the MMT, and based heavily on the reduction routines developed for processing of SDSS spectra.

Initially, the two dimensional images are corrected for cosmic ray contamination using the IDL version of L.A. Cosmic (van Dokkum, 2001) developed by J. Bloom.

Table 5.1. Central positions and exposure time for the 5 Hectospec fields

	Date[a]	RA(J2000)	Dec(J2000)	t_{exp}(min)
Run I	Jun 13	$21^h34^m00\overset{s}{.}0$	$00°06'00\overset{''}{.}0$	100
	Jun 15	$21^h34^m00\overset{s}{.}0$	$00°06'00\overset{''}{.}0$	100
	Jun 20	$21^h30^m00\overset{s}{.}0$	$00°06'00\overset{''}{.}0$	100
Run II	Nov 09	$23^h16^m00\overset{s}{.}0$	$-00°06'00\overset{''}{.}0$	120
	Nov 11	$23^h40^m00\overset{s}{.}0$	$-00°06'00\overset{''}{.}0$	180
	Nov 13	$02^h04^m00\overset{s}{.}0$	$-00°06'00\overset{''}{.}0$	80
	Nov 19	$02^h04^m00\overset{s}{.}0$	$-00°06'00\overset{''}{.}0$	120

[a]Dates in 2004

The 300 fiber trace locations are determined using dome flat spectra obtained during the same night as each observation; the CCD fringing and high frequency flat fielding variations are also removed using these dome flats. On nights when twilight images are obtained, these spectra are used to define a low-order correction to the flat field vector for each fiber.

Each configuration generally includes approximately 30 fibers located on blank regions of the sky. Using the bright sky lines in each spectrum, we adjust the initial wavelength solution, determined from HeNeAr comparison spectra, to compensate for any variations throughout the night. These sky lines are used further to determine any small amplitude multiplicative scale offset for each fiber, occurring due to small variations in the relative transmission differences between fibers not fully corrected using the flat-field spectra, before the median sky spectrum is subtracted.

The data are fluxed using SDSS calibration stars observed on the same configuration as the objects of interest. These F stars are cross-correlated against a grid of Kurucz (1993) model atmospheres to determine the best fit stellar spectrum. SDSS

photometry of the standard stars is then used to determine the absolution normalization of the standard star spectrum. The ratio of this master spectrum and the observed count rate is used to construct the fluxing vector for each exposure. After each exposure is extracted, corrected for heliocentric motion and flux calibrated, the spectra are de-reddened according galactic dust maps (Schlegel, Finkbeiner, & Davis, 1998) with the O'Donnell (1994) extinction curve. Finally, multiple exposures of a single field are combined to obtain the final spectrum. After 180 minute exposure on a $g = 22.0$ object, the typical signal-to-noise ratio at ~ 5000 Å reaches ~ 7 per pixel.

Redshifts are determined using programs available in the IDLSPEC2D package of IDL routines developed for the SDSS. For each observed spectrum, the best fit spectral template and redshift are obtained from a number of quasar, galaxy, and star spectra using χ^2 fits. The Hectospec has sufficient wavelength coverage for reliable redshift measurement. The success rate is better than 90% for $g < 22.0$. After the automatic identification, each redshift is examined by eye to guard against failed redshifts or misclassifications. Quasar identification is not easy for faint candidates with $g > 22.0$, especially when they also have weak emission lines. We correct the fraction of unidentifiable objects statistically.

As we mentioned in § 5.2.2, the quasar candidate density in the sky is set to be $\sim 15\%$ larger than the fiber density used for quasar survey, so we did not observe all candidates in the fields. We will correct the incompleteness arising from this fact in § 5.4.1.

5.3.2 Faint quasar sample

The preliminary sample of the SFQS consists of 414 quasars from 5 Hectospec fields (~ 3.9 deg^2). The sample has a redshift range from 0.32 to 4.96, with 119 objects at $z > 2.0$ and 23 objects at $z > 3.0$. The median value of the redshifts is 1.72, greater than the median redshift 1.47 in the SDSS DR3 (Schneider et al., 2005). Most of the non-quasar candidates are star-forming galaxies, A stars, and white dwarfs (WDs). For example, in Run II, non-quasar candidates consist of $\sim 40\%$
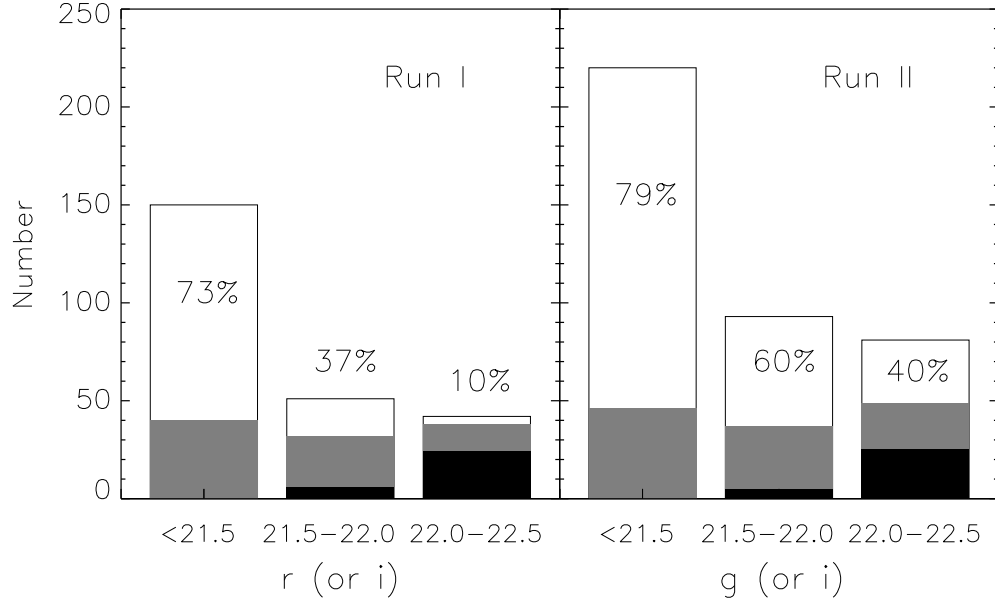
Figure 5.4 The numbers of candidates observed and the selection efficiencies in the two runs. The black areas are spectroscopically unidentifiable objects, the gray areas are identified as non-quasars, and the blank regions are identified as quasars. The fractions of quasars are also given within or above the bars. Note that i magnitude is used for high-z ($z \geq 3$) candidates.

star-forming galaxies, $\sim 30\%$ A or early type stars, $\sim 20\%$ WDs (including M star-WD pairs), and $\sim 10\%$ M or late type stars. Most of the A stars are from the mid-z quasar selection. The loci of these contaminant objects in color-color space, and why they are selected as quasar candidates are well addressed in Fan (1999) and Richards et al. (2002).

Figure 5.4 illustrates the numbers of candidates observed and the selection efficiencies in the two runs. In Figure 5.4, the black areas are unidentifiable objects, the gray areas are identified as non-quasars, and the blank regions are identified as quasars. The fractions of quasars are also given within or above the bars. The total selection efficiency in Run II is $\sim 66\%$, and the efficiency at $g < 21.5$ is as high as 79%. Much of the low efficiency is produced by the mid-z candidates, where the total efficiency and the efficiency at $g < 21.5$ are 43% and 35%, respectively. In Run I, the selection efficiency at $r > 22.0$ is only 10%. The average epoch number N_{epoch}
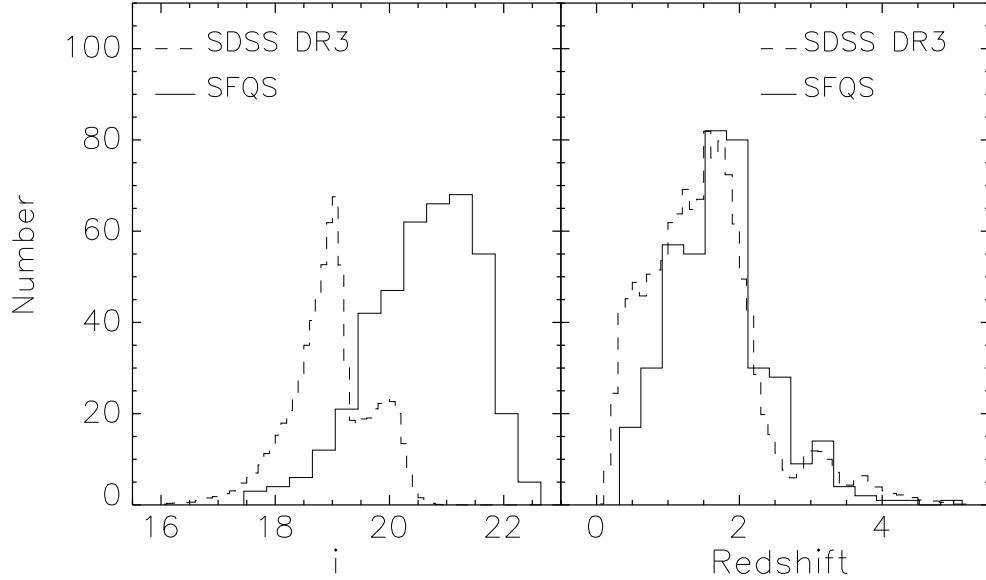
Figure 5.5 The i magnitude and redshift distributions of the SFQS sample compared with the SDSS main survey. The dashed profiles are from the SDSS DR3 (Schneider et al., 2005), and have been scaled to compare with our survey.

of the data in Run I is 7.4, smaller than 13.0 in Run II, so the photometric errors are relatively larger, and the quasar selection is thus less efficient. Due to the low efficiency at $r > 22.0$, the quasar selection in Run I is only complete to $r = 22.0$. In Run II, the quasar selection probes to $g = 22.5$. Note that for a quasar with a power-law continuum slope of -0.5 (see § 5.3.3), its g magnitude is fainter than its r magnitude by 0.15. We also improved the selection criteria in Run II based on Run I (see § 5.2.2), so the selection efficiency in Run II was increased.

Figure 5.5 gives the i magnitude and redshift distributions of the SFQS sample. The dashed profiles are from the SDSS DR3 (Schneider et al., 2005), and have been scaled to compare with our survey. The SFQS sample is about $2 \sim 3$ magnitudes fainter than the SDSS main survey as we see in the left panel. In the right panel, our survey peaks at a similar redshift $z \sim 1.6$ to the SDSS main survey, but contains a larger fraction of $2 < z < 3$ quasars due to our more complete selection of quasar candidates in this redshift range. There is a small dip at $z \approx 2.7$. It may be caused by the fact that we missed bright mid-z quasars in Run I.
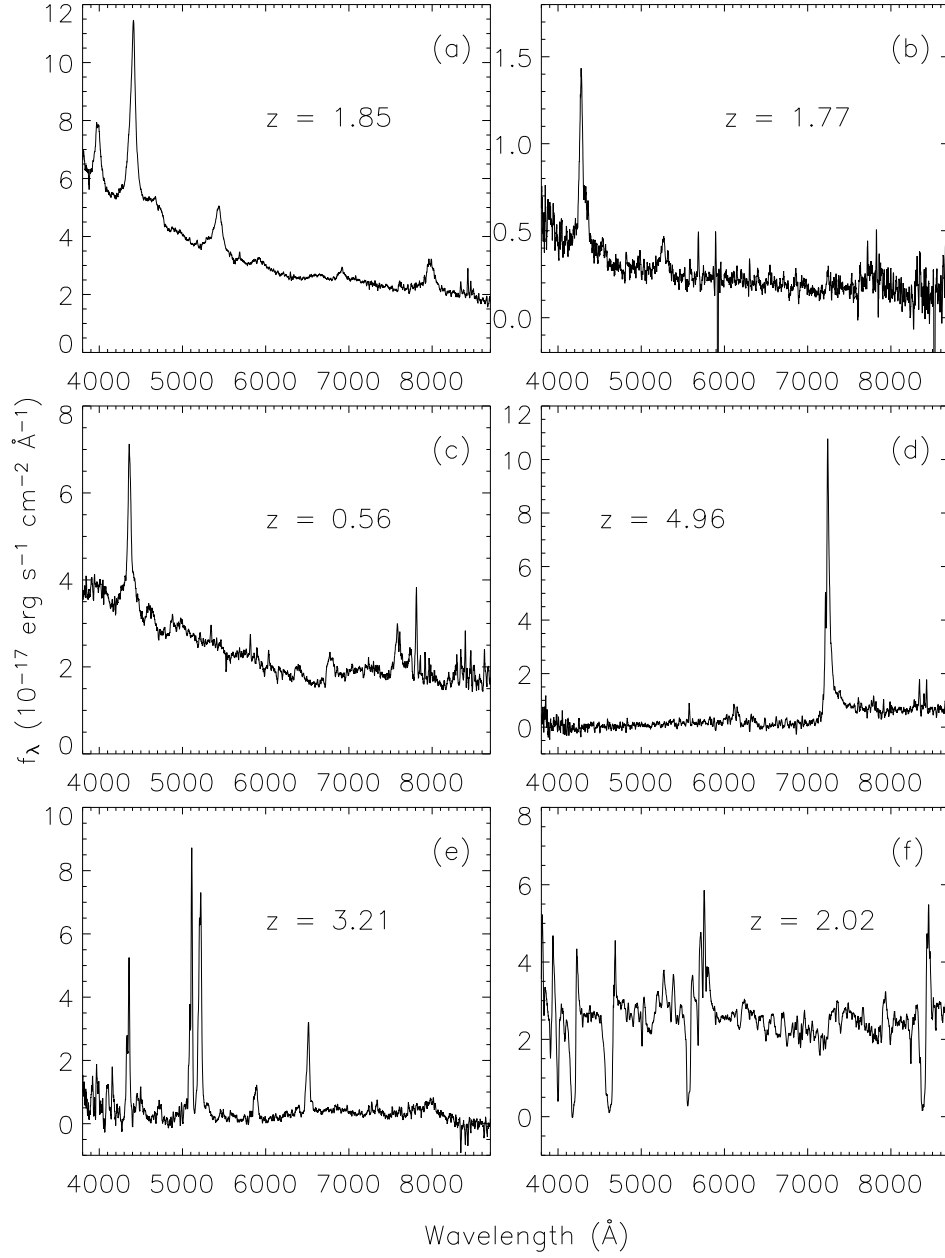
Figure 5.6 Six sample spectra obtained by MMT/Hectospec. The spectra are binned by 11 pixels. The redshift of each quasar is also given in the figure.

Figure 5.6 shows six sample spectra obtained by our survey: (a) A typical bright quasar with $g = 20.11$; (b) A typical faint quasar with $g = 22.36$; (c) A typical low-z quasar at $z = 0.56$; (d) The most distant quasar observed in the two runs at $z \sim 5$; (e) A high-z quasar with a broad CIII] emission line and a series of narrow emission lines such as Lyα, and CIV. (Zakamska et al., 2003); (f) A broad absorption line quasar at $z = 2.02$.

Table 5.2 presents the quasar catalog of the SFQS. Column 1 gives the name of each quasar, and column 2 is the redshift. Column 3 and 4 list the apparent magnitude g and the rest-frame absolute magnitude M_g. The slope α of the power-law continuum for each quasar is given in column 5. Measurements of M_g and α are discussed in the next subsection. The full Table 5.2 is in the APPENDIX A.

5.3.3 Determination of continuum properties

We determine the continuum properties for each quasar using the observed spectrum and the SDSS photometry. Hectospec gives spectra from ~ 3700 to ~ 9200 Å; however, at the faint end of the sample, the observed spectra have low signal-to-noise ratios and could be strongly effected by errors in flux calibration or sky subtraction. The accurate broadband photometry of the SDSS provides us an alternative way to determine the continuum properties from both the observed spectrum and the SDSS photometry (Fan et al., 2001c). For a given quasar, we obtain the intrinsic spectrum by fitting a model spectrum to the broadband photometry. The model spectrum is a power-law continuum plus emission lines. For the power-law continuum $f_\nu = A \times \nu^\alpha$, we do not assume a uniform slope $\alpha = -0.5$, instead, we determine the slope and the normalization A for each quasar. To obtain model emission lines, we measure the strength of the observed emission line with the highest signal-to-noise ratio. The strengths of other emission lines are determined using the line strength ratios from the composite spectrum given by Vanden Berk et al. (2001).

The SDSS magnitudes m^{model} for the model spectrum are directly calculated from the model spectrum itself. Then α and A are determined by minimizing the

Table 5.2. Quasar sample for the SFQS survey

Name (J2000 Coordinates)	Redshift	g	M_g	α
SDSS J231601.68−001237.0	2.00	21.69	-23.08	-0.23
SDSS J231548.40−003022.7	1.53	20.73	-23.60	-0.44
SDSS J231527.54−001353.8	1.33	20.97	-23.26	-0.54
SDSS J231541.51−003137.2	1.72	21.73	-22.61	-0.31
SDSS J231422.26+000315.7	3.22	21.38	-24.05	0.10
SDSS J231442.27−000937.2	3.30	21.09	-25.26	-0.49
SDSS J231534.22−002610.0	0.58	21.29	-21.02	-1.07
SDSS J231519.33−001129.5	3.06	22.17	-24.47	-1.10
SDSS J231504.04−001434.2	2.10	22.17	-23.05	-0.41
SDSS J231446.30−002206.9	2.97	21.97	-24.12	-0.69

Note. — The full table is given in APPENDIX A. The typical errors for a $g = 21.0$ quasar at $z = 2.0$ are, $\sigma_z < 0.01$, $\sigma_{M_g} = 0.08$, and $\sigma_\alpha = 0.15$.

differences between the model magnitudes m^{model} and the SDSS photometry m^{obs},

$$\chi^2 = \sum(\frac{m_i^{model} - m_i^{obs}}{\sigma_i^{obs}})^2, \tag{5.3}$$

where σ_i^{obs} is the SDSS photometry error. We fix the value of α in the range of $-1.1 < \alpha < 0.1$. In Equation 5.3, we only use the bands that are not dominated by Lyα absorption systems. With the information of intrinsic spectra and redshifts, we calculate the absolute magnitudes. The slope α and absolute magnitude M_g are given in Table 5.2.

5.4 Optical Luminosity Function of Faint Quasars

In this section, we correct for the photometric, coverage, and spectroscopic incompleteness and the morphology bias. We then use the traditional $1/V_a$ method (Avni & Bahcall, 1980) to derive a binned estimate of the luminosity function for the SFQS sample and model the luminosity function using maximum likelihood analysis.

5.4.1 Completeness corrections

The photometric incompleteness arises from the color selection of quasar candidates. It is described by the selection function, the probability that a quasar with a given magnitude, redshift, and intrinsic spectral energy distribution (SED) meets the color selection criteria (e.g. Fan et al., 2001c). By assuming that the intrinsic SEDs have certain distributions, we can calculate the average selection probability as a function of magnitude and redshift. To do this, we first calculate the synthetic distribution of quasar colors for a given (M_g, z), following the procedures in Fan (1999), Fan et al. (2001c) and Richards et al. (2006b). Then we calculate the SDSS magnitudes from the model spectra and incorporate photometric errors into each band. For an object with given (M_g, z), we generate a database of model quasars with the same (M_g, z). The detection probability for this quasar is then the fraction of model quasars that meet the selection criteria.

Figure 5.7 gives the selection probabilities as the function of M_g and z in the two runs. The contours are selection probabilities from 0.2 to 0.8 with an interval

of 0.2, and heavy lines (probability = 0.2) illustrate the limiting magnitudes. The solid circles are the locations of sample quasars. The two selection functions are different due to the different color selection criteria used. The striking difference is the detection probabilities in the mid-z range, where quasars are difficult to select by their SDSS colors. In Run I, the probabilities in the mid-z range are very low for luminous quasars. But in Run II, the selection in this range is greatly improved. This makes an almost homogeneous selection from $z = 0$ to $z > 5$. Due to this improved selection, we are able to correct for the incompleteness down to $M_g = -22.0$, -23.0, -24.0 at $z < 2$, $z < 3$, and $z < 4$, respectively.

The second incompleteness is the coverage incompleteness, which comes from the fact that we did not observe all candidates in the fields due to the limited fiber density of Hectospec. To correct this effect, we assume that the selection efficiency of unobserved candidates is the same as that of observed ones.

The third incompleteness, spectroscopic incompleteness, comes from the fact that we cannot identify some faint candidates due to their weak flux observed on Hectospec. To correct this incompleteness, we assume that unidentifiable candidates have the same selection efficiency of identified ones with the same magnitudes. From the two runs we know that, with the capacity of Hectospec and the integration time of ~ 180 minutes, the emission lines of a typical broad-line quasar with $g \sim 22.5$ should be visible in the Hectospec spectra, so unidentifiable candidates are either weak-line quasars, or not quasars. Therefore this correction may give an upper limit.

Another incompleteness arises from the morphology bias. The candidates we observed are point sources, but faint point sources could be mis-classified as extended sources by the SDSS photometric pipeline (e.g. Scranton et al., 2002). The best way to correct this incompleteness is to observe a sample of extended sources that satisfy our selection criteria, and find the fraction of quasars among them. The definition of star-galaxy classification in the SDSS photometric pipeline gives us an alternative way. In the SDSS photometric pipeline, an object is defined as a *galaxy* (extended object) if $psfMag - cmodelMag > 0.145$, where $psfMag$ is the PSF magnitude, and $cmodelMag$ is the composite model magnitude determined from the best-fitting
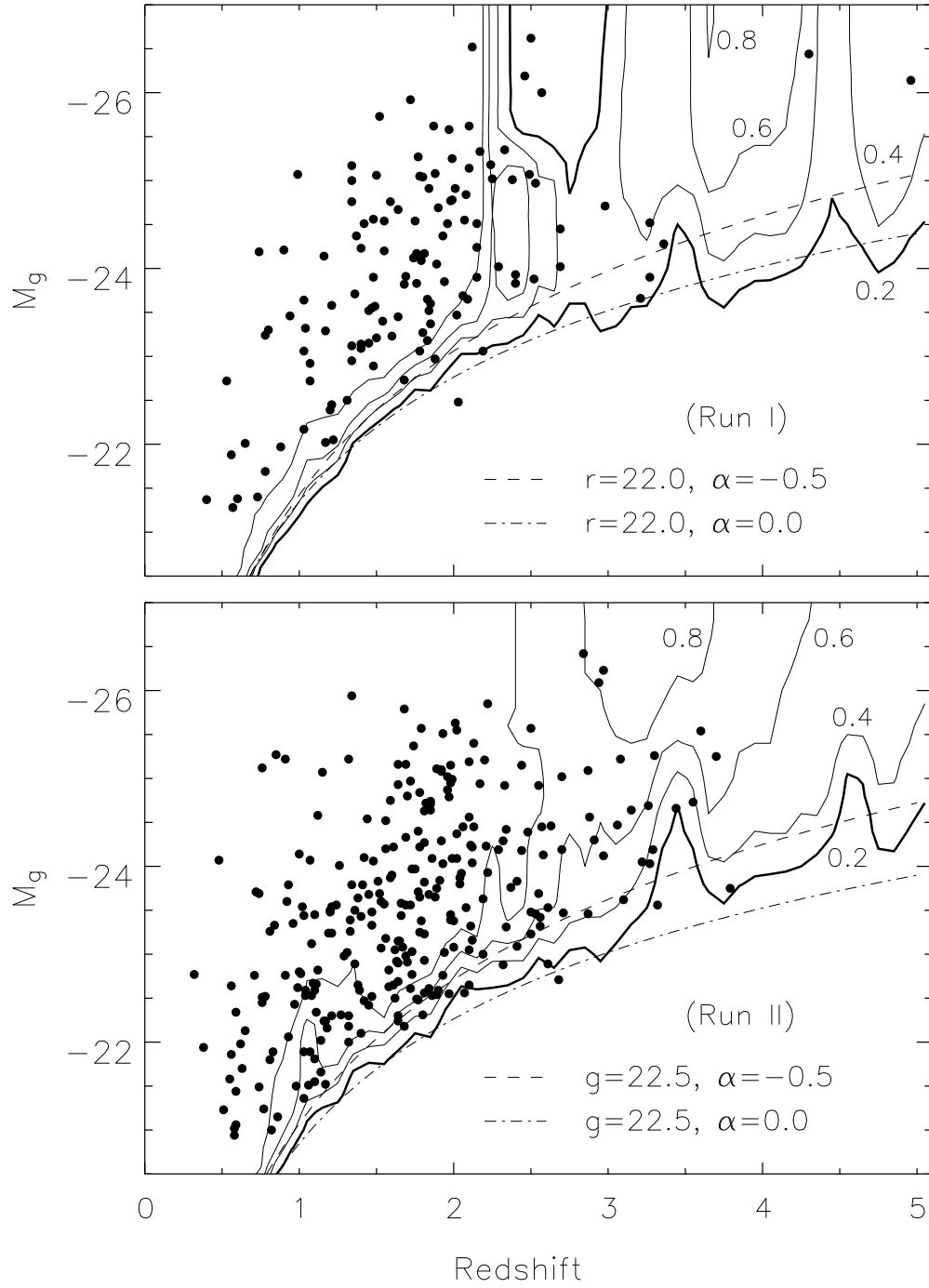
Figure 5.7 Selection function of faint quasars as a function of M_g and z. The contours are selection probabilities from 0.2 to 0.8 with an interval of 0.2. The solid circles are the locations of quasars in our sample. Heavy lines (probability = 0.2) illustrate the limiting magnitudes.

linear combination of the best-fitting de Vaucouleurs and exponential model for an object's light profile (Abazajian et al., 2004). Similar to Scranton et al. (2002), we define the difference between $psfMag$ and $cmodelMag$ as *concentration*. To correct the morphology bias, we plot the *concentration* distribution vs. object counts as shown in Figure 5.8, where the dash-dotted lines separate *stars* and *galaxies* by definition. At $g > 22.0$, the star locus and the galaxy locus begin to mix heavily, and the objects near the separation lines may be mis-classified. To estimate the real numbers of point and extended sources, we use double Gaussians to fit each component of the *star* and *galaxy* loci as shown in the figure. Then the fraction of point sources misclassified as extended ones are obtained from the best fits. They are 10% for $22.0 < g < 22.2$, 24% for $22.2 < g < 22.4$, and 31% for $22.4 < g < 22.5$.

In Run I and Run II we only select point sources. Although we have corrected the morphology bias, our sample could still be biased by not including objects in which the host galaxies are apparent. So the low-z QLF at the faint end may be affected by quasar host galaxies. We plan to observe a sample of extended sources, and correct the morphology bias and the effect of host galaxies in the next observing run.

5.4.2 $1/V_a$ estimate and maximum likelihood analysis

We derive a binned estimate of the luminosity function for the SFQS sample using the traditional $1/V_a$ method (Avni & Bahcall, 1980). The available volume for a quasar with absolute magnitude M and redshift z in a magnitude bin ΔM and a redshift bin Δz is

$$V_a = \int_{\Delta M} \int_{\Delta z} p(M, z) \frac{dV}{dz} dz dM, \tag{5.4}$$

where $p(M, z)$ is a function of magnitude and redshift and used to correct sample incompleteness. Then the luminosity function and the statistical uncertainty can be written as

$$\Phi(M, z) = \sum \frac{1}{V_a^i}, \quad \sigma(\Phi) = \left[\sum (\frac{1}{V_a^i})^2 \right]^{1/2}, \tag{5.5}$$
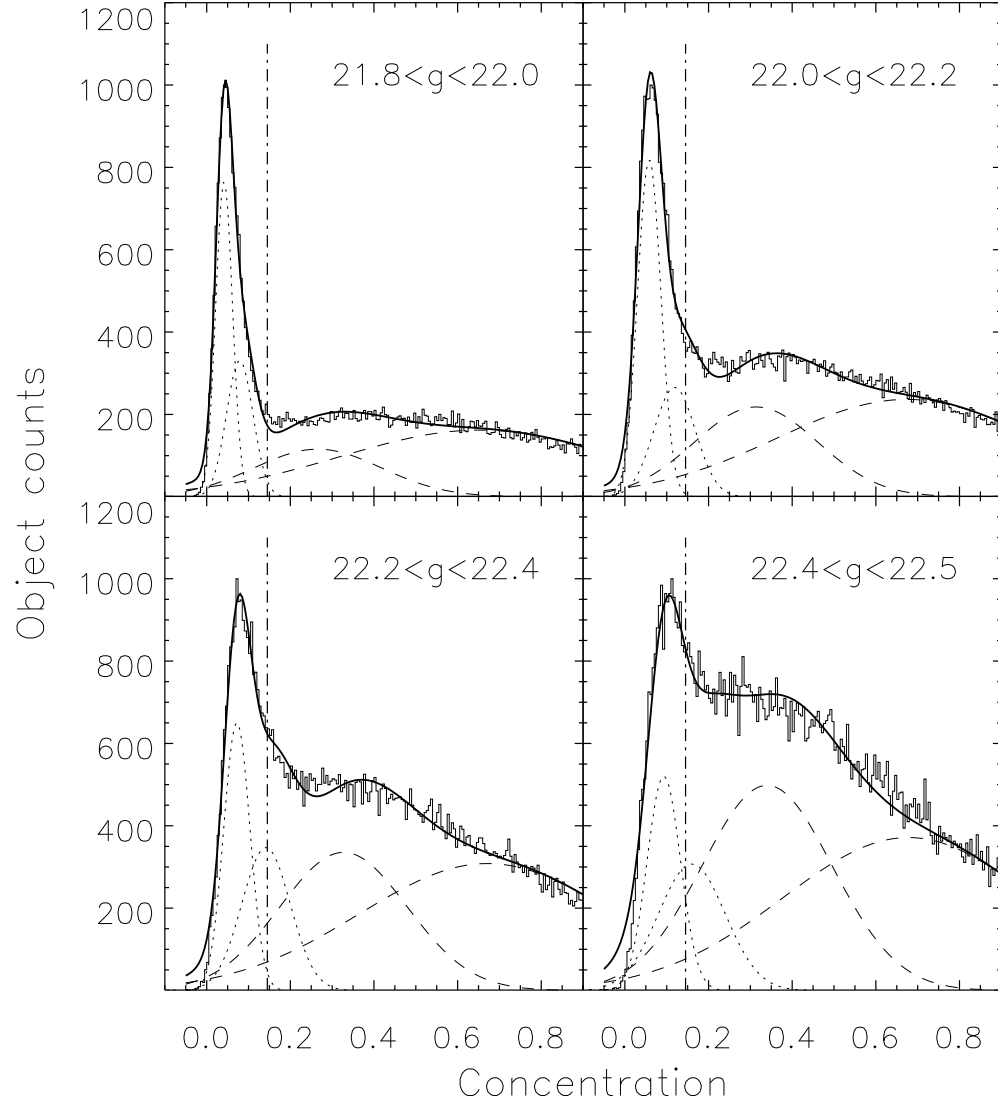
Figure 5.8 Correction for the morphology bias. The vertical dot-dashed lines separate *stars* and *galaxies* by the definition of the SDSS photometric pipeline. Dotted and dashed lines are the best fits of the double Gaussian components of *stars* and *galaxies*, respectively. Solid lines are the sum of all components.

where the sum is over all quasars in the bin. This is essentially the same as the revised $1/V_a$ method of Page & Carrera (2000), since $p(M, z)$ has already corrected the incompleteness at the flux limits.

The QLF derived from the $1/V_a$ estimate is shown in Figure 5.9, which gives the QLF from $z = 0.5$ to 3.6, with a redshift interval of $\Delta z \approx 0.5$. In each redshift bin, the magnitude bins are chosen to have exactly the same numbers of quasars except the brightest one. Solid symbols represent the QLF corrected for all four incompletenesses in § 5.4.1, and open symbols represent the QLF corrected for all incompletenesses except the spectroscopic incompleteness. Our sample contains two subsamples from Run I and Run II. The two subsamples are weighted by their available volumes in each magnitude-redshift bin when combined. In Run I, the selection efficiency at $r > 22.0$ is only 10%, so we do not include the quasars of $r > 22.0$ in the $1/V_a$ estimate. We also exclude the Run I quasars in the brightest bins at $2.0 < z < 3.0$, due to the low selection completeness in this range.

Our sample contains a small fraction of luminous quasars. By comparing the SFQS QLF with the results of the 2QZ, 2SLAQ, and SDSS (see Figure 5.11 and Figure 5.12 in § 5.5.3), one can see that the QLF has steep slopes at the bright end (from the 2QZ, 2SLAQ, or SDSS) and much flatter slopes at the faint end (from the SFQS), clearly showing a break in the QLF, thus we will use the double power-law form to model the QLF. At $z > 2.0$, quasars show strong density evolution. A double power-law QLF with density evolution requires at least six parameters, however, this sample is not large enough to determine so many parameters simultaneously. Therefore we break the sample to two subsamples, $0.5 < z < 2.0$ and $2.0 < z < 3.6$, and use fewer free parameters to model them separately, based on reasonable assumptions. We will model the low-z and high-z quasars simultaneously when we obtain more than 1000 quasars in the future.

5.4.2.1   QLF at $0.5 < z < 2.0$

As the first step, we try a single power-law form $\Phi(L) \propto L^\beta$ to model the observed QLF. The slope β determined from the best fit is -1.40, much flatter than the
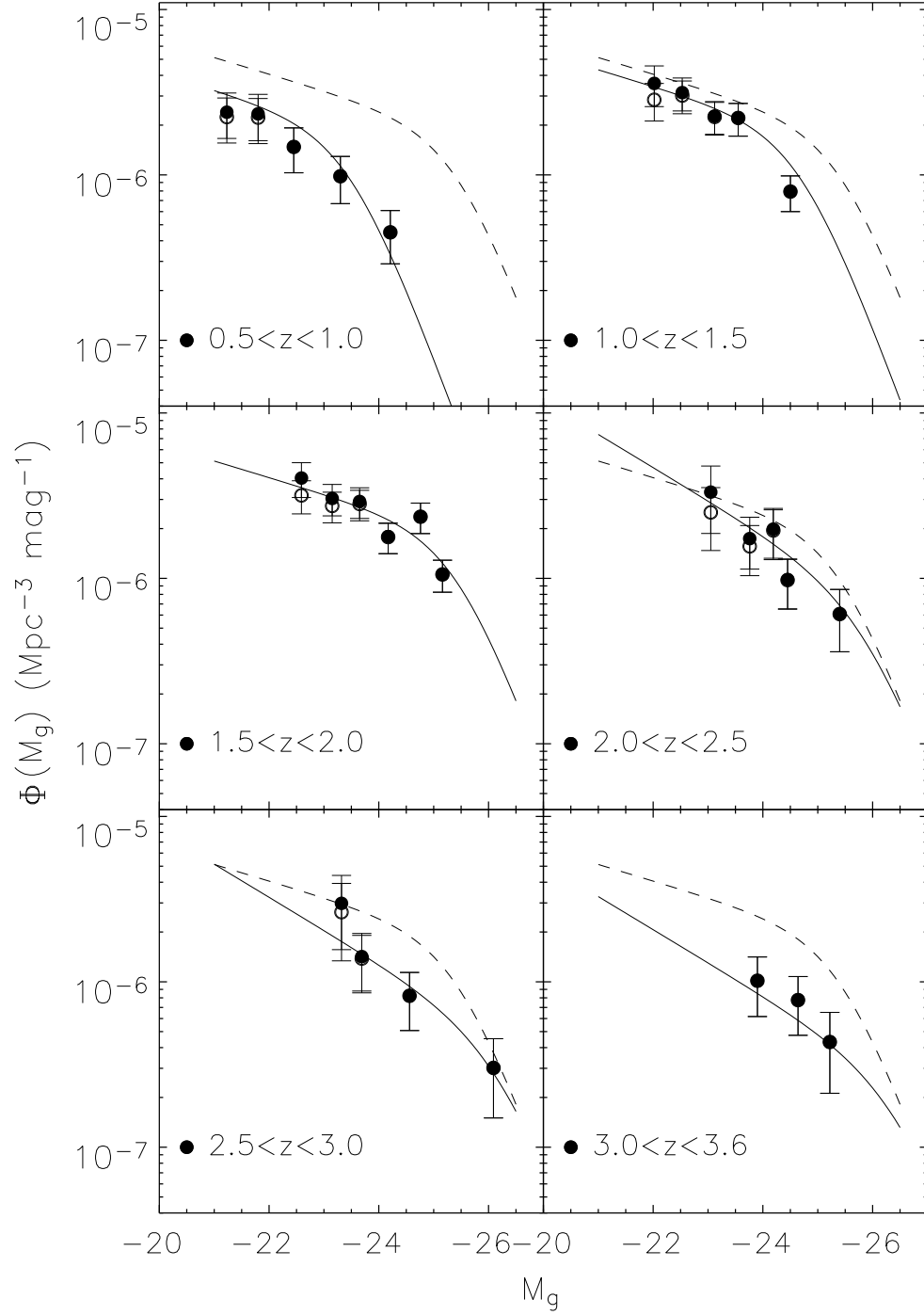
Figure 5.9 QLF derived from the traditional $1/V_a$ method. Solid circles represent the QLF corrected for all four incompletenesses in § 5.4.1, while open circles represent the QLF corrected for all incompletenesses except the spectroscopic incompleteness. Solid lines are the best model fits from § 5.4.2. For comparison, the dashed line is the best model fit of the QLF at $1.5 < z < 2.0$.

bright-end slopes $(-3.0 \sim -3.5)$ of the QLFs from the 2QZ (Boyle et al., 2000; Croom et al., 2004), SDSS (Richards et al., 2006b), and 2SLAQ (Richards et al., 2005). This confirms the existence of the break in the slope. We also use the single power-law form to model the three individual redshift bins. The best fit slopes at $0.5 < z < 1.0$, $1.0 < z < 1.5$, and $1.5 < z < 2.0$ are $-1.45^{+0.2}_{-0.3}$, $-1.40^{+0.1}_{-0.2}$, and $-1.35^{+0.1}_{-0.2}$, respectively. They are consistent within 1σ level, so there is no strong evolution in the slope at the faint end.

To characterize the QLF at $0.5 < z < 2.0$, we use the double power-law form with PLE, which expressed in magnitudes is,

$$\Phi_L(M_g, z) = \frac{\Phi(M_g^*)}{10^{0.4(\alpha+1)(M_g - M_g^*(z))} + 10^{0.4(\beta+1)(M_g - M_g^*(z))}}. \tag{5.6}$$

In the case of PLE models, the evolution of the characteristic magnitude $M_g^*(z)$ can be modeled as different forms, such as a second-order polynomial evolution $M_g^*(z) = M_g^*(0) - 2.5(k_1 z + k_2 z^2)$, an exponential form $M_g^*(z) = M_g^*(0) - 1.08k\tau$, where τ is the look-back time, or, a form of $M_g^*(z) = M_g^*(0) - 2.5k(1 + z)$ (e.g. Boyle et al., 2000; Croom et al., 2004). Croom et al. (2004) has shown that low-z QLF can be well fit by both second-order polynomial or exponential evolution in the Λ cosmology. In this chapter the quasar sample is still small, so we do not fit all models and justify their validity; instead, we take the exponential form, which uses fewer parameters.

We use maximum likelihood analysis to find the best fits. The likelihood function (e.g. Marshall et al., 1983; Fan et al., 2001c) can be written as

$$S = -2 \sum ln[\Phi(M_i, z_i)p(M_i, z_i)] + 2 \int \int \Phi(M, z)p(M, z)\frac{dV}{dz}dzdM, \tag{5.7}$$

where the sum is over all quasars in the sample. Our sample does not contain enough bright objects, which makes it difficult to determine the slope at the bright end. We thus fix the bright-end slope to the value of $\alpha = -3.25$ given by Croom et al. (2004). The best fits are, $\alpha = -3.25$ (fixed), $\beta = -1.25^{+0.10}_{-0.15}$, $k = 7.50^{+0.40}_{-0.35}$, $M_g^*(0) = -19.50^{+0.40}_{-0.35}$, and $\Phi(M_g^*) = 1.84 \times 10^{-6}$ Mpc^{-3} mag^{-1}. The χ^2 of this fit is 15.0 for 15 degrees of freedom by comparing the $1/V_a$ estimate and the model

prediction. The solid lines in Figure 5.9 are the best model fits. For comparison, the dashed lines are the best fit at $1.5 < z < 2.0$. One can see that the density of quasars increases from $z = 0.5$ to 2.0, then decreases at higher redshift.

As stated in § 5.4.1, the correction of the spectroscopic incompleteness may only provide an upper limit. In Figure 5.9, solid symbols represent the QLF corrected for all four incompleteness in § 5.4.1, and open symbols represent the QLF corrected for all incompleteness except the spectroscopic incompleteness. One can see that the spectroscopic incompleteness only affects the faintest bins. The best model fit shows that, without the correction for the spectroscopic incompleteness, the slope at $0.5 < z < 2.0$ flattens from $-1.25^{+0.10}_{-0.15}$ to $-1.10^{+0.10}_{-0.15}$. The variation in the slope is within 1σ level.

5.4.2.2 QLF at $2.0 < z < 3.6$

At $z > 2.0$, the QLF cannot be modeled by PLE, and density evolution is needed. We add a density evolution term $\rho_D(z)$ into the double power-law form to model the QLF at $z > 2.0$. The double power-law model with density evolution expressed in magnitudes is,

$$\Phi_H(M_g, z) = \frac{\Phi(M_g^*)\rho_D(z)}{10^{0.4(\alpha+1)(M_g - M_g^*(z))} + 10^{0.4(\beta+1)(M_g - M_g^*(z))}}, \tag{5.8}$$

where we take the exponential form for the evolution of characteristic magnitude $M_g^*(z)$ as we do for $z < 2$, and take an exponential form of $\rho_D(z) = 10^{-B(z-2)}$ for the density evolution at a given magnitude (e.g. Schmidt, Schneider, & Gunn, 1995; Fan et al., 2001c). The single power-law model with density evolution shows that the QLF at $2.0 < z < 3.6$ has a slope of -1.70, flatter than the bright-end slopes $(-2.5 \sim -3.5)$ from the COMBO-17 (Wolf et al., 2003), SDSS (Richards et al., 2006b) and Fan et al. (2001c). This indicates the existence of the break in the QLF at $2.0 < z < 3.6$.

We use the double power-law form with density evolution to model the observed QLF at $2.0 < z < 3.6$. As we do for $z < 2.0$, we fix the bright-end slope α as -3.25. The parameters k and $M_g^*(0)$ are also fixed to the values determined from

$0.5 < z < 2.0$. There are three parameters β, B, and $\Phi(M_g^*)$ that we need to derive. $\Phi(M_g^*)$ is not a free parameter, because Equations 6 and 8 must be consistent at $z = 2$. Figure 5.9 shows that, at $M_g \sim -23$, the density at $1.5 < z < 2.0$ and the density at $2.0 < z < 2.5$ are roughly the same. So we connect Equations 6 and 8 through $\Phi_L(M_g = -23, z = 2) = \Phi_H(M_g = -23, z = 2)$. Then $\Phi(M_g^*)$ can be derived from β and B by this relation. We use maximum likelihood analysis to determine the two free parameters β and B as well as $\Phi(M_g^*)$. The best fits are, $\beta = -1.55 \pm 0.20$, $B = 0.45 \pm 0.15$, and $\Phi(M_g^*) = 1.02 \times 10^{-6}$ Mpc^{-3} mag^{-1}. The χ^2 of this fit is 10.4 for 11 degrees of freedom. The solid lines in Figure 5.9 are the best model fits.

Our sample contains only 5 quasars at $z > 3.6$, which is lower than what we expected if the power-law slope of the QLF at $3.6 < z < 5.0$ is $\sim -2.4 \pm 0.2$ (Richards et al., 2006b). This result implies that the faint-end slope of the QLF at $3.6 < z < 5.0$ is also flatter than that at the bright end.

5.5 Discussion

5.5.1 Luminosity-dependent density evolution

It is convenient to show the quasar evolution by plotting the space density as a function of redshift. Our sample spans a large redshift range, covering the mid-z range with good completeness. Figure 5.10 gives the integrated comoving density as the function of z for three magnitude ranges, $M_g < -22.5$, -23.5, and -24.5, respectively. We use the redshift bins from $z = 0.4$ to 3.6 with an interval of $\Delta z = 0.4$. For the bins at $2.2 < z < 3.0$, we exclude quasars with $M_g < -24.5$ in Run I, due to the low selection completeness in this range. We also exclude incomplete bins in Figure 5.10. At low redshift, the space density steadily increases from $z \sim 0.5$ to ~ 2. Then it decreases toward high redshift. The quasar evolution peaks at $z \sim 2$ in the range of $M_g < -22.5$. Solid curves are integrated densities calculated from the best model fits in § 5.4.2, while dotted, dashed and dot-dashed curves represent the integrated densities from the SDSS (Richards et al., 2006b), 2QZ (Boyle et al.,

2000), and Schmidt, Schneider, & Gunn (1995, SSG), respectively. X-ray surveys indicate that X-ray selected quasars and AGNs exhibit so-called "cosmic downsizing": luminous quasars peak at an earlier epoch in the cosmic history than fainter AGNs (e.g. Ueda et al., 2003; Barger et al., 2005; Hasinger, Miyaji, & Schmidt, 2005). We cannot see the cosmic downsizing from the SFQS sample due to the small dynamical range in magnitude and large errors bars. However, the peak of $z \sim 2$ for the SFQS sample is later in cosmic time than the peak of $z \sim 2.5$ found from luminous quasar samples, such as the SDSS (Richards et al., 2006b).

5.5.2 Comparison to other surveys

In this section we compare the SFQS QLF with QLFs derived from the 2QZ (Boyle et al., 2000), SDSS (Richards et al., 2006b), 2SLAQ (Richards et al., 2005), COMBO-17 (Wolf et al., 2003), and CDF (Barger et al., 2005). The survey areas and magnitude limits are sketched in Figure 5.2. Because different surveys use different cosmological models, we convert their QLFs to the QLFs expressed in the cosmological model that we use. First, absolute magnitude M' is converted to M by $M' - M = -5log_{10}\frac{d'_L}{d_L}$, where d'_L and d_L are luminosity distances in different cosmologies. Then magnitudes in different wavebands are converted to M_g in the same cosmology by $M_g = M_\lambda + 2.5\alpha log_{10}\frac{\lambda_g}{\lambda}$, where α is the slope of the power-law continuum, and we assume $\alpha = -0.5$; λ_g and λ are the effective wavelengths of the two different wavebands. Finally spatial density ρ' in a M-z bin is converted to ρ by $\rho = \rho'\frac{V'_a}{V_a}$, where V_a and V'_a are available comoving volumes in the different cosmologies.

Figure 5.11 gives the comparison with the 2QZ (Boyle et al., 2000) and 2SLAQ (Richards et al., 2005) at $0.5 < z < 2.0$. Compared to the 2QZ and 2SLAQ, the SFQS probes to higher redshifts and fainter magnitudes. Solid circles and open triangles in Figure 5.11 are the SFQS QLF and 2SLAQ QLF, respectively. The dotted and dashed lines represent the 2QZ QLF, which is an average QLF calculated using $< \Phi(M,z) >= \frac{\int_{\Delta z}\Phi(M,z)dV}{\int_{\Delta z}dV}$, where $\Phi(M,z)$ is the best-fitting double power-law model with a second-order polynomial luminosity evolution from Boyle et al. (2000). The dashed-line parts are roughly the range that the observed 2QZ QLF
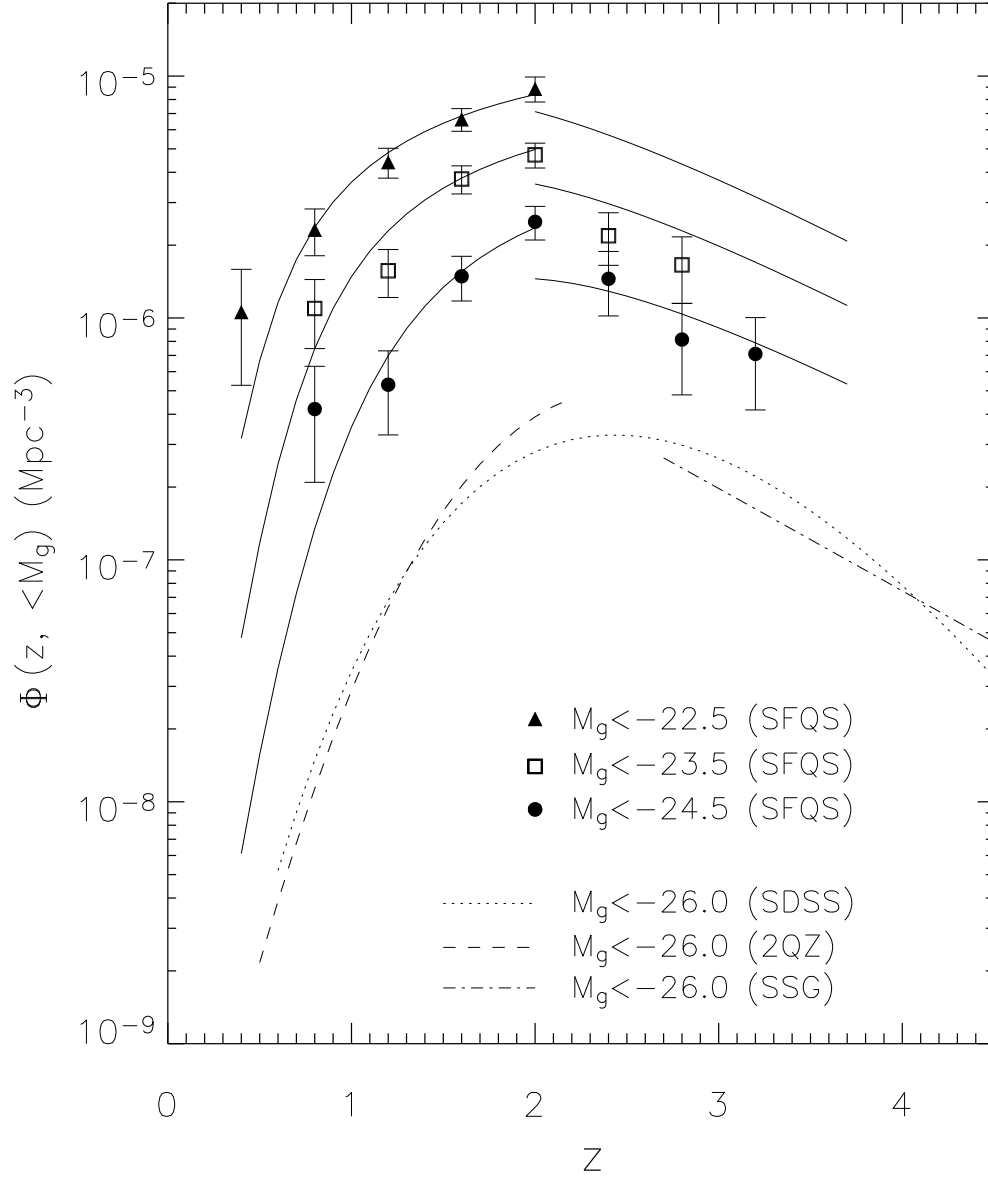
Figure 5.10 Integrated comoving density as a function of z for three magnitude ranges, $M_g < -22.5$, -23.5, and -24.5, respectively. The redshift bins are from $z = 0.4$ to 3.6 with the interval of $\Delta z = 0.4$. We do not include incomplete bins. Solid curves are integrated densities calculated from the best model fits in § 5.4.2, while dotted, dashed and dot-dashed curves are the integrated densities from the SDSS (Richards et al., 2006b), 2QZ (Boyle et al., 2000), and SSG (Schmidt, Schneider, & Gunn, 1995), respectively.

really covered (Boyle et al., 2000). The solid lines are the best model fits of the SFQS QLF. They give a good fit to all three QLFs. At the bright end of the QLF, the SFQS, 2QZ, and 2SLAQ agree well. At the faint end, the 2QZ predicts a higher density and a steeper slope than the SFQS. By combining the deep SFQS with the 2QZ and 2SLAQ, one can see that there is clearly a break in the QLF slope.

Figure 5.12 shows the comparison with the SDSS (Richards et al., 2006b) and COMBO-17 (Wolf et al., 2003) at $0.5 < z < 3.6$. The SDSS is a shallow survey covering a large redshift range. The COMBO-17 survey uses photometric redshifts, and collects quasars in an area of ≤ 1 deg^2. In Figure 5.12, solid circles and open triangles are the SFQS QLF and SDSS QLF, respectively. The dashed lines represent the COMBO-17 QLF, which is an average QLF calculated from the best model fitting of Wolf et al. (2003) using the same method that we did above. The solid lines are the best model fits of the SFQS QLF, and they give a reasonable fit to both SDSS and SFQS QLFs. The SFQS is more than 2 magnitudes deeper than the SDSS, but their QLFs are consistent at all redshifts. The combination of the two QLFs also shows the existence of a break in the slope. At $1.0 < z < 3.6$, the COMBO-17 QLF agrees well with the SFQS QLF, although it has a flatter slope than the SDSS at the bright end.

Figure 5.13 shows the comparison with the CDF survey of quasars and AGNs (Barger et al., 2005). Barger et al. (2005) determine the luminosity functions for both type I and type II AGNs selected from hard X-ray surveys, and find a downturn at the faint end of type I AGN luminosity function. We convert absolute magnitudes and X-ray luminosities to bolometric luminosities using the method given by Barger et al. (2005), and compare the SFQS QLF (solid circles) with the type I AGN hard X-ray luminosity function (open triangles and squares) of Barger et al. (2005) in Figure 5.13. At the bright end of the QLF, the two surveys are consistent at all redshifts. At the faint end, they agree well at $1.5 < z < 2.0$, however, at $0.5 < z < 1.5$, Barger et al. (2005) has significantly higher ($\sim 2\sigma$) densities. One can also see that the SFQS does not probe faint enough to reach the turndown seen by Barger et al. (2005).
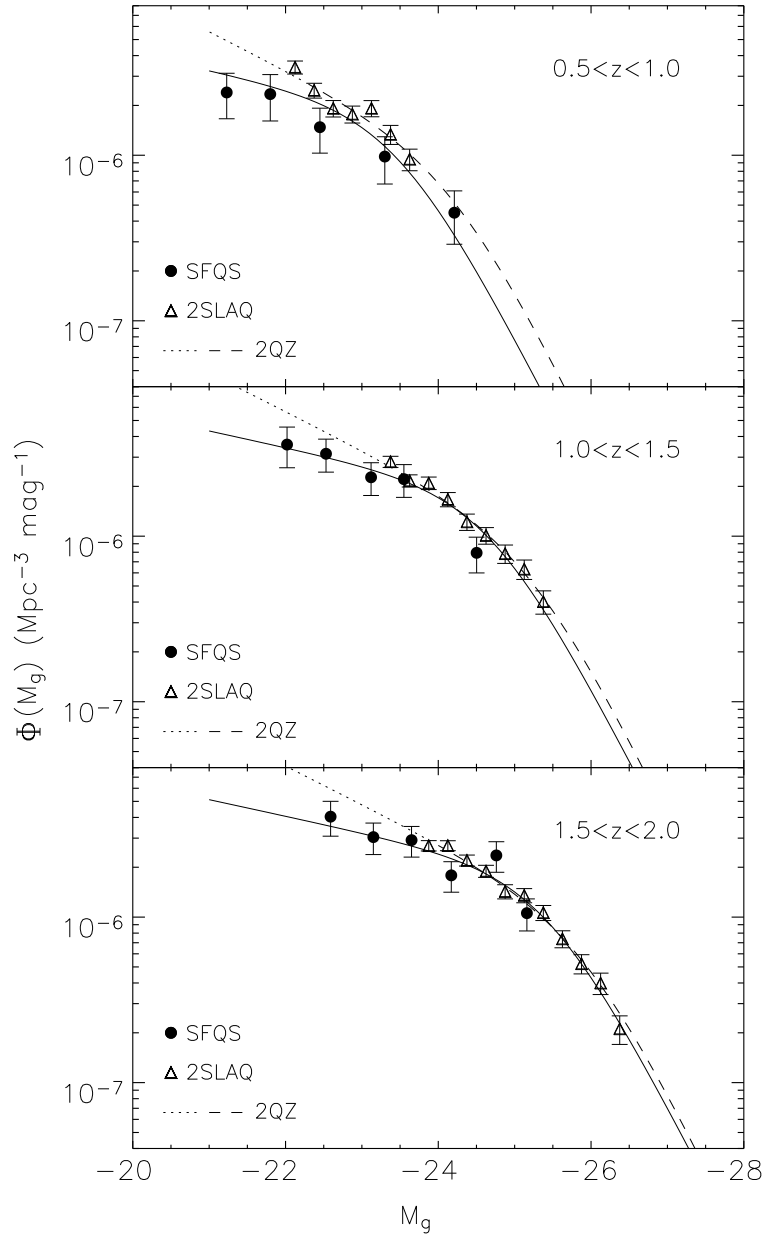
Figure 5.11 Comparison with the 2QZ (Boyle et al., 2000) and 2SLAQ (Richards et al., 2005). Solid circles and open triangles are the SFQS QLF and 2SLAQ QLF, respectively. The dotted and dashed lines represent the 2QZ QLF, calculated from the best model fits of Boyle et al. (2000). The dashed-line parts are roughly the range of luminosity that the observed 2QZ QLF actually covered (Boyle et al., 2000). The solid lines are the best model fits of the SFQS QLF.
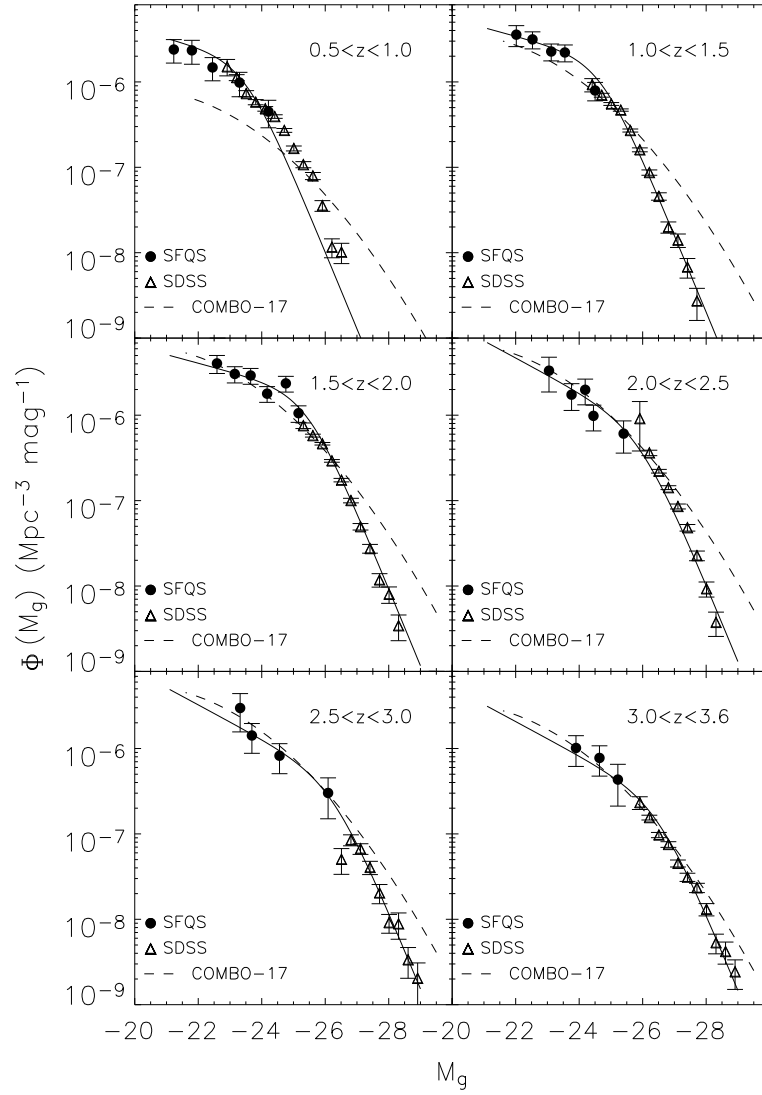
Figure 5.12 Comparison with the SDSS (Richards et al., 2006b) and COMBO-17 (Wolf et al., 2003). Solid circles and open triangles are the SFQS QLF and SDSS QLF, respectively. The dashed lines represent the COMBO-17 QLF, calculated from the best model fits of Wolf et al. (2003). The solid lines are the best model fits of the SFQS QLF.
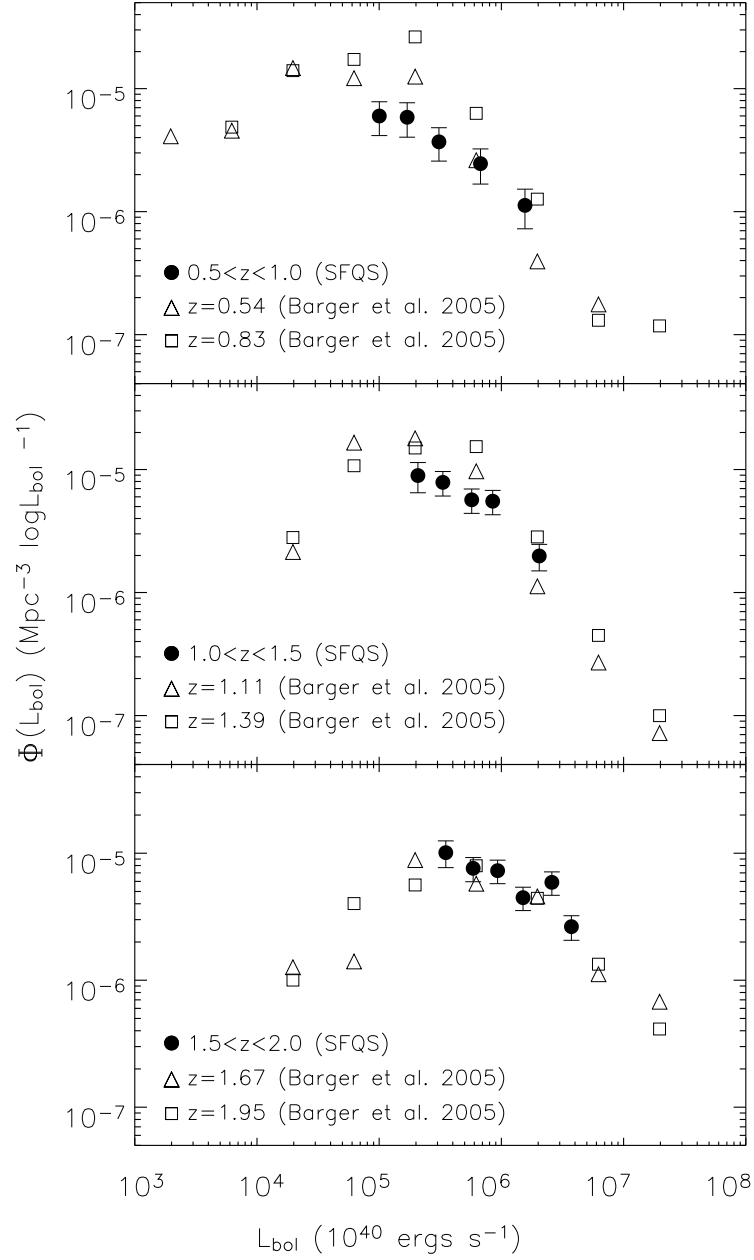
Figure 5.13 Comparison with the CDF survey (Barger et al., 2005). Solid circles represent the SFQS QLF. Open triangles and squares are from Figure 22 of Barger et al. (2005).

5.6   Summary

This chapter presents the preliminary results of a deep spectroscopic survey of faint quasars selected from the SDSS Southern Survey, a deep imaging survey, created by repeatedly scanning a 300 deg^2 area. Quasar candidates are selected from the co-added catalog of the deep data. With an average epoch number $N_{epoch} \sim 13$, the co-added catalog enables us to select much fainter quasars than the quasar spectroscopic sample in the SDSS main survey. We modify SDSS color selection to select quasar candidates, so that they cover a large redshift range at $z < 5$, including the range of $2 < z < 3$ with good completeness. Follow-up spectroscopic observations were carried out on MMT/Hectospec in two observing runs. With the capacity of Hectospec, the selection efficiency of faint quasars in Run II is $\sim 80\%$ at $g < 21.5$, and acceptable at $g > 21.5$ (60% for $21.5 < g < 22.0$ and 40% for $22.0 < g < 22.5$). The preliminary sample of the SFQS contains 414 quasars and reaches $g = 22.5$.

We use the $1/V_a$ method to derive a binned estimate of the QLF. By combining the SFQS QLF with the QLFs of the 2QZ, 2SLAQ, and SDSS, we conclude that there is a break in the QLF. We use the double power-law form with PLE to model the observed QLF at $0.5 < z < 2.0$, and the double power-law form with an exponential density evolution to model the QLF at $2.0 < z < 3.6$. The QLF slopes at the faint end (-1.25 at $0.5 < z < 2.0$ and -1.55 at $2.0 < z < 3.6$) are much flatter than the slopes at the bright end, indicating the existence of the break at all redshifts probed. The luminosity-dependent density evolution model shows that the quasar evolution at $M_g < -23.5$ peaks at $z \sim 2$, which is later in the cosmic time than the peak of $z \sim 2.5$ found from luminous quasar samples.

Our survey is compared to the 2QZ (Boyle et al., 2000), SDSS (Richards et al., 2006b), 2SLAQ (Richards et al., 2005), COMBO-17 (Wolf et al., 2003), and CDF (Barger et al., 2005). The SFQS QLF is consistent with the results of the 2QZ, SDSS, 2SLAQ and COMBO-17. The SFQS QLF at the faint end has a significantly lower density at $0.5 < z < 1.5$ than does the CDF. The preliminary sample of the

SFQS is still small, and statistical errors are large. We plan to obtain more faint quasars from future observations and establish a complete quasar sample with more than 1000 quasars over an area of 10 deg^2.

CHAPTER 6

FRACTION OF RADIO-LOUD QUASARS AS A FUNCTION OF REDSHIFT AND OPTICAL LUMINOSITY

6.1   Introduction

Although quasars were first discovered by their radio emission (e.g. Matthews & Sandage, 1963; Schmidt, 1963), it was soon found that the majority of quasars were radio-quiet (e.g. Sandage, 1965). Quasars are often classified into two broad categories, radio-loud and radio-quiet, based on their radio properties. There is mounting evidence that the distribution of radio-to-optical flux ratio for optically-selected quasars is bimodal (e.g. Kellermann et al., 1989; Miller, Peacock, & Mead, 1990; Visnovsky et al., 1992; Ivezić et al., 2002), although the existence of the bimodality has been questioned (e.g. Cirasuolo et al., 2003, but see also Ivezić et al. (2004a) for a response). Radio-loud and radio-quiet quasars are probably powered by similar physical mechanisms (e.g. Barthel, 1989; Urry & Padovani, 1995), and their radio properties are also correlated with host galaxy properties, central black hole masses, black hole spins, and accretion rates (e.g. Baum et al., 1995; Urry & Padovani, 1995; Best et al., 2005). Radio-loud quasars are likely to reside in more massive galaxies (e.g. Peacock, Miller, & Longair, 1986; Best et al., 2005), and harbor more massive central black holes (e.g. Laor, 2000; Lacy et al., 2001; McLure & Dunlop, 2004), than do radio-quiet quasars.

Roughly 10%−20% of all quasars are radio-loud (e.g. Kellermann et al., 1989; Urry & Padovani, 1995; Ivezić et al., 2002). However, the radio-loud fraction (RLF) of quasars may depend on redshift and optical luminosity. Some studies have found that the RLF tends to drop with increasing redshift (e.g. Peacock, Miller, & Longair, 1986; Miller, Peacock, & Mead, 1990; Visnovsky et al., 1992; Schneider et al., 1992) and decreasing luminosity (e.g. Padovani, 1993; Goldschmidt et al., 1999; Cirasuolo

et al., 2003), or evolves non-monotonically with redshift and luminosity (e.g. Hooper et al., 1995; Bischof & Becker, 1997), while others showed that the RLF does not differ significantly with redshift (e.g. Goldschmidt et al., 1999; Stern et al., 2000; Cirasuolo et al., 2003) or luminosity (e.g. Bischof & Becker, 1997; Stern et al., 2000).

From a sample of 4472 quasars from the Sloan Digital Sky Survey (SDSS; York et al., 2000), Ivezić et al. (2002) found that the RLF is independent of both redshift and optical luminosity when using marginal distributions of the whole sample; however, they noted that the approximate degeneracy between redshift and luminosity in the SDSS flux-limited sample may cause individual trends in redshift and luminosity to appear to cancel. By stacking the images of the Faint Images of the Radio Sky at Twenty-cm survey (FIRST; Becker et al., 1995), White et al. (2007) were able to probe the radio sky into nanoJansky regime. They found that the median radio loudness of SDSS-selected quasars is a declining function with optical luminosity. After correcting for this effect, they claimed that the median radio loudness is independent of redshift. In this chapter we use a sample of more than 30,000 optically-selected quasars from the SDSS, and break the redshift-luminosity dependence to study the evolution of the RLF. We will find that there are indeed strong trends in redshift and luminosity, and that they do in fact roughly cancel in the marginal distributions.

In § 6.2, we present our quasar sample from the SDSS. In § 6.3 we derive the RLF of quasars as a function of redshift and optical luminosity. We examine the effects of K corrections and sample incompleteness in § 6.4, and we give the discussion and summary in § 6.5 and § 6.6, respectively. We use a Λ-dominated flat cosmology with $H_0 = 70$ km s^{-1} Mpc^{-1}, $\Omega_m = 0.3$, and $\Omega_\Lambda = 0.7$ (e.g. Spergel et al., 2007).

6.2 The SDSS Quasar Sample

The SDSS (York et al., 2000) is an imaging and spectroscopic survey of the sky using a dedicated wide-field 2.5m telescope (Gunn et al., 2006). The imaging is carried out in five broad bands, *ugriz*, spanning the range from 3000 to 10,000 Å

(Fukugita et al., 1996; Gunn et al., 1998). From the resulting catalogs of objects, quasar candidates (Richards et al., 2002) are selected for spectroscopic follow-up. Spectroscopy is performed using a pair of double spectrographs with coverage from 3800 to 9200 Å, and a resolution $\lambda/\Delta\lambda$ of roughly 2000. The SDSS quasar survey spectroscopically targets quasars with $i < 19.1$ at low redshift ($z \leq 3$) and $i < 20.2$ at high redshift ($z \geq 3$). The low-redshift selection is performed in $ugri$ color space, and the high-redshift selection is performed in $griz$ color space. In addition to the optical selection, a SDSS object is also considered to be a primary quasar candidate if it is an optical point source located within $2\rlap{.}''0$ of a FIRST radio source. All SDSS magnitudes mentioned in this chapter have been corrected for Galactic extinction using the maps of Schlegel, Finkbeiner, & Davis (1998).

The sample we used is from the SDSS Data Release Three (DR3; Abazajian et al., 2005). The quasar catalog of the DR3 consists of 46,420 objects with luminosities larger than $M_i = -22$ (Schneider et al., 2005). The area covered by the catalog is about 3732 deg^2. We reject 4683 objects that are not covered by the FIRST survey, and we only use the quasars which were selected on their optical colors (i.e., the quasars with one or more of the following target selection flags: QSO_HIZ, QSO_CAP and QSO_SKIRT; see Richards et al. 2002) to avoid the bias introduced by the FIRST radio selection. The final sample consists of 31,835 optically-selected quasars from the SDSS DR3 catalog, and covers a redshift range of $0 < z \leq 5$ and a luminosity range of $-30 \leq M_i < -22$.

To include both core-dominated (hereafter FR1) and lobe-dominated (hereafter FR2) quasars, we match our sample to the FIRST catalog (White et al., 1997) with a matching radius $30''$. For the quasars that have only one radio source within $30''$, we match them again to the FIRST catalog within $5''$ and classify the matched ones as FR1 quasars. The quasars that have multiple entries within $30''$ are classified as FR2 quasars. The sample contains 2566 FIRST-detected quasars, including 1944 FR1 quasars and 622 FR2 quasars.

We use the integrated flux density (f_{int}) in the FIRST catalog to describe the 20 cm radio emission. The total radio flux density of each FR2 quasar is determined

using all of the radio components within $30''$. We note that we have excluded those FR2 quasars whose separations between lobes are greater than $1'$. In fact, FR2 quasars represent a small fraction of the SDSS DR3 catalog, and FR2 quasars with diameters greater than $1'$ are even rarer (de Vries, Becker, & White, 2006). These numbers are too small to affect the statistics below. Therefore we do not use more sophisticated procedures (e.g. Ivezić et al., 2002; de Vries, Becker, & White, 2006) to select FR2 quasars.

6.3 RLF of Quasars as a Function of Redshift and Optical Luminosity

We define a radio-loud quasar based on its R parameter, the rest-frame ratio of the flux density at 6 cm (5 GHz) to the flux density at 2500 Å (e.g. Stocke et al., 1992). For a given quasar, we calculate its observed flux density f_{6cm} at rest-frame 6 cm from f_{int} (if detected) assuming a power-law slope of -0.5 (e.g. Ivezić et al., 2004b); and we determine its observed flux density f_{2500} at rest-frame 2500 Å by fitting a model spectrum to the SDSS broadband photometry (Fan et al., 2001b; Jiang et al., 2006b; Richards et al., 2006b). The model spectrum is a power-law continuum ($f_\nu = A\nu^\alpha$) plus a series of emission lines extracted from the quasar composite spectrum (Vanden Berk et al., 2001). We integrate the model spectrum over the redshifted SDSS bandpasses to compare with the observed magnitudes. The parameters α and A are determined by minimizing the differences between the model spectrum magnitudes m^{model} and the SDSS photometry m^{obs}:

$$\chi^2 = \sum \left(\frac{m_i^{model} - m_i^{obs}}{\sigma_i^{obs}} \right)^2, \qquad (6.1)$$

where σ_i^{obs} is the estimated SDSS photometry error in the ith SDSS filter. We constrain α to be in the range $-1.1 < \alpha < 0.1$, and only use the bands that are not dominated by Lyman forest absorption systems. Finally f_{2500} is computed from the power-law continuum using the best-fit values of α and A, and the radio loudness R is obtained by

$$R = f_{6cm}/f_{2500}. \qquad (6.2)$$

The absolute magnitude M_{2500} at rest-frame 2500 Å is calculated from f_{2500}.

The FIRST survey has a 5σ peak flux density limit of about 1.0 mJy (Becker et al., 1995), although this limit is not perfectly uniform across the sky. For a quasar detected by FIRST, we determine the relevant limit directly from the FIRST catalog, while for a quasar undetected by FIRST, we measure the limit at the position of the nearest radio source (usually within $10'$). We find that the median value of the limits is 0.98 mJy, which has already included the effect of "CLEAN bias" (Becker et al., 1995; White et al., 1997). Only $\sim 4\%$ of the quasars have limits above 1.1 mJy, so we use 1.1 mJy as the FIRST detection limit for our sample.

Many sources in the FIRST images are resolved. The resolution effect causes FIRST to become more incomplete for extended objects near the detection limit (Becker et al., 1995; White et al., 1997). Furthermore, FR2 quasars are more incomplete than FR1 quasars for integrated flux densities. For example, a double-lobe radio source with two identical components suffers from incompleteness twice as high as a single-component source of the same total flux density. Figure 6.1 (provided by R. L. White, private communication) shows the FIRST completeness as a function of integrated flux density. The completeness is computed using the observed size distribution and rms values of integrated flux densities from the FIRST survey for SDSS quasars, and has included all effects mentioned above. Quasars with $f_{int} > 5$ mJy have a completeness fraction $g_{comp} \approx 1$ (100%); while for a quasar with 1.1 mJy $< f_{int} < 5$ mJy, its g_{comp} is measured from the curve. To correct for sample incompleteness, we use the weight of $1/g_{comp}$ when we calculate the numbers of radio-loud quasars.

When quasars with $R > 10$ are defined as radio-loud (e.g. Kellermann et al., 1989), FIRST is able to detect radio-loud quasars down to $i \approx 18.9$ based on Equation 6.2, the K corrections we applied and the FIRST detection limit of 1.1 mJy. The left panel of Figure 6.2 shows the redshift and absolute magnitude distribution of our sample.

In flux-limited surveys, redshift and luminosity are artificially correlated, making it difficult to separate the dependence of the RLF on redshift or luminosity. To break
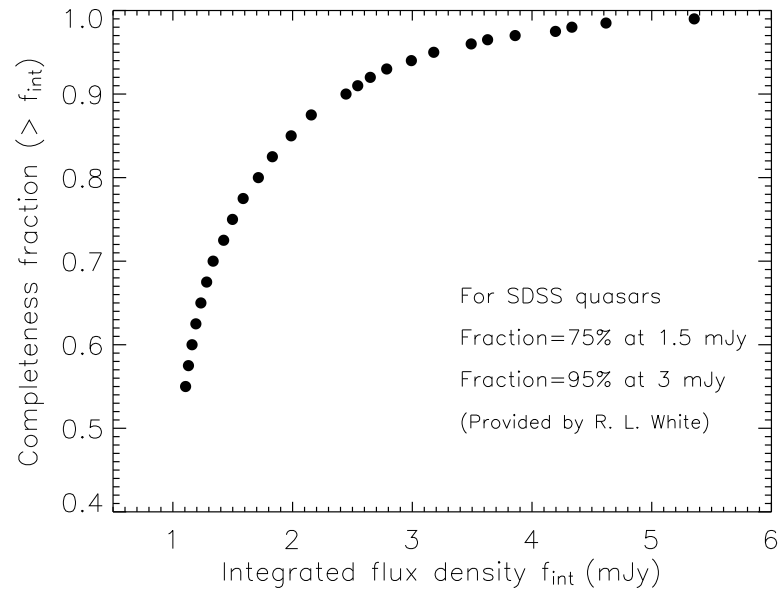
Figure 6.1 The FIRST completeness as a function of integrated flux density (provided by R. L. White, private communication). The completeness is computed using the observed size distribution of SDSS quasars and rms values of integrated flux densities from the FIRST survey.
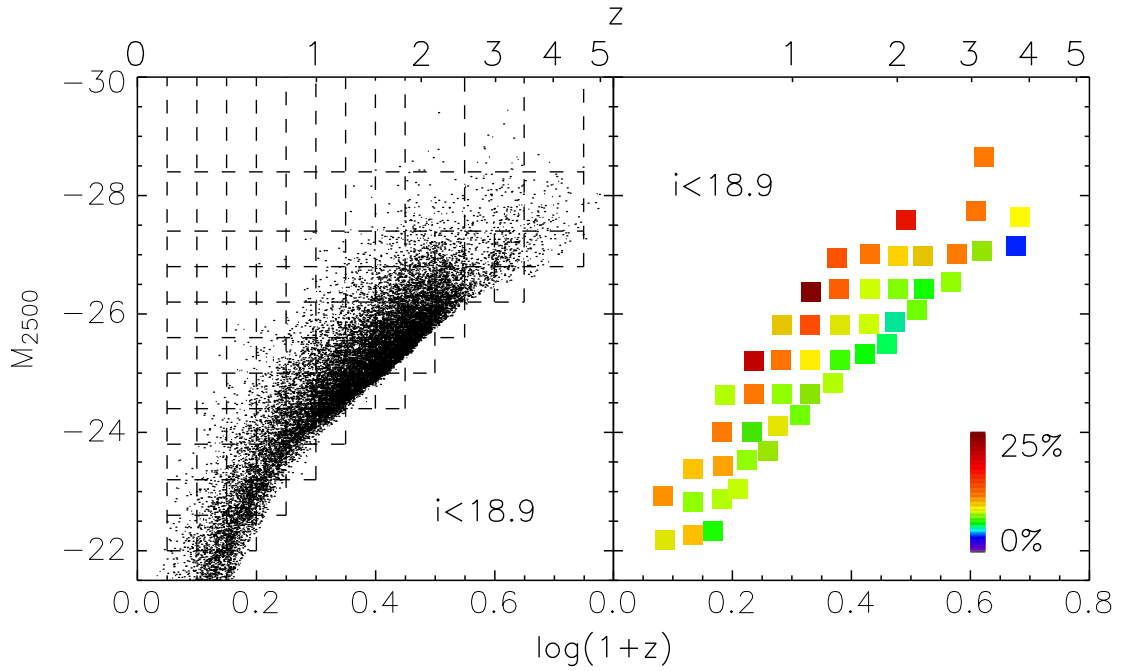
Figure 6.2 Left panel: Redshift and absolute magnitude distribution for 20,473 quasars with $i < 18.9$ in our sample. The M_{2500}–z plane is divided into small grids to break the redshift-luminosity dependence. RLFs of quasars are calculated in individual grids. Right panel: The R-based RLFs in individual M_{2500}–z bins. The square for each subsample is positioned at the median values of M_{2500} and z in that subsample. The RLF of quasars declines with increasing redshift and decreasing luminosity.
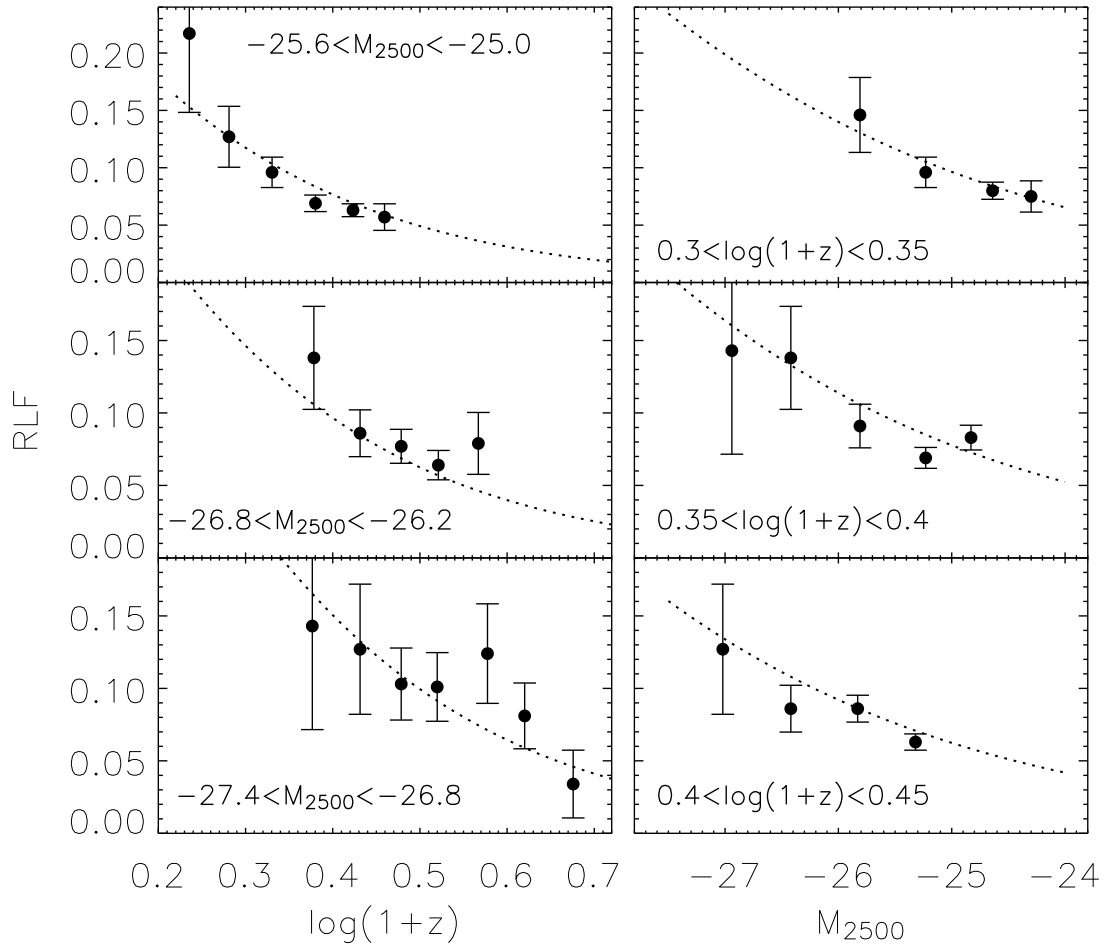
Figure 6.3 RLF in three small redshift ranges and three small magnitude ranges. Dotted lines are the best model fits.

this degeneracy, we divide the M_{2500}–z plane into small grids. RLFs in individual M_{2500}–z grids are calculated and presented as squares in the right panel of Figure 6.2, where the square for each subsample is located at the median values of M_{2500} and z in that subsample. The RLF declines with increasing redshift and decreasing luminosity. One can see the trend more clearly in Figure 6.3, in which we plot the RLF in three small redshift ranges and three small magnitude ranges.

We assume a simple relation to model the RLF as a function of redshift and

absolute magnitude,

$$\log\left(\frac{RLF}{1-RLF}\right) = b_0 + b_z \log(1+z) + b_M(M_{2500} + 26), \qquad (6.3)$$

where b_0, b_z and b_M are constants. We use the RLFs calculated from the grids that include more than one radio-loud quasar, and use median values of z and M_{2500} in each grid. Statistical uncertainties are estimated from Poisson statistics. The best fitting results found by regression fit are, $b_0 = -0.132 \pm 0.116$, $b_z = -2.052 \pm 0.261$, and $b_M = -0.183 \pm 0.025$. This implies that when RLF $\ll 1$, RLF $\propto (1+z)^{-2.052} L_{opt}^{0.458}$, where L_{opt} is the optical luminosity. The χ^2 of this fit is 52.8 for 47 degrees of freedom (DoF), and the confidence levels of b_z and b_M are shown in Figure 6.4. The null hypothesis that $b_z = 0$ and $b_M = 0$ is rejected at $> 5\sigma$ significance. The results are projected onto two-dimensional plots in the left panels of Figure 6.5, where filled circles are the RLFs calculated from individual grids in Figure 6.2 and dashed lines are the best fits. The upper panel shows the RLF as a function of redshift after correcting for the luminosity dependence. At $M_{2500} = -26$, the RLF drops from $\sim$24.3% to $\sim$4.1% as the redshift increases from 0.5 to 3. The lower panel shows the RLF as a function of luminosity after correcting for the redshift dependence. At $z = 0.5$, the RLF decreases rapidly from $\sim$24.3% to $\sim$5.6% as the luminosity decreases from $M_{2500} = -26$ to $M_{2500} = -22$. Therefore the RLF of quasars is a strong function of both redshift and optical luminosity.

To probe whether the trend seen in Equation 6.3 is related to the radio-loud criterion adopted, we define a radio-loud quasar if R is greater than 30 instead of 10. In this case FIRST is able to detect radio-loud quasars down to $i \approx 20.0$. We calculate RLFs for the quasars with $i < 20.0$ using the same method illustrated in Figure 6.2, and model the RLF with Equation 6.3. The best fitting parameters are given in Table 6.1 and the confidence levels of b_z and b_M are shown in Figure 6.4. Figure 6.5 shows the RLF as a function of redshift and luminosity. The relation gives similar results for both radio-loud criteria. We note that the sample of $i < 20.0$ at $z < 3$ is not complete since some bins in M_{2500}–z space are not sampled by SDSS. However, this incompleteness does not bias our results because we are considering
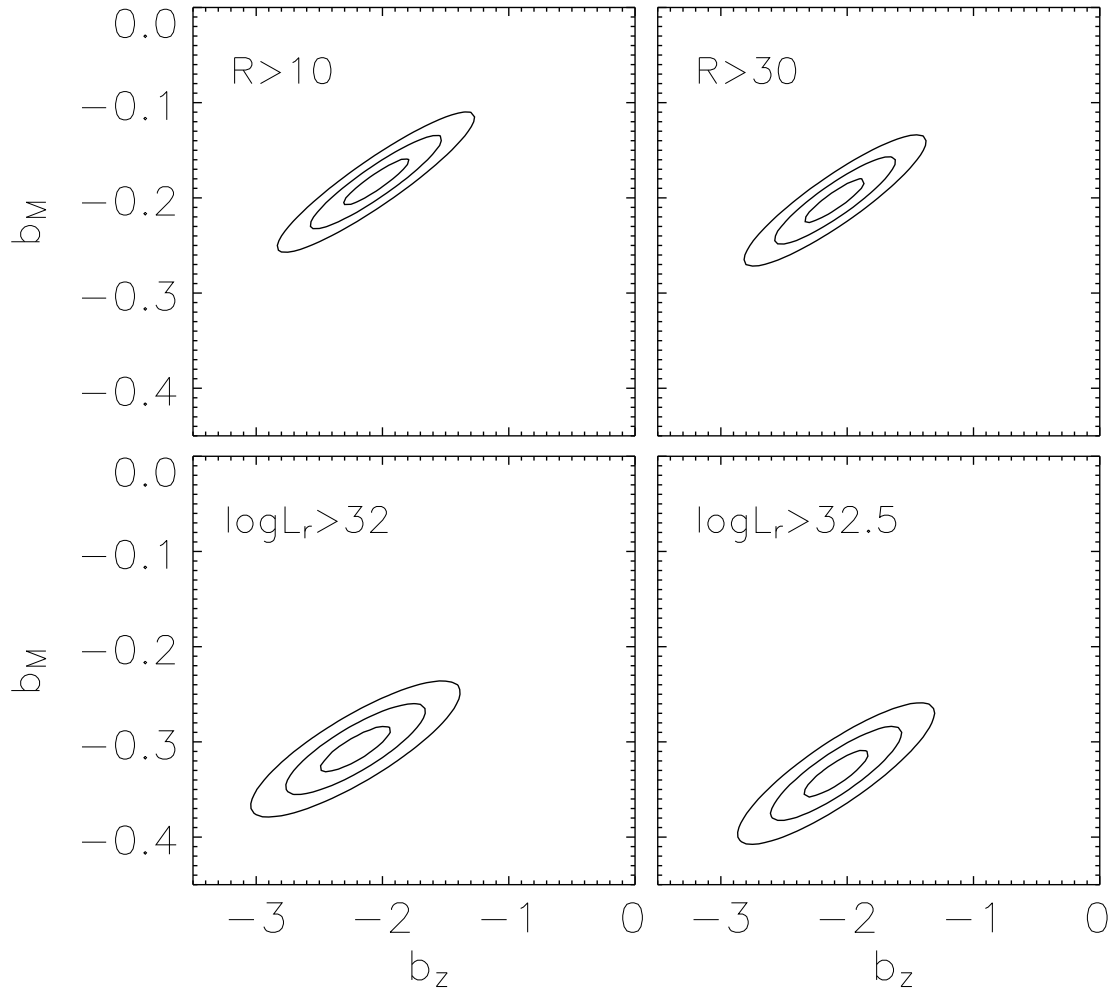
Figure 6.4 1σ, 2σ and 3σ confidence regions for b_z vs. b_M.
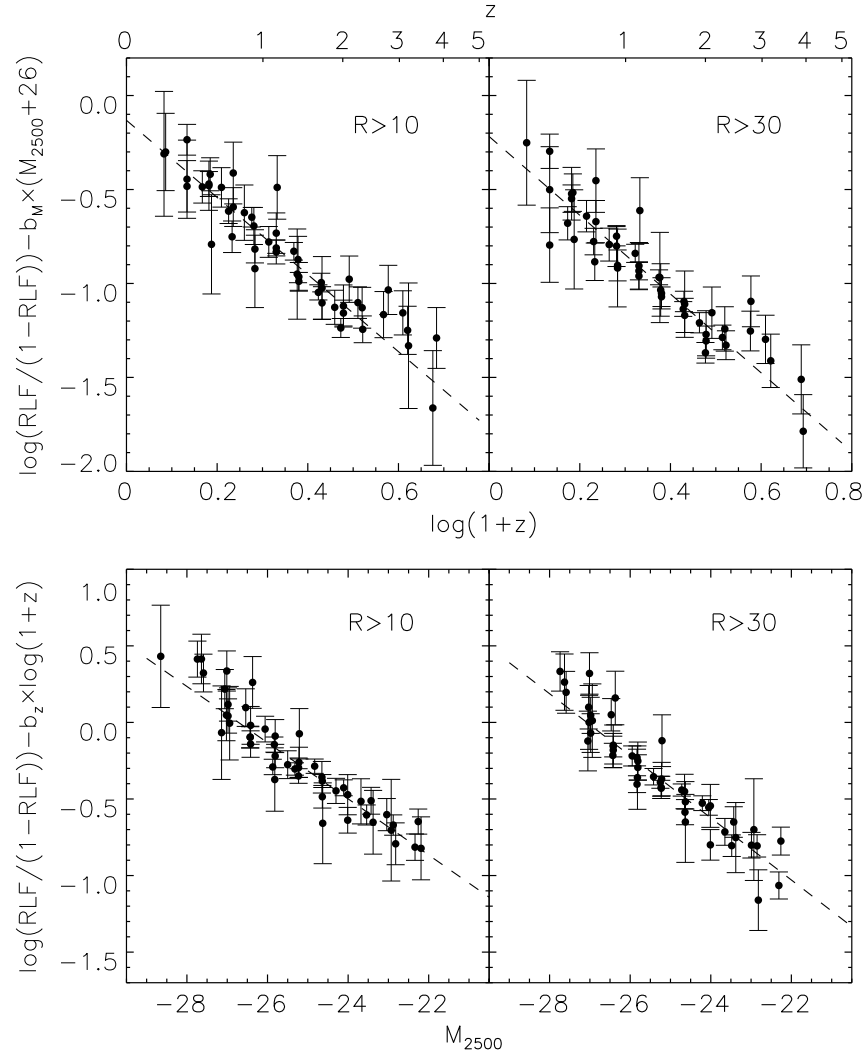
Figure 6.5 The R-based RLF as a function of z and M_{2500}. The upper panels show the RLF as a function of redshift after correcting for the luminosity dependence and the lower panels show the RLF as a function of luminosity after correcting for the redshift dependence. Filled circles are RLFs calculated from individual M_{2500}–z grids and dashed lines are the best model fits. Poisson errors are also given in the figure.

the RLF for optically-selected quasars. Another definition of a radio-loud quasar is based on the radio luminosity of an object (e.g. Peacock, Miller, & Longair, 1986; Miller, Peacock, & Mead, 1990; Hooper et al., 1995; Goldschmidt et al., 1999). As we do for the R-based RLF, we use two criteria to define radio-loud quasars: L_r (luminosity density at rest-frame 6 cm) $> 10^{32}$ ergs s^{-1} Hz^{-1} and $L_r > 10^{32.5}$ ergs s^{-1} Hz^{-1}. In the two cases, FIRST is able to detect radio-loud quasars up to $z \sim 2.1$ and 3.5, respectively. We model the RLF using Equation 6.3 and repeat the analysis. The best fitting results are shown in Table 6.1, and Figures 6.4 and 6.6. The RLF based on L_r is correlated with z and M_{2500} in the same manner as the R-based criteria.

6.4 Effects of the K Corrections and Sample Incompleteness

When applying the K corrections, we assumed that the slope of the radio continuum is -0.5 and used a model spectrum to determine the optical continuum slope. To investigate the effect of the K corrections, we performed several experiments. First, for a given quasar at z, we calculated its f_{2500} and M_{2500} from the magnitude in the SDSS band whose effective wavelength is closest to $2500(1 + z)$ Å assuming a slope of -0.5 (Test 1). As before, we corrected for the contribution from emission lines. Because the SDSS $ugriz$ photometry covers a wavelength range of 3000 to 10,000 Å, the K corrections for $z < 3$ require no extrapolation. Second, we assumed two extreme cases for the radio and optical slopes: in Test 2, we took the optical slope to be 0.0 and the radio slope as -1.0, while in Test 3, the optical slope was -1.0 and the radio slope was 0.0. The results of the fit to Equation 6.3 are listed in Table 6.1. The values of b_z and b_M recalculated under these tests differ by less than 2σ from the original values, and the null hypothesis that $b_z = 0$ and $b_M = 0$ is rejected at $> 5\sigma$ significance in all these tests. Therefore the effect of the K corrections on our conclusions is small.

We investigated the reliability of the relation described by Equation 6.3 for different definitions of radio loudness and for luminosities in different optical bands.

Table 6.1. Results of fits to Equation 6.3

Sample	χ^2	DoF	b_0	b_z	b_M	$\mathrm{Cov}(b_z, b_M)$[a]
$R > 10$	52.8	47	-0.132 ± 0.116	-2.052 ± 0.261	-0.183 ± 0.025	0.0059
$R > 30$	50.7	45	-0.218 ± 0.110	-2.096 ± 0.240	-0.203 ± 0.023	0.0050
$\log L_r > 32$	30.3	35	-0.053 ± 0.122	-2.214 ± 0.277	-0.307 ± 0.024	0.0055
$\log L_r > 32.5$	45.2	41	-0.216 ± 0.118	-2.088 ± 0.260	-0.333 ± 0.025	0.0055
Test 1 ($R > 10$)	62.1	48	-0.328 ± 0.115	-1.639 ± 0.259	-0.141 ± 0.024	0.0058
Test 2 ($R > 10$)	64.4	46	-0.292 ± 0.116	-1.693 ± 0.259	-0.165 ± 0.024	0.0058
Test 3 ($R > 10$)	57.0	46	-0.308 ± 0.114	-1.722 ± 0.261	-0.123 ± 0.024	0.0058
Test 4 ($R > 10$)	53.6	46	-0.142 ± 0.120	-2.115 ± 0.268	-0.194 ± 0.025	0.0063
Test 5 ($R > 10$)	78.9	46	0.120 ± 0.102	-2.924 ± 0.258	-0.254 ± 0.022	0.0054
Test 6 ($R > 10$)	51.9	41	-0.104 ± 0.148	-2.137 ± 0.347	-0.185 ± 0.032	0.0106
Test 7 ($R > 30$)	49.2	45	-0.213 ± 0.128	-2.115 ± 0.286	-0.202 ± 0.027	0.0071

[a]Covariance between b_z and b_M.
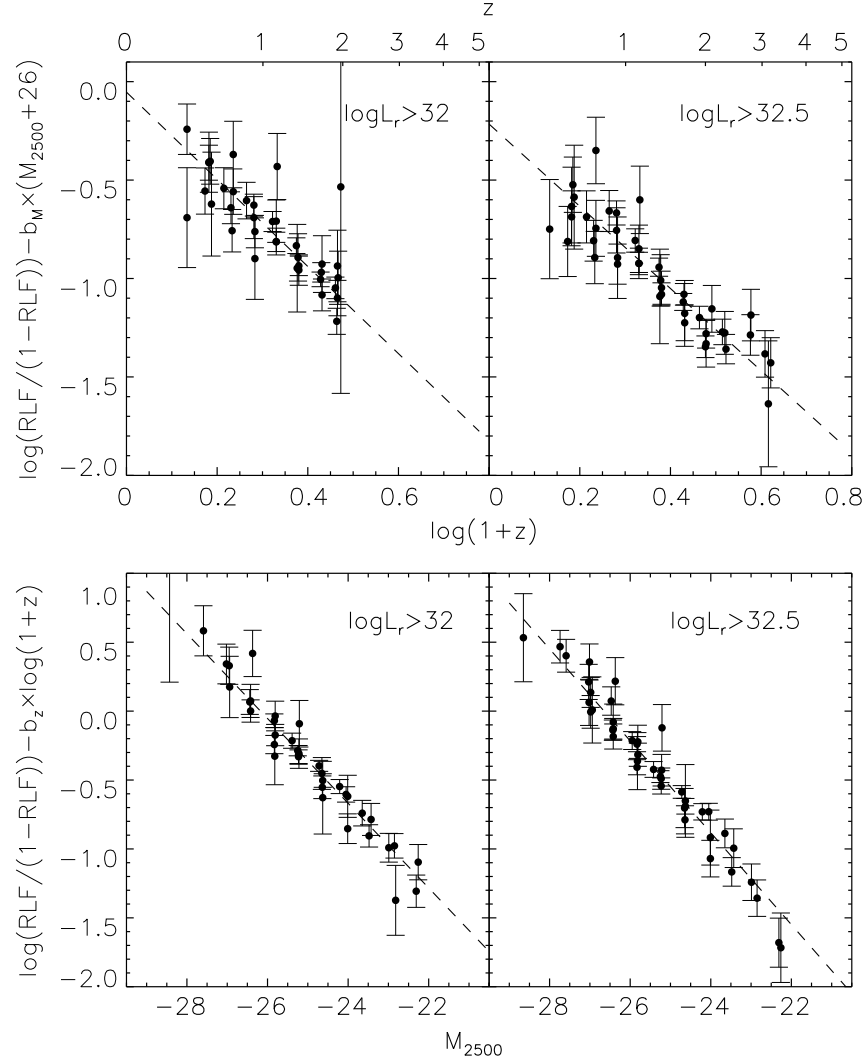
Figure 6.6 The L_r-based RLF as a function of z and M_{2500}. The upper panels show the RLF as a function of redshift after correcting for the luminosity dependence and the lower panels show the RLF as a function of luminosity after correcting for the redshift dependence. Filled circles are RLFs calculated from individual $M_{2500}-z$ grids and dashed lines are the best model fits. Poisson errors are also given in the figure.

For example, we defined the R parameter as the rest-frame ratio of the flux density at 6 cm to the flux density at 4400 Å (e.g. Kellermann et al., 1989) instead of 2500 Å, and we repeated the analysis in § 6.3 (Test 4). In Test 5, we determined the RLF as a function of z and M_i (instead of M_{2500}). M_i is the absolute magnitude in the rest-frame i band, and was calculated using the method described in § 6.3. The results are listed in Table 6.1. In these cases the RLF is still strongly dependent on redshift and luminosity, and the relation described by Equation 6.3 is not sensitive to the details of how radio loudness is defined.

When examining the dependence of the RLF on M_{2500} and z, we note that contours of constant RLF in Figure 6.2 roughly coincide with contours of constant apparent magnitude. This is illustrated in Figure 6.7(a), which shows that for different redshift bins, the relation between the RLF and *apparent i magnitude* is independent of redshift at $i > 17.5$. The RLF does decrease with redshift at $i < 17.5$, although with large error bars. This "conspiracy" of strong dependence of the RLF on apparent magnitude raises the concern that our results have been affected by flux-dependent selection effects. In this chapter we are considering the RLF for optically-selected quasars, and the SDSS color selection is highly complete at $z < 2.2$ (Richards et al., 2006b), so optical selection effects are not likely to seriously affect the RLF determination. However, the SDSS quasar selection becomes increasingly incomplete for objects with very red intrinsic colors ($\alpha < -1.5$, Fan et al., 2001b; Richards et al., 2002), especially at high redshift. White et al. (2007) found a strong correlation between radio loudness and optical color using the SDSS sample. We reproduce this dependence in the upper panel of Figure 6.8. The RLF rises with increasing $\Delta(g-i)$, which is the difference between the observed $g-i$ and the median $g - i$ color of quasars at that redshift, following Hopkins et al. (2004). To examine whether this RLF-color dependence affects the relation in Equation 6.3, we divide the quasar sample into several $\Delta(g-i)$ bins, and calculate the RLF as a function of M_{2500} and z for each bin of *intrinsic* quasar colors. We find that although the average RLF increases toward redder continuum, the RLF is still a strong function of M_{2500} and z within each bin, similar to the relation shown in Equation 6.3. The lower

panel of Figure 6.8 gives an example for the bin of $-0.1 < \Delta(g-i) < 0.1$. Note that more than 80% of the quasars in the sample lie in the range of $-0.3 < \Delta(g-i) < 0.2$, within which the RLF-color relation is relatively flat. Therefore, although we can not determine accurately the RLF evolution for the reddest few percent of quasars where SDSS is incomplete, the strong correlation between the RLF and both redshift and luminosity is not strongly affected by the RLF-color relation over the color range in which the SDSS selection is essentially complete.

In order to examine radio selection effects, we performed the following tests.

1. Did we miss FR1 quasars due to the $5''$ radio catalog matching? We used a $10''$ matching instead, and found that the number of FR1 quasars increases by only 3.7%. We also found that these additional sources increase the RLF by similar factors at both high and low redshift and both high and low luminosity, and thus have little effect on b_z or b_M.

2. Did we measure the radio fluxes of FR2 quasars correctly? We compared FIRST with the NRAO VLA Sky Survey (NVSS; Condon et al., 1998), which has a resolution of $45''$. The FIRST and NVSS fluxes of most FR2 quasars are in good agreement. FIRST has a resolution of $5''$ and may overresolve radio sources larger than about $10''$. These sources are rare and very bright in radio (usually > 50 mJy), well above the radio-loud division in our analysis.

3. Were there quasars detected by NVSS but not by FIRST? We matched our sample to the NVSS catalog within $15''$. We found that about 6% of the matched quasars were not detected by FIRST, and 80% of these additional sources are FR1 sources with offsets more than $5''$ from the SDSS positions. They increase the RLF by similar factors at both high and low redshift and both high and low luminosity, and thus do not significantly change the trend in the RLF.

4. How did the incompleteness of FIRST at the detection limit affect our results? In Section 3 we use 1.1 mJy as the FIRST detection limit, and we correct for
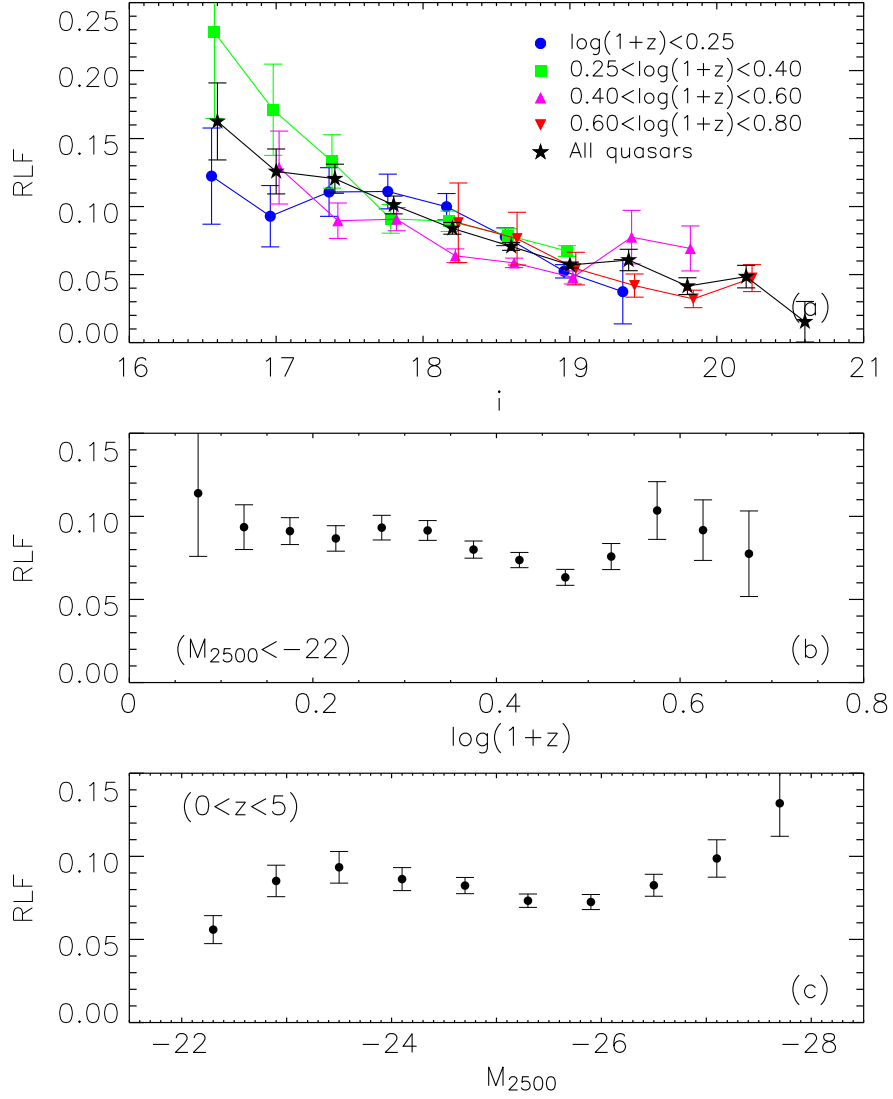
Figure 6.7 (a): RLF as a function of apparent magnitude i for five redshift bins. The RLF declines with increasing i, and the curves for different redshift bins follow the same RLF–i dependence. (b) and (c): Marginal RLF as a function of redshift and luminosity for our sample. The marginal RLF is roughly independent of both redshift and luminosity due to the $M_{2500}–z$ degeneracy.
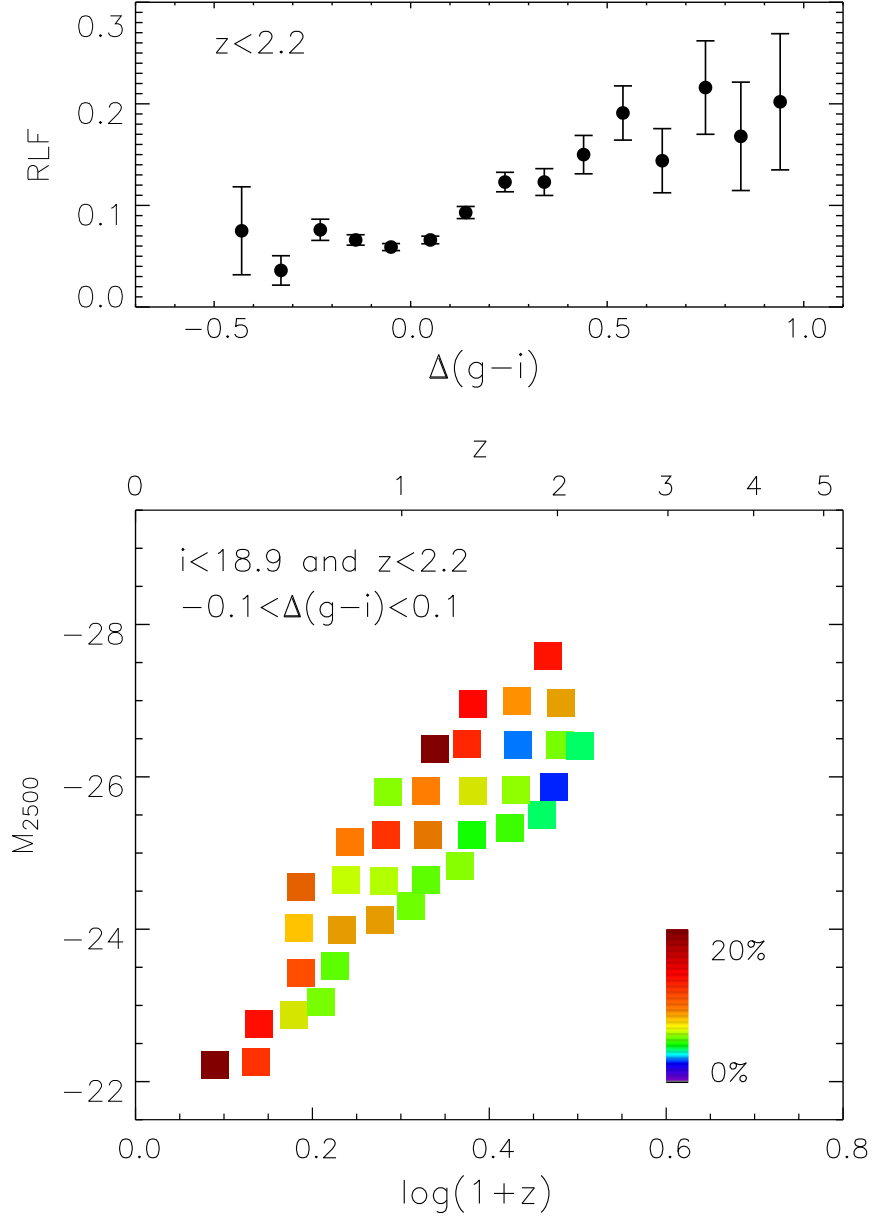
Figure 6.8 Upper panel: RLF as a function of $\Delta(g-i)$. The RLF rises with increasing $\Delta(g-i)$ at $z < 2.2$. Lower panel: RLF as a function of z and M_{2500} in a small color range of $-0.1 < \Delta(g-i) < 0.1$.

the incompleteness caused by the resolution effect. Here we set two tests to examine the incompleteness near the FIRST limit. In Test 6 we use a limit of 1.5 mJy (the corresponding $i \sim 18.6$) to determine the RLF for $R > 10$; while in Test 7 we use a limit of 3 mJy (the corresponding $i \sim 18.9$) to calculate the RLF for $R > 30$. Note that the FIRST completeness measured from the completeness curve in Figure 6.1 is 75% at 1.5 mJy and 95% at 3 mJy. The results of the tests are given in Table 6.1, and they show the similar trend of the RLF on redshift and optical luminosity as we obtained above.

Therefore, based on these tests we conclude that the strong dependence of the RLF on M_{2500} and z is highly likely to be physical, and the radio incompleteness and selection effects we have considered are not responsible for the dependence, though we cannot rule out other unexplored selection effects.

6.5 Discussion

Most of the previous studies of the RLF are based on samples of tens to hundreds of quasars. Considering that the RLF is only $\sim 10\%$ on average, these samples are not large enough to study the two-dimensional distribution of the RLF on M_{2500} and z. This makes it difficult to uncover the relation of Equation 6.3 using only the marginal distribution of the RLF. We calculate the marginal RLF as a function of M_{2500} and z for our sample, which is shown in Figures 6.7(b) and 6.7(c). One can see the marginal RLF is roughly independent of both M_{2500} and z, because the dependence on M_{2500} and z roughly cancel out due to the M_{2500}–z degeneracy. This result is in quantitative agreement with the marginal RLF derived by Ivezić et al. (2002).

It has been suggested that high-redshift quasars show little difference in their rest-frame UV/optical and X-ray properties from those of low-redshift quasars. Their emission-line strengths and UV continuum shapes are very similar to those of low-redshift quasars (e.g. Barth et al., 2003; Pentericci et al., 2003; Fan et al., 2004), the emission line ratios indicate solar or supersolar metallicity in emission-line re-

gions as found in low-redshift quasars (e.g. Hamann & Ferland, 1999; Dietrich et al., 2003b; Maiolino et al., 2003), and the optical-to-X-ray flux ratios and X-ray continuum shapes show little evolution with redshift (e.g. Strateva et al., 2005; Steffen et al., 2006; Shemmer et al., 2006). These measurements suggest that most quasar properties are not sensitive to the cosmic age. However, Figure 6.5 shows that the RLF evolves strongly with redshift, thus the evolution of the RLF places important constraints on models of quasar evolution and the radio emission mechanism.

Equation 6.3 implies a strong correlation between the RLF and optical luminosity. Using a large sample of low-redshift ($0.03 < z < 0.3$) AGNs, Best et al. (2005) find that radio-loud AGNs tend to reside in old, massive galaxies, and that the fraction of radio-loud AGNs is a strong function of stellar mass or central black hole mass (e.g., the fraction increases from zero at a stellar mass of 10^{10}M$_\odot$ to 30% at a stellar mass of 5×10^{11}M$_\odot$). Assuming that optical luminosity is roughly proportional to black hole mass (Peterson et al., 2004), their radio-loud fraction of AGNs is also a strong function of optical luminosity. This is in qualitative agreement with Equation 6.3, although our quasars are more luminous than their low-redshift AGNs.

Equation 6.3 also shows that the RLF is a strong function of redshift. By stacking FIRST images of SDSS-selected quasars, White et al. (2007) recently found that the median R is a declining function with optical luminosity. After correcting for this effect, they claimed that the median R is independent of redshift, which seems inconsistent with our result that the RLF is a strong negative function of redshift. However, the median R and the RLF are not identical. The median R is determined by the majority of quasars with low R values (i.e. radio-quiet quasars); while the RLF is the fraction of quasars exceeding a threshold in R, and therefore corresponds to the behavior of the small fraction of quasars with high R values (i.e. radio-loud quasars). There are two natural ways to interpret the evolution of the RLF with redshift (e.g. Peacock, Miller, & Longair, 1986): (1) This may be due to the cosmological evolution of quasar radio properties, such as R and L_r. For instance, a decreasing R results in a decreasing RLF for increasing redshift. (2) This could be

simply caused by the density evolution of different populations of quasars (e.g. radio-loud and radio-quiet quasars). The results of White et al. (2007) may have ruled out the first explanation and leave the second one: the different density evolution behaviors for the two classes of quasars. For instance, there are more radio-loud quasars at low redshift, but the fraction of radio-loud quasars is small, so they do not change the median R, which is still dominated by radio-quiet quasars. This claim is based on stacked FIRST images. To distinguish between the two explanations, one needs to determine the radio luminosity function of quasars in different redshift ranges, including the radio-quiet population, going to radio fluxes much fainter than those probed by FIRST. Deep surveys such as the Cosmic Evolution Survey (Schinnerer et al., 2004) that cover a wide redshift range and reach low luminosity in both optical and radio wavelengths are needed to interpret the evolution of the RLF.

6.6 Summary

We use a sample of more than 30,000 optically-selected quasars from SDSS to determine the RLF of quasars as a function of redshift and optical luminosity. The sample covers a large range of redshift and luminosity. We study the RLF using different criteria to define radio-loud quasars. After breaking the degeneracy between redshift and luminosity, we find that the RLF is a strong function of both redshift and optical luminosity: the RLF decreases rapidly with increasing redshift and decreasing luminosity. The relation can be described by a simple model, given by Equation 6.3. We have done a series of tests to examine the impact of flux-related selection effects, and find that the dependence of the RLF on redshift and luminosity is highly likely to be physical.

The RLF is one of a few quasar properties that strongly evolve with redshift, so the evolution of the RLF places important constraints on models of quasar evolution and the radio emission mechanism. By comparing our results with the behavior of the median R derived from stacked FIRST images, we find that the evolution of

the RLF with redshift could be explained by the different density evolution for radio-loud and radio-quiet quasars. Substantially deeper wide-angle radio surveys which obtain fluxes for the radio-quiet population are needed to fully understand the physical nature of this evolution.

CHAPTER 7

QUASARS WITH STRONG NITROGEN EMISSION LINES FROM SDSS

7.1   Introduction

Quasars with prominent nitrogen emission lines at 1486 Å or 1750 Å are rare. A well known example is Q0353-383, a luminous quasar showing strong N IV] λ1486, N III] λ1750, and N V λ1240 emission lines (Osmer & Smith, 1980; Baldwin et al., 2003). Baldwin et al. (2003) claimed that the unusual nitrogen emission in Q0353-383 is likely due to high metallicity in the broad line region of the quasar; the metallicity measured from line strength ratios involving N V, N IV], and N III] is $\sim$15 times the solar abundance.

   The Sloan Digital Sky Survey (SDSS; York et al., 2000) provides statistically significant samples to study these nitrogen-rich (N-rich) quasars. From a sample of $\sim$ 5600 objects in the SDSS First Data Release Quasar Catalog (Schneider et al., 2003), Bentz et al. (2004) reported on 20 N-rich quasars in the redshift range $1.6 < z < 4.1$. The fraction of N-rich quasars in their sample is about 0.4%. By comparing with other quasars, they found that the N-rich quasars tend to have stronger Lyα emission lines, and stronger but narrower C IV λ1549 and C III] λ1909 emission lines. The two quasars with the strongest N IV] and N III] lines in the Bentz et al. (2004) sample have been studied in detail by Dhanda et al. (2007). Recently Glikman et al. (2007) discovered two quasars with strong N IV] lines from a sample of 23 faint quasars at $3.7 < z < 5.1$. They suspected that the high detection rate of N-rich quasars is due to the low luminosity and high redshift of the sample.

   The number of known N-rich quasars is still small, and most of their properties remain unclear, such as the UV/optical continuum slopes, emission line strengths and widths, and central black hole masses, etc. In this chapter, we present 293 N-rich quasars at $z > 1.7$ selected from the SDSS Fifth Data Release (DR5) Quasar

Catalog (Schneider et al., 2007). In § 7.2, we introduce our sample selection. We measure various properties of these quasars and compare them with those of other SDSS quasars in § 7.3. A short summary is given in § 7.4. We use a Λ-dominated flat cosmology with $H_0 = 70$ km s^{-1} Mpc^{-1}, $\Omega_m = 0.3$, and $\Omega_\Lambda = 0.7$ (Spergel et al., 2007). We use EW and FWHM to denote *rest-frame* equivalent width and full width at half maximum, respectively.

7.2   Sample Selection

The SDSS is an imaging and spectroscopic survey using a dedicated wide-field 2.5m telescope (Gunn et al., 2006). The imaging is carried out in five broad bands, $ugriz$, spanning the range from 3000 to 10,000 Å (Fukugita et al., 1996); spectroscopy is performed using a pair of double spectrographs with coverage from 3800 to 9200 Å, and a resolution $\lambda/\Delta\lambda$ of roughly 2000. The SDSS quasar survey spectroscopically targets quasars with $i < 19.1$ at low redshift ($z \leq 3$) and $i < 20.2$ at high redshift ($z \geq 3$). Quasar candidates are mostly selected in $ugri$ and $griz$ color space (Richards et al., 2002). An SDSS object is also considered to be a primary quasar candidate if it is located within $2''$ of a radio source of the Faint Images of the Radio Sky at Twenty-cm survey (FIRST; Becker et al., 1995). The sample we use is from the SDSS DR5 Quasar Catalog. The catalog consists of 77,429 quasars with luminosities larger than $M_i = -22$ (Schneider et al., 2007).

To find quasars with prominent N IV] or N III] emission lines, we searched 25,941 quasar spectra with $i < 20.1$ in the redshift range $1.7 < z < 4.0$. The search was done by visual inspection of each spectrum. This step results in a sample of 380 N-rich quasar candidates. We then measured the rest-frame EW and FWHM for each detected N IV] or N III] line as follows. We estimate the local continuum by fitting a power-law to the spectra at both sides of the line. After subtraction of this continuum, a Gaussian profile is fitted to the line, and the EW and FWHM are computed from the best-fitted component. Our final selection criterion of N-rich quasars is EW > 3 Å. This cut is chosen for the following reasons: (1) In most

quasar spectra, the significance of the detection of a EW = 3 Å nitrogen line is greater than 5σ; (2) The 3 Å cut is significantly larger than typical EW values for the two nitrogen lines (see § 7.3.2); (3) Bentz et al. (2004) used a similar selection cut. A total of 293 quasars in our sample meet this criterion, including 43 quasars with strong N IV] lines and 279 quasars with strong N III] lines (29 quasars have both lines). Table 7.1 presents the catalog of the N-rich quasars. Column (1) gives the name of each quasar, and column (2) lists the redshift. Column (3) shows the SDSS i-band magnitude corrected for Galactic extinction. All other quantities will be explained in § 7.3. The full Table 7.1 is in the APPENDIX B.

Figure 7.1 shows four good examples of the selected quasars. Figure 7.2 shows the rest-frame EW and FWHM distributions of N III]. Figure 7.3 compares the redshift distributions of the N-rich quasars and SDSS DR5 quasars at $z > 1.7$. The distributions are consistent at most redshift ranges except for the ranges of $2.5 < z < 2.9$ and $z > 3.5$. At $2.5 < z < 2.9$, the higher fraction of the N-rich quasars is caused by the higher SDSS quasar selection efficiency due to stronger Lyα emission in these quasars (§ 7.3.2). The lower fraction of the N-rich quasars at $z > 3.5$ is likely due to the lower signal-to-noise ratios (SNRs) of the spectra at $\lambda \geq 8000$ Å.

7.3   Results

We detect 293 quasars with prominent N IV] or N III] emission lines from 25,941 SDSS quasars at $1.7 < z < 4.0$. This is the largest N-rich quasar sample to date. The fraction of N-rich quasars is about 1.1%, significantly higher than 0.4% (20 out of 5600) found by Bentz et al. (2004), who used a similar EW selection cut in a similar redshift range. This is likely because detecting weak lines in spectra of moderate SNRs is difficult for automated codes. Based on repeated selections of N-rich quasars by visual inspection from a subset of 2000 quasars, we estimate that the completeness at EW > 3 Å is greater than 80%. In this section we compare various properties of the N-rich quasars with those of 'normal' SDSS quasars.

Table 7.1. SDSS DR5 N-rich Quasar Catalog

Name (J2000.0 Coordinates)	Redshift	i^a	α	EW (Å)						Fe II/Mg II	M_{2500}	R
				N IV]	N III]	Si IV	C IV	C III]	Mg II			
SDSS J124032.96+674810.8	1.701	18.91	-0.63	...	4.0	...	27.1	31.2	11.4	4.2	-25.27	...
SDSS J082247.75+071154.7	1.703	18.85	-0.46	...	5.3	...	35.6	27.1	14.6	2.5	-25.30	...
SDSS J100643.89+395222.7	1.705	18.89	-0.85	...	4.2	...	101.7	22.8	...	...	-25.26	...
SDSS J141000.79+641010.4	1.707	18.46	-1.15	...	4.1	...	...	37.4	21.8	3.1	-25.66	...
SDSS J105645.42+414016.2	1.708	18.71	-0.32	...	3.0	...	26.6	20.5	7.8	4.4	-25.48	...
SDSS J105743.11+532231.4	1.708	18.52	-0.57	...	3.4	...	41.0	21.2	15.9	2.4	-25.70	...
SDSS J075230.44+272619.8	1.708	18.25	-0.62	...	3.3	...	67.2	41.4	24.4	1.8	-25.87	...
SDSS J151557.86+383604.3	1.710	18.24	-0.94	...	3.6	...	...	45.2	16.9	2.9	-25.96	...
SDSS J115419.40+145555.3	1.711	17.98	-0.87	...	3.6	...	...	15.9	...	...	-26.30	...
SDSS J162923.06+462311.2	1.718	18.95	-0.39	...	3.2	...	43.6	28.8	13.8	2.9	-25.28	232.6
SDSS J145349.70+482740.3	1.720	18.81	-1.07	...	5.1	...	19.9	20.6	...	...	-25.52	71.4
SDSS J074220.27+343213.3	1.724	19.77	-0.92	...	4.8	...	...	...	...	...	-24.41	4.3
SDSS J161118.02+393350.9	1.724	17.82	-0.57	...	3.9	...	30.9	16.6	...	...	-26.38	1901.2
SDSS J081710.54+235223.9	1.732	18.61	-0.40	4.9	6.7	...	8.1	13.7	...	...	-25.58	...
SDSS J145958.75-013742.4	1.738	18.84	-1.44	...	6.9	...	...	45.1	...	...	-25.35	...
SDSS J084057.02+054733.4	1.742	18.15	-1.50	...	4.3	...	24.4	24.3	...	...	-26.25	...
SDSS J123354.39+150203.7	1.744	18.13	-1.29	...	5.1	...	34.3	22.8	15.2	2.5	-26.18	...
SDSS J084117.24+083753.4	1.746	18.11	-1.04	...	5.6	...	39.8	26.5	15.6	2.7	-26.17	...
SDSS J111559.52+633813.6	1.746	18.04	-1.12	...	3.4	...	46.5	25.3	...	...	-26.15	22.7
SDSS J231608.20+132334.5	1.748	18.42	-1.23	...	9.1	...	52.6	27.5	...	...	-25.84	...

^{a}Corrected for Galactic extinction.

Note. — The full Table 7.1 appears in the electronic edition of the *Astrophysical Journal*.
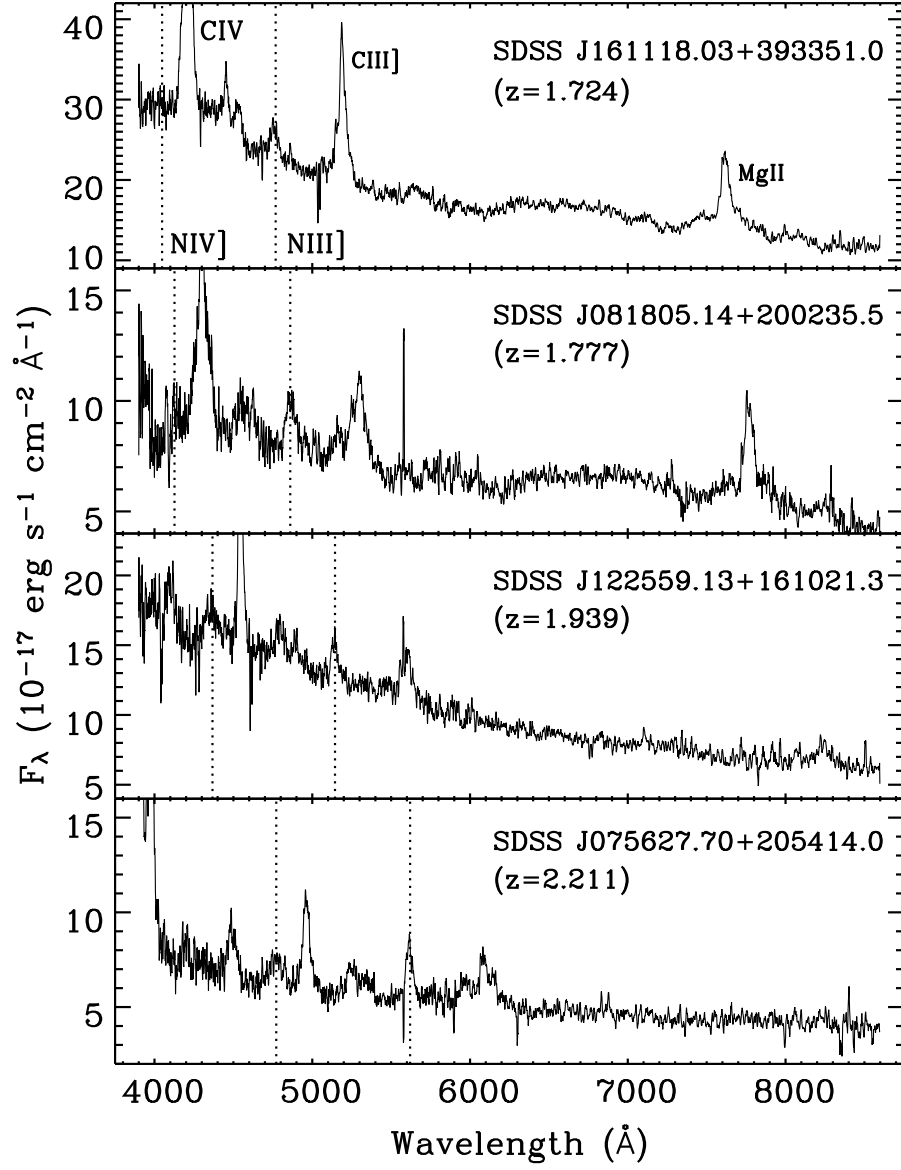
Figure 7.1 Spectra of four N-rich quasars, smoothed by a boxcar of 5 pixels. The dotted lines indicate the positions of N IV] and N III]. The first two quasars show strong N III] lines and the last two quasars show both N IV] and N III] lines.
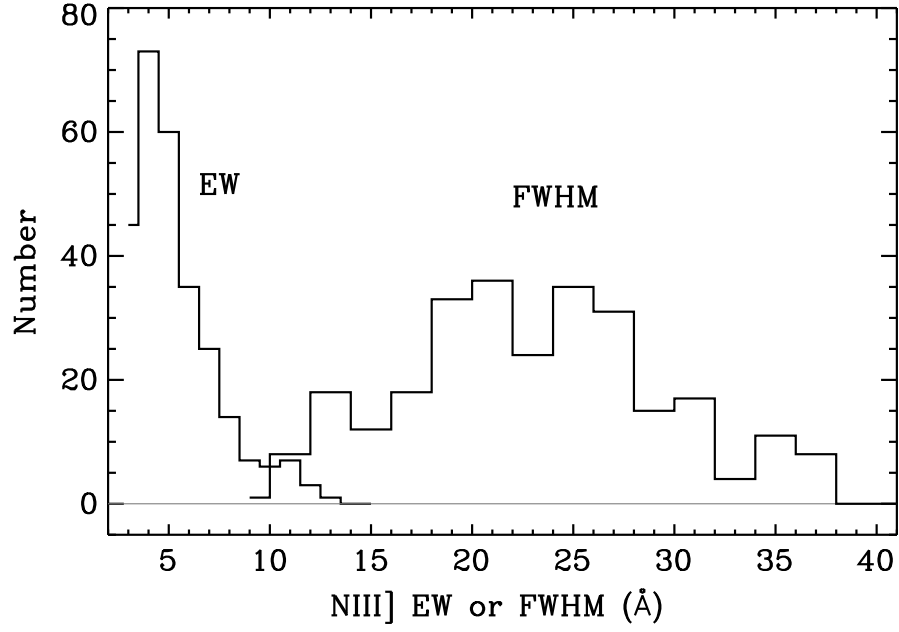
Figure 7.2 Rest-frame EW and FWHM distributions of N III].
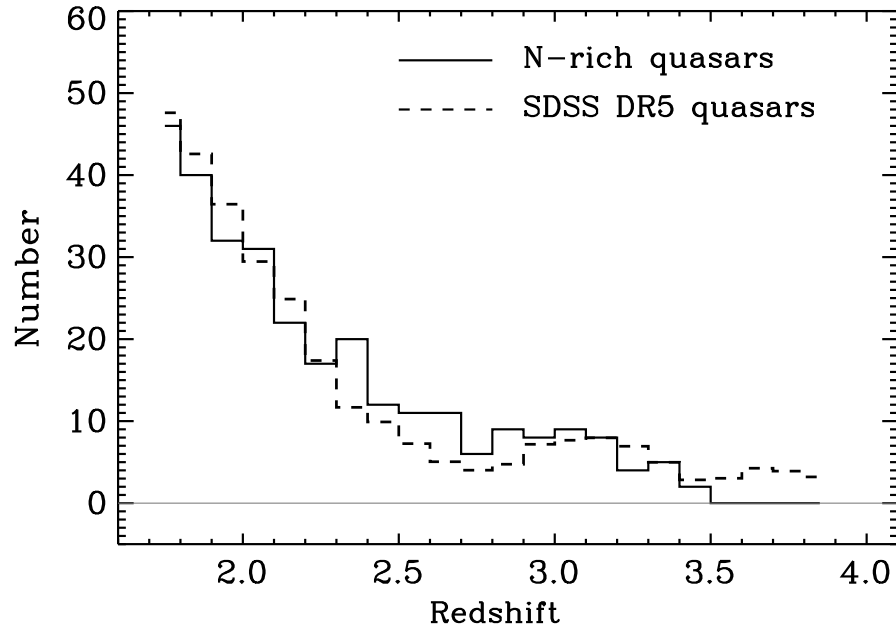
Figure 7.3 Redshift distributions of the N-rich quasars and SDSS DR5 quasars. The histogram for the SDSS DR5 quasars has been scaled to match the number of the N-rich quasars.

7.3.1 Continuum and emission line properties of N-rich quasars

To analyze the emission line properties of each N-rich quasar, we fit a power-law ($f_\nu \propto \nu^\alpha$) to regions with very little contribution from line emission. The quasar spectrum was first scaled to its r-band magnitude and thereby placed on an absolute flux scale. After fitting and subtraction of the power-law continuum, we fit the following individual emission lines. (1) Si IV $\lambda1396$ if $i < 19.0$ and $z > 1.9$. We use a single Gaussian profile to fit this line. (2) C IV if $i < 19.5$. We use a single Gaussian and double Gaussians to fit this line respectively, and we choose the best fit. (3) C III] if $i < 19.5$ and $z < 3.5$. The weak Al III $\lambda1857$ line is often detected in the blue wing of the C III] line. We use two Gaussian profiles to fit these two lines simultaneously if Al III is apparent, otherwise C III] is fitted using a single Gaussian component. We also note that there is usually a contamination from the weak Si III] $\lambda1892$ line. We do not remove this contamination because the decomposition of the C III] and Si III] lines is difficult and the strength of Si III] is minor compared to C III].All models are visually inspected, and the emission lines severely affected by absorption lines are discarded from our analysis. The EW and FWHM are measured from the best fits. The results are shown in Table 7.1. Column 2 of Table 7.2 lists the median values of EW and FWHM for each line. The median value of the power-law slopes is also given in Table 7.2. The slope is slightly redder than the slope in the Vanden Berk et al. (2001) composite spectrum ($\alpha_\nu = -0.44$). In most cases the spectral quality is not good enough to allow more sophisticated fittings as Baldwin et al. (2003) and Dhanda et al. (2007) did, or to allow reliable modeling of weak emission lines such as He II $\lambda1640$ and O III] $\lambda1663$. The Lyα, N V, and Si II $\lambda1262$ lines are usually heavily blended, so modeling their profiles requires high quality spectra. We discuss their average properties in § 7.3.2.

In the above analysis we do not consider the UV Fe II emission that contaminates most of the UV spectral region. The most prominent Fe II emission line complex is at $2200\text{Å} \lesssim \lambda \lesssim 3000$ Å (Vestergaard & Wilkes, 2001). At $\lambda < 2200$ Å, the Fe II emission is weak, and does not significantly affect the measurements of strong emission lines.

Table 7.2. Rest-frame Emission Line Properties

Parameter	N-rich quasars	SDSS quasars
α	–0.68±0.40	–0.64±0.57
Si IV EW (Å)	8.1±3.3	8.1±3.4
Si IV FWHM (Å)	22.9±5.4	26.3±8.3
C IV EW (Å)	36.9±16.6	36.1±19.7
C IV FWHM (Å)	18.9±8.7	27.9±11.0
C III] EW (Å)	21.8±9.4	23.8±9.0
C III] FWHM (Å)	37.2±14.9	50.5±21.0
Mg II EW (Å)	13.7±5.0	11.1±4.6
Mg II FWHM (Å)	41.6±7.8	43.1±12.0
Fe II/Mg II	3.6±1.3	3.5±1.4
[a]Lyα EW (Å)	71.0	50.0
[a]Lyα FWHM (Å)	10.6	15.8
[a]N V EW (Å)	24.6	17.8
[a]N V FWHM (Å)	18.0	19.0
[a]O I EW (Å)	3.7	1.8
[a]O I FWHM (Å)	14.8	14.1
[a]C IV EW (Å)	38.4	39.6
[a]C IV FWHM (Å)	18.6	24.0
[a]C III] EW (Å)	23.4	24.9
[a]C III] FWHM (Å)	35.1	44.9

[a]Derived from the composite spectra in § 7.3.2.

Note. — The errors are 1σ rms of the distributions.

At $z > 2.1$, the strong Fe II complex is moving out of the SDSS spectral coverage, making it difficult to measure the Fe II emission. However, Fe abundance is of interest, and the Fe II/Mg II $\lambda2800$ ratio is important for understanding chemical abundances in quasars (e.g. Hamann & Ferland, 1999; Dietrich et al., 2002). We fit and measure the Fe II emission for quasars with $i < 19.0$ and $z < 2.1$. The modeling is done as an iteration over a power-law fit to the continuum emission and a model fit to the Fe II emission using a scaled and broadened version of the Fe II template of Vestergaard & Wilkes (2001). The Fe II template is broadened by convolving the template with Gaussians with a range of sigmas. In the first iteration a power-law is fitted to the continuum windows. Upon subtraction of this primary continuum fit multiple broadened copies of the Fe II template are scaled to regions which predominantly contain Fe emission. The broadened and scaled Fe II template that provides the best fit is selected and subtracted. Then another power-law fit to the continuum emission is performed. The iteration of the continuum and Fe II fitting is repeated until convergence is obtained. See Vestergaard & Wilkes (2001) for the detailed process. All models are visually inspected, and poor fits (due to low SNRs or strong absorptions) are discarded from our analysis.

After the subtraction of the Fe II emission and power-law continuum we fit the Mg II line using a Gaussian profile and measure its EW and FWHM from the best fit. We calculate the flux of the Fe II complex by integrating the best-fitting Fe II template from 2200 to 3090 Å (e.g. Dietrich et al., 2002). The results are shown in Table 7.1, and their mean values are shown in Table 7.2. The mean value of the Fe II/Mg II ratios is 3.6 with a scatter 1.3, consistent with previous measurements in normal quasars (e.g. Iwamuro et al., 2002).

7.3.2 Comparison between N-rich quasars and 'normal' quasars

To find differences between N-rich quasars and 'normal' quasars, we draw a quasar sample three times larger than the sample of the N-rich quasars from the SDSS DR5 quasar catalog by random selection. The sample has i-band magnitudes brighter than 20.1 and redshift distribution similar to that of the N-rich sample shown in

Figure 7.3. We measure continuum and emission line properties for this sample using the methods outlined in § 7.3.1. The results are given in Column 3 of Table 7.2. The comparison in Table 7.2 shows that most of the properties in the two samples are very consistent, including the continuum slopes, the Fe II/Mg II ratios, and the EWs and FWHM of most emission lines. The only apparent difference is the FWHM of C IV and C III]; their values in the N-rich sample are about 25–30% smaller than those in the SDSS DR5 sample. This was also noticed by Bentz et al. (2004).

We compare the luminosity distributions of the two quasar samples. We measure m_{2500}, the apparent AB magnitude at rest-frame 2500 Å, based on $m_{2500} = -2.5 \times \log{(f_{2500})} - 48.60$, where f_{2500} is the monochromatic flux density (in units of $\mathrm{erg\,sec^{-1}\,cm^{-2}\,Hz^{-1}}$) at rest-frame 2500 Å. The flux density f_{2500} is derived using the best-fitted continuum. We then determine the absolute magnitude M_{2500} from m_{2500}. We find that the distributions of M_{2500} for the two samples are similar, although the N-rich sample is about 0.5 magnitude brighter on average. This is caused by our selection; we may have missed some faint N-rich quasars where SNRs are low and nitrogen lines are difficult to identify. However, the difference of 0.5 magnitude is too small for the Baldwin effect (Baldwin, 1977) to impact the comparison of the EWs.

To compare the overall properties of continua and emission lines, we construct composite spectra for the two samples. Each spectrum is placed in the rest frame and scaled so that its continuum at 1450 Å is equal to 1 (arbitrary units). The scaled spectra are then averaged without any weights. This is to avoid bias introduced by the Baldwin effect if we use weights involving SNRs. The two composite spectra are shown in Figure 7.4. They have similar shapes from 1000 to 3000 Å. By definition the N IV] and N III] lines in the N-rich spectrum are stronger. In the SDSS DR5 spectrum, the EW of N III] is 0.40 ± 0.06 Å, consistent with 0.44 ± 0.03 Å in the Vanden Berk et al. (2001) composite spectrum; the EWs of N IV] is -0.04 ± 0.06 Å, consistent with no detection. We measure the properties of Lyα and N V as follows. After the subtraction of the power-law continuum, we fit the Lyα, N V, and Si II lines

simultaneously using four Gaussian profiles, with the first two profiles representing the broad and narrow components of Lyα and the last two profiles representing N v and Si ii. For Lyα, we only fit its red half side and mirror the fit around the peak for the EW and FWHM measurements. The EWs and FWHM for the lines are determined using the methods described in § 7.3.1. The results are shown in Table 7.2. Errors in these measurements are negligible owing to the high SNRs of the composite spectra. Compared to normal quasars, the N-rich quasars have $\sim 40\%$ stronger Lyα and N v emission, and $\sim 100\%$ stronger O i $\lambda 1304$ emission. Their C iv and C iii] line widths are 20–25% smaller, as we find in § 7.3.1.

The radio-loud fraction (RLF) of optically-selected quasars is a strong function of redshift and optical luminosity. We calculate the RLF for our N-rich sample following Jiang et al. (2007b). Radio loudness R is defined by $R = f_{6cm}/f_{2500}$, where f_{6cm} is the observed flux density at rest-frame 6 cm derived from FIRST (if detected) assuming a power-law slope of -0.5. When quasars with $R > 10$ are defined as radio-loud, FIRST is able to detect radio-loud quasars down to $i \approx 18.9$ (Jiang et al., 2007b). We find that the RLF in the N iii]-rich quasars is 26% and in the N iv]-rich quasars is 69%. The RLF in quasars with both N iv] and N iii] lines even reaches 80%, significantly higher than the RLF $\sim 8\%$ found in normal SDSS quasars with similar redshift and luminosity (Jiang et al., 2007b). This suggests that the N iv] and N iii] emission in these quasars are related to the quasar radio properties.

Central black hole masses of quasars can be estimated using mass scaling relations based on broad emission line widths and continuum luminosities. The scaling relations are written as $M_{BH} \propto FWHM^2 L_{opt}^{\beta}$, where L_{opt} is optical luminosity and $\beta \approx 0.5$. Strong emission lines such as Mg ii and C iv have been widely used to determine black hole masses (e.g. McLure & Dunlop, 2004; Vestergaard & Peterson, 2006; Shen et al., 2008). Based on the similar luminosities and FWHM of Mg ii in Table 7.2, the black hole masses in the two quasar subsets are consistent.

Photoionization models have shown that a series of emission-line ratios can be used to estimate gas metallicity in the broad line region of quasars (Hamann et
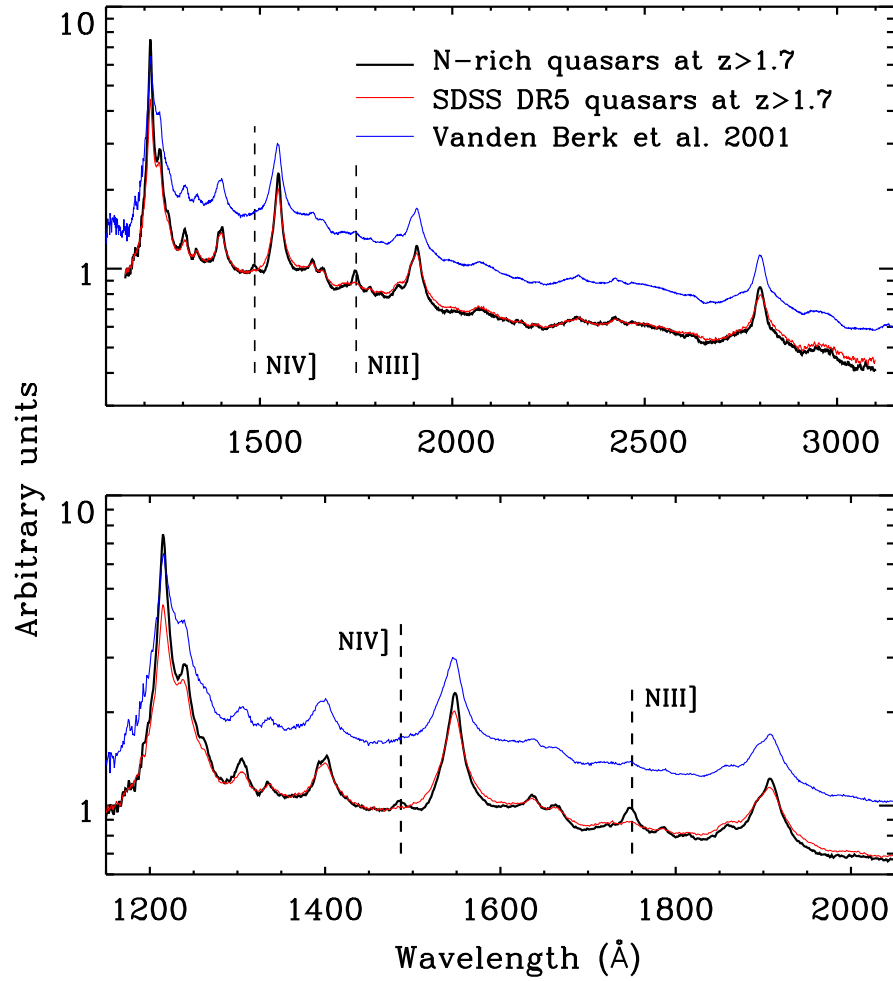
Figure 7.4 Composite spectra for the N-rich quasars (black) and SDSS DR5 quasars (red) at $z > 1.7$. The dashed lines indicate the positions of N IV] and N III]. For comparison, the blue lines show the composite spectrum of Vanden Berk et al. (2001).

al., 2002; Nagao et al., 2006). In particular, the relative nitrogen abundance is a good metallicity indicator if it serves as a secondary element so that N/O$\propto$O/H. By definition, N-rich quasars have much stronger N IV] or N III] emission. They also have stronger Lyα and N V emission. Since N V, N IV], and N III] have a range of critical densities and ionization parameters, stronger N V, N IV], and N III] emission shows higher nitrogen abundance, and higher metallicities if the relation N/O$\propto$O/H holds in these quasars. For example, a $\sim 40\%$ stronger N V/C IV ratio in N-rich quasars in Table 7.2 indicates a $\sim 40\%$ higher metallicity according to Hamann et al. (2002). However, the strengths of most other emission lines in N-rich quasars are similar to those in normal quasars, and thus the metallicities measured from line ratios other than nitrogen (Nagao et al., 2006) would be consistent for the two samples, which is contrary to the results from nitrogen. Therefore, stronger N V, N IV], and N III] emission in N-rich quasars may not indicate a higher overall metallicity; instead, it simply means a larger nitrogen abundance. The nitrogen enrichment in these quasars could significantly deviate from the usual N/O$\propto$O/H scaling.

7.4   Summary

We have obtained a sample of 293 SDSS quasars with strong N IV] or N III] emission lines at $z > 1.7$. The fraction of N-rich quasars is about 1.1%. The comparison between these N-rich quasars and normal quasars shows that the two quasar subsets have similar: (1) redshift and luminosity distributions; (2) UV continuum slopes; (3) line strengths and widths for most emission lines; and (4) central black hole masses. However, the N-rich quasars have: (1) $\sim 40\%$ stronger Lyα and N V emission. Strong nitrogen emission in all ionization states indicates high overall nitrogen abundances. (2) $20 - 25\%$ narrower widths of the C IV and C III] lines; and (3) a much higher RLF. Almost all the quasars with both N IV] and N III] lines are radio-loud.

The most intriguing difference between the two quasar subsets is the much higher RLF of N-rich quasars. We notice that Q0353-383 is also a radio-loud quasar with $R \approx 130$ based on the optical observation of Osmer & Smith (1980) and the radio

observation of Condon et al. (1998). Also the N IV] and N III] lines are rarely seen in normal galaxies, but they seem more common in luminous radio galaxies with AGN signatures. For example, the two lines were detected at $\geq 5\sigma$ significance in 67% radio galaxies in the sample of Vernet et al. (2001). All these results indicate that the nitrogen abundance is tightly related to quasar radio properties: perhaps the high nitrogen abundance in N-rich quasars is an indicator of a special quasar evolution stage, in which the radio activity is also very strong. Detailed models, which are beyond the scope of this letter, have to explain all the distinguishing features of N-rich quasars found in this work.

CHAPTER 8

SUMMARY AND FUTURE WORK

In CHAPTER 2 we present Gemini NIR spectroscopic observations of six luminous quasars at $z = 5.8 \sim 6.3$. Five of them were observed using Gemini-South/GNIRS, which provides a simultaneous wavelength coverage of 0.9–2.5 μm in cross dispersion mode. The other source was observed in K band with Gemini-North/NIRI. We calculate line strengths for all detected emission lines and use their ratios to estimate gas metallicity in the BLRs of the quasars. The metallicity is found to be supersolar with a typical value of ~ 4 $Z_\odot$, and a comparison with low-redshift observations shows no strong evolution in metallicity up to $z \sim 6$. The Fe II/Mg II ratio of the quasars is 4.9 ± 1.4, consistent with low-redshift measurements. We estimate central BH masses of 10^9 to 10^{10} $M_\odot$ and Eddington luminosity ratios of order unity. We identify two Mg II $\lambda\lambda 2796,2803$ absorbers with rest equivalent width $W_0^{\lambda 2796} > 1$ Å at $2.2 < z < 3$ and three Mg II absorbers with $W_0^{\lambda 2796} > 1.5$ Å at $z > 3$ in the spectra, with the two most distant absorbers at $z = 4.8668$ and 4.8823, respectively. The redshift number densities (dN/dz) of Mg II absorbers with $W_0^{\lambda 2796} > 1.5$ Å are consistent with no cosmic evolution up to $z > 4$.

In CHAPTER 3 we present *Spitzer* observations of thirteen $z \sim 6$ quasars using IRAC and MIPS. All the quasars except SDSS J0005−0006 were detected with high S/N in the four IRAC channels and the MIPS 24μm band, while SDSS J0005−0006 was marginally detected in the IRAC 8.0μm band, and not detected in the MIPS 24μm band. We find that most of these quasars have prominent emission from hot dust as evidenced by the observed 24μm fluxes. Their SEDs are similar to those of low-redshift quasars at rest-frame 0.15−3.5 μm, suggesting that accretion disks and hot-dust structures for these sources already have reached maturity. However, SDSS J0005−0006 has an unusual SED that lies significantly below low-redshift SED templates at rest-frame 1 and 3.5 μm, and thus shows a strong NIR deficit and no

hot-dust emission. Type I quasars with extremely small NIR-to-optical flux ratios like SDSS J0005–0006 are not found in low-redshift quasar samples, indicating that SDSS J0005−0006 has different dust properties at high redshift. We combine the *Spitzer* observations with X-ray, UV/optical, mm/submm and radio observations to determine bolometric luminosities for all the quasars. We find that the four quasars with central BH mass measurements have Eddington ratios of order unity.

In *Spitzer* cycle-3, we obtained deep MIPS 24μm images (3 hours) for SDSS J0005–0006, but still did not detect this object. In *Spitzer* cycle-4 we observed 9 more quasars at $z \sim 6$, and we discovered another hot-dust-free quasar SDSS J0303–0019 ($z = 6.07$), which was not detected in our MIPS 24μm images with one-hour exposure. The two quasars both have very narrow emission lines (Lyα widths ~ 1600 km s^{-1}). But they are still type 1 quasars with blue UV continuum. We define these quasars (line widths less than 2000 km s^{-1}) as narrow-line type 1 quasars (NLQ1s). The two NLQ1s at $z \sim 6$ are not simply the luminous counterparts of narrow-line Seyfert 1 galaxies (NLS1s), since NLS1s tend to have stronger IR emission compared to other Seyfert galaxies.

As we discussed in CHAPTER 3, there are two major possibilities to explain the existence of the two hot-dust-free quasars at high redshift. One is the cosmic dust evolution, i.e., the dust properties at $z \sim 6$ differ from those in lower-redshift quasars. This predicts that such quasars only exist at high redshift. The other one is the quasar evolution, i.e., these NLQ1s could be in their early evolution stage, and have not had time to form mature dust tori around them. This predicts that such objects exist at all redshifts. The fact that we did not find any low-redshift NLQ1s so far seems to favor the first explanation. However, this could be due to the selection effect. Our search in the SDSS database shows that NLQ1s (FWHM < 2000 km s^{-1}) only count for ≤ 1 % of the SDSS quasars at $z < 5$. Current *Spitzer* observations have not yet sampled any of these rare objects, while wide-field surveys such as SWIRE do not go deep enough.

To differentiate the two models, we are observing 10 NLQ1s spanning a redshift range of $1 < z < 4.5$ in *Spitzer* cycle-5. These NLQ1s were selected from the SDSS

quasar catalog and have emission line widths (C IV and/or Mg II) between 1500 and 1900 km s^{-1}. If a significant fraction of this sample turn out to be hot-dust free, then the existence of the two hot-dust-free quasars at $z \sim 6$ cannot be explained by the cosmic dust evolution. However, we must pay attention to the following two facts. One is that the two high-redshift quasars have normal X-ray emission, so the narrow emission lines are not caused by strong obscuration. For the purpose of comparison, the 10 NLQ1s at low redshift may not have strong obscuration either. We plan to observe them in the next *Chandra* cycle. The other one is that the fraction of NLQ1s at $z \sim 6$ is much higher than the fraction at lower redshift. Even most of the 10 NLQ1s do not have hot dust, the fraction of hot-dust-free quasars at $z \sim 6$ is still significantly higher than that in low-redshift quasars, if most hot-dust-free quasars are NLQ1s.

In CHAPTER 4 we present the discovery of five quasars at $z \sim 6$ selected from 260 deg^2 of the SDSS southern survey, a deep imaging survey obtained by repeatedly scanning a stripe along the Celestial Equator. The five quasars with $20 < z_{AB} < 21$ are 1–2 magnitudes fainter than the luminous $z \sim 6$ quasars discovered in the SDSS main survey. These quasars, combined with another $z \sim 6$ quasar known in this region, make a complete flux-limited quasar sample at $z_{AB} < 21$. The sample spans the redshift range $5.85 \leq z \leq 6.12$ and the luminosity range $-26.5 \leq M_{1450} \leq -25.4$. We use the $1/V_a$ method to determine that the comoving quasar spatial density at $\langle z \rangle = 6.0$ and $\langle M_{1450} \rangle = -25.8$ is $(5.0 \pm 2.1) \times 10^{-9}$ Mpc^{-3} mag^{-1}. We model the bright-end QLF at $z \sim 6$ as a power law $\Phi(L_{1450}) \propto L_{1450}^{\beta}$. The slope β calculated from a combination of our sample and the luminous SDSS quasar sample is -3.1 ± 0.4, significantly steeper than the slope of the QLF at $z \sim 4$. Based on the derived QLF, we find that the quasar/AGN population cannot provide enough photons to ionize the intergalactic medium (IGM) at $z \sim 6$ unless the IGM is very homogeneous and the luminosity (L_{1450}^*) at which the QLF power law breaks is very low.

The quasars in this chapter were selected from the SDSS coadded images with 5–18 runs, and they are not deep enough to probe the break luminosity in the QLF.

Currently the SDSS deep stripe has been scanned more than 60 times, reaching ~ 3 magnitudes deeper than the main survey when co-added. The depth and the area coverage enable us to discover fainter and higher-redshift quasars. We are performing a deeper survey of $z \sim 6$ quasars down to $z_{AB} \sim 22$ or even ~ 22.5 in this region. We have obtained two quasars with $z_{AB} > 21$, with the faintest one at $z_{AB} = 21.6$. We expect to obtain a flux-limited sample with $z_{AB} < 22.5$, and reach the break luminosity in the QLF in the near future. The challenge of this survey is the follow-up spectroscopic observations. Even with the new upgraded deeply-depleted red chip on MMT, quasar candidates with $z_{AB} \sim 22$ can be barely identified in 30 min under normal weather conditions.

In CHAPTER 5 we present our deep spectroscopic survey of faint quasars in the SDSS southern survey. Quasar candidates were selected from the deep data with good completeness over $0 < z < 5$, and 2 to 3 magnitudes fainter than the SDSS main survey. Spectroscopic follow-up was carried out on the 6.5m MMT with Hectospec. The sample of this SDSS faint quasar survey (SFQS) covers ~ 3.9 deg^2, contains 414 quasars, and reaches $g = 22.5$. The overall selection efficiency is $\sim 66\%$ ($\sim 80\%$ at $g < 21.5$); the efficiency in the most difficult redshift range ($2 < z < 3$) is better than 40%. We use the $1/V_a$ method to derive a binned estimate of the QLF and model the QLF using maximum likelihood analysis. The best model fits confirm previous results showing that the QLF has steep slopes at the bright end and much flatter slopes (-1.25 at $z \leq 2.0$ and -1.55 at $z \geq 2.0$) at the faint end, indicating a break in the QLF slope. Using a luminosity-dependent density evolution model, we find that the quasar density at $M_g < -22.5$ peaks at $z \sim 2$, which is later in cosmic time than the peak of $z \sim 2.5$ found from surveys of more luminous objects. The SFQS QLF is consistent with the results of the 2dF QSO Redshift Survey, the SDSS, and the 2dF-SDSS LRG and QSO Survey, but probes fainter quasars.

As we mentioned in CHAPTER 5, the current SFQS sample is still small, and the QLF at $z > 2.0$ is not well determined (due to the limited number of quasars in this redshift range). We plan to use MMT/Hectospec to carry out a larger ($10 \sim 20$ deg^2) spectroscopic survey of faint quasars/AGNs at $z > 2.2$. At $z > 2.2$, the strong

Lyα emission line enters the wavelength range that Hectospec covers, so it becomes much easier to identify quasars from low S/N spectra. Our pilot observations show that we are able to reach $i \sim 23$ for quasars at $z > 2.2$ using Hectospec with only 60 min exposure.

In CHAPTERs 6 and 7 we present two interesting topics about low-redshift quasars. In CHAPTER 6 we determine the radio-loud fraction (RLF) of quasars as a function of redshift and optical luminosity, using a sample of optically-selected quasars from SDSS. The sample contains more than 30,000 objects and spans a redshift range of $0 < z \leq 5$ and a luminosity range of $-30 \leq M_i < -22$. We use both the radio-to-optical flux ratio (R parameter) and radio luminosity to define radio-loud quasars. After breaking the degeneracy between redshift and luminosity due to the flux-limited nature of the sample, we find that the RLF of quasars decreases with increasing redshift and decreasing luminosity. The relation can be described in the form of $\log(\mathrm{RLF}/(1\text{–}\mathrm{RLF})) = b_0 + b_z \log(1 + z) + b_M(M_{2500} + 26)$, where M_{2500} is the absolute magnitude at rest-frame 2500 Å, and b_z, $b_M < 0$. When using $R > 10$ to define radio-loud quasars, we find that $b_0 = -0.132 \pm 0.116$, $b_z = -2.052 \pm 0.261$, and $b_M = -0.183 \pm 0.025$. The RLF at $z = 0.5$ declines from 24.3% to 5.6% as luminosity decreases from $M_{2500} = -26$ to $M_{2500} = -22$, and the RLF at $M_{2500} = -26$ declines from 24.3% to 4.1% as redshift increases from 0.5 to 3, suggesting that the RLF is a strong function of both redshift and luminosity. We also examine the impact of flux-related selection effects on the RLF determination using a series of tests, and find that the dependence of the RLF on redshift and luminosity is highly likely to be physical, and the selection effects we considered are not responsible for the dependence.

In CHAPTER 7 we report on 293 quasars with strong N IV] λ1486 or N III] λ1750 emission lines (rest-frame equivalent width > 3 Å) at $1.7 < z < 4.0$ selected from the SDSS Fifth Data Release. These nitrogen-rich (N-rich) objects comprise $\sim 1.1\%$ of the SDSS quasars. The comparison between the N-rich quasars and other quasars shows that the two quasar subsets share many common properties. We also confirm previous results that N-rich quasars have much stronger Lyα and N V λ1240

emission lines. Strong nitrogen emission in all ionization states indicates high overall nitrogen abundances in these objects. We find evidence that the nitrogen abundance is closely related to quasar radio properties. The RLF in the N III]-rich quasars is 26% and in the N IV]-rich quasars is 69%, significantly higher than $\sim 8\%$ measured in other quasars with similar redshift and luminosity. Therefore, the high nitrogen abundance in N-rich quasars could be an indicator of a special quasar evolution stage, in which the radio activity is also strong.

APPENDIX A

QUASAR SAMPLE FOR THE SFQS SURVEY

Column 1: Quasar name

Column 2: Redshift

Column 3: SDSS g magnitude

Column 4: Absolute g-band magnitude

Column 5: Power-law continuum slope ($f_\nu \propto \nu^\alpha$)

Table A.1.   Quasar Sample for the SFQS Survey

Name (J2000 Coordinates)	Redshift	g	M_g	α
SDSS J231601.68−001237.0	2.00	21.69	−23.08	−0.23
SDSS J231548.40−003022.7	1.53	20.73	−23.60	−0.44
SDSS J231527.54−001353.8	1.33	20.97	−23.26	−0.54
SDSS J231541.51−003137.2	1.72	21.73	−22.61	−0.31
SDSS J231422.26+000315.7	3.22	21.38	−24.05	0.10
SDSS J231442.27−000937.2	3.30	21.09	−25.26	−0.49
SDSS J231534.22−002610.0	0.58	21.29	−21.02	−1.07
SDSS J231519.33−001129.5	3.06	22.17	−24.47	−1.10
SDSS J231504.04−001434.2	2.10	22.17	−23.05	−0.41
SDSS J231446.30−002206.9	2.97	21.97	−24.12	−0.69
SDSS J231504.13−001635.0	2.06	20.52	−24.45	−0.22
SDSS J231448.45−002005.5	1.88	20.83	−23.65	−0.14
SDSS J231537.39−001100.4	1.86	21.72	−22.53	0.10
SDSS J231432.38−001250.5	0.58	21.34	−20.94	−1.10
SDSS J231533.75−000602.0	2.10	22.26	−22.65	−0.73
SDSS J231512.82−000852.7	1.85	21.39	−24.74	−1.10
SDSS J231459.75−001309.0	2.55	21.43	−23.69	−0.12
SDSS J231522.26−000857.4	1.64	21.64	−22.90	−0.39
SDSS J231417.58−000537.4	1.85	20.98	−24.71	−1.10
SDSS J231423.92−001002.4	1.84	20.69	−23.68	−0.05
SDSS J231456.13−000509.4	0.74	21.49	−21.49	−0.80
SDSS J231440.42−000810.1	1.51	20.88	−23.83	−0.68
SDSS J231458.39−000550.4	1.70	21.77	−22.91	−0.53
SDSS J231424.19−000811.0	1.76	21.64	−22.49	0.06
SDSS J231436.88−000259.4	1.32	21.69	−22.18	−0.34
SDSS J231429.20+000720.4	1.93	21.76	−22.76	−0.28
SDSS J231521.34+000052.1	2.56	21.65	−23.32	−0.09
SDSS J231502.74+000853.5	1.69	21.28	−22.98	−0.06
SDSS J231436.31+001121.1	2.05	20.58	−23.92	0.04
SDSS J231500.77+002047.2	1.81	22.26	−23.23	−1.10
SDSS J231531.28+000752.6	2.12	20.69	−24.04	−0.08
SDSS J231524.06+001023.4	2.17	20.55	−24.94	−0.62
SDSS J231509.70+001504.0	1.56	20.60	−24.20	−0.69
SDSS J231548.39+000723.9	3.26	21.80	−24.69	−0.64
SDSS J231531.47+001531.1	2.04	20.82	−23.87	0.02
SDSS J231608.87−000034.6	2.11	22.31	−23.32	−0.64
SDSS J231556.45+001336.8	1.81	21.48	−22.93	−0.23
SDSS J231622.74+002404.5	1.77	20.67	−23.71	−0.17

Table A.1 (cont'd)

Name (J2000 Coordinates)	Redshift	g	M_g	α
SDSS J231612.63+001959.7	1.17	22.35	−21.52	−0.31
SDSS J231609.86+001608.5	1.41	20.90	−23.79	−0.79
SDSS J231613.37+000334.6	1.38	21.48	−22.65	−0.30
SDSS J231648.94+001920.7	0.81	21.37	−21.80	−1.10
SDSS J231638.26+001654.4	2.71	21.72	−23.47	−0.49
SDSS J231718.48+002039.5	1.10	22.08	−21.55	−0.39
SDSS J231632.48+000804.9	0.91	20.59	−22.76	−0.79
SDSS J231649.90+001136.8	1.64	22.40	−22.24	−0.38
SDSS J231647.83+001234.5	1.42	20.25	−24.10	−0.49
SDSS J231731.07+001225.5	1.59	20.41	−23.87	−0.38
SDSS J231703.95+000903.5	1.03	22.28	−21.36	−0.77
SDSS J231735.25+001415.5	2.53	21.99	−23.46	−0.58
SDSS J231735.69+000531.1	3.70	22.56	−25.25	−1.10
SDSS J231738.45+001154.6	1.58	21.72	−22.82	−0.43
SDSS J231708.37+000311.8	2.68	22.00	−22.71	0.10
SDSS J231747.31+001147.4	2.10	21.14	−24.56	−1.06
SDSS J231742.36+000757.4	1.27	21.92	−22.31	−0.94
SDSS J231644.70+000042.7	2.19	21.96	−23.00	−0.44
SDSS J231721.82−000222.0	1.52	20.81	−23.69	−0.53
SDSS J231629.44−000047.2	2.34	21.82	−24.42	−1.10
SDSS J231805.75+000034.7	1.11	21.35	−22.66	−0.93
SDSS J231758.23−000145.1	3.27	21.36	−24.03	0.10
SDSS J231733.78−000255.8	2.32	22.22	−22.88	−0.54
SDSS J231725.14−000453.0	1.64	22.30	−22.69	−0.93
SDSS J231706.69−000346.4	1.16	21.46	−22.24	−0.41
SDSS J231736.85−001415.8	0.72	19.16	−23.71	−1.10
SDSS J231719.53−001154.8	1.53	21.33	−23.07	−0.60
SDSS J231735.45−001052.8	1.39	21.99	−22.59	−0.87
SDSS J231726.20−001035.2	1.73	21.95	−22.77	−0.39
SDSS J231708.19−001146.4	1.93	21.82	−24.03	−1.10
SDSS J231750.85−001749.1	2.32	20.83	−24.29	−0.26
SDSS J231712.34−001244.4	2.08	21.08	−23.53	0.00
SDSS J231640.79−000818.5	0.64	22.22	−19.85	0.03
SDSS J231744.81−001805.4	1.07	21.46	−21.89	−0.13
SDSS J231704.67−001903.6	1.98	21.29	−23.39	−0.20
SDSS J231616.40−000756.3	1.12	20.86	−22.82	−0.38
SDSS J231617.48−000718.6	0.59	21.54	−21.06	−1.10
SDSS J231655.14−002940.4	0.98	22.25	−21.50	−0.80

Table A.1   (cont'd)

Name (J2000 Coordinates)	Redshift	g	M_g	α
SDSS J231656.44−002240.9	3.08	21.33	−25.22	−0.75
SDSS J231653.93−002617.0	1.10	20.34	−23.45	−0.63
SDSS J231650.03−002047.5	1.09	21.02	−22.67	−0.31
SDSS J231657.55−002629.7	1.31	21.75	−23.02	−1.10
SDSS J231619.46−003015.0	1.42	21.19	−22.47	0.10
SDSS J231624.34−003009.1	1.97	21.92	−22.55	−0.20
SDSS J231612.72−002250.7	0.63	20.69	−21.70	−0.64
SDSS J231610.69−000330.6	1.29	21.23	−22.98	−0.51
SDSS J231719.36+001807.3	2.41	21.60	−23.09	0.10
SDSS J231711.41−000613.6	1.72	20.85	−23.56	−0.26
SDSS J231732.23+000346.6	0.51	20.95	−21.23	−1.10
SDSS J231714.42−000455.0	2.94	19.74	−26.09	−0.45
SDSS J231719.96−001906.5	0.76	20.69	−22.45	−1.04
SDSS J231618.33−001016.2	1.62	21.88	−23.05	−0.74
SDSS J231624.16−001336.0	2.29	21.39	−24.19	−0.61
SDSS J233827.72−002200.4	1.26	19.73	−24.01	−0.10
SDSS J233848.81−001831.0	1.21	21.18	−23.54	−1.10
SDSS J233907.99−002959.2	1.84	21.74	−22.61	−0.01
SDSS J233839.04−000912.8	2.12	21.30	−24.22	−0.78
SDSS J233917.10+000225.4	1.21	20.71	−23.24	−0.53
SDSS J233836.86+001349.4	1.38	20.39	−23.64	−0.19
SDSS J233909.44+000459.1	3.44	22.00	−24.66	−0.30
SDSS J233901.46−002131.4	1.98	22.18	−23.45	−0.82
SDSS J233842.94−003036.1	2.70	20.18	−25.02	−0.10
SDSS J233917.28−002022.4	1.04	21.57	−22.59	−1.10
SDSS J233849.17−001325.6	1.99	20.38	−24.99	−0.78
SDSS J233837.99−001353.8	2.70	21.38	−24.19	−0.38
SDSS J233807.84−001317.6	2.61	21.84	−23.53	−0.22
SDSS J233750.68−001513.3	1.82	20.75	−24.72	−0.93
SDSS J233807.40−000728.0	1.63	21.62	−22.92	−0.37
SDSS J233753.09−000645.0	1.78	20.70	−24.84	−1.10
SDSS J233924.90−000600.5	1.90	22.08	−22.59	−0.24
SDSS J233845.45−000331.8	2.97	19.85	−26.23	−0.36
SDSS J233806.64+000754.8	2.12	21.55	−23.16	−0.41
SDSS J233902.93−000104.4	1.10	21.57	−22.59	−1.01
SDSS J233806.62+000631.3	0.92	20.17	−23.60	−1.10
SDSS J233843.20+000913.9	1.92	20.60	−24.29	−0.47
SDSS J233849.51+001149.8	1.19	20.73	−23.24	−0.52

Table A.1 (cont'd)

Name (J2000 Coordinates)	Redshift	g	M_g	α
SDSS J233839.11+001807.7	1.36	21.16	−22.89	−0.33
SDSS J233938.05+000952.6	1.04	21.03	−22.53	−0.42
SDSS J233944.57+001016.1	1.47	21.51	−22.52	−0.16
SDSS J233940.23+001220.2	2.56	22.33	−23.42	−0.75
SDSS J234006.05+001541.0	2.13	20.96	−24.45	−0.86
SDSS J234003.27+001647.4	2.11	21.79	−24.24	−0.95
SDSS J233954.28+000543.4	2.21	21.61	−24.23	−1.10
SDSS J234026.13+000904.5	3.10	21.89	−23.62	0.10
SDSS J234042.33+001650.0	1.92	20.67	−25.10	−1.10
SDSS J234024.55+001506.9	1.65	21.30	−23.15	−0.28
SDSS J234004.84+000415.3	2.87	21.57	−23.46	0.10
SDSS J234027.26+001422.2	2.41	21.40	−23.83	−0.52
SDSS J234052.35+001148.7	2.48	20.32	−24.39	−0.25
SDSS J234012.98+000201.2	1.32	21.89	−22.00	−0.22
SDSS J234019.49−000321.2	2.88	21.37	−24.56	−0.48
SDSS J234101.13+000032.2	2.63	20.41	−24.46	0.10
SDSS J234052.72−000044.1	1.85	20.11	−24.64	−0.35
SDSS J234048.99−000708.1	1.01	21.06	−22.78	−1.03
SDSS J234139.90−000719.8	0.93	21.49	−22.06	−0.93
SDSS J234040.31−000642.4	1.14	22.10	−21.66	−0.46
SDSS J234141.09−000503.1	0.86	22.07	−21.15	−1.03
SDSS J234033.47−000558.3	1.48	20.44	−24.06	−0.55
SDSS J234135.94−001326.7	0.99	21.30	−22.62	−1.00
SDSS J234028.47−000912.4	1.61	22.07	−22.65	−0.59
SDSS J234027.43−000834.2	1.45	20.68	−23.68	−0.51
SDSS J234057.76−002431.7	1.61	20.34	−24.22	−0.37
SDSS J234029.67−001634.6	1.00	20.84	−22.80	−0.56
SDSS J234103.45−002341.5	1.80	22.44	−22.31	−0.42
SDSS J234020.63−002408.3	2.20	20.22	−25.21	−0.49
SDSS J234006.67−001644.7	1.08	21.73	−22.53	−1.00
SDSS J234007.97−001527.4	1.11	21.42	−22.34	−0.50
SDSS J234030.83−002700.8	2.00	21.15	−23.38	0.04
SDSS J234009.54−001656.0	1.03	20.31	−23.44	−0.55
SDSS J234015.43−003356.0	1.91	21.22	−23.84	−0.57
SDSS J234015.73−002834.5	3.29	22.10	−24.19	−0.25
SDSS J233939.00−002151.5	0.77	21.83	−21.24	−1.10
SDSS J233951.89−002907.0	2.61	21.69	−22.89	0.10
SDSS J233943.87−003132.6	1.56	21.44	−23.18	−0.54

Table A.1 (cont'd)

Name (J2000 Coordinates)	Redshift	g	M_g	α
SDSS J233947.36−001459.8	2.02	20.76	−24.09	−0.31
SDSS J233947.14−003457.3	1.47	20.77	−23.48	−0.35
SDSS J233913.04−003320.9	1.77	22.36	−22.48	−0.50
SDSS J233917.87−002943.5	1.34	18.72	−25.94	−0.79
SDSS J233934.42−002932.6	2.02	20.73	−25.55	−1.10
SDSS J234042.74+000646.7	2.19	21.20	−23.63	−0.20
SDSS J233954.48+000006.7	2.37	22.17	−23.76	−1.10
SDSS J234023.52−000431.4	1.32	21.81	−22.30	−0.52
SDSS J234137.04−000038.5	2.33	20.93	−24.92	−1.09
SDSS J234021.91−000941.5	2.50	20.56	−25.57	−0.95
SDSS J234059.86−002734.6	2.50	21.65	−23.48	−0.17
SDSS J020309.32−001746.5	1.10	21.96	−21.81	−0.42
SDSS J020305.23−001951.7	1.36	21.27	−23.50	−1.10
SDSS J020327.45+000842.4	2.91	22.51	−24.30	−1.10
SDSS J020340.92−002437.6	2.04	21.35	−23.80	−0.83
SDSS J020323.80−002428.0	1.69	20.87	−24.33	−0.92
SDSS J020333.53−002819.3	1.69	20.84	−23.56	−0.17
SDSS J020340.21−002238.5	1.92	20.29	−25.08	−0.82
SDSS J020323.59−002259.3	1.33	20.59	−23.39	−0.05
SDSS J020304.92−002437.2	1.24	20.47	−23.56	−0.31
SDSS J020346.42−001334.7	1.45	22.04	−22.42	−0.64
SDSS J020333.02−000845.9	1.81	20.85	−24.63	−1.10
SDSS J020306.09−001338.7	1.20	20.71	−23.50	−0.58
SDSS J020329.18−001203.7	1.14	22.39	−22.02	−1.10
SDSS J020252.82−001634.5	3.55	21.99	−24.73	0.04
SDSS J020328.34−000903.0	0.97	21.08	−22.43	−0.57
SDSS J020243.19−001431.8	0.82	21.96	−21.00	−0.99
SDSS J020218.46−000609.4	2.02	21.02	−24.37	−1.10
SDSS J020221.85+000009.9	1.58	22.23	−22.63	−0.89
SDSS J020302.57+000216.8	1.89	21.49	−23.75	−0.68
SDSS J020231.97+000526.4	1.08	20.59	−23.12	−0.52
SDSS J020229.43+000844.8	0.76	20.27	−22.51	−0.46
SDSS J020346.05−000233.5	1.64	21.79	−22.30	−0.14
SDSS J020225.34+000833.9	1.94	22.34	−23.02	−1.10
SDSS J020245.82+000848.5	2.22	21.85	−23.93	−1.10
SDSS J020345.25−000006.3	3.15	22.66	−24.64	−1.10
SDSS J020241.27+001311.6	0.78	20.81	−22.52	−1.10
SDSS J020359.95−000014.2	1.62	22.14	−22.50	−0.46

Table A.1 (cont'd)

Name (J2000 Coordinates)	Redshift	g	M_g	α
SDSS J020400.35+000142.2	3.32	22.25	−23.56	−0.04
SDSS J020351.49+001051.3	0.56	20.35	−21.86	−1.04
SDSS J020342.18+001104.2	1.68	22.49	−22.18	−0.42
SDSS J020410.20+001023.7	2.44	20.52	−24.18	0.10
SDSS J020410.03+000349.9	1.64	21.70	−23.15	−0.89
SDSS J020421.41+001311.5	0.93	19.24	−23.79	−0.18
SDSS J020414.38+000718.0	1.89	22.09	−22.54	−0.26
SDSS J020509.34+001950.2	1.77	20.87	−24.40	−0.98
SDSS J020447.32+001344.7	2.44	20.30	−25.15	−0.32
SDSS J020434.90+000908.3	1.99	21.04	−24.09	−0.48
SDSS J020511.71+001232.8	0.83	21.45	−21.89	−1.10
SDSS J020512.07+001830.7	1.47	21.54	−23.33	−1.09
SDSS J020447.94+000633.6	1.81	21.88	−22.56	−0.06
SDSS J020512.72+001536.3	0.55	20.80	−21.58	−1.10
SDSS J020532.10+001113.5	1.73	20.28	−23.97	−0.02
SDSS J020536.97+000553.7	1.81	21.99	−24.27	−1.10
SDSS J020555.18+000440.1	1.67	21.42	−23.08	−0.25
SDSS J020516.81+000116.5	1.66	21.91	−23.44	−1.10
SDSS J020538.10+000347.8	1.79	20.70	−23.38	0.10
SDSS J020523.65−000103.9	1.73	22.21	−23.03	−0.91
SDSS J020457.39−000334.9	1.78	21.31	−23.65	−0.67
SDSS J020435.48−000427.3	1.17	21.72	−22.24	−0.52
SDSS J020516.68−000708.5	1.18	21.89	−22.16	−0.80
SDSS J020535.69−001220.0	1.03	21.70	−21.89	−0.93
SDSS J020440.07−000715.7	3.79	23.09	−23.75	0.10
SDSS J020543.76−001534.9	2.50	22.34	−23.23	−0.88
SDSS J020538.79−001425.2	1.40	22.00	−22.10	−0.49
SDSS J020505.38−001626.1	0.59	20.72	−21.44	−0.48
SDSS J020513.55−001446.6	1.81	21.36	−23.82	−0.78
SDSS J020502.07−001505.8	2.07	22.16	−22.56	−0.09
SDSS J020532.78−001918.3	1.86	20.50	−24.09	−0.27
SDSS J020516.25−001630.6	2.34	21.87	−23.31	−0.51
SDSS J020455.19−002618.8	1.66	21.33	−23.58	−0.67
SDSS J020431.13−001641.3	1.78	21.87	−23.25	−0.98
SDSS J020421.69−002811.6	1.06	22.25	−21.51	−0.82
SDSS J020404.53−003102.7	1.21	21.76	−22.30	−0.52
SDSS J020516.98+001040.5	1.34	20.63	−23.79	−0.62
SDSS J020442.34+002141.3	2.57	21.30	−24.45	−0.67

Table A.1 (cont'd)

Name (J2000 Coordinates)	Redshift	g	M_g	α
SDSS J020416.39−000003.6	2.58	21.09	−24.13	−0.18
SDSS J020443.42+001816.9	2.87	20.23	−25.09	−0.14
SDSS J020451.83−000649.8	1.40	20.88	−23.43	−0.54
SDSS J020543.63−001041.8	2.55	20.89	−24.92	−0.59
SDSS J020510.83−001924.5	1.55	20.54	−23.57	0.01
SDSS J020502.81−001739.1	3.60	21.03	−25.54	−0.06
SDSS J020523.88−001639.6	0.65	20.08	−22.13	−0.10
SDSS J020327.40−001626.0	1.02	19.96	−23.54	−0.34
SDSS J020511.38+000046.2	1.98	19.94	−24.95	−0.34
SDSS J020251.01−000917.1	0.38	19.17	−21.94	−0.23
SDSS J233958.78−002736.1	0.62	20.53	−21.98	−1.29
SDSS J233939.85+001938.1	2.84	19.95	−26.42	−0.78
SDSS J231515.38−002923.8	2.10	20.00	−25.19	−0.26
SDSS J231621.99+002333.5	0.91	18.30	−25.22	−0.50
SDSS J020340.40−000201.8	1.74	19.31	−25.37	−0.53
SDSS J231446.50−000717.5	0.74	19.26	−23.69	−0.58
SDSS J231500.81−001831.3	1.32	18.68	−25.22	−0.11
SDSS J231503.28−002711.0	0.96	20.27	−23.35	−0.54
SDSS J231509.35+001026.3	0.85	17.48	−25.27	0.04
SDSS J231759.63−000733.2	1.15	18.96	−25.07	−0.62
SDSS J231644.49−002114.1	1.72	19.30	−24.97	−0.08
SDSS J231747.78+000615.8	0.84	19.79	−23.33	−0.63
SDSS J231742.60+000535.1	0.32	17.94	−22.77	−0.26
SDSS J231732.39−002211.0	1.59	19.53	−24.75	−0.42
SDSS J231635.00−002841.8	0.76	17.46	−25.12	−0.06
SDSS J231545.56−001923.9	1.93	20.01	−25.51	−0.88
SDSS J231546.87−000557.7	1.69	19.45	−25.16	−0.43
SDSS J231535.04+000127.8	0.59	20.12	−22.34	−1.25
SDSS J231445.11+000837.1	1.12	18.97	−24.58	−0.19
SDSS J231540.31+001848.4	2.01	19.22	−25.63	−0.33
SDSS J231654.02+000837.3	2.13	19.59	−25.40	−0.08
SDSS J231710.78+000859.6	1.68	19.23	−25.79	−0.70
SDSS J231726.31+001751.4	1.56	19.86	−24.52	−0.38
SDSS J231651.73+002314.9	1.79	18.93	−25.57	−0.15
SDSS J234110.27−002341.5	1.00	19.26	−24.14	−0.31
SDSS J233908.80−000637.8	0.48	17.58	−24.07	−0.32
SDSS J231521.10−000546.4	0.56	19.54	−22.64	−0.61
SDSS J231645.07+001114.8	1.64	20.35	−24.93	−1.06

Table A.1 (cont'd)

Name (J2000 Coordinates)	Redshift	g	M_g	α
SDSS J231623.34+002412.8	2.22	19.41	−25.85	−0.32
SDSS J231728.94+001703.0	0.81	19.49	−23.26	−0.20
SDSS J233820.63+000706.6	1.20	20.72	−23.48	−0.77
SDSS J233952.77−000840.1	0.71	19.88	−22.76	−0.39
SDSS J234018.95−000929.8	1.75	20.74	−23.97	−0.70
SDSS J234016.92+001335.7	1.89	19.54	−25.11	−0.16
SDSS J020240.71−001438.5	1.96	19.72	−24.87	−0.06
SDSS J020502.12−002343.3	1.97	19.95	−24.79	−0.21
SDSS J020523.55−000143.4	1.78	19.98	−24.22	0.01
SDSS J020319.92+002240.8	1.07	19.47	−24.07	−0.43
SDSS J020516.74+001510.8	1.60	20.19	−23.90	−0.11
SDSS J020341.34−000235.1	1.98	19.89	−25.15	−0.45
SDSS J020303.13−001022.2	1.96	19.54	−25.02	−0.23
SDSS J020312.50−001304.1	1.44	19.60	−24.54	−0.29
SDSS J020350.47−000751.2	1.64	19.56	−25.16	−0.45
SDSS J020537.87+000405.7	1.70	19.63	−24.80	−0.32
SDSS J213334.31−002127.9	1.88	21.70	−22.97	−0.14
SDSS J213214.83+000810.5	1.55	20.28	−24.54	−0.72
SDSS J213404.61−001906.6	0.73	21.65	−21.40	−1.02
SDSS J213408.80−002336.9	2.10	19.98	−25.62	−0.92
SDSS J213423.93−002128.6	2.10	20.84	−25.14	−1.10
SDSS J213349.62−000602.0	0.80	20.01	−23.30	−1.05
SDSS J213332.12−001630.2	1.94	21.20	−23.85	−0.39
SDSS J213316.19−000630.8	1.90	20.47	−24.69	−0.55
SDSS J213235.96−001350.7	2.50	18.76	−26.62	−0.36
SDSS J213245.05−000941.4	1.68	21.85	−22.73	−0.36
SDSS J213226.61−000908.0	4.30	22.66	−26.44	−0.69
SDSS J213310.24+000023.1	2.06	21.38	−23.69	−0.38
SDSS J213219.36−000800.5	3.27	21.79	−24.52	−0.30
SDSS J213300.46+000039.7	1.85	21.54	−23.60	−0.68
SDSS J213220.83+000219.5	2.98	21.01	−24.71	−0.36
SDSS J213220.99−000022.2	1.37	19.87	−24.37	−0.37
SDSS J213222.85+000116.3	1.50	19.82	−25.06	−0.75
SDSS J213204.11+000656.7	3.36	21.23	−24.28	0.10
SDSS J213310.43+000548.1	1.88	20.61	−25.08	−1.02
SDSS J213216.17+001447.7	1.50	21.59	−23.21	−0.82
SDSS J213202.72+001104.3	1.47	20.83	−23.55	−0.39
SDSS J213216.12+001057.1	2.15	20.99	−24.51	−0.75

Table A.1 (cont'd)

Name (J2000 Coordinates)	Redshift	g	M_g	α
SDSS J213225.38+001241.9	0.40	19.90	−21.37	−0.69
SDSS J213252.26+000938.2	1.22	22.02	−22.05	−0.56
SDSS J213231.84+002324.0	0.94	19.58	−23.46	−0.05
SDSS J213241.56+002126.3	1.76	20.19	−23.83	0.10
SDSS J213226.54+002618.9	1.99	19.73	−25.25	−0.26
SDSS J213249.76+002113.3	1.84	21.92	−23.52	−0.88
SDSS J213325.99+001344.2	0.88	21.17	−21.97	−0.66
SDSS J213256.31+002724.1	1.97	20.45	−25.58	−1.10
SDSS J213331.58+002652.0	1.69	21.10	−23.91	−0.72
SDSS J213336.60+003228.2	1.34	20.88	−23.12	−0.46
SDSS J213404.42+001555.4	1.60	21.10	−23.23	−0.42
SDSS J213401.83+002200.2	2.69	20.91	−24.02	0.10
SDSS J213429.47+003118.4	4.13	21.32	−27.89	−1.10
SDSS J213357.75+001604.4	1.55	20.13	−24.20	−0.30
SDSS J213417.73+002417.8	1.93	21.40	−24.37	−1.10
SDSS J213411.57+002802.1	1.34	19.55	−25.00	−0.77
SDSS J213425.43+003052.7	2.09	21.38	−23.65	−0.36
SDSS J213424.16+003252.0	1.75	19.64	−24.54	0.03
SDSS J213422.71+001646.4	1.45	21.49	−23.52	−1.10
SDSS J213446.24+002951.0	2.29	20.45	−24.02	0.10
SDSS J213500.27+002422.5	1.54	21.13	−23.40	−0.43
SDSS J213522.14+001602.8	0.53	19.15	−22.72	−0.50
SDSS J213451.54+001548.3	1.31	21.30	−22.50	−0.50
SDSS J213438.54+001304.0	1.34	18.92	−25.17	−0.43
SDSS J213525.17+001015.5	1.03	20.16	−23.64	−0.67
SDSS J213420.09+000729.5	2.49	20.97	−25.07	−1.10
SDSS J213459.71+000456.6	1.03	21.15	−22.17	−0.16
SDSS J213442.97+000151.7	2.08	20.76	−24.84	−1.10
SDSS J213534.68−000113.4	0.57	20.88	−21.28	−0.72
SDSS J213354.83+000425.4	2.38	20.56	−25.01	−0.36
SDSS J213445.29−000330.6	2.33	20.36	−25.35	−0.34
SDSS J213502.89−000510.0	2.40	21.20	−23.93	−0.48
SDSS J213500.41−001706.9	1.21	20.17	−23.58	−0.24
SDSS J213413.85−000217.3	1.64	19.89	−24.67	−0.37
SDSS J213456.46−001058.3	1.17	20.65	−23.29	−0.51
SDSS J213417.76−000142.9	1.20	21.19	−22.39	−0.28
SDSS J213436.48−001230.0	1.84	20.14	−24.91	−0.60
SDSS J213326.18+002039.8	1.76	20.83	−24.17	−0.55

Table A.1 (cont'd)

Name (J2000 Coordinates)	Redshift	g	M_g	α
SDSS J213402.54+003107.6	1.85	21.57	−23.37	−0.49
SDSS J213455.08+001056.9	3.28	19.14	−27.33	−0.51
SDSS J213414.35+000711.0	1.99	20.77	−24.78	−0.87
SDSS J213504.15+000348.5	1.64	21.07	−23.45	−0.41
SDSS J213451.82+000240.7	1.03	20.55	−23.06	−0.50
SDSS J212956.71−001610.4	2.53	20.81	−24.97	−0.63
SDSS J212832.66−000317.3	2.69	20.97	−24.45	−0.47
SDSS J212840.13−000259.9	1.45	21.89	−23.15	−1.10
SDSS J212924.87−000734.3	2.46	19.26	−26.19	−0.27
SDSS J212850.73−000258.7	2.15	21.75	−23.90	−1.03
SDSS J212825.23+000958.8	1.74	20.88	−24.12	−0.71
SDSS J212902.09+001906.3	3.27	22.16	−23.90	−0.22
SDSS J213014.92+000320.7	1.77	19.75	−25.27	−0.62
SDSS J213041.01−002059.8	0.56	20.55	−21.88	−1.00
SDSS J213001.17−001642.7	1.79	21.28	−24.09	−0.91
SDSS J213015.16−002120.6	1.81	20.99	−24.17	−0.66
SDSS J212951.40−001804.3	3.21	21.57	−23.66	0.10
SDSS J212947.31−000508.4	0.60	20.93	−21.38	−0.50
SDSS J212847.07−001146.0	1.07	21.06	−22.72	−0.48
SDSS J212903.45−000942.0	1.52	19.43	−25.73	−1.06
SDSS J212935.04+000110.4	2.02	21.50	−23.47	−0.54
SDSS J212904.55−000508.2	1.42	19.84	−24.51	−0.40
SDSS J212830.36−000839.3	2.15	20.84	−24.24	−0.25
SDSS J212849.18−000115.3	2.52	20.99	−23.88	−0.10
SDSS J212822.73−000135.2	0.99	18.23	−25.07	−0.25
SDSS J212912.42+000236.0	1.16	19.97	−24.14	−0.56
SDSS J212924.35+000638.5	1.40	19.67	−24.23	0.07
SDSS J212823.85+001141.2	1.34	21.08	−22.95	−0.17
SDSS J212909.66+001214.4	1.34	19.42	−24.76	−0.33
SDSS J212939.66+000815.4	2.01	19.72	−24.91	−0.03
SDSS J212851.34+001759.8	2.24	19.99	−25.18	−0.13
SDSS J212950.01+001158.0	2.57	20.33	−26.00	−1.10
SDSS J212918.57+002051.9	1.96	20.48	−24.51	−0.33
SDSS J212917.94+003109.7	2.40	21.76	−23.83	−0.85
SDSS J212919.56+002437.2	1.48	21.53	−22.89	−0.32
SDSS J212916.91+003028.8	2.19	21.64	−23.06	0.10
SDSS J212958.09+003125.9	0.78	19.43	−23.24	−0.28
SDSS J212944.44+002641.0	1.17	21.75	−22.02	−0.29

Table A.1 (cont'd)

Name (J2000 Coordinates)	Redshift	g	M_g	α
SDSS J212952.15+003244.5	1.87	19.24	−25.62	−0.37
SDSS J213003.65+001542.3	1.48	20.11	−23.90	0.10
SDSS J213007.76+001001.0	2.07	21.60	−24.55	−1.10
SDSS J213016.27+003009.6	1.68	21.25	−23.82	−0.76
SDSS J213001.56+002746.6	1.80	20.18	−25.04	−0.70
SDSS J212959.48+003437.3	1.07	20.76	−22.92	−0.35
SDSS J213001.06+003434.7	1.89	21.07	−24.05	−0.56
SDSS J213008.93+002609.9	4.96	25.98	−26.14	0.10
SDSS J213005.18+001727.5	1.83	21.18	−23.65	−0.38
SDSS J213006.69+001939.9	0.65	20.33	−22.01	−0.34
SDSS J213039.52+002744.0	1.49	20.47	−23.57	0.04
SDSS J213031.52+001133.2	1.78	21.72	−23.06	−0.37
SDSS J213121.24+002355.3	1.78	20.61	−25.05	−1.10
SDSS J213126.70+002006.6	1.83	21.42	−23.18	−0.24
SDSS J213125.52+001910.4	2.12	18.30	−26.52	−0.07
SDSS J213143.59+001854.9	1.59	20.39	−24.76	−1.00
SDSS J213121.46+001006.7	0.78	21.11	−21.69	−1.01
SDSS J213159.39+001312.7	1.40	21.53	−23.14	−0.75
SDSS J213032.09+000407.0	1.98	20.51	−24.77	−0.65
SDSS J213103.36+000135.2	1.80	21.53	−23.27	−0.54
SDSS J213144.12−000907.7	2.25	20.69	−25.02	−1.09
SDSS J213057.37−000103.3	0.90	18.75	−24.21	−0.04
SDSS J213132.46−000505.9	1.21	21.71	−22.45	−0.45
SDSS J213136.72−001350.8	1.48	19.90	−24.56	−0.38
SDSS J213106.65−000956.9	1.40	22.04	−23.09	−1.10
SDSS J213058.58−000627.6	2.03	21.76	−22.48	0.10
SDSS J213107.45−001229.1	0.74	18.73	−24.19	−0.76
SDSS J213021.35+000002.7	1.04	20.81	−23.32	−1.10
SDSS J213105.55−001526.6	1.36	20.69	−23.71	−0.61
SDSS J213022.88+002720.6	2.17	20.45	−25.33	−1.10
SDSS J212947.13+002026.2	1.72	18.81	−25.92	−0.39
SDSS J213314.56+000031.8	1.81	22.14	−22.42	−1.70
SDSS J213359.12+002020.3	2.23	22.13	−22.72	−1.03
SDSS J213124.61+002057.1	2.18	22.06	−23.34	−1.36

APPENDIX B

SDSS DR5 NITROGEN-RICH QUASAR CATALOG

Column 1: Quasar name

Column 2: Redshift

Column 3: SDSS i magnitude

Column 4: Power-law continuum slope ($f_\nu \propto \nu^\alpha$)

Column 5: N IV] equivalent width

Column 6: N III] equivalent width

Column 7: Si IV equivalent width

Column 8: C IV equivalent width

Column 9: C III] equivalent width

Column 10: Mg II equivalent width

Column 11: The Fe II/Mg II ratio

Column 12: Absolute magnitude at rest-frame 2500 Å

Column 13: Radio loudness

Table B.1.   SDSS DR5 Nitrogen-Rich Quasar Catalog

Name (J2000 Coordinates)	Redshift	i^a	α	EW (Å)						Fe II/Mg II	M_{2500}	R
				N IV]	N III]	Si IV	C IV	C III]	Mg II			
SDSS J124032.96+674810.8	1.701	18.91	−0.63	...	4.0	...	27.1	31.2	11.4	4.2	−25.27	...
SDSS J082247.75+071154.7	1.703	18.85	−0.46	...	5.3	...	35.6	27.1	14.6	2.5	−25.30	...
SDSS J100643.89+395222.7	1.705	18.89	−0.85	...	4.2	...	101.7	22.8	...	...	−25.26	...
SDSS J141000.79+641010.4	1.707	18.46	−1.15	...	4.1	...	...	37.4	21.8	3.1	−25.66	...
SDSS J105645.42+414016.2	1.708	18.71	−0.32	...	3.0	...	26.6	20.5	7.8	4.4	−25.48	...
SDSS J105743.11+532231.4	1.708	18.52	−0.57	...	3.4	...	41.0	21.2	15.9	2.4	−25.70	...
SDSS J075230.44+272619.8	1.708	18.25	−0.62	...	3.3	...	67.2	41.4	24.4	1.8	−25.87	...
SDSS J151557.86+383604.3	1.710	18.24	−0.94	...	3.6	...	...	45.2	16.9	2.9	−25.96	...
SDSS J115419.40+145555.3	1.711	17.98	−0.87	...	3.6	...	...	15.9	...	...	−26.30	...
SDSS J162923.06+462311.2	1.718	18.95	−0.39	...	3.2	...	43.6	28.8	13.8	2.9	−25.28	...
SDSS J145349.70+482740.3	1.720	18.81	−1.07	...	5.1	...	19.9	20.6	...	...	−25.52	232.6
SDSS J074220.27+343213.3	1.724	19.77	−0.92	...	4.8	...	...	...	...	...	−24.41	71.4
SDSS J161118.02+393350.9	1.724	17.82	−0.57	...	3.9	...	30.9	16.6	...	...	−26.38	4.3
SDSS J081710.54+235223.9	1.732	18.61	−0.40	4.9	6.7	...	8.1	13.7	...	...	−25.58	1901.2
SDSS J145958.75−013742.4	1.738	18.84	−1.44	...	6.9	...	...	45.1	...	...	−25.35	...
SDSS J084057.02+054733.4	1.742	18.15	−1.50	...	4.3	...	24.4	24.3	...	...	−26.25	...
SDSS J123354.39+150203.7	1.744	18.13	−1.29	...	5.1	...	34.3	22.8	15.2	2.5	−26.18	...
SDSS J084117.24+083753.4	1.746	18.11	−1.04	...	5.6	...	39.8	26.5	15.6	2.7	−26.17	...
SDSS J111559.52+633813.6	1.746	18.04	−1.12	...	3.4	...	46.5	25.3	...	...	−26.15	22.7
SDSS J231608.20+132334.5	1.748	18.42	−1.23	...	9.1	...	52.6	27.5	...	...	−25.84	...
SDSS J111049.28+054551.7	1.749	19.06	−0.47	...	3.8	...	49.2	24.5	...	...	−25.32	...
SDSS J103346.66+415353.7	1.753	19.07	−0.47	...	4.9	...	33.3	25.9	...	...	−25.20	...
SDSS J120323.50+383444.5	1.753	18.94	−0.35	...	5.8	...	25.7	26.0	12.0	3.0	−25.35	...

Table B.1 (cont'd)

Name (J2000 Coordinates)	Redshift	i^a	α	EW (Å)						Fe II/Mg II	M_{2500}	R
				N IV]	N III]	Si IV	C IV	C III]	Mg II			
SDSS J092000.28+591701.4	1.755	19.37	−0.47	...	8.0	...	21.3	25.9	...	...	−24.87	...
SDSS J233843.69−103252.3	1.757	18.98	0.00	...	3.6	...	26.2	22.7	...	...	−25.04	...
SDSS J123055.31+645455.9	1.759	18.84	−0.35	...	4.2	...	25.4	38.9	11.0	2.8	−25.47	...
SDSS J112711.75−011407.8	1.760	19.02	−0.87	...	5.7	...	17.0	33.4	...	...	−25.21	...
SDSS J143352.38+451612.7	1.760	18.96	−0.05	3.5	8.3	...	18.6	15.6	7.1	4.4	−25.28	...
SDSS J090440.58+523028.4	1.766	17.94	−1.07	...	3.3	...	63.2	24.1	11.5	2.0	−26.42	...
SDSS J125617.53−001918.2	1.770	19.62	−0.70	...	6.4	...	...	...	...	...	−24.66	...
SDSS J151100.30+560958.9	1.771	18.85	−1.31	...	7.2	...	52.2	20.3	...	...	−25.58	...
SDSS J020357.29+003310.6	1.772	19.21	−0.28	...	4.6	...	69.3	21.7	...	...	−24.96	...
SDSS J092307.83+461210.1	1.772	18.93	−0.60	...	3.0	...	55.7	27.1	14.7	3.7	−25.34	...
SDSS J094745.85+111354.0	1.773	18.26	−0.78	...	5.3	...	36.1	12.6	...	...	−25.97	1463.4
SDSS J141642.36+513906.9	1.773	17.71	−0.30	...	3.7	...	40.0	13.6	9.4	5.0	−26.51	...
SDSS J085530.98+044237.4	1.774	18.94	−1.06	...	4.2	...	34.5	19.8	21.2	3.3	−25.36	...
SDSS J134848.72+253511.8	1.775	18.67	0.09	...	7.3	...	12.2	22.0	6.0	6.1	−25.62	...
SDSS J081805.14+200235.4	1.777	18.71	−1.28	...	12.4	...	42.9	21.9	...	...	−25.52	...
SDSS J233611.64−095427.4	1.780	18.36	−0.47	...	5.0	...	...	17.9	6.0	2.6	−25.97	12.3
SDSS J153322.52+010543.5	1.781	18.94	−1.48	...	6.0	...	...	19.7	...	...	−25.39	...
SDSS J125040.20+134550.1	1.784	18.80	−0.35	...	5.4	...	25.6	24.2	10.5	4.2	−25.39	...
SDSS J080712.05+065344.2	1.786	19.09	−0.69	...	3.9	...	58.3	18.0	...	...	−25.25	...
SDSS J155003.70+031325.0	1.788	17.35	−1.29	6.7	...	...	25.0	12.9	14.6	1.9	−26.98	22.5
SDSS J090902.55+580356.9	1.793	18.91	−1.63	3.7	6.2	...	...	43.9	...	...	−25.26	...
SDSS J105505.38+300649.6	1.797	18.62	−0.58	...	4.1	...	28.9	35.4	...	...	−25.83	...
SDSS J094344.53+510657.9	1.798	19.01	−0.80	...	6.2	...	23.8	14.5	...	...	−25.26	...

Table B.1 (cont'd)

Name (J2000 Coordinates)	Redshift	i^a	α	EW (Å)						Fe II/Mg II	M_{2500}	R
				N IV]	N III]	Si IV	C IV	C III]	Mg II			
SDSS J162151.74+340559.0	1.803	16.83	−0.57	⋯	4.0	⋯	⋯	20.5	8.0	4.1	−27.58	⋯
SDSS J121347.74+373726.8	1.804	18.16	−1.24	⋯	4.9	⋯	⋯	31.3	15.1	1.9	−26.17	⋯
SDSS J161243.14+251608.8	1.805	18.59	−1.11	⋯	3.3	⋯	⋯	23.6	⋯	⋯	−25.66	⋯
SDSS J101307.08+611646.3	1.807	19.20	−0.70	⋯	4.6	⋯	34.2	16.0	⋯	⋯	−25.15	⋯
SDSS J111443.21+131118.8	1.808	18.40	−0.57	⋯	4.3	⋯	45.7	30.0	⋯	⋯	−25.89	⋯
SDSS J114450.17+440016.6	1.808	18.13	−0.33	⋯	5.6	⋯	19.3	17.3	8.8	5.1	−26.24	⋯
SDSS J105817.06+414341.9	1.809	18.68	−0.78	⋯	4.6	⋯	⋯	39.8	20.2	2.9	−25.42	⋯
SDSS J091537.52+004647.6	1.810	20.04	−0.95	⋯	10.5	⋯	⋯	⋯	⋯	⋯	−24.46	⋯
SDSS J101117.21+512540.9	1.814	18.29	−0.60	⋯	3.5	⋯	50.0	25.5	⋯	⋯	−26.00	⋯
SDSS J233707.39+154332.9	1.819	18.97	−0.24	⋯	4.7	⋯	63.1	58.2	19.9	3.2	−25.27	⋯
SDSS J114231.31+065549.3	1.820	18.06	−0.86	⋯	3.1	⋯	38.7	16.8	⋯	⋯	−26.28	⋯
SDSS J084226.21+030723.5	1.829	19.05	−0.41	⋯	4.1	⋯	29.6	19.8	⋯	⋯	−25.33	⋯
SDSS J083941.94+032914.4	1.830	19.60	−0.87	⋯	7.1	⋯	⋯	⋯	⋯	⋯	−24.73	⋯
SDSS J103729.59+043716.7	1.833	18.53	−0.43	⋯	5.3	⋯	29.4	19.7	12.1	2.1	−25.87	⋯
SDSS J143434.37+543913.4	1.836	18.40	−0.68	⋯	4.9	⋯	46.5	31.7	13.7	6.1	−25.84	⋯
SDSS J120111.70+045105.7	1.837	18.61	−1.69	⋯	5.7	⋯	⋯	25.1	⋯	⋯	−25.82	⋯
SDSS J100128.61+502756.8	1.839	17.31	−0.36	⋯	3.7	⋯	28.5	24.5	12.0	2.8	−27.08	⋯
SDSS J093927.94+054056.8	1.840	18.96	−0.68	⋯	5.8	⋯	33.5	28.7	11.3	4.1	−25.39	⋯
SDSS J150418.76−015039.7	1.840	17.79	−1.22	⋯	3.6	⋯	⋯	18.3	⋯	⋯	−26.68	34.8
SDSS J125414.27+024117.5	1.841	18.26	−1.03	7.0	9.4	⋯	20.0	16.8	9.8	1.8	−26.17	38.7
SDSS J124047.02+144831.0	1.842	18.61	−1.17	4.6	4.7	⋯	29.2	6.8	8.3	3.5	−25.82	107.7
SDSS J131403.48+415203.9	1.845	18.45	−1.05	⋯	4.2	⋯	40.6	31.4	15.7	4.0	−25.92	⋯
SDSS J094917.82+350938.2	1.853	18.88	−1.02	⋯	5.1	⋯	64.8	31.6	34.1	1.6	−25.34	⋯

Table B.1 (cont'd)

Name (J2000 Coordinates)	Redshift	i^a	α	EW (Å)						Fe II/Mg II	M_{2500}	R
				N IV]	N III]	Si IV	C IV	C III]	Mg II			
SDSS J110906.32+640704.9	1.853	17.27	−0.85	...	3.2	...	...	27.1	...	...	−27.07	8.0
SDSS J223308.78−085445.4	1.853	18.66	−0.14	...	4.6	...	...	29.5	16.2	4.2	−25.57	...
SDSS J170731.74+221151.3	1.857	18.90	−1.08	...	6.5	...	44.9	24.7	13.8	3.7	−25.47	...
SDSS J102545.40+595638.4	1.867	18.61	−0.81	...	8.3	...	65.9	27.9	...	...	−25.77	...
SDSS J144059.82+435241.6	1.867	18.99	−0.27	...	4.2	...	38.3	26.3	12.1	3.2	−25.43	...
SDSS J154833.02+540003.1	1.867	19.08	−0.41	4.3	...	...	32.7	18.8	...	...	−25.30	...
SDSS J154921.05+550600.0	1.869	18.40	−0.29	...	4.4	...	48.4	19.8	10.1	3.8	−25.89	24.4
SDSS J074606.63+364544.4	1.870	19.08	−1.30	...	11.3	...	79.5	38.3	...	...	−25.21	179.4
SDSS J132742.92+003532.6	1.874	18.28	−1.34	...	5.4	...	...	17.7	...	...	−26.13	...
SDSS J091639.78+390833.8	1.875	19.04	−0.66	...	7.4	...	33.5	14.3	...	...	−25.35	226.1
SDSS J032933.97−004801.0	1.878	18.63	−1.13	...	6.3	...	29.2	29.3	15.7	2.3	−25.82	...
SDSS J120750.06+332426.5	1.878	19.90	−0.81	...	8.3	...	...	...	...	...	−24.59	...
SDSS J123017.45+644707.4	1.884	20.03	−0.90	...	11.2	...	...	...	...	...	−24.35	...
SDSS J134419.43+403220.0	1.884	17.73	−1.53	...	3.0	...	55.1	31.9	...	...	−26.58	...
SDSS J134941.93+313441.4	1.884	19.02	−0.29	...	4.8	...	33.0	26.6	...	...	−25.41	...
SDSS J110504.73+122230.0	1.894	18.26	−0.56	...	4.9	...	20.2	16.6	8.4	3.8	−26.31	...
SDSS J141140.91+024107.6	1.897	18.28	−0.99	...	5.0	...	...	27.7	14.2	3.0	−26.15	...
SDSS J170648.49+212918.0	1.901	19.09	−0.83	...	5.0	...	32.3	23.9	...	...	−25.60	...
SDSS J082521.94+453705.0	1.910	19.40	−1.01	...	3.9	...	40.7	37.2	...	...	−25.12	1049.6
SDSS J120243.13+650606.8	1.913	18.55	−0.72	...	4.3	...	...	20.2	...	...	−26.04	...
SDSS J141608.47−003712.3	1.918	18.88	−0.74	...	4.2	10.2	43.4	23.7	11.9	6.1	−25.61	...
SDSS J004600.26−002122.4	1.919	19.81	−0.86	...	7.9	...	...	...	...	...	−24.71	...
SDSS J171521.20+311532.8	1.921	19.44	−1.01	3.2	4.7	...	30.6	8.4	...	...	−25.04	...

Table B.1 (cont'd)

Name (J2000 Coordinates)	Redshift	i^a	α	EW (Å)						Fe II/Mg II	M_{2500}	R
				N IV]	N III]	Si IV	C IV	C III]	Mg II			
SDSS J122559.13+161021.2	1.939	18.56	−0.66	7.0	5.8	4.0	13.3	10.5	...	...	−26.13	89.8
SDSS J085913.99+501409.1	1.930	18.88	−0.40	1.5	3.7	12.0	40.6	24.3	17.2	3.9	−25.55	...
SDSS J161326.22+064958.6	1.941	17.72	−1.46	4.7	6.4	18.7	38.8	...	...	...	−26.82	36.7
SDSS J020022.01−084512.0	1.943	18.28	−1.15	...	4.7	...	...	29.7	...	...	−26.17	52.0
SDSS J081625.40+064535.1	1.946	18.79	−1.29	2.9	10.7	7.6	47.9	27.9	...	...	−25.87	...
SDSS J014517.82+135602.2	1.948	18.75	−0.68	...	4.1	9.1	23.9	20.9	...	...	−25.66	...
SDSS J153226.67+421855.3	1.953	18.91	−0.45	3.1	5.0	8.2	44.1	18.2	11.5	6.5	−25.65	...
SDSS J110600.57+622636.0	1.956	19.39	−0.07	4.9	...	...	59.5	23.3	...	...	−25.04	...
SDSS J075623.51+252917.9	1.958	18.44	−0.86	...	4.5	6.1	42.0	29.1	19.2	3.7	−26.12	...
SDSS J160655.95+285519.1	1.958	18.07	−0.70	...	4.2	6.6	9.9	11.7	5.8	8.4	−26.56	...
SDSS J112750.31−012904.1	1.960	19.05	−0.47	5.3	4.5	...	61.4	34.9	...	...	−25.43	...
SDSS J122142.44+584254.0	1.960	18.55	−0.38	3.9	4.2	9.2	51.9	17.7	...	...	−25.90	...
SDSS J103019.25+375545.8	1.961	18.91	−0.95	...	4.6	7.4	41.7	13.1	...	...	−25.72	...
SDSS J105928.23+603252.2	1.963	19.08	−0.54	...	7.1	...	30.2	18.2	...	...	−25.38	...
SDSS J123500.75+012041.6	1.964	18.73	−0.51	...	3.0	4.7	37.6	28.1	...	...	−25.73	67.1
SDSS J000118.40−010221.8	1.968	19.38	−0.87	...	4.5	...	49.5	45.5	...	...	−25.14	...
SDSS J000759.40+150822.6	1.968	18.84	−0.77	...	4.6	6.1	57.7	19.5	...	...	−25.62	...
SDSS J010119.85+145635.2	1.978	18.68	−0.53	...	3.4	...	...	19.2	14.2	4.7	−25.80	...
SDSS J135820.65+102503.4	1.968	18.32	−0.99	...	5.8	...	...	23.9	14.1	3.2	−26.29	...
SDSS J142756.71+473148.4	1.970	19.07	−0.49	...	4.4	...	35.2	30.8	...	...	−25.65	...
SDSS J120537.04+474705.3	1.973	18.42	−0.67	...	7.3	13.6	...	32.9	15.9	6.4	−26.14	65.4
SDSS J132551.56−013509.6	1.975	19.64	−0.63	...	6.6	...	...	...	...	...	−24.90	...
SDSS J090030.36+015154.9	1.985	18.41	−1.63	...	3.8	...	...	37.2	...	...	−26.08	...

Table B.1 (cont'd)

Name (J2000 Coordinates)	Redshift	i^{a}	α	EW (Å)						Fe II/Mg II	M_{2500}	R
				N IV]	N III]	Si IV	C IV	C III]	Mg II			
SDSS J084023.97+065844.8	1.987	18.38	-0.73	...	3.1	8.1	36.9	24.1	14.0	1.8	-26.30	...
SDSS J123255.00+554123.7	1.987	18.14	-0.61	...	4.3	14.6	64.9	24.0	15.4	3.6	-26.42	...
SDSS J081038.17+421821.0	1.992	18.78	-0.39	...	4.1	5.3	33.2	21.2	13.7	4.8	-25.75	...
SDSS J154651.75+525313.1	2.003	19.02	-1.31	...	12.1	...	51.1	28.6	...	...	-25.54	...
SDSS J162411.38+220428.0	2.005	19.11	-0.65	...	3.3	...	25.4	17.3	...	...	-25.56	...
SDSS J115650.75+435521.4	2.010	20.07	-0.51	...	5.9	...	...	...	...	...	-24.61	3136.9
SDSS J091031.35+010151.9	2.013	18.61	-0.85	...	5.5	15.4	46.7	20.9	21.7	2.8	-25.99	...
SDSS J015407.18-095527.8	2.015	18.61	-0.61	...	3.5	7.1	28.7	14.1	...	...	-26.13	13.0
SDSS J151716.79+591627.1	2.021	18.97	-0.50	...	4.6	10.8	31.7	18.1	7.6	4.3	-25.70	...
SDSS J145815.22+003908.7	2.022	18.88	-0.44	...	4.3	9.3	29.5	39.9	10.4	4.6	-25.81	208.7
SDSS J082016.11+081215.9	2.024	19.04	-0.32	...	6.6	...	62.0	25.0	...	...	-25.45	...
SDSS J135536.48+363011.3	2.024	18.81	-0.95	...	5.7	10.0	39.0	11.4	18.2	3.6	-25.89	...
SDSS J093935.12+364000.9	2.030	17.58	-1.18	...	3.4	11.3	45.5	20.7	...	...	-27.06	...
SDSS J105607.40+611335.7	2.031	19.35	-1.26	...	8.5	...	...	36.6	...	...	-25.19	...
SDSS J023252.80-001351.1	2.033	18.65	-0.74	...	4.7	...	...	25.6	...	...	-26.08	...
SDSS J093035.07+464408.4	2.033	18.70	-0.99	...	3.1	7.3	20.9	16.3	...	...	-26.35	1972.9
SDSS J125532.99-001642.6	2.036	18.90	-0.30	...	4.0	6.2	36.6	28.7	13.9	4.9	-25.74	...
SDSS J074033.26+285838.8	2.039	18.91	-0.61	...	4.5	6.4	33.2	16.8	...	...	-25.63	...
SDSS J031200.70-063007.1	2.041	18.93	-0.92	...	4.1	5.6	48.6	14.2	...	...	-25.89	...
SDSS J153122.56+564710.3	2.044	19.37	-0.46	...	3.3	...	44.4	22.3	...	...	-25.20	...
SDSS J093857.17+424829.3	2.050	18.48	-0.90	...	4.8	14.7	29.0	29.7	13.6	2.6	-26.25	22.2
SDSS J103020.91+364809.6	2.053	18.80	-0.65	...	5.0	8.6	56.3	27.4	...	...	-25.78	38.8
SDSS J135144.85-032050.8	2.058	18.70	-0.46	...	4.5	7.2	31.2	20.1	6.8	3.3	-26.13	...

Table B.1 (cont'd)

| Name (J2000 Coordinates) | Redshift | i^a | α | EW (Å) | | | | | | Fe II/Mg II | M_{2500} | R |
				N IV]	N III]	Si IV	C IV	C III]	Mg II			
SDSS J235408.38+143153.5	2.061	18.89	−0.45	...	4.8	8.8	27.9	41.6	14.6	2.5	−25.82	...
SDSS J164125.22+225704.0	2.063	18.74	−0.79	...	6.2	11.1	19.7	16.0	...	...	−26.11	2121.8
SDSS J155355.38+324513.3	2.064	18.90	−1.11	...	7.8	...	...	44.7	...	...	−25.82	17.4
SDSS J133701.78+022807.8	2.066	19.11	−0.47	4.9	5.1	...	11.7	11.7	...	...	−25.60	79.0
SDSS J102250.16+483631.1	2.047	18.61	−0.87	...	5.8	...	...	19.0	11.7	5.0	−26.11	...
SDSS J080244.40+215845.3	2.068	18.62	−0.98	...	5.3	9.1	34.8	26.1	12.8	2.1	−26.18	...
SDSS J113434.52−033726.5	2.068	17.94	−0.98	...	3.5	6.5	49.4	18.1	...	...	−26.80	25.3
SDSS J111311.17+120519.9	2.086	18.82	−0.45	2.3	3.1	7.2	25.6	18.5	10.8	7.1	−25.92	...
SDSS J080325.04+174239.0	2.092	18.25	−0.44	...	3.3	5.9	33.3	14.8	8.9	4.6	−26.47	...
SDSS J165508.72+373244.6	2.092	18.88	−0.67	...	3.5	10.2	12.0	18.3	...	...	−26.01	83.7
SDSS J130846.76−005047.0	2.093	18.81	−0.25	...	4.7	11.6	55.9	27.2	22.3	3.1	−25.79	...
SDSS J130811.96+113609.2	2.101	17.70	−1.87	...	3.6	11.2	35.1	24.8	...	...	−27.29	...
SDSS J171712.87+640344.7	2.103	18.59	−0.26	...	4.6	7.3	38.6	15.4	...	...	−26.13	...
SDSS J113423.00+150059.2	2.108	18.68	−0.21	...	5.5	...	...	31.1	...	...	−25.96	...
SDSS J111343.43+105954.6	2.114	18.94	−0.63	...	3.8	11.0	28.9	26.6	...	...	−25.87	...
SDSS J152632.33+422932.1	2.118	18.93	−0.75	...	8.8	11.7	28.4	17.2	...	...	−26.00	...
SDSS J100308.64+105048.6	2.122	19.36	−0.73	...	3.3	...	39.6	36.4	...	...	−25.39	775.5
SDSS J131138.39+650031.4	2.122	19.07	−0.35	...	3.0	...	53.7	17.9	...	...	−25.74	...
SDSS J154644.24+311711.3	2.122	19.16	−1.10	...	3.3	...	36.5	18.6	...	...	−25.62	168.4
SDSS J095851.12+390745.1	2.125	18.26	−1.22	...	5.0	12.2	23.7	27.3	...	...	−26.56	...
SDSS J075524.11+342134.5	2.126	17.12	−0.93	...	3.2	7.9	26.0	18.3	...	...	−27.62	...
SDSS J083744.01+420643.9	2.130	18.75	−0.94	...	3.7	10.3	48.2	21.8	...	...	−26.02	170.6
SDSS J110708.54+371734.6	2.130	18.76	−0.39	2.1	3.3	5.8	24.7	6.9	...	...	−25.99	...

Table B.1 (cont'd)

Name (J2000 Coordinates)	Redshift	i^a	α	EW (Å)						Fe II/Mg II	M_{2500}	R
				N IV]	N III]	Si IV	C IV	C III]	Mg II			
SDSS J113638.66+011031.7	2.131	19.41	−0.85	5.9	4.7	...	52.7	20.8	...	...	−25.54	...
SDSS J103002.65+322429.0	2.134	19.62	−0.81	...	8.4	...	...	...	...	...	−25.30	...
SDSS J085750.12+263634.3	2.139	18.09	−1.05	...	3.6	7.2	25.1	12.0	...	...	−26.79	...
SDSS J092502.71+322639.6	2.140	18.58	−1.34	...	4.4	...	...	23.7	...	...	−26.37	...
SDSS J102052.01+454515.9	2.143	18.92	−0.62	...	7.5	16.7	74.0	27.1	...	...	−25.90	...
SDSS J154417.14+311945.4	2.144	19.37	−0.67	5.0	...	...	...	21.8	...	...	−25.48	...
SDSS J140217.98+041111.1	2.146	19.06	−0.54	...	3.7	...	39.9	17.9	...	...	−25.72	...
SDSS J103638.14+124745.9	2.156	18.66	−0.52	...	3.8	7.8	42.3	16.9	...	...	−26.11	...
SDSS J093801.18+090004.4	2.159	18.06	−1.21	...	7.1	8.0	41.6	25.9	...	...	−26.78	...
SDSS J120250.49+322545.7	2.163	18.99	−0.70	...	5.4	8.7	31.9	20.9	...	...	−25.89	...
SDSS J111048.93+045608.0	2.208	18.80	−0.93	...	4.5	11.1	37.6	19.5	...	...	−26.13	584.2
SDSS J160816.96+235148.4	2.209	18.88	−1.00	...	5.1	6.9	50.6	...	...	...	−26.08	...
SDSS J075627.70+205413.9	2.211	19.10	−1.07	6.1	7.8	...	12.5	16.4	...	...	−25.87	...
SDSS J092225.69+611530.6	2.227	18.42	−0.55	5.3	...	7.2	69.7	16.0	...	...	−26.45	...
SDSS J113036.42+151253.1	2.227	18.56	−0.54	...	5.3	10.1	78.4	23.7	...	...	−26.32	...
SDSS J131551.68+132620.6	2.234	18.43	−0.62	...	3.5	9.4	46.2	24.7	...	...	−26.50	...
SDSS J113601.00+652533.6	2.238	19.15	−0.56	...	4.5	...	36.0	22.1	...	...	−25.80	...
SDSS J224019.01+144435.5	2.242	18.32	−1.22	...	3.1	8.2	23.9	23.0	...	...	−26.67	...
SDSS J081342.09+344235.2	2.245	18.32	−0.85	...	6.9	7.5	...	26.1	...	...	−26.48	...
SDSS J075646.71+415851.8	2.250	18.46	−0.91	...	3.4	11.7	47.9	26.1	...	...	−26.54	...
SDSS J124143.43+402451.9	2.283	18.16	−0.53	3.4	3.1	7.8	48.4	17.2	...	...	−26.75	...
SDSS J024204.58−003835.7	2.288	19.79	−0.12	...	5.0	...	...	...	...	...	−24.82	...
SDSS J035722.94−052837.1	2.289	19.09	−0.79	...	4.4	...	60.0	27.4	...	...	−25.89	...

Table B.1 (cont'd)

Name (J2000 Coordinates)	Redshift	i^a	α	EW (Å)						Fe II/Mg II	M_{2500}	R
				N IV]	N III]	Si IV	C IV	C III]	Mg II			
SDSS J223841.88+142154.9	2.290	19.02	−0.74	...	7.2	...	...	45.9	...	...	−26.04	...
SDSS J085522.87+375425.9	2.296	18.75	−0.72	...	4.7	10.1	50.6	23.5	...	...	−26.21	...
SDSS J151052.61+473903.9	2.298	18.74	−0.64	...	3.8	7.8	45.6	14.1	...	...	−26.30	...
SDSS J025505.93+001446.7	2.299	19.21	−1.00	...	9.1	...	...	18.6	...	...	−25.90	82.6
SDSS J093152.76+343920.6	2.305	19.45	−0.60	...	3.1	...	43.5	24.6	...	...	−25.58	186.0
SDSS J104749.54+320303.6	2.323	19.75	−0.32	...	5.9	...	...	...	...	...	−25.39	...
SDSS J081630.09+202831.5	2.315	18.74	−0.53	1.2	3.2	6.4	31.7	14.6	...	...	−26.37	...
SDSS J150937.02+401713.9	2.315	18.96	−0.67	...	3.3	6.3	66.0	14.6	...	...	−26.07	160.1
SDSS J141056.25+541608.5	2.316	19.01	−0.73	...	8.8	...	58.8	37.4	...	...	−26.00	66.0
SDSS J121113.56+044946.2	2.318	18.88	−0.45	...	5.9	7.8	37.0	14.2	...	...	−26.15	...
SDSS J105136.03+384118.1	2.320	18.14	−0.64	...	3.9	8.1	52.2	23.9	...	...	−26.82	...
SDSS J101844.22+040801.1	2.329	20.05	−0.60	...	10.8	...	...	...	...	...	−25.17	...
SDSS J120414.37+351800.5	2.338	18.71	−0.42	...	8.7	...	16.1	22.2	...	...	−26.36	...
SDSS J094732.09+325220.5	2.340	19.02	−0.76	3.3	6.7	...	...	23.2	...	...	−26.14	234.7
SDSS J142915.19+343820.3	2.351	18.53	−0.75	...	4.0	10.9	56.8	26.1	...	...	−26.48	...
SDSS J113826.65+045412.4	2.352	19.06	−0.30	...	8.4	...	24.4	45.4	...	...	−26.03	...
SDSS J090642.39+014503.1	2.357	19.51	−0.68	...	4.9	...	...	...	...	...	−25.51	...
SDSS J225425.42−011320.4	2.347	19.71	−0.69	...	13.3	...	...	...	...	...	−25.49	...
SDSS J092316.45+332116.3	2.360	18.35	−0.67	...	4.0	3.6	9.2	12.8	...	...	−26.70	...
SDSS J131446.65+040609.4	2.361	18.90	−0.54	5.2	3.3	4.0	79.1	15.9	...	...	−26.10	...
SDSS J083234.75+285205.9	2.362	18.81	−0.53	...	4.3	6.4	46.0	12.0	...	...	−26.32	...
SDSS J162346.09−002218.1	2.370	19.90	−1.40	...	6.2	...	...	...	...	...	−25.42	...
SDSS J014504.35+125214.1	2.384	19.47	−1.35	...	5.7	...	44.9	11.6	...	...	−25.73	...

Table B.1 (cont'd)

Name (J2000 Coordinates)	Redshift	i^{a}	α	EW (Å)						Fe II/Mg II	M_{2500}	R
				N IV]	N III]	Si IV	C IV	C III]	Mg II			
SDSS J123120.55+072552.6	2.390	17.77	−1.04	...	4.0	9.1	27.7	...	...	...	−27.42	95.3
SDSS J142947.70+114316.7	2.408	18.91	−0.25	...	7.3	...	30.8	11.9	...	...	−26.13	...
SDSS J032118.22−010539.9	2.411	17.60	−2.43	...	7.1	...	...	13.5	...	...	−27.78	...
SDSS J101111.22+341548.6	2.412	18.33	−0.46	...	3.5	8.5	61.2	25.3	...	...	−26.79	296.2
SDSS J140224.15+003002.2	2.417	18.56	−0.56	...	4.2	10.3	22.3	20.1	...	...	−26.54	...
SDSS J085220.46+473458.4	2.420	19.97	−0.34	...	9.8	...	...	...	...	...	−25.11	1561.2
SDSS J002223.29−091702.5	2.423	19.84	−0.90	...	11.4	...	...	...	...	...	−25.40	...
SDSS J104713.16+353115.6	2.438	19.58	−0.77	...	9.7	...	...	...	...	...	−25.70	472.8
SDSS J133802.28+502625.6	2.448	18.05	−0.48	...	5.8	10.6	28.2	14.3	...	...	−27.17	...
SDSS J154534.59+511228.9	2.453	19.34	−0.71	...	3.4	...	19.7	12.7	...	...	−25.95	19.5
SDSS J093955.52+520717.7	2.457	19.77	−0.93	8.5	...	...	...	...	...	...	−25.45	166.6
SDSS J031348.34−010433.0	2.468	18.91	−0.53	...	5.9	7.2	38.5	17.1	...	...	−26.32	...
SDSS J143048.84+481102.7	2.499	19.56	−0.35	6.3	10.0	...	...	...	...	...	−25.63	46.5
SDSS J074447.27+212000.4	2.502	19.96	−0.89	...	4.2	...	...	...	...	...	−25.38	1774.5
SDSS J164148.19+223225.2	2.506	18.80	−0.52	4.7	10.5	...	...	15.8	...	...	−26.50	88.7
SDSS J081626.72+253249.3	2.510	18.56	−0.89	...	3.1	11.3	45.1	20.9	...	...	−26.82	...
SDSS J154125.46+534813.0	2.543	18.89	−0.25	...	5.1	5.8	20.2	19.5	...	...	−26.29	2507.2
SDSS J104318.88+004747.2	2.552	19.17	−1.32	...	6.5	...	31.7	18.6	...	...	−26.29	...
SDSS J133923.77+632858.4	2.558	19.22	−0.37	4.0	5.0	...	62.9	19.9	...	...	−26.06	6466.5
SDSS J130423.24+340438.1	2.559	18.59	−0.47	2.3	7.1	3.1	16.0	5.1	...	...	−26.79	86.7
SDSS J015500.44+010600.2	2.562	19.75	−1.40	...	7.9	...	...	...	...	...	−25.86	121.5
SDSS J013724.43−082419.9	2.566	18.44	−1.06	...	6.3	9.6	57.7	49.9	...	...	−26.93	...
SDSS J121238.39+675920.5	2.573	18.35	−0.49	...	4.2	...	49.2	20.0	...	...	−26.89	...

Table B.1 (cont'd)

Name (J2000 Coordinates)	Redshift	i^a	α	EW (Å)						Fe II/Mg II	M_{2500}	R
				N IV]	N III]	Si IV	C IV	C III]	Mg II			
SDSS J114023.06+372815.1	2.580	18.45	−0.66	...	4.1	8.2	42.0	13.2	...	...	−26.90	100.1
SDSS J164130.57+393434.2	2.612	18.98	−0.68	...	5.5	5.4	74.3	34.5	...	...	−26.43	...
SDSS J090115.18+371822.8	2.617	18.97	−1.70	...	10.6	21.7	65.9	46.0	...	...	−26.57	...
SDSS J145817.52−004115.7	2.618	18.69	−0.53	...	3.0	10.1	36.0	22.0	...	...	−26.62	...
SDSS J093355.72+084043.0	2.629	19.17	−0.87	...	7.6	...	30.8	23.3	...	...	−26.24	...
SDSS J104229.19+381111.2	2.645	18.11	−0.53	3.8	5.9	3.2	10.5	2.3	...	...	−27.28	52.5
SDSS J170322.41+231243.3	2.625	18.02	−1.29	...	4.6	...	...	26.8	...	...	−27.47	...
SDSS J081643.53+264634.1	2.638	18.98	−0.98	...	3.6	11.9	31.6	20.3	...	...	−26.48	...
SDSS J130421.41+634114.4	2.638	19.27	−0.81	...	4.5	...	...	22.9	...	...	−26.09	...
SDSS J085343.32+370402.3	2.641	19.09	−1.19	...	4.1	...	...	26.0	...	...	−26.39	...
SDSS J040913.78−060839.0	2.685	19.04	−1.62	8.9	7.3	...	...	25.4	...	...	−26.60	...
SDSS J081322.09+003018.6	2.695	19.49	−0.44	...	3.7	...	...	8.8	...	...	−25.86	...
SDSS J003815.92+140304.5	2.717	19.66	−0.64	...	9.4	...	...	...	...	...	−25.62	...
SDSS J160943.35+522550.8	2.703	18.58	−0.83	...	4.3	...	...	12.6	...	...	−26.92	9.4
SDSS J084104.49+420818.9	2.758	19.22	−1.18	4.1	5.8	...	75.3	28.2	...	...	−26.33	...
SDSS J093724.55+444602.6	2.761	19.96	−0.32	5.2	...	...	...	...	...	...	−25.40	...
SDSS J154621.25+521303.3	2.775	19.05	−2.84	...	6.4	...	89.2	64.5	...	...	−26.85	...
SDSS J123148.93+134924.4	2.789	19.71	−0.03	...	7.5	...	...	...	...	...	−25.40	...
SDSS J145953.20+372822.4	2.801	19.47	−0.55	...	6.6	...	...	19.4	...	...	−25.92	...
SDSS J151658.64+032849.6	2.851	19.23	−1.06	5.3	...	...	...	30.4	...	...	−26.29	...
SDSS J074520.21+415725.4	2.845	19.02	−0.36	4.6	7.8	...	26.5	20.0	...	...	−26.40	250.2
SDSS J093531.83+363317.6	2.857	18.35	−0.42	...	3.4	4.0	38.2	12.3	...	...	−27.08	1842.2
SDSS J140432.99+072846.9	2.876	18.77	−0.26	3.2	4.9	4.7	16.6	10.3	...	...	−26.66	1272.4

Table B.1 (cont'd)

Name (J2000 Coordinates)	Redshift	i^a	α	EW (Å)						Fe II/Mg II	M_{2500}	R
				N IV]	N III]	Si IV	C IV	C III]	Mg II			
SDSS J152553.89+513649.1	2.882	16.54	−0.99	...	3.8	...	...	19.0	...	...	−29.04	...
SDSS J232329.91−090155.1	2.882	19.27	−0.52	...	4.7	...	53.9	19.9	...	...	−26.21	...
SDSS J144241.74+100533.9	2.924	18.76	−0.68	...	4.0	6.9	35.9	20.0	...	...	−26.81	...
SDSS J114112.29+004759.0	2.893	19.01	−0.40	...	8.5	...	52.5	17.2	...	...	−26.36	...
SDSS J154405.35+284516.6	2.897	19.82	−0.30	...	7.2	...	...	...	...	...	−25.51	...
SDSS J140038.14+560624.6	2.906	19.41	−1.06	4.7	...	...	23.8	10.5	...	...	−26.36	83.6
SDSS J093643.51+292713.6	2.926	18.06	−0.34	...	3.5	5.7	29.2	12.4	...	...	−27.43	21.7
SDSS J090221.10+412524.8	2.939	19.68	−0.88	8.2	...	...	...	...	...	...	−25.88	...
SDSS J092656.94+602504.2	2.956	19.06	−0.65	4.2	...	...	43.1	16.1	...	...	−26.48	...
SDSS J124158.18+123059.3	2.971	19.52	−0.37	...	10.2	...	...	...	...	...	−26.00	119.6
SDSS J144752.46+582420.3	2.983	18.20	−0.36	3.2	3.6	2.7	21.4	3.8	...	...	−27.30	182.8
SDSS J103327.08+563829.5	3.018	20.08	−1.40	...	6.2	...	...	...	...	...	−25.88	...
SDSS J112127.96+123816.1	3.018	19.88	−0.50	...	17.7	...	...	...	...	...	−25.64	...
SDSS J223408.99+000001.6	3.025	17.08	−0.79	3.6	3.5	5.0	7.7	5.1	...	...	−28.66	...
SDSS J094851.42+493538.9	3.000	19.49	−0.76	...	4.8	...	...	23.9	...	...	−26.11	...
SDSS J233930.00+003017.3	3.051	18.52	−0.92	...	5.1	7.6	22.9	14.3	...	...	−27.33	156.1
SDSS J133701.39−024630.3	3.050	18.41	−0.71	2.4	3.9	...	...	13.4	...	...	−27.29	265.7
SDSS J105922.31+663806.2	3.075	19.84	−0.45	6.3	3.9	...	25.5	...	...	...	−25.70	...
SDSS J140641.51+585214.0	3.079	19.44	−1.48	...	3.0	...	...	6.0	...	...	−26.65	...
SDSS J073912.95+412737.4	3.094	19.55	−1.67	...	6.5	...	...	...	...	...	−26.61	...
SDSS J114538.74+072148.4	3.090	19.34	−0.70	...	12.3	...	...	37.7	...	...	−26.29	...
SDSS J123450.00+375530.3	3.138	19.04	−0.17	...	4.7	...	17.1	19.0	...	...	−26.50	21.6
SDSS J092104.30+034150.5	3.140	18.79	−0.42	4.2	...	...	33.9	36.9	...	...	−26.81	...

Table B.1 (cont'd)

Name (J2000 Coordinates)	Redshift	i^a	α	EW (Å)						Fe II/Mg II	M_{2500}	R
				N IV]	N III]	Si IV	C IV	C III]	Mg II			
SDSS J162102.73+491921.5	3.143	19.32	−0.49	...	5.2	...	52.4	51.4	...	...	−26.20	...
SDSS J170704.87+644303.2	3.163	18.33	−0.79	5.1	2.5	6.9	40.8	15.3	...	...	−27.52	...
SDSS J160210.30+281744.3	3.164	19.08	−0.69	...	6.4	...	...	34.5	...	...	−26.57	...
SDSS J084715.16+383110.0	3.182	18.24	−0.39	...	6.6	3.9	14.9	9.2	...	...	−27.43	1080.4
SDSS J091159.25+274742.3	3.183	20.09	−0.32	...	7.0	...	...	...	...	...	−25.48	...
SDSS J101409.07+414505.4	3.186	19.76	−0.68	...	5.7	...	...	...	...	...	−25.99	...
SDSS J094054.56+054903.5	3.235	18.69	−0.51	...	6.5	...	...	24.5	...	...	−27.05	...
SDSS J085534.40+510632.7	3.240	18.73	−0.56	...	5.0	...	...	16.8	...	...	−27.10	17.5
SDSS J144805.84+440806.4	3.284	19.74	0.19	5.2	10.9	...	...	...	...	...	−25.68	...
SDSS J122017.06+454941.1	3.283	17.76	−1.25	...	4.7	...	...	14.2	...	...	−28.27	...
SDSS J150800.30+582707.5	3.305	19.01	−0.21	...	4.0	...	50.5	19.9	...	...	−26.59	...
SDSS J150217.11+355459.0	3.350	18.67	−0.54	...	4.2	11.4	40.5	23.2	...	...	−27.21	...
SDSS J012530.85−102739.8	3.352	18.02	−0.49	...	4.8	9.5	28.0	25.1	...	...	−27.78	...
SDSS J164737.91+255337.9	3.376	19.97	−0.37	...	15.4	...	...	...	...	...	−25.72	...
SDSS J083749.59+364145.4	3.400	18.55	−0.43	...	6.6	...	...	21.3	...	...	−27.26	199.3
SDSS J083251.03+065738.5	3.426	20.04	−0.35	3.6	...	...	...	...	...	...	−25.54	...
SDSS J160652.65+335426.1	3.474	20.08	0.75	...	27.1	...	...	...	...	...	−24.88	...

REFERENCES

Abazajian, K., et al. 2004, AJ, 128, 502

Abazajian, K., et al. 2005, AJ, 129, 1755

Adelman-McCarthy, J. K., et al. 2007, ApJS, 172, 634

Adelman-McCarthy, J. K., et al. 2008, ApJS, 175, 297

Antonucci, R., et al. 1993, ARA&A, 31, 473

Avni, Y., & Bahcall, J. N. 1980, ApJ, 235, 694

Baldwin, J. A. 1977, ApJ, 214, 679

Baldwin, J., Ferland, G., Korista, K., & Verner, D. 1995, ApJ, 455, L119

Baldwin, J. A., Hamann, F., Korista, K. T., Ferland, G. J., Dietrich, M., & Warner, C. 2003, ApJ, 583, 649

Baldwin, J. A., Ferland, G. J., Korista, K. T., Hamann, F., & LaCluyzé, A. 2004, ApJ, 615, 610

Barger, A. J., Cowie, L. L., Mushotzky, R. F., Yang, Y., Wang, W. H., Steffen, A. T., & Capak, P. 2005, AJ, 129, 578

Barth, A. J., Martini, P., Nelson, C. H., & Ho, L. C. 2003, ApJ, 594, L95

Barthel, P. D. 1989, ApJ, 336, 606

Baum, S. A., Zirbel, E. L., & O'Dea, C. P. 1995, ApJ, 451, 88

Becker, R. H., White, R. L., & Helfand, D. J. 1995, ApJ, 450, 559

Bechtold, J., et al. 2003, ApJ, 588, 119

Becker, R. H., et al. 2001, AJ, 122, 2850

Bentz, M. C., Hall, P. B., & Osmer, P. S. 2004, AJ, 128, 561

Bertin, E., Mellier, Y., Radovich, M., Missonnier, G., Didelon, P., & Morin, B. 2002, Astronomical Data Analysis Software and Systems XI, 281, 228

Bertoldi, F., et al. 2003, A&A, 406, L55

Bertoldi, F., et al. 2003, A&A, 409, L47

Best, P. N., Kauffmann, G., Heckman, T. M., Brinchmann, J., Charlot, S., Ivezić, Ž., & White, S. D. M. 2005, MNRAS, 362, 25

Bischof, O. B., & Becker, R. H., AJ, 113, 2000

Blanton, M. R., Lin, H., Lupton, R. H., Maley, F. M., Young, N., Zehavi, I., & Loveday, J. 2003, AJ, 125, 2276

Blanton, M. R., et al. 2005, AJ, 129, 2562

Bouwens, R. J., Illingworth, G. D., Blakeslee, J. P., & Franx, M. 2006, ApJ, 653, 53

Boyle, B. J., Shanks, T., & Peterson, B. A. 1988, MNRAS, 235, 935

Boyle, B. J., & Terlevich, R. J. 1998, MNRAS, 293, L49

Boyle, B. J., Shanks, T., Croom, S. M., Smith, R. J., Miller, L., Loaring, N., & Heymans, C. 2000, MNRAS, 317, 1014

Brandt, W. N., et al. 2001, AJ, 121, 591

Brandt, W. N., et al. 2002, ApJ, 569, L5

Brown, M. J. I., et al. 2006, ApJ, 638, 88

Bunker, A. J., Stanway, E. R., Ellis, R. S., & McMahon, R. G. 2004, MNRAS, 355, 374

Carilli, C. L., Bertoldi, F., Omont, A., Cox, P., McMahon, R. G., & Isaak, K. G. 2001, AJ, 122, 1679

Carilli, C. L., et al. 2004, AJ, 128, 997

Carilli, C. L., et al. 2007, ApJ, 666, L9

Charlton, J. C., & Churchill, C. W. 1998, ApJ, 499, 181

Charmandaris, V., et al. 2004, ApJS, 154, 142

Chiu, K., Fan, X., Leggett, S. K., Golimowski, D. A., Zheng, W., Geballe, T. R., Schneider, D. P., & Brinkmann, J. 2006, AJ, 131, 2722

Churchill, C. W., Kacprzak, G. G., & Steidel, C. C. 2005, Proceedings IAU Colloquium No. 199, Probing Galaxies through Quasar Absorption Lines, P. R. Williams, C. Shu, and B. Ménard, eds., astro-ph/0504392

Churchill, C. W., Mellon, R. R., Charlton, J. C., Jannuzi, B. T., Kirhakos, S., Steidel, C. C., & Schneider, D. P. 2000, ApJ, 543, 577

Cirasuolo, M., Magliocchetti, M., Celotti, A., & Danese, L. 2003, MNRAS, 341, 993

Coleman, G. D., Wu, C.-C., & Weedman, D. W. 1980, ApJS, 43, 393

Condon, J. J. 1992, ARA&A, 30, 575

Condon, J. J., Cotton, W. D., Greisen, E. W., Yin, Q. F., Perley, R. A., Taylor, G. B., & Broderick, J. J. 1998, AJ, 115, 1693

Cool, R. J., et al. 2006, AJ, 132, 823

Croom, S. M., Smith, R. J., Boyle, B. J., Shanks, T., Miller, Outram, P. J., & L., Loaring, N. 2004, MNRAS, 317, 1014

Croton, D. J., et al. 2006, MNRAS, 365, 11

de Vries, W. H., Becker, R. H., & White, R. L. 2006, AJ, 131, 666

Dhanda, N., Baldwin, J. A., Bentz, M. C., & Osmer, P. S. 2007, ApJ, 658, 804

Dietrich, M., Appenzeller, I., Vestergaard, M., & Wagner, S. J. 2002, ApJ, 564, 581

Dietrich, M., Appenzeller, I., Hamann, F., Heidt, J., Jäger, K., Vestergaard, M., & Wagner, S. J. 2003, A&A, 398, 891

Dietrich, M., Hamann, F., Appenzeller, I., & Vestergaard, M. 2003, ApJ, 596, 817

Dietrich, M., & Hamann, F. 2004, ApJ, 611, 761

Dijkstra, M., Haiman, Z., & Loeb, A. 2004, ApJ, 613, 646

Djorgovski, S. G., Castro, S., Stern, D., & Mahabal, A. A. 2001, ApJ, 560, L5

Douglas, L. S., Bremer, M. N., Stanway, E. R., & Lehnert, M. D. 2007, MNRAS, 376, 1393

Eisenstein, D. J., et al. 2001, AJ, 122, 2267

Elston, R., Bechtold, J., Hill, G. J., & Ge, J. 1996, ApJ, 456, L13

Elston, R. J., et al. 2006, ApJ, 639, 816

Elvis, M., et al. 1994, ApJS, 95, 1

Elvis, M., Marengo, M, & Karovska, M. 2002, ApJ, 567, L107

Fabricant, D., et al. 2005, PASP, 117, 1411

Fan, X. 1999, AJ, 117, 2528

Fan, X., et al. 1999, AJ, 118, 1

Fan, X., et al. 2000a, AJ, 120, 1167

Fan, X., et al. 2000b, AJ, 119, 1

Fan, X., et al. 2001a, AJ, 122, 2833

Fan, X., et al. 2001b, AJ, 121, 31

Fan, X., et al. 2001c, AJ, 121, 54

Fan, X., Narayanan, V. K., Strauss, M. A., White, R. L., Becker, R. H., Pentericci, L., & Rix, H.-W. 2002, AJ, 123, 1247

Fan, X., et al. 2003, AJ, 125, 1649

Fan, X., et al. 2004, AJ, 128, 515

Fan, X., et al. 2006a, AJ, 131, 1203

Fan, X., et al. 2006b, AJ, 132, 117

Fan, X., Carilli, C. L., & Keating, B. 2006c, ARA&A, 44, 415

Farrah, D., Priddey, R., Wilman, R., Haehnelt, M., & McMahon, R. 2004, ApJ, 611, L13

Fazio, G., et al. 2004, ApJS, 154, 10

Fechner, C., Baade, R., & Reimers, D. 2004, A&A, 418, 857

Fioc, M., & Rocca-Volmerange, B. 1997, A&A, 326, 950

Foltz, C. B., Weymann, R. J., Morris, S. L., & Turnshek, D. A. 1987, ApJ, 317, 450

Fontanot, F., et al. 2007, A&A, 461, 39

Freudling, W., Corbin, M. R., & Korista, K. T. 2003, ApJ, 587, L67

Frey, S., Paragi, Z., Mosoni, L., Gurvits, L. I. 2005, A&A, 436, L13

Friaca, A. C. S., & Terlevich, R. J. 1998, MNRAS, 298, 399

Fukugita, M., Ichikawa, T., Gunn, J. E., Doi, M., Shimasaku, K., & Schneider, D. P. 1996, AJ, 111,1748

Glikman, E., Helfand, D. J., & White, R. L. 2006, ApJ, 640, 579

Glikman, E., Djorgovski, S. G., Stern, D., Bogosavljević, M., & Mahabal, A. 2007, ApJ, 663, L73

Gnedin, N. Y., & Ostriker, J. P. 1997, ApJ, 486, 581

Gnedin, N. Y., 2008, ApJ, 673, L1

Goldschmidt, P., Kukula, M. J., Miller, L., & Dunlop, J. S. 1999, ApJ, 511, 612

Goldschmidt, P., & Miller, L. 1998, MNRAS, 293, 107

Golimowski, D. A., et al. 2004, AJ, 127, 3516

Goodrich, R. W., et al. 2001, ApJ, 561, L23

Gordon, K. D., et al. 2005, PASP, 117, 503

Goto, T. 2006, MNRAS, 371, 769

Gray, A. G., Moore, A. W., Nichol, R. C., Connolly, A. J., Genovese, C., & Wasserman, L. 2004, ASPC, 314, 249

Greggio, L., & Renzini, A. 1983, A&A, 118, 217

Gunn, J. E., & Peterson, B. A. 1965, ApJ, 142, 1633

Gunn, J. E., et al. 1998, AJ, 116, 3040

Gunn, J. E., et al. 2006, AJ, 131, 2332

Haas, M., et al. 2000, A&A, 354, 453

Haas, M., et al. 2003, A&A, 402, 87

Hamann, F., & Ferland, G. 1992, ApJ, 391, L53

Hamann, F., & Ferland, G. 1993, ApJ, 418, 11

Hamann, F., & Ferland, G. 1999, ARA&A, 37, 487

Hamann, F., Korista, K. T., Ferland, G. J., Warner, C., & Baldwin, J. 2002, ApJ, 564, 592

Hamann, F., Warner, C., Dietrich, M., & Ferland, G. 2007, in ASP Conference Proceedings, the Central Engine of Active Galactic Nuclei, ed. L. C. Ho and J.-M. Wang (San Francisco: ASP), in press (astro-ph/0701503)

Hasinger, G., Miyaji, T., & Schmidt, M. 2005, A&A, 441, 417

Hawkins, M. R. S., & Véron, P. 1995, MNRAS, 275, 1102

Heger, A., & Woosley, S. E. 2002, ApJ, 567, 532

Hewett, P. C., Foltz, C. B., & Chaffee, F. H. 1993, ApJ, 406, L43

Hines, D. C., Krause, O., Rieke, G. H., Fan, X., Blaylock, M., & Neugebauer, G. 2006, ApJ, 641, L85

Hogg, D. W., Finkbeiner, D. P., Schlegel, D. J., & Gunn, J. E. 2001, AJ, 122, 2129

Hooper, E. J., Impey, C. D., Foltz, C. B., & Hewett, P. C. 1995, ApJ, 445, 62

Hopkins, P. F., et al. 2004, AJ, 128, 1112

Hopkins, P. F., Hernquist, L., Cox, T. J., Di Matteo, T., Martini, P., Robertson, B., & Springel, V. 2005, ApJ, 630, 705

Hopkins, P. F., Hernquist, L., Cox, T. J., Di Matteo, T., Robertson, B., & Springel, V. 2006, ApJS, 163, 1

Hopkins, P. F., Richards, G. T., & Hernquist, L. 2007, ApJ, 654, 731

Hughes, D. H., Dunlop, J. S., & Rawlings, S. 1997, MNRAS, 289, 766

Ivezić, Ž., et al. 2002, AJ, 124, 2364

Ivezić, Ž., et al. 2004, AN, 325, 583

Ivezić, Ž., et al. 2004, in *AGN Physics with the Sloan Digital Sky Survey*, eds. G. T. Richards and P. B. Hall, ASP Conference Series, Vol. 311, p. 347 (also astro-ph/0310569)

Ivezić, Ž., et al. 2004, in *Multiwavelength AGN Surveys*, eds. R. Mujica and R. Maiolino, World Scientific Publishing Company, Singapore, p. 53 (also astro-ph/0403314)

Iwamuro, F., Motohara, K., Maihara, T., Kimura, M., Yoshii, Y., & Doi, M. 2002, ApJ, 565, 63

Iwamuro, F., Kimura, M., Eto, S., Maihara, T., Motohara, K., Yoshii, Y., & Doi, M. 2004, ApJ, 614, 69

Jannuzi, B. T., & Dey, A. 1999, in ASP Conf. Ser. 191, Photometric Redshifts and High-Redshift Galaxies, ed. R. J. Weymann, L. J. Storrie-Lombardi, M. Sawicki, & R. J. Brunner (San Francisco: ASP), 111

Jiang, L., et al. 2006, AJ, 132, 2127

Jiang, L., et al. 2006, AJ, 131, 2788

Jiang, L., et al. 2007, AJ, 134, 1150

Jiang, L., et al. 2007, ApJ, 656, 680

Jiang, L., et al. 2008a, AJ, 135, 1057

Jiang, L., et al. 2008b, ApJ, 679, 962

Kashikawa, N., et al. 2006, ApJ, 648, 7

Kauffmann, G., & Haehnelt, M. 2000, MNRAS, 311, 576

Kellermann, K. I., Sramek, R., Schmidt, M., Shaffer, D. B., & Green, R. 1989, AJ, 98, 1195

Kelly, B. C., Bechtold, J., Siemiginowska, A., Aldcroft, T., & Sobolewska, M. 2007, ApJ, 657, 116

Kennefick, J. D., Djorgovski, S. G., & De Carvalho, R. R. 1995, AJ, 110, 2553

Knapp, G. R., et al. 2004, AJ, 127, 3553

Kollmeier, J. A., et al. 2006, ApJ, 648, 128

Koo, D. C., & Kron, R. G. 1988, ApJ, 325, 92

Krist, J. 2002, Tiny Tim/SIRTF User's Guide (Pasadena: SSC)

Kurk, J. D. et al. 2007, ApJ, 669, 32

Kurucz, R. 1993, ATLAS9 Stellar Atmosphere Programs and 2 km/s grid. Kurucz CD-ROM No. 13. Cambridge, Mass.: Smithsonian Astrophysical Observatory, 1993, 13

La Franca, F. & Cristiani, S. 1997, AJ, 113, 1517

Lacy, M., Laurent-Muehleisen, S. A., Ridgway, S. E., Becker, R. H., & White, R. L. 2001, ApJ, 551, L17

Laor, A. 2000, ApJ, 543, L111

Li, Y., et al. 2007, ApJ, 665, 187

Lodato, G., & Natarajan, P. 2007, MNRAS, 377, L64

Loeb, A., & Haiman, Z. 1997, ApJ, 490, 571

Lupton, R. H., Gunn, J. E., & Szalay, A. S. 1999, AJ, 118, 1406

Lupton, R. H., Gunn, J. E., Ivezić, Ž., Knapp, G. R., Kent, S., & Yasuda, N. 2001, in *Astronomical Data Analysis Software and Systems X*, edited by F. R. Harnden Jr., F. A. Primini, and H. E. Payne, ASP Conference Proceedings, 238, 269

Madau, P., Haardt, F., & Rees, M. J. 1999, ApJ, 514, 648

Madau, P., & Rees, M. J. 2001, ApJ, 551, L27

Mahabal, A., Stern, d., Bogosavljević, M., Djorgovski, S. G., & Thompson, D. 2005, ApJ, 634, L9

Maiolino, R., Juarez, Y., Mujica, R., Nagar, N. M., & Oliva, E. 2003, ApJ, 596, L155

Maiolino, R., et al. 2004, Nature, 431, 533

Maiolino, R., Oliva, E., Ghinassi, F. Pedani, M., Mannucci, F., Mujica, R., & Juarez, Y. 2004, A&A, 420, 889

Marshall, H. L., Avni, Y., Tananbaum, H., & Zamorani, G. 1983, ApJ, 269, 35

Marshall, H. L., Avni, Y., Braccesi, A., Huchra, J. P., Tananbaum, H., Zamorani, G. & Zitelli, V. 1984, ApJ, 283, 50

Marshall, H. L. 1985, ApJ, 299, 109

Martini, P., & Weinberg, D. H. 2001, ApJ, 547, 12

Mathis, J. S. 1990, ARA&A, 28, 37

Matteucci, F., & Recchi, S. 2001, ApJ, 558, 351

Matthews, T. A., & Sandage, A. R. 1963, ApJ, 138, 30

McGreer, I. D., Becker, R. H., Helfand, D. J., & White, R. L. 2006, ApJ, 652, 157

McIntosh, D. H., Rix, H. W., Rieke, M. J., & Foltz, C. B. 1999, ApJ, 517, L73

McLure, R. J., & Dunlop, J. S. 2004, MNRAS, 352, 1390

McQuinn, M., Hernquist, L., Zaldarriaga, M., & Dutta, S. 2007, MNRAS, 381, 75

Meiksin, A. 2005, MNRAS, 356, 596

Miller, L., Peacock, J. A., & Mead, A. R. G. 1990, MNRAS, 244, 207

Miralda-Escudé, J., Haehnelt, M., & Rees, M. J. 2000, ApJ, 530, 1

Mushotzky, R. F., Cowie, L. L., Barger, A. J., & Arnaud, K. A. 2000, Nature, 404, 459

Nagao, T., Marconi, A., & Maiolino, R. 2006, A&A, 447, 157

Nenkova, M., Ivezić, Ž., & Elitzur, M. 2002, ApJ, 570, L9

Nestor, D. B., Turnshek, D. A., & Rao, S. M. 2005, ApJ, 628, 637

Neugebauer, G., Green, R. F., Matthews, K., Schmidt, M., Soifer, B. T., & Bennett, J. 1987, ApJS, 63, 615

Newberg, H. J., & Yanny, B. 1997, ApJS, 113, 89

O'Donnell, J. E. 1994, ApJ, 422, 158

Oke, J. B., & Gunn, J. E. 1983, ApJ, 266, 713

Osmer, P. S., & Smith, M. G. 1980, ApJS, 42, 333

Padovani, P. 1993, MNRAS, 263, 461

Page, M. J., & Carrera, F. J. 2000, MNRAS, 311, 433

Peacock, J. A., Miller, L., & Longair M. S. 1986, MNRAS, 218, 265

Pei, Y. C. 1995, ApJ, 438, 623

Peng, C. Y., et al. 2006, ApJ, 649, 616

Pentericci, L., et al. 2002, AJ, 123, 2151

Pentericci, L., et al. 2003, A&A, 410, 75

Peterson, B. M. 1997, An introduction to active galactic nuclei, Publisher: Cambridge, New York Cambridge University Press, 1997 Physical description xvi, 238 p. ISBN 0521473489

Peterson, B. M., et al. 2004, ApJ, 613, 682

Petric, A. O., et al. 2003, AJ, 126, 15

Pier, J. R., Munn, J. A., Hindsley, R. B., Hennessy, G. S., Kent, S. M., Lupton, R. H., & Ivezic, Z. 2003, AJ, 125, 1559

Polletta, M., Courvoisier, T. J. -L., Hooper, E. J., & Wilkes, B. J. 2000, A&A, 362, 75

Priddey, R. S., Isaak, K. G., McMahon, R. G., Robson, E. I., & Pearson, C. P. 2003, MNRAS, 344, L74

Prochter, G. E., Prochaska, J. X., & Burles, S. M. 2006, ApJ, 639, 766

Reach, W. T., et al. 2005, PASP, 117, 978

Rees, M. J., & Volonteri, M. 2006, Proceedings IAU Symposium No. 238, Black Holes: from Stars to Galaxies – across the Range of Masses, V. Karas and G. Matt, eds., astro-ph/0701512

Richards, G. T., et al. 2002, AJ, 124, 1

Richards, G. T., et al. 2004, AJ, 127, 1305

Richards, G. T., et al. 2005, MNRAS, 360, 839

Richards, G. T., et al. 2006, ApJS, 166, 470

Richards, G. T., et al. 2006, AJ, 131, 2766

Rieke, G. H., & Lebofsky, M. J. 1981, ApJ, 250, 87

Rieke, G. H., et al. 2004, ApJS, 154, 25

Robson, I., Priddey, R. S., Isaak, K. G., & McMahon, R. G. 2004, MNRAS, 351, L29

Salvaterra, R., Haardt, F., & Volonteri, M. 2007, MNRAS, 374, 761

Sandage, A. 1965, ApJ, 141, 1560

Schinnerer, E., et al. 2004, AJ, 128, 1974

Schlegel, D. J., Finkbeiner, D. P., & Davis, M. 1998, ApJ, 500, 525

Schmidt, M. 1963, Nature, 197, 1040

Schmidt, M., & Green, R. F., et al. 1983, ApJ, 269, 352

Schmidt, M., Schneider, D. P., & Gunn, J. E. 1995, AJ, 110, 68

Schneider, D. P., Schmidt, M., & Gunn, J. E. 1991, AJ, 101, 2004

Schneider, D. P., van Gorkom, J. H., Schmidt, M., & Gunn, J. E. 1992, AJ, 103, 1451

Schneider, D. P., et al. 2003, AJ, 126, 2579

Schneider, D. P., et al. 2005, AJ, 130, 367

Schneider, D. P., et al. 2007, AJ, 134, 102

Schneider, G., & Stobie, E. 2002, in ASP Conf. Ser. 281, Astronomical Data Analysis Software and Systems XI, ed. D. A. Bohlender, D. Durand, & T. H. Handley (San Francisco: ASP), 382

Schwartz, D. A., & Virani, S. N. 2004, ApJ, 615, L21

Scranton, R., et al. 2002, ApJ, 579, 48

Seyfert, C. 1943, ApJ, 97, 28

Shankar, F., & Mathur, S. 2007, ApJ, 660, 1051

Sheinis, A. I., Bolte, M., Epps, H. W., Kibrick, R. I., Miller, J. S., Radovan, M. V., Bigelow, B. C., & Sutin, B. M. 2002, PASP, 114, 851

Shemmer, O., Brandt, W. N., Vignali, C., Schneider, D. P., Fan, X., Richards, G. T., & Strauss, M. A. 2005, ApJ, 630, 729

Shemmer, O., et al. 2006, ApJ, 644, 86

Shen, Y., et al. 2007, AJ, 133, 2222

Shen, Y., Greene, J. E., Strauss, M. A, Richards, G. T., & Schneider, D. P. 2008, ApJ, in press (astro-ph/0709.3098)

Siebenmorgen, R., Haas, M., Krügel, E., & Schulz, B. 2005, A&A, 436, 5L

Silverman, B. W. 1986, Density Estimation for Statistics and Data Analysis, Monographs on Statistics and Applied Probability, Vol. 26 (London: Chapman & Hall)

Skrutskie, M. F., et al. 2006, AJ, 131, 1163

Smith, J. A., et al. 2002, AJ, 123, 2121

Spergel, D. N., et al. 2003, ApJS, 148, 175

Spergel, D. N., et al. 2007, ApJS, 170, 377

Srbinovsky, J. A., & Wyithe, J. S. B. 2007, MNRAS, 374, 627

Steffen, A. T., et al. 2006, AJ, 131, 2826

Steidel, C. C., Kollmeier, J. A., Shapley, A. E., Churchill, C. W., Dickinson, M., & Pettini, M. 2002, ApJ, 570, 526

Steidel, C. C., & Sargent, W. L. W. 1992, ApJS, 80, 1

Stern, D., Djorgovski, S. G., Perley, R. A., de Carvalho, R. R., & Wall, J. V. 2000, AJ, 119, 1526

Stern, D., et al. 2003, ApJ, 596, L39

Stocke, J. T., Morris, S. L., Weymann, R. J., & Foltz, C. B. 1992, ApJ, 396, 487

Stoughton, C., et al. 2002, AJ, 123, 485

Strateva, I. V., Brandt, W. N., Schneider, D. P., Vanden Berk, D. G., & Vignali, C. 2005, AJ, 130, 387

Strauss, M. A. et al. 2002, AJ, 124, 1810

Szentgyorgyi, A. H., Cheimets, P., Eng, R., Fabricant, D. G., Geary, J. C., Hartmann, L., Pieri, M. R., & Roll, J. B. 1998, Proc. SPIE, 3355, 242

Tananbaum, H., et al. 1979, ApJ, 234, L9

Trump, J. R., et al. 2006, ApJS, 165, 1

Tucker, D., et al. 2006, AN, 327, 821 Roll, J. B. 1998, Proc. SPIE, 3355, 242

Ueda, Y., Akiyama, M., Ohta, K., & Miyaji, T. 2003, ApJ, 598, 886

Urry, C. M., & Padovani P. 1995, PASP, 107, 803

Vanden Berk, D. E., et al. 2001, AJ, 122, 549

van Dokkum, P. G. 2001, PASP, 113, 1420

Venemans, B. P., McMahon, R. G., Warren, S. J., Gonzalez-Solares, E. A., Hewett, P. C., Mortlock, D. J., Dye, S., & Sharp, R. G. 2007, MNRAS, 376, L76

Venkatesan, A., Schneider, R., & Ferrara, A. 2004, MNRAS, 349, L43

Vernet, J., Fosbury, R. A. E., Villar-Martín, M., Cohen, M. H., Cimatti, A., di Serego Alighieri, S., & Goodrich, R. W. 2001, A&A, 366, 7

Vestergaard, M. & Wilkes, B. J. 2001, ApJS, 134, 1

Vestergaard, M. 2004, ApJ, 601, 676

Vestergaard, M., & Peterson, B. M. 2006, ApJ, 641, 689

Vignali, C., Brandt, W. N., Schneider, D. P., & Kaspi, S. 2005, AJ, 129, 2519

Vilkoviskij, E. Y., & Irwin, M. J. 2001, MNRAS, 321, 4

Visnovsky, K. L., Impey, C. D., Foltz, C. B., Hewett, P. C., Weymann, R. J., & Morris, S. L. 1992, ApJ, 391, 560

Volonteri, M., & Rees, M. J. 2006, ApJ, 650, 669

Walter, F., et al. 2003, Nature, 424, 406

Walter, F., et al. 2004, ApJ, 615, L17

Wandel, A., Peterson, B. M., & Malkan, M. A. 1999, ApJ, 526, 579

Wang, R., et al. 2007, AJ, 134, 617

Wang, R., et al. 2008, AJ, 135, 1201

Wang, R., et al. 2008, AJ, submitted

Warren, S. J., et al. 2007, MNRAS, 375, 213

Warren, S. J., Hewett, P. C., & Osmer, P. S. 1994, ApJ, 421, 412

Werner, M. W., et al. 2004, ApJS, 154, 1

White, R. L., Becker, R. H., Helfand, D. J., & Gregg, M. D. 1997, ApJ, 475, 479

White, R. L., Helfand, D. J., Becker, R. H., Glikman, E., & de Vries, W. 2007, ApJ, 654, 99

Wilkes, B. J. 2001, New Astronomy Reviews, 45, 641

Willott, C. J., Delfosse, X., Forveille, T., Delorme, P., & Gwyn, S. D. J. 2005, ApJ, 633, 630

Willott, C. J., 2007, AJ, 134, 2435

Wisotzki, L. 2000, A&A, 353, 853

Wolf, C., Wisotzki, L., Borch, A., Dye, S. Kleinheinrich, M., & Meisenheimer, K. 2003, A&A, 408, 499

Worsley, M. A., et al. 2005, MNRAS, 357, 1281

Wyithe, J. S. B., & Loeb, A. 2003, ApJ, 595, 614

Wyithe, J. S. B., & Padmanabhan, T. 2006, MNRAS, 372, 1681

Yan, H., & Windhorst, R. A. 2004, ApJ, 612, L93

York, D. G., et al. 2000, AJ, 120, 1579

Zakamska, N. L., et al. 2003, AJ, 2125, 2144

Zamorani, G., et al. 1981, ApJ, 245, 357

Zheng, W., Kriss, G. A., Telfer, R. C., Grimes, J. P., & Davidsen, A. F. 1997, ApJ, 475, 469